



University  
of Glasgow

Maddock, Christie Alisa (2010) *On the dynamics, navigation and control of a spacecraft formation of solar concentrators in the proximity of an asteroid*. PhD thesis, University of Glasgow.

<http://theses.gla.ac.uk/1572/>

Copyright and moral rights for this thesis are retained by the author

A copy can be downloaded for personal non-commercial research or study, without prior permission or charge

This thesis cannot be reproduced or quoted extensively from without first obtaining permission in writing from the Author

The content must not be changed in any way or sold commercially in any format or medium without the formal permission of the Author

When referring to this work, full bibliographic details including the author, title, awarding institution and date of the thesis must be given

ON THE DYNAMICS, NAVIGATION AND CONTROL  
OF A SPACECRAFT FORMATION OF SOLAR  
CONCENTRATORS IN THE PROXIMITY OF AN  
ASTEROID

CHRISTIE ALISA MADDOCK

Submitted in Fulfilment of the  
Degree of Doctor of Philosophy

Department of Aerospace Engineering  
Faculty of Engineering  
University of Glasgow



© MADDOCK, Christie: 2010

Christie Alisa Maddock: *On the dynamics, navigation and control of a spacecraft formation of solar concentrators in the proximity of an asteroid*, Doctor of Philosophy, Department of Aerospace Engineering, Faculty of Engineering, University of Glasgow  
© 2010

ADVISORS:

Dr. Gianmarco Radice  
Dr. Massimiliano Vasile

EXAMINERS:

Prof Colin McInnes, Strathclyde University  
Dr David Anderson, University of Glasgow

LOCATION:

Glasgow, Scotland

DATE:

February 23, 2010

## EXECUTIVE SUMMARY

---

In 2004, astronomers first sighted the asteroid 2004 MN4, later to be named Apophis. Based on tracking data, in 2029 the asteroid will have a close approach with the Earth. Depending on the outcome of that fly-by, due to the interaction with the Earth's gravity field, it has the potential to set up two possible impact dates in 2036 and 2037. Apophis is only one of 6330 Near Earth Objects (NEO) currently being monitored, with 1067 listed as potentially hazardous. While the probability of an impact is currently very low, it is not impossible. It is estimated that on average, a 100 m diameter asteroid impacts every 100 years, an event equivalent to 2000 atomic bombs. Due the potential danger posed by an impact, many scientists in the last few decades have proposed several deflection methods.

Based on a quantitative comparison of the various options for NEO deflection, one of the more interesting and promising methods employs solar sublimation to actively deviate the orbit of the asteroid. The original concept envisioned a single large reflector; this idea was expanded to a formation of spacecraft orbiting in the vicinity of the NEO, each equipped with a smaller concentrator assembly capable of focusing the solar power at a distance around 1 km and greater. This relieved the strict constraint on the proximity to the asteroid surface, mitigating the effects of the inhomogeneous gravity field, as well as temperature concerns by the high magnification ratio.

This purpose of this thesis is to ascertain whether solar sublimation is a viable method for the deflection of a Near Earth Asteroid. From a research view point, the methods and analysis are applicable to proximal motion around a celestial body, in particular one with a non-Keplerian or irregular orbit as in the case here with the orbit being constantly altered by the deflection action and subject to perturbations, such as solar radiation pressure.

Two concepts, and the corresponding dynamics and control, are presented based on previous trade-off and optimisation studies. The first uses a paraboloidic reflector to concentrate the solar radiation onto a solar-pumped laser, which is then directed onto a specific spot on the NEO by a small directional mirror. The spacecraft orbits are designed to fly in formation with the asteroid around the Sun, and are based on the orbital element differences. The formation orbits were optimised for two objective functions, one minimising the range while restricting the orbit to outside a limit sphere (in order to avoid the non-linearities of the close-proximity gravitation field of the asteroid), and the other maximising the distance in the  $x$ - $z$  plane in order to avoid the debris plume. A feedback control law is presented for the orbital maintenance required to counteract the solar radiation pressure (due primarily to the large surface area of the primary reflector), and the third-body effects due to the gravitational field of the asteroid.

The second option takes advantage of the balance between the gravity attraction of the NEO and solar pressure acting on the collector. Instead of using a laser and directional mirror, the mirror focuses the light directly onto the asteroid surface, controlling the beam by adjusting the focal point of the primary reflector. By altering the shape of the mirror surface, both the focal point and the vector of the solar radiation pressure can be manipulated. This has the advantage of being frequency independent, compared to the laser which is restricted to a given wavelength but is in closer proximity to the asteroid. A minimal amount of control, on the order of  $10^{-5}$  N,

is required to keep the spacecraft at an artificial equilibrium point, which oscillates with true anomaly.

A key requirement for the successful implementation of the multi-mirror approach is that each spacecraft must know its position relative to both the NEO and the other spacecraft in the formation, and be able to find and maintain the direction of the beam onto a precise spot on the surface of the asteroid. An interesting navigation strategy is proposed based on the attitude measurements, the inertial position of each spacecraft, the intersatellite position and velocity measurements, and a 2D image from a rotating onboard camera. Once the formation is deployed in the vicinity of the NEO, one spacecraft is temporarily designated as leader and searches the predicted location of the NEO until it is within the field of view of the camera. Using simple geometry, the centroid of the image is determined, and aligned with the boresight of the camera. The pointing vector from the lead spacecraft is then relayed to the whole formation. Once all the spacecraft have acquired the centre of the NEO, the spacecraft-asteroid range can be triangulated. The navigational data is used for both the orbital control of the spacecraft and for the beam pointing.

The results of simulations of a hypothetical deflection mission of the NEO Apophis are presented for the dynamics, control, attitude and navigation, accounting for solar radiation pressure, the gravity field of the asteroid, and the deviation of the NEO orbit. The results show that both concepts provide the required deflection with a feasible mass at launch, solving most of the issues related to the solar sublimation method.

One of the critical aspects of this deflection concept is properly placing the concentrators in the proximity of the asteroid in order to avoid the plume impingement and the occultation from the asteroid itself. Issues regarding the contamination of the mirrors are addressed and compared with the simulated deflections predicted considering no contamination. Lastly, initial system mass budgets are presented.

## CONTENTS

---

Executive Summary	iii
Contents	v
List of Figures	vii
List of Tables	xviii
Nomenclature	xix
Dedication and Acknowledgments	xxv
Declaration	xxvi
Publications	xxvii
1 Introduction	1
1.1 Purpose and report structure	1
1.2 Near Earth Objects	2
1.2.1 Classification of Asteroids	3
1.2.2 Deflection of Near Earth Objects	6
1.2.3 Comparison of NEO Deflection Methods	8
1.2.4 Solar sublimation	11
2 System Design	14
2.1 Conceptual Design	14
2.1.1 Fixed mirror configuration	15
2.1.2 Adaptive mirror configuration	17
2.2 Optical Systems	18
2.2.1 Solar properties	18
2.2.2 Direct imaging	21
2.2.3 Collimating lens	26
2.2.4 Solar-pumped laser	29
2.2.5 Discussion	33
2.3 Mass Budget	34
3 Orbital Dynamics and Control	41
3.1 Background	41
3.1.1 Introduction to formation flying	41
3.1.2 Proximal motion	45
3.2 Asteroid deflection model	50
3.3 Funnel orbit dynamics	58
3.3.1 Optimisation of the initial state vector	58
3.4 Artificial equilibrium points	75
3.4.1 AEP in three dimensional space	80
3.5 Perturbations	85
3.5.1 Solar radiation pressure	85

3.5.2	Third body effects	87
3.6	Funnel control	87
3.6.1	Proximity-quotient control law	93
3.6.2	Orbital maintenance control law	93
3.6.3	Discussion	98
3.7	Control of AEPs	112
3.7.1	Adaptive mirror with laser	112
3.7.2	Adaptive mirror with direct imaging	115
4	Navigation and Orbit Determination	120
4.1	Introduction	120
4.2	Coordinate transformation	120
4.3	Simulation model	121
4.4	Discussion	126
5	Deflection Simulations	139
5.1	Simulation results	139
5.1.1	Trade-off optimisation	155
5.2	Debris contamination	160
5.3	Enhanced Yarkovsky Effect	167
5.4	Discussion	168
6	Conclusion	171
6.1	Future work	172
A	Analytical derivations of proximal motion equations	174
A.1	Non-linear relative equations of motion	174
A.2	Linear relative equations of motion	177
B	Optimisation routines	184
B.1	Optimisation procedure	184
B.2	General problem formulation	184
B.3	Behavioural-based search	185
B.4	Domain decomposition	187
B.5	Single versus multiple objective optimisation	188
B.6	Constraint handling technique	189
B.7	Preliminary optimisation test cases	190
C	Equations for the Proximity-Quotient control law	194
C.1	Derivation of equations	194
C.2	Discussion	200
D	Funnel control results	209
	Bibliography	254

## LIST OF FIGURES

---

Figure 1	The inner Solar System from the Sun to Jupiter, including the Main Asteroid belt, Trojans, Greeks and Hildas clusters.	4
Figure 2	Known objects in the Kuiper belt and outer Solar System.	4
Figure 3	Orbits of four asteroids representing each of the four classes of NEAs.	5
Figure 4	Total number of discovered Near Earth Objects by date.	6
Figure 5	Sets of Pareto optimal solutions for various deflection methods evaluating warning time, achieved deflection distance and initial mass in orbit of the spacecraft.	9
Figure 6	Schematic illustration of a solar collector deflection system.	12
Figure 7	Possible configurations for the mirror assembly.	16
Figure 8	Definition of mirror-centric relative reference frame $\mathcal{M}$ .	18
Figure 9	Single mirror projecting the Sun onto a 2D focal point.	19
Figure 10	ASTM Standard Extraterrestrial Spectrum Reference.	20
Figure 11	Composite of total solar irradiance	21
Figure 12	Angle between mirror surface normal and incoming rays.	22
Figure 13	Example of direct imaging of the solar disk using an 100 m diameter, fixed paraboloidal reflector, and showing the difference in beam directions and widths at the maximum and minimum angle of reflection $\phi$ .	23
Figure 14	Direct imaging of solar disk on Apophis using an adaptive paraboloidal reflector. The mirror is located along the $y$ -axis, and the asteroid is located at the minimum beam width, at 780 m.	24
Figure 15	Analysis of the image of Sun	25
Figure 16	Lens configuration for collimating parallel incoming solar rays	27
Figure 17	Effect of off-axis rays on the lenses	28
Figure 18	Radiator area vs. radiator temperature	30
Figure 19	Nd:YAG absorption bands compared with the standard extraterrestrial solar spectrum.	32
Figure 20	Surface area of reflector versus number of spacecraft, for various concentration ratios.	40
Figure 21	Formation flying missions.	43
Figure 22	Hill reference frames for a chief-deputy spacecraft formation.	46
Figure 23	Geometric representation of the true $\nu$ and eccentric $E$ anomalies of an elliptical Keplerian orbit.	49
Figure 24	Ellipsoid model used for the asteroid.	51
Figure 25	Orbit of the NEO Apophis, compared to the orbits of the Mars, Earth and Venus.	52
Figure 26	Definition of deviation distance at the MOID.	53
Figure 27	Relative error between the linear and nonlinear forms of the proximal motion equations as a function of the ratio of the maximum $\delta r/r$ .	54
Figure 28	Amount of time a point spends under the spot beam on the asteroid surface versus minimum required power density level for sublimation, for a nominal 1 m diameter spot.	57

Figure 29	The cross-comparison of the best 30 solutions of $\xi_x$ found using EPIC. The distances are measured in km, velocities in $10^{-9}$ km/s and time in MJD2000. 60
Figure 30	Orthographic view of the optimal formation orbit, including the initial state vector (shown as a diamond), and location relative to Apophis (shown as a brown circle). 61
Figure 31	Orbit of Apophis showing the optimal $t_0$ for the two solutions. 62
Figure 32	Orthographic view of the formation orbit optimised over an 1 year period, showing the initial state vector (shown as a diamond), and location relative to Apophis (shown as a brown circle). 63
Figure 33	Cross-comparison of the solution vector $\xi_T$ for the SOO using EPIC. 64
Figure 34	Range of all optimised values for the objective function $J_T$ from all runs. 65
Figure 35	Comparison of the values for the solution vector $\xi_k$ for each of the results of the optimisation. 65
Figure 36	Orbital geometry of solutions from family A, $J_T \approx 2.9$ . 66
Figure 37	Orbital geometry of solutions from family B, $J_T \approx 45.6$ . 66
Figure 38	Orbital geometry of solutions from family C, $J_T \approx 80.4$ . 67
Figure 39	Illustration of debris plume relative to the desired spacecraft formation orbit. 68
Figure 40	Overview of all Pareto-optimal orbits for objective functions $J_{D1}$ and $J_{D2}$ . The initial state is shown as a circle on the orbits, with the asteroid located in the centre of the Hill frame. 69
Figure 41	Cross comparison of the solution vector $\xi$ for the MOO using EPIC. 71
Figure 42	Optimal Pareto front for MOO illustrating the trade-off in accuracy of the beam. The red circles represent the two solution points given in Table 16. 71
Figure 43	Formation orbit minimising the $J_{D3}$ value. 72
Figure 44	Formation orbit minimising the $J_{D4}$ value. 73
Figure 45	Definition of mirror-centric relative reference frame 76
Figure 46	Angular misalignment between the position vector and SRP. 77
Figure 47	Example of AEP at $20^\circ$ from the radial direction. 78
Figure 48	Increase in the spot size as a function of the elevation above the $y$ axis. 78
Figure 49	Artificial equilibrium points for different mirror sizes. 79
Figure 50	Variation of the equilibrium points for an ellipsoidal model 80
Figure 51	Balance between solar pressure and gravity forces for different concentration ratios, where $r\text{-Sp}$ denotes the line where the two forces are in balance, $\Sigma F = 0$ . 81
Figure 52	Spacecraft configuration with respect to the asteroid. 82
Figure 53	Conceptual spacecraft configuration using AEPs in three dimensions. 83
Figure 54	Reference frame for the three dimensional mirror design. 83
Figure 55	Single 3D mirror projecting the Sun onto a focal point. 84
Figure 56	Vectors of solar radiation pressure on a fixed mirror configuration. 85

Figure 57	Force due to solar radiation pressure on the various surfaces of the spacecraft. 88
Figure 58	Total force due to solar radiation pressure. 89
Figure 59	Force due to third body effects from the NEO. 90
Figure 60	Total perturbing force acting on the spacecraft. 91
Figure 61	Effect of total perturbing acceleration on the spacecraft orbit parameters. 92
Figure 62	Variation in the orbital elements over one orbit of Apophis. 96
Figure 63	Formation orbits for test cases, shown in the Hill reference frame $\mathcal{A}$ relative to Apophis, located at (0,0). The initial position at $t_0$ is shown as a solid circle on the orbit. 98
Figure 64	Integration control law for spacecraft formation $\delta\mathbf{k}_{5/1}$ at time step of $\delta t = 1$ s using the fixed mirror configuration with a system efficiency of 25%. 100
Figure 65	Integration control law for spacecraft formation $\delta\mathbf{k}_{5/1}$ at time step of $\delta t = 1$ s using the fixed mirror configuration with a system efficiency of 25%. 101
Figure 66	Integration control law for spacecraft formation $\delta\mathbf{k}_{5/1}$ at time step of $\delta t = 10$ s using the fixed mirror configuration with a system efficiency of 25%. 102
Figure 67	Integration control law for spacecraft formation $\delta\mathbf{k}_{5/1}$ at time step of $\delta t = 10$ s using the fixed mirror configuration with a system efficiency of 25%. 103
Figure 68	Integration control law for spacecraft formation $\delta\mathbf{k}_{5/1}$ at time step of $\delta t = 60$ s using the fixed mirror configuration with a system efficiency of 25%. 104
Figure 69	Integration control law for spacecraft formation $\delta\mathbf{k}_{5/1}$ at time step of $\delta t = 60$ s using the fixed mirror configuration with a system efficiency of 25%. 105
Figure 70	Least squares control law for spacecraft formation $\delta\mathbf{k}_{5/1}$ at time step of $\delta t = 1$ s using the fixed mirror configuration with a system efficiency of 25% and weights, $W = [1e-6, 1e6, 1, 1, 1, 1]$ . 106
Figure 71	Least squares control law for spacecraft formation $\delta\mathbf{k}_{5/1}$ at time step of $\delta t = 1$ s using the fixed mirror configuration with a system efficiency of 25% and weights, $W = [1e-6, 1e6, 1, 1, 1, 1]$ . 107
Figure 72	Least squares control law for spacecraft formation $\delta\mathbf{k}_{5/1}$ at time step of $\delta t = 10$ s using the fixed mirror configuration with a system efficiency of 25% and weights, $W = [1e-6, 1e6, 1, 1, 1, 1]$ . 108
Figure 73	Least squares control law for spacecraft formation $\delta\mathbf{k}_{5/1}$ at time step of $\delta t = 10$ s using the fixed mirror configuration with a system efficiency of 25% and weights, $W = [1e-6, 1e6, 1, 1, 1, 1]$ . 109
Figure 74	Least squares control law for spacecraft formation $\delta\mathbf{k}_{5/1}$ at time step of $\delta t = 60$ s using the fixed mirror configuration with a system efficiency of 25% and weights, $W = [1e-6, 1e6, 1, 1, 1, 1]$ . 110
Figure 75	Least squares control law for spacecraft formation $\delta\mathbf{k}_{5/1}$ at time step of $\delta t = 60$ s using the fixed mirror configuration with a system efficiency of 25% and weights, $W = [1e-6, 1e6, 1, 1, 1, 1]$ . 111
Figure 76	Variation of the equilibrium points with the true anomaly for $A_M = 196 \text{ m}^2$ . 112

Figure 77	Control profile for orbit maintenance for ( $A = 196 \text{ m}^2, \beta = 139^\circ, \nu_0 = \pi$ ) maintaining a fixed position in the Hill frame	114
Figure 78	Control profile for orbit maintenance for ( $A = 196 \text{ m}^2, \beta = 139^\circ$ ) following the motion of the AEP.	114
Figure 79	Control for following AEP for a non-spherical asteroid	115
Figure 80	Spacecraft mass after fuel consumption for Lyapunov controlled AEPs.	117
Figure 81	Variation in position over one orbit shown in the local mirror reference frame, for Lyapunov controlled AEPs.	118
Figure 82	Thrust magnitude for Lyapunov controlled AEPs.	119
Figure 83	Camera reference frame $\mathcal{Z}$ shown in inertial frame (not to scale).	121
Figure 84	Quaternions and rotational angle $\psi$ for transformation from inertial $\mathcal{O}$ to camera $\mathcal{Z}$ reference frame, for orbit $\delta\mathbf{k}_{5/1}$ .	122
Figure 85	Quaternions and rotational angle $\psi$ for transformation from inertial $\mathcal{O}$ to camera $\mathcal{Z}$ reference frame, for orbit $\delta\mathbf{k}_{5/3}$ .	122
Figure 86	Quaternions and rotational angle $\psi$ for transformation from inertial $\mathcal{O}$ to camera $\mathcal{Z}$ reference frame, for orbit $\delta\mathbf{k}_{5/5}$ .	123
Figure 87	Navigation strategy using on-board cameras.	123
Figure 88	Asteroid representations for navigation simulation.	124
Figure 89	Positions of the estimated centres relative to the actual centre of Apophis with camera A and error set B, taken at a nominal true anomaly $\nu = 20^\circ$ .	126
Figure 90	Mean and standard deviation (shown as error bars) of estimated centres relative to the actual centre of Apophis in the heliocentric inertial reference frame $\mathcal{O}$ , over one full orbit using 5 spacecraft each with camera A, error set A (no errors).	128
Figure 91	Mean and standard deviation (shown as error bars) of estimated centres relative to the actual centre of Apophis in the heliocentric inertial reference frame $\mathcal{O}$ , over one full orbit using 5 spacecraft each with camera A, error set B.	129
Figure 92	Mean and standard deviation (shown as error bars) of estimated centres relative to the actual centre of Apophis in the heliocentric inertial reference frame $\mathcal{O}$ , over one full orbit using 5 spacecraft each with camera A, error set C.	130
Figure 93	Mean and standard deviation (shown as error bars) of estimated centres relative to the actual centre of Apophis in the heliocentric inertial reference frame $\mathcal{O}$ , over one full orbit using 5 spacecraft each with camera A, error set D.	131
Figure 94	Mean and standard deviation (shown as error bars) of estimated centres relative to the actual centre of Apophis in the heliocentric inertial reference frame $\mathcal{O}$ , over one full orbit using 5 spacecraft each with camera B, error set A (no errors).	132
Figure 95	Mean and standard deviation (shown as error bars) of estimated centres relative to the actual centre of Apophis in the heliocentric inertial reference frame $\mathcal{O}$ , over one full orbit using 5 spacecraft each with camera B, error set B.	133
Figure 96	Mean and standard deviation (shown as error bars) of estimated centres relative to the actual centre of Apophis in the heliocentric inertial reference frame $\mathcal{O}$ , over one full orbit using 5 spacecraft each with camera B, error set C.	134

Figure 97	Mean and standard deviation (shown as error bars) of estimated centres relative to the actual centre of Apophis in the heliocentric inertial reference frame $\mathcal{O}$ , over one full orbit using 5 spacecraft each with camera B, error set D. 135
Figure 98	Mean and standard deviation (shown as error bars) of estimated centres relative to the actual centre of Apophis in the heliocentric inertial reference frame $\mathcal{O}$ , over one full orbit using 5 spacecraft each with camera C, error set A (no errors). 136
Figure 99	Mean and standard deviation (shown as error bars) of estimated centres relative to the actual centre of Apophis in the heliocentric inertial reference frame $\mathcal{O}$ , over one full orbit using 5 spacecraft each with camera C, error set B. 137
Figure 100	Mean and standard deviation (shown as error bars) of estimated centres relative to the actual centre of Apophis in the heliocentric inertial reference frame $\mathcal{O}$ , over one full orbit using 5 spacecraft each with camera C, error set C. 138
Figure 101	Deviation of Keplerian elements for Apophis, with a warning time of 5 years before the 2036 potential impact for a deviation distance of 384400 km in 2036. 140
Figure 102	Concentration ratio vs required thrust time for a single 60 m diameter mirror using direct imaging to achieve a deflection of 20000 km at the 2036 MOID. 141
Figure 103	Concentration ratio vs required thrust time for a single 60 m diameter mirror using the laser to achieve a deflection of 20000 km at the 2036 MOID. 142
Figure 104	Effect of orbital location at the start of thrust period, on the required duration to achieve a deflection of 10000 km at $t_{\text{MOID}} = 64796.56736$ MJD using a single 60 m mirror with direct imaging ( $C_r = 1000$ ). 143
Figure 105	Total asteroid debris mass expelled by sublimation vs a system concentration factor which is composed of the number of spacecraft in the formation multiplied by the individual concentration ratio of each onboard focusing system. 144
Figure 106	Deflection distance for various concentration ratios and number of spacecraft, assuming a 2 m aperture diameter primary mirror with laser ( $\eta_{sys} = 25\%$ ), a warning time of $5T_A$ (1617 days), and a thrust period of $5T_A$ (1617 days). 145
Figure 107	Deflection distance for various concentration ratios and number of spacecraft, assuming a 5 m aperture diameter primary mirror with laser ( $\eta_{sys} = 25\%$ ), a warning time of $2T_A$ (647 days), and a thrust period of $2T_A$ (647 days). 145
Figure 108	Deflection distance for various concentration ratios and number of spacecraft, assuming a 5 m aperture diameter primary mirror with laser ( $\eta_{sys} = 25\%$ ), a warning time of $4T_A$ (1294 days), and a thrust period of $2T_A$ (647 days). 146
Figure 109	Deflection distance for various concentration ratios and number of spacecraft, assuming a 5 m aperture diameter primary mirror with laser ( $\eta_{sys} = 25\%$ ), a warning time of $6T_A$ (1941 days), and a thrust period of $2T_A$ (647 days). 146

Figure 110	Deflection distance for various concentration ratios and number of spacecraft, assuming a 10 m aperture diameter primary mirror with laser ( $\eta_{sys} = 25\%$ ), a warning time of $2T_A$ (647 days), and a thrust period of $2T_A$ (647 days). 147
Figure 111	Deflection distance for various concentration ratios and number of spacecraft, assuming a 10 m aperture diameter primary mirror with laser ( $\eta_{sys} = 25\%$ ), a warning time of $4T_A$ (1294 days), and a thrust period of $2T_A$ (647 days). 147
Figure 112	Deflection distance for various concentration ratios and number of spacecraft, assuming a 10 m aperture diameter primary mirror with laser ( $\eta_{sys} = 25\%$ ), a warning time of $6T_A$ (1941 days), and a thrust period of $2T_A$ (647 days). 148
Figure 113	Deflection distance for various concentration ratios and number of spacecraft, assuming a 20 m aperture diameter primary mirror with laser ( $\eta_{sys} = 25\%$ ), a warning time of $2T_A$ (647 days), and a thrust period of $2T_A$ (647 days). 148
Figure 114	Deflection distance for various concentration ratios and number of spacecraft, assuming a 20 m aperture diameter primary mirror with laser ( $\eta_{sys} = 25\%$ ), a warning time of $4T_A$ (1294 days), and a thrust period of $4T_A$ (1294 days). 149
Figure 115	Deflection distance for various concentration ratios and number of spacecraft, assuming a 20 m aperture diameter primary mirror with laser ( $\eta_{sys} = 25\%$ ), a warning time of $6T_A$ (1941 days), and a thrust period of $2T_A$ (647 days). 149
Figure 116	Deflection distance for various concentration ratios and number of spacecraft, assuming a 30 m diameter adaptive mirror with direct imaging ( $\eta_{sys} = 90\%$ ), a warning time of $5T_A$ (1617 days), and a thrust period of $5T_A$ (1617 days). 150
Figure 117	Deflection distance for various concentration ratios and number of spacecraft, assuming a 60 m diameter adaptive mirror with direct imaging ( $\eta_{sys} = 90\%$ ), a warning time of $6T_A$ (1941 days), and a thrust period of $2T_A$ (647 days). 150
Figure 118	Deflection distance for various concentration ratios and number of spacecraft, assuming a 60 m diameter adaptive mirror with direct imaging ( $\eta_{sys} = 90\%$ ), a warning time of $1T_A$ (323 days), and a thrust period of $1T_A$ (323 days). 151
Figure 119	Deflection distance for various warning and thrust times and number of spacecraft, assuming a 20 m diameter adaptive mirror with a laser ( $\eta_{sys} = 25\%$ ) and a concentration ratio of 2000. 151
Figure 120	Deflection distance for various warning and thrust times and number of spacecraft, assuming a 5 m diameter adaptive mirror with a laser ( $\eta_{sys} = 25\%$ ) and a concentration ratio of 2000. 152
Figure 121	Deflection distance for various warning and thrust times and number of spacecraft, assuming a 5 m diameter adaptive mirror with a laser ( $\eta_{sys} = 25\%$ ) and a concentration ratio of 3000. 152

Figure 122	Deflection distance for various warning and thrust times and number of spacecraft, assuming a 50 m diameter adaptive mirror with direct imaging ( $\eta_{sys} = 90\%$ ) and a concentration ratio of 50. 153
Figure 123	Deflection distance for various warning and thrust times and number of spacecraft, assuming a 65 m diameter adaptive mirror with direct imaging ( $\eta_{sys} = 90\%$ ) and a concentration ratio of 70. 153
Figure 124	Deflection distance for various warning and thrust times and number of spacecraft, assuming a 65 m diameter adaptive mirror with direct imaging ( $\eta_{sys} = 90\%$ ) and a concentration ratio of 100. 154
Figure 125	Pareto front for primary mirror aperture diameter, spacecraft mass and deflection distance at the MOID. 157
Figure 126	Pareto front for primary mirror aperture diameter, number of spacecraft in the formation, and concentration ratio. 157
Figure 127	Pareto front for concentration ratio, spacecraft mass and deflection distance at the MOID. 158
Figure 128	Pareto front for number of spacecraft in the formation, primary mirror aperture diameter and warning time. 158
Figure 129	Pareto front for number of spacecraft in the formation, spacecraft mass and deflection distance at the MOID. 159
Figure 130	Height (or depth) of contaminant on mirror surface, and power degradation factor for a 7 year sample mission, operating with a 20 m aperture diameter fixed mirror. 162
Figure 131	Deflection as a function of concentration ratio and number of spacecraft, including mirror contamination, for a 2 m primary mirror, a warning and thrust time of $5T_A$ and a system efficiency of 25%. See Fig. 106 for comparison. 163
Figure 132	Deflection as a function of concentration ratio and number of spacecraft, including mirror contamination, for a 10 m primary mirror, a warning and thrust time of $4T_A$ and a system efficiency of 25%. See Fig. 111 for comparison. 163
Figure 133	Deflection as a function of concentration ratio and number of spacecraft, including mirror contamination, for a 20 m primary mirror, a warning and thrust time of $4T_A$ and a system efficiency of 25%. See Fig. 114 for comparison. 164
Figure 134	Deflection as a function of concentration ratio and number of spacecraft, including mirror contamination, for a 30 m primary mirror, a warning and thrust time of $5T_A$ and a system efficiency of 90%. See Fig. 116 for comparison. 164
Figure 135	Deflection as a function of the warning time and number of spacecraft, including mirror contamination, for a 20 m primary mirror, concentration ratio of 2000 and a system efficiency of 25%. See Fig. 119 for comparison. 165
Figure 136	Deflection as a function of the warning time and number of spacecraft, including mirror contamination, for a 50 m primary mirror, concentration ratio of 50 and a system efficiency of 90%. See Fig. 122 for comparison. 165

Figure 137	Deflection as a function of the warning time and number of spacecraft, including mirror contamination, for a 65 m primary mirror, concentration ratio of 100 and a system efficiency of 90%. See Fig. 124 for comparison. 166	
Figure 138	Total thrust due to combined Yarkovsky and solar pressure effects. 168	
Figure 139	Deflection achievable with the enhanced Yarkovsky effect. 169	
Figure 140	Inertial Cartesian system of the central body $\mathcal{O}\{\hat{i}, \hat{j}, \hat{k}\}$ and perifocal coordinate system $\mathcal{P}\{\hat{x}, \hat{y}, \hat{z}\}$ , where $x$ points towards the periapsis of the orbit, $x$ - $y$ lie in the orbital plane and $z$ is normal to $x$ - $y$ . 175	
Figure 141	Hill Cartesian reference frames for objects $A$ and $B$ , including vectors. NOTE: the diagram is not to scale. 175	
Figure 142	Action selection mechanism for individualistic behaviour. 186	
Figure 143	Overall algorithm for the Multiagent Collaborative Search (MACS) 187	
Figure 144	Hybrid domain decomposition and stochastic search. 188	
Figure 145	Admissible Pareto front for the test case $DEB$ . 191	
Figure 146	Admissible Pareto fronts for the test case $ZDT4$ . 192	
Figure 147	In-plane angle $\alpha$ of thrust acceleration vector $\mathbf{u}$ which lies in the orbital plane and measured positive clockwise from the tangential axis; and the out-of-plane angle $\beta$ , measured from the orbital plane and positive in the direction of the angular momentum vector. 195	
Figure 148	Values of $dQ/dt$ for the range of thrust angles $\alpha, \beta$ , and weights $W = [1, 0, 0, 0, 0]$ . The maximum $\blacktriangle$ and minimum $\blacktriangledown$ points for $dQ/dT$ found by the local optimiser are indicated. 202	
Figure 149	Values of $dQ/dt$ for the range of thrust angles $\alpha, \beta$ , and weights $W = [0, 1, 0, 0, 0]$ . The maximum $\blacktriangle$ and minimum $\blacktriangledown$ points for $dQ/dT$ found by the local optimiser are indicated. 203	
Figure 150	Values of $dQ/dt$ for the range of thrust angles $\alpha, \beta$ , and weights $W = [0, 0, 1, 0, 0]$ . The maximum $\blacktriangle$ and minimum $\blacktriangledown$ points for $dQ/dT$ found by the local optimiser are indicated. 203	
Figure 151	Values of $dQ/dt$ for the range of thrust angles $\alpha, \beta$ , and weights $W = [0, 0, 0, 1, 0]$ . The maximum $\blacktriangle$ and minimum $\blacktriangledown$ points for $dQ/dT$ found by the local optimiser are indicated. 204	
Figure 152	Values of $dQ/dt$ for the range of thrust angles $\alpha, \beta$ , and weights $W = [0, 0, 0, 0, 1]$ . The maximum $\blacktriangle$ and minimum $\blacktriangledown$ points for $dQ/dT$ found by the local optimiser are indicated. 204	
Figure 153	Change in orbital elements during a transfer around the Earth, with $a$ from 7452.7 $\rightarrow$ 9000 km, and $e$ from 0.2 $\rightarrow$ 0.4. The variance between the initial to final orbit for other free parameters are: $(i_T - i_0) = \Delta i = 3.9082e-8$ rad, $\Delta\Omega = 1.8859e-7$ rad and $\Delta\omega = -0.01812$ rad. 206	
Figure 154	Orbital transfer shown in the Earth-centric inertial (ECI) reference frame. The total transfer time is 3.5 days. 207	
Figure 155	Direction of thrust vector calculated by $\dot{Q}_n$ . The maximum magnitude of the applied thrust is 60 N, for a 2000 kg spacecraft. 208	



Figure 172	Least squares control law for spacecraft formation $\delta\mathbf{k}_{5/2}$ at time step of $\delta t = 60$ s using the fixed mirror configuration with a system efficiency of 25% and weights, $W = [1e-6, 1e6, 1, 1, 1, 1]$ . 226
Figure 173	Least squares control law for spacecraft formation $\delta\mathbf{k}_{5/2}$ at time step of $\delta t = 60$ s using the fixed mirror configuration with a system efficiency of 25% and weights, $W = [1e-6, 1e6, 1, 1, 1, 1]$ . 227
Figure 174	Least squares control law for spacecraft formation $\delta\mathbf{k}_{5/3}$ at time step of $\delta t = 60$ s using the fixed mirror configuration with a system efficiency of 25% and weights, $W = [1e-6, 1e6, 1, 1, 1, 1]$ . 228
Figure 175	Least squares control law for spacecraft formation $\delta\mathbf{k}_{5/3}$ at time step of $\delta t = 60$ s using the fixed mirror configuration with a system efficiency of 25% and weights, $W = [1e-6, 1e6, 1, 1, 1, 1]$ . 229
Figure 176	Least squares control law for spacecraft formation $\delta\mathbf{k}_{5/4}$ at time step of $\delta t = 60$ s using the fixed mirror configuration with a system efficiency of 25% and weights, $W = [1e-6, 1e6, 1, 1, 1, 1]$ . 230
Figure 177	Least squares control law for spacecraft formation $\delta\mathbf{k}_{5/4}$ at time step of $\delta t = 60$ s using the fixed mirror configuration with a system efficiency of 25% and weights, $W = [1e-6, 1e6, 1, 1, 1, 1]$ . 231
Figure 178	Least squares control law for spacecraft formation $\delta\mathbf{k}_{5/5}$ at time step of $\delta t = 60$ s using the fixed mirror configuration with a system efficiency of 25% and weights, $W = [1e-6, 1e6, 1, 1, 1, 1]$ . 232
Figure 179	Least squares control law for spacecraft formation $\delta\mathbf{k}_{5/5}$ at time step of $\delta t = 60$ s using the fixed mirror configuration with a system efficiency of 25% and weights, $W = [1e-6, 1e6, 1, 1, 1, 1]$ . 233
Figure 180	Integration control law for spacecraft formation $\delta\mathbf{k}_{5/2}$ at time step of $\delta t = 1$ s using the fixed mirror configuration with a system efficiency of 25%. 234
Figure 181	Integration control law for spacecraft formation $\delta\mathbf{k}_{5/2}$ at time step of $\delta t = 1$ s using the fixed mirror configuration with a system efficiency of 25%. 235
Figure 182	Integration control law for spacecraft formation $\delta\mathbf{k}_{5/3}$ at time step of $\delta t = 1$ s using the fixed mirror configuration with a system efficiency of 25%. 236
Figure 183	Integration control law for spacecraft formation $\delta\mathbf{k}_{5/3}$ at time step of $\delta t = 1$ s using the fixed mirror configuration with a system efficiency of 25%. 237
Figure 184	Integration control law for spacecraft formation $\delta\mathbf{k}_{5/4}$ at time step of $\delta t = 1$ s using the fixed mirror configuration with a system efficiency of 25%. 238
Figure 185	Integration control law for spacecraft formation $\delta\mathbf{k}_{5/4}$ at time step of $\delta t = 1$ s using the fixed mirror configuration with a system efficiency of 25%. 239
Figure 186	Integration control law for spacecraft formation $\delta\mathbf{k}_{5/5}$ at time step of $\delta t = 1$ s using the fixed mirror configuration with a system efficiency of 25%. 240
Figure 187	Integration control law for spacecraft formation $\delta\mathbf{k}_{5/5}$ at time step of $\delta t = 1$ s using the fixed mirror configuration with a system efficiency of 25%. 241

Figure 188	Integration control law for spacecraft formation $\delta\mathbf{k}_{5/2}$ at time step of $\delta t = 10$ s using the fixed mirror configuration with a system efficiency of 25%. 242
Figure 189	Integration control law for spacecraft formation $\delta\mathbf{k}_{5/2}$ at time step of $\delta t = 10$ s using the fixed mirror configuration with a system efficiency of 25%. 243
Figure 190	Integration control law for spacecraft formation $\delta\mathbf{k}_{5/3}$ at time step of $\delta t = 10$ s using the fixed mirror configuration with a system efficiency of 25%. 244
Figure 191	Integration control law for spacecraft formation $\delta\mathbf{k}_{5/3}$ at time step of $\delta t = 10$ s using the fixed mirror configuration with a system efficiency of 25%. 245
Figure 192	Integration control law for spacecraft formation $\delta\mathbf{k}_{5/4}$ at time step of $\delta t = 10$ s using the fixed mirror configuration with a system efficiency of 25%. 246
Figure 193	Integration control law for spacecraft formation $\delta\mathbf{k}_{5/4}$ at time step of $\delta t = 10$ s using the fixed mirror configuration with a system efficiency of 25%. 247
Figure 194	Integration control law for spacecraft formation $\delta\mathbf{k}_{5/5}$ at time step of $\delta t = 10$ s using the fixed mirror configuration with a system efficiency of 25%. 248
Figure 195	Integration control law for spacecraft formation $\delta\mathbf{k}_{5/5}$ at time step of $\delta t = 10$ s using the fixed mirror configuration with a system efficiency of 25%. 249
Figure 196	Integration control law for spacecraft formation $\delta\mathbf{k}_{5/3}$ at time step of $\delta t = 60$ s using the fixed mirror configuration with a system efficiency of 25%. 250
Figure 197	Integration control law for spacecraft formation $\delta\mathbf{k}_{5/3}$ at time step of $\delta t = 60$ s using the fixed mirror configuration with a system efficiency of 25%. 251
Figure 198	Integration control law for spacecraft formation $\delta\mathbf{k}_{5/5}$ at time step of $\delta t = 60$ s using the fixed mirror configuration with a system efficiency of 25%. 252
Figure 199	Integration control law for spacecraft formation $\delta\mathbf{k}_{5/5}$ at time step of $\delta t = 60$ s using the fixed mirror configuration with a system efficiency of 25%. 253

## LIST OF TABLES

---

Table 1	Tholen taxonomy of asteroid types	5
Table 2	Strategy Dominance for Apophis, with no TRL applied.	11
Table 3	Strategy Dominance for Apophis, with TRL applied.	11
Table 4	Dimensions of lens assembly	29
Table 5	Mass budget A, $\rho_M = 5 \text{ kg/m}^2$ .	34
Table 6	Mass budget B, $\rho_M = 0.5 \text{ kg/m}^2$ .	35
Table 7	Mass budget C, $\rho_M = 0.05 \text{ kg/m}^2$ .	35
Table 8	Adaptive primary mirror plus laser.	37
Table 9	Fixed primary mirror plus laser.	37
Table 10	Primary solar array plus laser, using standard solar array technology.	38
Table 11	Primary solar array plus laser, using advanced solar array technology.	38
Table 12	Required number of spacecraft for a primary aperture area of $2827 \text{ m}^2$ and a concentration ratio of 2500.	39
Table 13	Estimated and observed orbital and physical properties of Apophis 99942.	51
Table 14	Values for the best results for each family of objection function $J_T$ and the corresponding solution vector $\xi_k$ .	64
Table 15	Boundaries on search space for the initial state vector $\xi_k$ .	70
Table 16	Values for the objective functions and solution vector $\xi_k$ for the end limits of the Pareto front for the MOO.	74
Table 17	Test case formation orbits, $\delta\mathbf{k}$ parameters.	97
Table 18	Errors on positional and angular measurements.	125
Table 19	Parameters of on-board camera (all dimensions are assumed square).	126
Table 20	Error range statistics on the estimation of the NEO inertial position, for the 5 spacecraft formation.	127
Table 21	Mirror design parameters for optimisation.	155
Table 22	Component mass parameters for optimisation.	155
Table 23	Temperature parameters for optimisation.	156
Table 24	Parameters for the two preliminary test cases for EPIC.	191
Table 25	Comparison of the average Euclidian distances between 500 uniformly space points on the optimal Pareto front for various optimisation algorithms.	193
Table 26	Minimum and maximum values of $dQ/dt$ corresponding to Figures 148–152.	201
Table 27	Cross reference between figure numbers and simulation inputs for the results in Appendix D.	209

## NOMENCLATURE

---

### ACRONYMS

ACO	Ant Colony Optimisation
ACT	Advanced Concepts Team (under ESA)
AEP	Artificial Equilibrium Points
AI	Artificial Intelligence
ATSM	American Society for Testing and Materials
AU	Astronomical Unit (149597870.7 km)
CCD	Charged Coupled Device
CFRP	Carbon Fibre Reinforced Plastic
CODATA	Committee on Data for Science and Technology
DE	Differential Evolution
DLR	Deutsches Zentrum für Luft- und Raumfahrt
EA	Evolutionary Algorithm
ECI	Earth-Centric Inertial reference frame
EPIC	Evolutionary Programming and Interval Computation
ESA	European Space Agency
FEED	Field Emission Electric Propulsion
FOV	Field of View
GEO	Geosynchronous Earth Orbit
GMT	Greenwich Mean Time
GNC	Guidance, Navigation and Control
HCW	Hill-Clohessy-Wiltshire equations
IAE	Inflatable Antenna Experiment
IAU	International Astronomical Union
IR	Infra-red
JAXA	Japan Aerospace Exploration Agency
JPL	Jet Propulsion Laboratory (under NASA)
LEO	Low Earth Orbit
LISA	Laser Interferometer Space Antenna
MACS	Multiagent Collaborative Search
MAXIM	Micro-arcsecond X-ray Imaging Mission
MJD	Modified Julian Days, days
MJD2000	Modified Julian Days since 01 January 2000 12:00:00 GMT, days
MMS	Magnetosphere Multiscale Mission
MOID	Minimum Orbital Interception Distance
MOO	Multi-Objective Optimisation
NASA	National Aeronautics and Space Administration
NEO/A	Near Earth Object/Asteroid
NOAA	National Oceanic and Atmospheric Administration (USA)
PHO/A	Potentially Hazardous Object/Asteroid
PROBA	Project for Onboard Autonomy
PSO	Particle Swarm Optimisation
RAAN	Right Ascension of the Ascending Node ( $\Omega$ )
RF	Radio Frequency
SIRA	Solar Imaging Radio Array
SMA	Semi-major axis

SOO	Single Objective Optimisation
SpaceART	University of Glasgow Space Advanced Research Team
SQP	Sequential Quadratic Programming
SRP	Solar Radiation Pressure
SSSB	Small Solar System Bodies
TBD	To be determined
TNO	Trans-Neptunian Objects
TPF	Terrestrial Planet Finder
TRL	Technology Readiness Level
UAV	Unmanned Aerial Vehicles
UV	Ultra-violet

#### COORDINATE SYSTEMS

$\mathcal{A}$	Relative rotating asteroid-centric Hill reference frame ( $\hat{x}$ radial, $\hat{y}$ transverse, $\hat{z}$ normal/angular momentum)
$\mathcal{M}$	Relative rotating mirror-centric reference frame ( $\hat{x}, \hat{y}$ are the translated radial and transversal axes from the asteroid Hill frame $\mathcal{A}$ , rotated by an in-plane angle $\beta$ , $\hat{z}$ is in the direction of spacecraft angular momentum)
$\mathcal{O}$	Inertial heliocentric reference frame ( $\hat{x}$ is towards the vernal equinox $\Upsilon$ , $\hat{y}$ in the orbital plane orthogonal to $\hat{x}$ , $\hat{z}$ in normal to the Earth orbital plane)
$\mathcal{S}$	Relative rotating spacecraft-centric Hill reference frame ( $\hat{x}$ radial, $\hat{y}$ transverse, $\hat{z}$ normal)
$\mathcal{Z}$	Relative rotating camera-centric reference frame ( $\hat{z}$ in direction of bore-sight of camera field of view, $\hat{y}$ in direction of angular momentum, and the $x$ - $y$ plane forming the image plane)

#### MATHEMATICAL OPERATORS

$\square \cdot \square$	Matrix multiplication
$\square \wedge \square$	Cross (or vector) product of two vectors
$\square', \square''$	First and second derivatives with respect to the true anomaly $\nu$
$\square_A \prec \square_B$	Dominance of set B over set A
$\dot{\square}, \ddot{\square}$	First and second derivatives with respect to time
$\hat{\square}$	Unit vector
$\in$	Is an element of
$\langle \square, \square \rangle$	Dot (or scalar) product of two vectors
$[\square]$	Cardinality of a set
$\propto$	Proportional to
$\subset, \subseteq$	Proper, and Improper subset of a set
$\supset, \supseteq$	Proper, and Improper superset of a set
$\bar{\square}$	Mean value
$\ \square\ $	Norm of a vector
$ \square $	Absolute value

#### SUBSCRIPTS

0	Initial value
$\odot, sun$	Sun
$\oplus, \earth$	Earth
$A$	Asteroid
$AU$	Value taken at a distance of 1 AU

<i>C</i>	Chief
<i>D</i>	Deputy
<i>dev</i>	Deviation
<i>exp</i>	Expelled mass
<i>f</i>	Focal location or distance
<i>g</i>	Gap or hole in mirror to allow light to pass through to the other side
<i>i, j</i>	$i^{\text{th}}$ or $j^{\text{th}}$ value in a set
<i>ineq</i>	Inequality (used with constraints in optimisation)
<i>ir</i>	Infra-red
<i>L</i>	Laser
<i>light</i>	Light projected onto the asteroid
<i>lim</i>	Limit or boundary condition
<i>M</i>	Mirror
<i>max</i>	Maximum allowable value
<i>pert</i>	Perturbations
<i>R</i>	Radiator
<i>r</i>	At distance $r$
<i>rot</i>	Rotational
<i>sa</i>	Solar arrays used for power conversion for the indirect pumped laser
<i>sc</i>	Spacecraft
<i>sp</i>	Solar panels
<i>spot</i>	Illuminated spot beam on asteroid surface
<i>T</i>	Target value

#### VARIABLES

$\alpha$	Absorptivity, % or In-plane thrust angles for Q-law control, rad
$\beta$	Sun aspect angle, rad or Out-of-plane thrust angles for Q-law control, rad
$\chi$	Thermal diffusivity of the material
$\Upsilon$	Thrust, N
$\Delta\beta$	Angle between the incoming sunlight and the direction of the focal point of the mirror, rad
$\ell$	Distance from a point on the reflector to the focal point, m
$\epsilon$	Elevation angle of the artificial equilibrium point, rad
$\epsilon_{bb}$	Black body emissivity
$\eta$	Efficiency, % or Effectivity for Q-law control or Keplerian orbital element product, $\sqrt{1 - e^2}$
$\gamma$	Angular out-of-plane component in gravity field, rad
$\kappa$	Angular in-plane component in gravity field, rad
$\kappa_A$	Thermal conductivity
$\lambda$	Wavelength, m
$\Lambda$	Scattering factor
$\mathcal{U}$	Angle between $\ell$ and the optical axis of the reflector, rad
$\mu$	Gravitational constant ( $\mu_{\odot} = 132724487690 \text{ km}^3/\text{s}^2$ )
$\nu$	True anomaly, rad
$\Omega$	Right ascension of the ascending node (RAAN), rad
$\omega$	Argument of periapsis, rad
$\Phi$	State transition matrix
$\phi$	Angle of reflection between mirror normal and incoming (or outgoing) ray, rad

$\psi$	Euler angle, rad
$\rho$	Density, g/m <sup>2</sup>
$\sigma$	Stefan-Boltzmann constant, $5.670400 \times 10^{-8}$ W/m <sup>2</sup> K <sup>4</sup>
$\sigma_{\square}$	Coefficient of reflectivity, %
$\tau$	Torque, N·m
$\tau_0$	Oscillation period of a molecule, s
$\Theta$	Elevation angle of spacecraft in the asteroid Hill reference frame $\mathcal{A}$ , rad
$\theta$	True latitude ( $\nu + \omega$ ), rad
$v$	Variable used in Gauss equations in the $v$ - $n$ - $h$ frame
$v_c$	Absorption coefficient of forsterite
$\varepsilon_{\odot}$	Solar disk half angle, rad
$\varphi_{vf}$	Angular view factor equal to the angle between the laser beam and the directional steering mirror, rad
$\varpi$	Variable used in calculation of $\delta r(\delta \mathbf{k})$
$\varrho$	Variable used in calculation of $\delta r(\delta \mathbf{k})$
$\varsigma$	Albedo
$\vartheta_{spot}$	Angular resolution required for the spot beam, rad
$\xi$	Variable used in calculation of $\delta r(\delta \mathbf{k})$
$\xi_{\mathbf{x}}, \xi_{\mathbf{k}}$	State vector for optimisation of orbital dynamics
$\zeta$	Variable used in calculation of $\delta r(\delta \mathbf{k})$
<b>A</b>	Matrix of Gauss planetary equations
<b>b</b>	Matrix used in least squares control law
$a$	Semi-major axis of an ellipse, m
$A$	Area, m <sup>2</sup>
$a_1, b_1, c_1$	Radial dimensions of an ellipse, m
$b$	Semi-minor axis of an ellipse, m
$c$	Speed of light, 299792.458 km/s <sup>2</sup> or heat capacity, J/kg·K
$c_A$	Heat capacity
$C_r$	Concentration ratio
$C_{20}, C_{22}$	Harmonic coefficients for a second-order, second-degree gravity field
$C_{ineq}$	Inequality constraint in optimisation
<b>D</b>	Directional cosine matrix
$D$	Domain
$d$	Diameter, m
<b>e</b>	Euler vector
$E$	Energy, J
$e$	Eccentricity
$E_a$	Activation energy, J
<b>F</b>	Transformation matrix between a set of Hill frame components and a set of orbital element differences
$\mathbf{F}_{\square}, F_{\square}$	Force, N
$f_{\ell}$	Optical focal length, m
$H$	Enthalpy of sublimation, J
$h$	Angular momentum, or height, m
$i$	Inclination, rad
$I_i$	Dominance index
$I_{sp}$	Engine specific impulse, s
$J$	Objective function
$j_c$	Jet constant

$\delta \mathbf{k}$	Set of Keplerian orbital element differences between two orbits, $[\delta a, \delta e, \delta i, \delta \Omega, \delta \omega, \delta M]$
$\mathbf{k}$	Set of Keplerian orbital parameters $[a, e, i, \Omega, \omega, \nu]$
$k$	Elastic coefficient
$K$	Conductivity of a material, W/m·K
$k_B$	Boltzmann constant, $1.3806504 \times 10^{-23}$ J/K
$L$	Distance, or depth, from the surface of the asteroid, m
$l$	Length, m
$m$	Mass, kg
$M$	Mean anomaly, rad or deflection method (used in comparison study only)
$M$	Molecular mass, kg
$\mathbf{n}$	Normal vector
$N$	Total number of solutions in a set
$n$	Mean motion, m/s or index of refraction
$n_{sc}$	Number of spacecraft in the formation
$\mathbf{p}$	Set of points on the surface of simulated NEO mapped onto the 2D camera plane
$p$	Semi-latus rectum, m
$P$	Power, W
$P_0$	Solar power at 1 AU ( $S_0/c$ ), W
$px$	Pixel, m
$q$	Quaternions
$Q, Q^*$	Control functions
$Q_{cond}$	Heat loss due to conduction, J
$Q_{rad}$	Heat loss due to radiation, J
$\delta \mathbf{r}, \delta \mathbf{r}$	Position vector representing the difference between two vectors where the order of magnitude is such that $\delta \mathbf{r} \ll \mathbf{r}_1, \mathbf{r}_2$
$\mathbb{R}$	Real number
$\mathbf{r}, r$	Position or radius, m
$\bar{R}$	Gas constant (8.314472 J/K·mol)
$Re$	Reynolds number
$\mathbf{s}$	Acceleration induced by solar radiation pressure, m/s <sup>2</sup>
$S_0$	Solar flux at a distance of 1 AU (1367 W/m <sup>2</sup> )
$\bar{t}_{res}$	Average time of residence of a contaminant on a surface, s
$T$	Temperature, K
$t$	Time, s
$T_A$	Orbital period of the NEA, days
$\mathbf{u}, u$	Control acceleration, m/s <sup>2</sup>
$U_{20+22}$	Gravitational potential function for a second-order, second-degree gravity field
$\delta v, \delta \mathbf{v}$	Velocity vector corresponding to the position vector $\delta \mathbf{r}$
$\mathbf{v}, v$	Velocity, m/s
$\bar{v}_{exp}$	Average velocity of particles of expelled debris, m/s
$V$	Lyapunov function
$w$	Rotational velocity, rad/s
$W$	Weights
$\mathbf{X}$	Vector of position and velocity components in a Cartesian Hill reference frame $[\delta \mathbf{r}, \delta \mathbf{v}] = [x, y, z, \dot{x}, \dot{y}, \dot{z}]$
$\mathbf{x}^*$	Equilibrium state
$x, y, z$	Cartesian coordinate values

#### REMARKS

All numerical simulations were run using Mathworks' Matlab<sup>®</sup> v.2007a, 2007b and 2008a on both Windows XP and UNIX servers. Analytical simulations were run using Wolfram Mathematica<sup>®</sup> v.6.

Unless otherwise stated, values for physical constants are consistent with those published in 2006 by the Committee on Data for Science and Technology (CODATA), found on [physics.nist.gov/constants](http://physics.nist.gov/constants) (link valid as of February 23, 2010) or in Mohr et al. (2006).

#### COLOPHON

The typographic style is presented in *The Elements of Typographic Style* by Bringhurst (2002). It is available for L<sup>A</sup>T<sub>E</sub>X via CTAN as `classicthesis`, and is produced by André Miede.

Passion holds up the bottom of  
the universe and genius paints  
up its roof.

*Chang Ch'ao*

## DEDICATION

---

This work is dedicated to my grandparents: Jean and Jack McDonald, Dorothy and Ralph Maddock, who just by living their life, have shown me what a wonderful thing life can be if you choose to live it.

To Henry, Tristan and Elliot: you have wonderful examples in your parents to look up to. I know I do.

My parents Dave and Marg, and brother Rob also deserve mention, much love and thanks. Lastly, to my anchor in the rain, I owe you everything.

## ACKNOWLEDGMENTS

---

Many people directly, and indirectly, contributed to the technical results of this dissertation, and deserve both mention and thanks.

*Dr Massimiliano Vasile* was an instrumental and invaluable contributor to many of the ideas and approaches used within this research. *Drs Joan Pau Sanchez Cuartielles* and *Camilla Colombo*, also from the Glasgow Space Advanced Research Team, for their respective work on the comparison of NEO deflection methods, development of the analytical deflection formulas and of the thrust model for the solar sublimation method. Along with these three, *Matteo Ceriotti*, *Nicolas Croisard*, *Daniel Novak*, *Dr Edmondo Minisci* and many other members of the Space ART, deserve thanks for their many hours of diligent work creating and correcting the astrotoolbox, and for their suggestions, contributions and advice on this research.

*Dr Marco Molina* from Gavazzi Space, for his suggestions on the conceptual analysis of the cooling system for the laser options and *Dr Marc Sorel* from the Electronics Engineering department at the University of Glasgow for his help on the current and future state of the art for semiconductor lasers and innovative solar arrays.

*Prof Colin McInnes* from Strathclyde University, for his contributions to the current states of research and technology for solar reflectors and deployable structures in space, and to the mass budgets. *Dr Leopold Summerer*, from the Advanced Concepts Team at ESA, for insightful advice and feedback regarding the study as a whole.

Lastly, I would like to thank *Dr Gianmarco Radice*, my advisor, for his guidance and assistance. He encouraged me to come to the University of Glasgow, and make my dream happen.

## DECLARATION

---

I hereby declare that this submission is my own work and that, to the best of my knowledge and belief, it contains no material previously published or written by another person nor material which to a substantial extent has been accepted for the award of any other degree or diploma of the university or other institute of higher learning, except where due acknowledgment has been made in the text.

*Glasgow, Scotland, February 23, 2010*



---

Christie Alisa Maddock

## PUBLICATIONS

---

Some ideas and figures have appeared previously in the following publications:

Maddock C., Sanchez Cuartielles J. P., Vasile M., Radice G., *Comparison of Single and Multi-Spacecraft Configurations for NEA Deflection by Solar Sublimation*, Proceedings from New Trends in Astrodynamics and Applications III, American Institute of Physics **886**: 303–316, September 2006.

Maddock C., Vasile M., *Optimal Design for a NEO Tracking Spacecraft Formation*, IEEE Congress on Evolutionary Computing, Singapore, September 2007.

Maddock C., Vasile M., *Design of Optimal Spacecraft-Asteroid Formation Through a Hybrid Global Optimization Approach*, International Journal of Intelligent Computing and Cybernetics **1**(2): 239–268, 2008.

Vasile M., Maddock C., Radice G., *Mirror Formation Control in the Vicinity of an Asteroid*, AIAA/AAS Astrodynamics Specialists Conference, Hawaii USA, August 2008.

Maddock C., Vasile M., *Extension of the Proximity-Quotient Control Law for Low-Thrust Propulsion*, 59th International Astronautical Congress (IAC), Astrodynamics Symposium: Guidance and Control, Glasgow UK, September 2008.

Vasile M., Maddock C., Radice G., McInnes C., *NEO Deflection through a Multi-Mirror System*, ESA Call for Proposals: Encounter 2029, Final Report for Ariadna Study Contract 08/4301, Technical officer: Summerer L., March 2009.

Maddock C., Vasile M., McInnes C., Radice G., Summerer L., *Designs of Multi-Spacecraft Swarms for Deflection of Apophis by Solar Sublimation*, IAA Planetary Defense Conference, Spain, April 2009.

Vasile M., Maddock C., Summerer L., *Conceptual design of a multi-mirror system for asteroid deflection*, 27th International Symposium on Space Technology and Science, Japan, July 2009. Also accepted for the ISTS Special Issue of Transactions of JSASS (Japan Society for Aeronautical and Space Sciences), Space Technology Japan, [in press], 2009.

Vasile M., Maddock C., *On the Deflection of Asteroids with Mirrors*, Celestial Mechanics and Dynamical Astronomy, [in press], 2010.

## INTRODUCTION

---

Neither the appellation of planets, nor that of comets, can with any propriety of language be given to these two stars ... [They] resemble small stars so much as hardly to be distinguished from them. From this, their asteroidal appearance, if I take my name, and call them Asteroids; reserving for myself however the liberty of changing that name, if another, more expressive of their nature, should occur.

*Sir William Herschel (1802) on the discovery of Ceres and Pallas*

### 1.1 PURPOSE AND REPORT STRUCTURE

The aim of this doctoral dissertation is to answer the question: is solar sublimation a viable option for the deflection of a Near Earth Asteroid? From a research view point, the methods and analysis are applicable to proximal motion around a celestial body, in particular one with a non-Keplerian or irregular orbit as in the case here with the orbit being constantly altered by the deflection action and subject to perturbations, such as solar radiation pressure.

The starting point of this research is the basic conceptual idea of Lunan (1992) and Melosh and Nemchinov (1993) to concentrate sunlight in order to heat up the surface of the asteroid causing the rocky material to vapourise thereby altering the orbit, with a number of limitations and challenges discussed in a later report by Kahle et al. (2006). The rationale behind wanting to investigate this particular asteroid deflection option further, is based on the outcome of a quantitative analysis by Colombo et al. (2006) and Sanchez Cuartielles et al. (2007) from the Space Advanced Research Team at the University of Glasgow which compared a wide variety of deflection methods. The results showed that on the basis of current readiness level of the required technology and the effectiveness of the method at deviating the asteroid, solar sublimation was the best method for long term operations.

Chapter 1 introduces the reader to the field of Near Earth Objects and more specifically, Near Earth Asteroids and the potential hazard they pose to our civilisation. Many ideas and concepts have been proposed in order to deflect asteroids, spawned in part by the awareness and interest of popular science and the media. The ideas range from speculation to a few preliminary mathematical analyses and simulations, but overall not many. The concept and history behind solar sublimation, and the comparison between deflection methods are discussed in more detail.

Chapter 2 presents the design aspects related to the system as a whole. The first step was to come up with a set of conceptual systems based on the single mirror baseline of Melosh, and expanding it to cover many mirrors distributed over multiple spacecraft. These conceptual designs are of the mechanisms for the collection, magnification and re-direction of the solar radiation; specifically, fixed or adaptive mirror(s), and optical systems such as lens or lasers are presented. The properties of the Sun play an important part in the analysis of the optical systems, in particular the effect of non-parallel rays on collimating systems is analysed. Section 2.2 also details three different options – direct imaging, collimating lens and laser – for the focusing and beaming system. Section 2.3 presents an estimation of the mass budget for the spacecraft based on technologies at different readiness levels.

Chapter 3 presents a detailed analysis of two different options for the orbital dynamics and control of a spacecraft formation. A background and review of the current state of the art is first shown for the field of formation flying. In particular, the mathematical modelling of proximal motion is discussed. Based on these models, one design is developed based on a chief-deputy formation structure using the orbital element differences method developed by Schaub and Junkins (2003). A control law for the orbital maintenance is developed that compensates for the solar radiation pressure, third body gravitational effects from the asteroid and the continuous deviation of the asteroid orbit. A second design, developed in parallel, aims at placing spacecraft at ‘artificial equilibrium points’ where the asteroid gravity field and the solar radiation pressure are instantaneously in balance. Simulations of the required orbital control, and the effect of the gravitational model are shown.

Chapter 4 presents a novel proposal for the orbit determination. A key requirement of the orbital dynamics and control is that each spacecraft must have a highly accurate knowledge of the relative position of the asteroid in order to correctly align the spot beams. In addition it is of interest to monitor the exact inertial position of the asteroid in order to track the deviation and predict the new altered orbit. A navigation strategy, and simulations results are presented.

Chapter 5 presents the simulation results for the deflection distance that can be achieved, as a function of the warning time, thrust duration, number of spacecraft, and mirror surface area. An analysis of the effect of contamination from the debris is shown in Section 5.2. Section 5.3 examines the enhanced Yarkovsky effect that is produced by raising the temperature of a section on the asteroid surface.

The concluding remarks and discussion on future work is presented in Chapter 6.

There are four Appendices in total. Appendix A presents the a detailed mathematical derivation of the nonlinear (A.1) and linearised (A.2) forms of the proximal motion equations. Appendix B gives further background information into the optimiser used in this research study. Appendix C shows the work done on implementing and adapting a Lyapunov-based control law developed by Petropoulos (2003). While ultimately it was not used in the simulations due to a number of drawbacks, the work done, nevertheless, is still of interest to anyone interested in using this approach. Finally, Appendix D contains the complete set of simulation results for the control algorithm presented in Section 3.6.

## 1.2 NEAR EARTH OBJECTS

In 2006, the International Astronomical Union (IAU) passed Resolution B5 which formally defined three terms to describe celestial bodies within our solar system.

A *planet* is a celestial body that (a) is in orbit around the Sun, (b) has sufficient mass for its self-gravity to overcome rigid body forces so that it assumes a hydrostatic equilibrium (nearly round) shape, and (c) has cleared the neighbourhood around its orbit.

A *dwarf planet* is a celestial body that (a) is in orbit around the Sun, (b) has sufficient mass for its self-gravity to overcome rigid body forces so that it assumes a hydrostatic equilibrium (nearly round) shape, (c) has not cleared the neighbourhood around its orbit, and (d) is not a spacecraft.

All other objects, except satellites, orbiting the Sun shall be referred to collectively as *Small Solar System Bodies*. These currently include most of the solar system asteroids, most Trans-Neptunian Objects (TNOs), comets, and other small bodies.

These ‘Small Solar System Bodies’ (SSSB) are more idiomatically known as asteroids, which are any solid bodies in space smaller than a planet, comets, defined as asteroids with visible tails, and meteoroids, which are anything with a diameter smaller than 10 m [Beech and Steel, 1995].

The vast majority of SSSB can be found grouped together into distinct regions within the solar system. The two largest asteroid groupings are: the main asteroid belt between Mars and Jupiter and the Kuiper belt, on the outskirts from Neptune. Figure 1\* shows the general distribution of asteroids in the inner solar system, while Fig. 2† shows those in the outer solar system.

### 1.2.1 Classification of Asteroids

Asteroids, after the Greek word *asteroeides* meaning “star-like”, are classified in a number of different ways depending on the field. The two main areas of interest for this study are: the composition of the asteroid and the orbital characteristics.

The physical characteristics of the asteroid itself are generally determined by examining the spectral shape, color, and albedo (or percentage of solar radiation reflected by the surface of the asteroid). In 1975, three scientists from the USA analysed 110 asteroids [Chapman et al., 1975], and found that  $\sim 90\%$  fell relatively evenly into two main groups: named C for dark carbonaceous objects, and S for stony or siliceous objects. This classification system has been since expanded, resulting in the most common system in use today, the Tholen taxonomy [Tholen, 1989]. Table 1 lists the main and sub-classes, albedo range and estimated composition material of the asteroid bodies [Bus et al., 2002; Bus and Binzel, 2002].

Near Earth Objects (NEO), or more specifically Asteroids (NEA) are defined as any asteroid (or minor celestial body) with a perihelion less than 1.3 AU and an apohelion larger than 0.983 AU, where 1 AU is the average distance between the Earth and the Sun (around 150 million km). NEOs can also include comets and meteoroids, however for this study only asteroids were investigated.

The orbital properties of NEAs can be grouped into four categories based on the semi-major axis  $a$ , radius of apoapsis  $r_a$  and/or radius of periapsis  $r_p$ , described as follows [NASA Near Earth Object program, 2009b]:

---

\*Source image at <http://en.wikipedia.org/wiki/File:InnerSolarSystem-en.png>, last accessed on February 23, 2010.

†Source image at [http://en.wikipedia.org/wiki/File:Outersolarsystem\\_objectpositions\\_labels\\_comp.png](http://en.wikipedia.org/wiki/File:Outersolarsystem_objectpositions_labels_comp.png), last accessed on February 23, 2010.

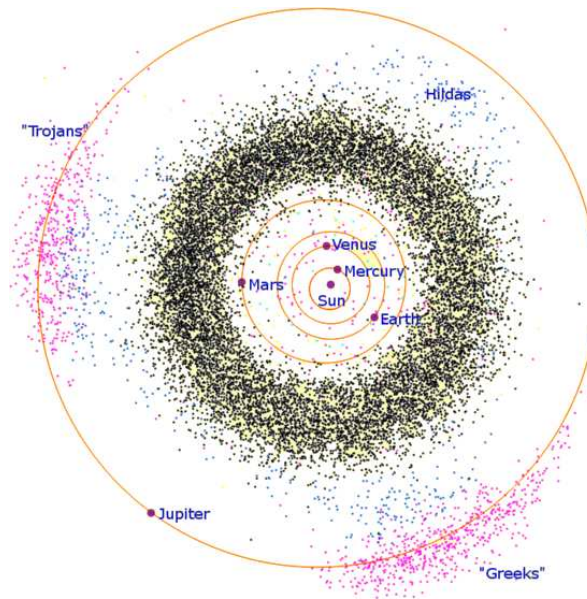


Figure 1: The inner Solar System from the Sun to Jupiter, including the Main Asteroid belt (black), and the Jovian Trojans, Greeks (pink) and Hildas (blue) clusters. This image was created using JPL DE-405 ephemeris database for the planets, and the Minor Planet Center database for the asteroids, published 2006 Jul 06.

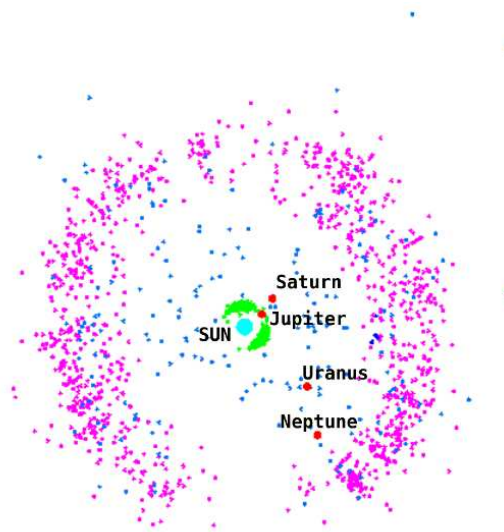


Figure 2: Known objects in the Kuiper belt (and outer Solar System) derived from data from the Minor Planet Center. The Kuiper belt objects (KBO) are in pink, the green show the Trojans and Greeks around Jupiter (also seen in Fig. 1) and in blue are the Trojans around Neptune.

Table 1: Tholen taxonomy of asteroid types

Type	Subtype	Albedo	Composition
C	B, E, F, G	0.03–0.10	Anhydrous silicates, hydrated phyllosilicate minerals, organic polymers, magnetite and sulfides
S	K, L	0.10–0.22	Iron and magnesium silicates
X	M, E, P	0.3+	Organic rich silicates, carbon and anhydrous silicates

**ATIRA** Asteroids whose orbits are contained entirely within the orbit of the Earth (named after asteroid 163693 Atira), where  $r_a \leq 0.983$  AU. There are currently 10 discovered Atira class asteroids.

**ATENS** Earth-crossing asteroids with semi-major axes smaller than Earth (named after asteroid 2062 Aten), where  $a < 1$  AU,  $r_a \geq 0.983$  AU. There are currently 505 discovered Atens class asteroids.

**APOLLOS** Earth-crossing asteroids with semi-major axes larger than Earth (named after asteroid 1862 Apollo), where  $a \geq 1$  AU,  $r_p \leq 1.0167$  AU. This is the largest class, with 3368 asteroids.

**AMORS** Earth-approaching asteroids with orbits exterior to Earth's but interior to Mars (named after asteroid 1221 Amor), where  $a > 1$  AU,  $1.0167$  AU  $< r_p \leq 1.3$  AU. This is the second largest class with 2363 discovered objects.

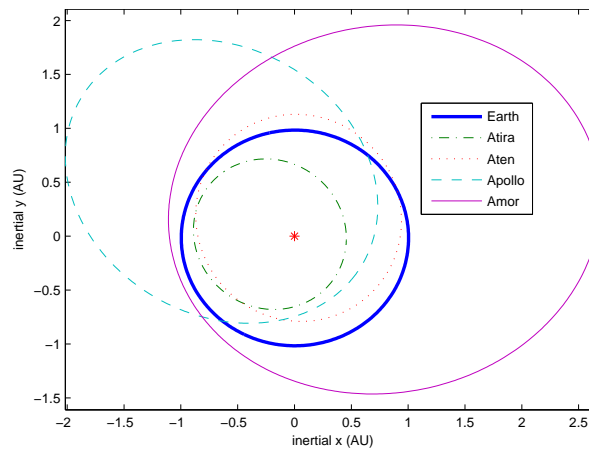


Figure 3: Orbits of four asteroids representing each of the four classes of NEAs.

Figure 3 shows the orbits of four asteroids – 163693 Atira, 2062 Aten, 1862 Apollo, 1221 Amor – representing the four classes of NEAs. A subclass of these NEAs are called Potentially Hazardous Asteroids, defined by the NASA Near Earth Object program (2009b) as:

Potentially Hazardous Asteroids (PHAs) are currently defined based on parameters that measure the asteroid's potential to make threatening close

approaches to the Earth. Specifically, all asteroids with an Earth Minimum Orbit Intersection Distance (MOID) of 0.05 AU or less and an absolute magnitude  $H$  of 22.0 or less are considered PHAs. In other words, asteroids that can't get any closer to the Earth (i.e. MOID) than 0.05 AU (roughly 7,480,000 km) or are smaller than about 150 m in diameter (i.e.  $H = 22.0$  with assumed albedo of 13%) are not considered PHAs.

As of August 2009, there are 1067 known PHAs out of total of 6246 NEAs, and 6330 NEOs. Of the PHAs detected, 145 are estimated to be over 1 km in diameter<sup>‡</sup>. Figure 4 shows the total number of NEO, NEA and PHAs that were discovered each year.

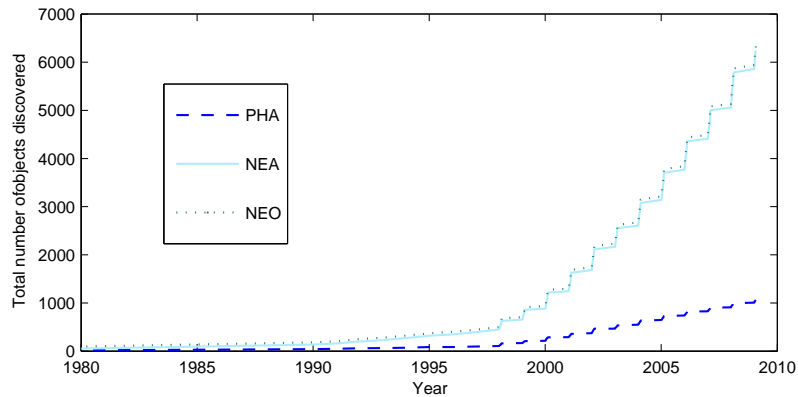


Figure 4: Total number of discovered Near Earth Objects by date [NASA Near Earth Object program, 2009b].

### 1.2.2 Deflection of Near Earth Objects

Although much less frequent than most natural hazards, cosmic impacts represent the most extreme known threat in terms of damage and casualties. As we know from the end Cretaceous impact of 65 Ma, the global effects of such catastrophes can include mass extinction of species.

— David Morrison (2006)

Small celestial bodies like Near Earth Objects (NEO) have become a common subject of study because of their importance in uncovering the mysteries of the formation, evolution and composition of the solar system. Among all the asteroids, NEOs have stepped into prominence because they are among the easiest celestial bodies to see, and even reach from Earth, in some cases with less demanding trajectories than a simple Earth-Moon transfer.

Over the last decade, the potential of an asteroid impacting Earth has stimulated intense debate among the scientific community about the monitoring and orbit prediction of the thousands of objects orbiting near Earth, and as the next step, possible deviation methods.

In 1992, a NASA report estimated that there was a total population of about 1100 Near Earth Objects larger than 1 km in diameter, leading to an impact frequency

<sup>‡</sup>Data on all minor bodies within the solar system are published in monthly circulars by The Minor Planet Center (<http://www.cfa.harvard.edu/iau/mpc.html>) at the Smithsonian Astrophysical Observatory under auspice of the International Astronomical Union (IAU). Link valid as of February 23, 2010.

of about one in half a million years. For NEOs between 50 and 100 m in diameter (the lower limit of an object's atmospheric penetration) it was estimated there were half a million NEOs with an impact frequency of about one every thousand years [Near-Earth Object Science Definition Team, 2003].

The effect of an asteroid impact is often compared against either natural phenomena such as earthquakes or volcanos, or large nuclear explosions. Using this metric, objects 50 to 150 m in diameter are thought to result primarily in airbursts while those around 300 m in diameter can destroy a small European country [Morrison, 2006]. "The nominal yearly average [...] associated with PHO impact is estimated by [NASA] to be approximately 300 casualties worldwide, plus the attendant property damage and destruction. About 17% of the risk is attributed to regional damage from smaller land impacts, 53% to water impacts and the ensuing tsunamis, and 30% to the risk of global climatic disruption caused by large impacts." [Near-Earth Object Science Definition Team, 2003]

The two most notorious impacts in recorded history are the K-T event, mentioned above, which is thought to have killed off the dinosaurs and launched the Earth into an ice age, and the Tunguska event, an airburst in June 1908 over Siberia that resulted in a 2000 km<sup>2</sup> crater. More recently though, a number of objects have penetrated the atmosphere of Earth. On 15 September 2007, a stony meteorite actually impacted the ground near the village of Carancas in the Peruvian Altiplano, resulting in a 15 m diameter crater. The asteroid, under 2 m in diameter by the time it hit the Earth with a mass of  $7 \times 10^9$ – $12 \times 10^9$  kg, should have burned up quickly in the atmosphere with no effect according to the prediction models. In October 2008, a small meteoroid (2008 TC3) was discovered by the Catalina Sky Survey in Arizona only one day before it hit the atmosphere over northern Sudan, resulting in a "brilliant fireball" equivalent to a kiloton of TNT.

In addition to ground based monitoring programmes, a sizable number of space missions have been planned and/or launched over the past two decades.

GALILEO (1989-2003) visited two NEOs, 951 Gaspra and 243 Ida, en route to Jupiter and its moons,

NEAR SHOEMAKER (1996–2001), or Near Earth Asteroid Rendezvous was the first NASA mission to a NEA (433 Eros),

DEEP SPACE 1 (1998–2001) which performed fly-bys of the comets 9969 Braille and 19P/Borrelly,

STARDUST (1999–2006), a successful sample-return mission to the comet Wild 2,

HAYABUSA (2003–2010), a Japanese sample-return mission to the asteroid 25143 Itokawa which in 2005 reached and observed the NEA however failed to land,

ROSETTA (2004–), an ongoing ESA orbiter-lander mission to perform a fly-by of two asteroids (2867 Šteins, 21 Lutetia) on route to the comet 67P/Churyumov-Gerasimenko,

DEEP IMPACT (2005–) mission to the comet 9P/Tempel, which both orbited the comet and sent a secondary probe to collide with the comet nucleus, and is now on an extended mission to study the comet Hartley-2,

DAWN (2007–2015), a NASA spacecraft which will orbit around first the asteroid Vesta then around Ceres both located in the main Asteroid belt,

DON QUIJOTE (estimated launch 2011), an ambitious ESA mission which will orbit a target asteroid (still TBD, but most likely either 2002 AT4 or 1989 ML) and test the capability to deflect the orbit through a high velocity impactor.

### 1.2.3 Comparison of NEO Deflection Methods

In order to predict the effects of a deflection strategy, some studies have addressed the asteroid deviation problem with either an analytical approach [Colombo et al., 2009; Vasile and Colombo, 2008; Izzo, 2005; Scheeres and Schweickart, 2004; Conway, 2001] or a numerical procedure based on a  $n$ -body model [Carusi et al., 2002].

A few studies included a partial comparative assessment of the numerous proposed mitigation strategies [Hall and Ross, 1997]. Some of these emphasize a classification system based on NEO/spacecraft coupling, other systems are based on technology readiness and a third category on time to impact and/or intervention on the asteroid.

The different deflection techniques can be grouped into several families depending on the type of asteroid-spacecraft interaction:

- Techniques producing an impulsive change in the linear momentum of the asteroid, such as kinetic impactors and nuclear interceptors [Tedeschi et al., 1995; McInnes, 2003; Smith et al., 2004],
- Techniques actively producing a controlled continuous low-thrust, such as attached propulsion devices (e.g., electric/chemical engines, solar sails) [Scheeres and Schweickart, 2004] or gravitational tugs [Lu and Love, 2005],
- Techniques producing a passive low-thrust by an induced change of the thermo-optical properties of the asteroid surface, such as enhanced Yarkovsky effect or enhanced emissivity through white paint [Spitale, 2002],
- Techniques producing a controlled thrust by the ablation of the asteroid surface, e.g., through laser beams [Ivashkin, 2004; Park and Mazanek, 2005; Yoo et al., 2009] or solar mirrors [Melosh et al., 1994; Maddock et al., 2007], or
- Techniques producing a multi-impulsive change of the asteroid linear momentum by the ejection of surface material, such as the mass driver [Olds et al., 2004].

This research dissertation was part of a triad of studies undertaken at the University of Glasgow on the subject of the deflection of NEAs. The other two dissertations are on deflection models and mission analysis for asteroid hazard mitigation by Sanchez Cuartielles (2009), and optimal trajectory design for interception and deflection of Near Earth Objects by Colombo (2009).

As part of their research, Sanchez and Colombo performed a comparison of a number of deflection methods proposed in the literature: Nuclear Interceptor, Kinetic Impactor, Low Thrust, Mass Driver, Solar Collector and Gravity Tug. The comparison was based on a multi-criteria approach: 1) miss distance at the Earth, 2) warning time (i.e. time between launch and expected impact with the Earth) and 3) mass into space, were simultaneously used to assess the optimality of a particular method. These three criteria express quantitatively how easy deflecting an asteroid with a given method is and whether the given deviation strategy can be implemented with present launch capabilities. The warning time in particular, in addition to giving quantitative information on the time to react (how far in advance one would need to know that an impact is going to occur), gives an indication on the time available to react if the

deflection fails. The analysis simulated potential missions for a wide range of launch opportunities for each method, over a period of 20 years, in order to characterise the optimality of a particular method. Figure 5 shows the Pareto fronts for four popular deflection methods: nuclear interceptor, kinetic impactor, gravity tug and solar collector.

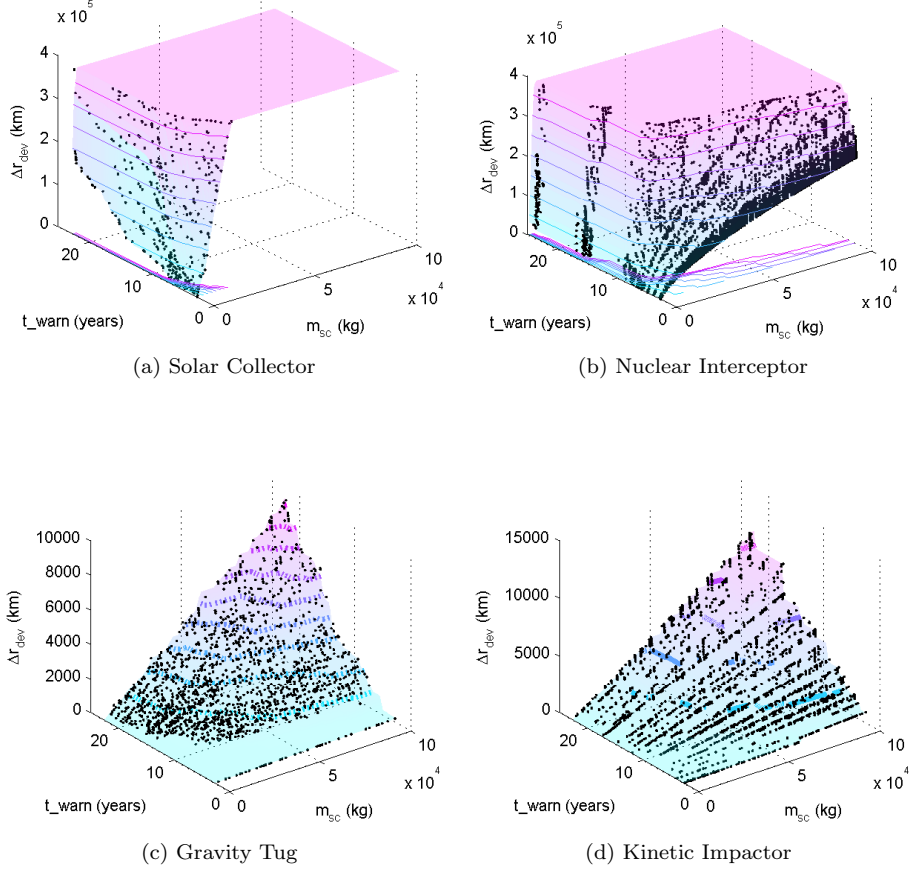


Figure 5: Sets of Pareto optimal solutions for various deflection methods evaluating: warning time  $t_{warn}$ , initial mass in orbit of the spacecraft  $m_{sc}$  and achieved deflection distance  $\Delta r_{dev}$  (figures from Sanchez Cuartielles et al. (2009)). Each dot represents one complete deflection mission.

In order to account for real mission opportunities and the three criteria at the same time, the concept of set dominance was introduced [Sanchez Cuartielles et al., 2009]: given a pair of deflection methods A and B, method A dominates method B if the number of mission opportunities of A that are dominating the mission opportunities of B is higher than the number of mission opportunity of B dominating the mission opportunities of A, where one mission (composed of launch, transfer, interception and deviation segments) is dominant over another mission if all the three criteria are better. In other words, one method is considered better than another if there

were more mission opportunities with a better value for all the three criteria. In mathematical terms, this is expressed as,

$$M_A \prec M_B \quad \longrightarrow \quad \frac{1}{N_A} \sum_{i=1}^{N_A} d_i(M_A) < \frac{1}{N_B} \sum_{j=1}^{N_B} d_j(M_B) \quad (1.1)$$

given

$$d_i(M_A) = \begin{cases} 1 & \text{if } I_i(M_A) > 0 \\ 0 & \text{if } I_i(M_A) = 0 \end{cases} \quad (1.2)$$

$$I_i(M_A) = \left| \{j \mid \mathbf{f}_i^A \prec \mathbf{f}_j^B\} \right| \quad (1.3)$$

where  $M$  is the deflection method,  $N$  is the total number of the solutions in the Pareto set and  $\square_A \prec \square_B$  denotes dominance of method B over method A. If the value of the dominance index  $I_i$  is 0, it means that there are no solutions in the Pareto optimal set of strategy B with all three criteria better than the three criteria associated to element  $i$ .

In addition to the three evaluation criteria, a Technology Readiness Level<sup>§</sup> (TRL) factor was applied to all missions, delaying the warning time in order to account for the required time to bring the current technology to TRL 9.

This comparison approach required the development of a mathematical model for each of the deflection methods. Note that some methods were excluded from the comparison because they require an excessively long warning time (e.g., methods based on the Yarkovsky effect); other methods instead were considered either equal to or less efficient counterpart of the methods already included in the comparison (e.g., surface ablation with a laser powered with a nuclear reactor instead of solar sublimation).

Tables 2 – 3 are excerpts from Sanchez Cuartielles et al. (2009); Sanchez Cuartielles (2009) showing the dominance of the six different strategies applied to a deflection mission to the asteroid Apophis, one of nine test cases analysed in the original study. The values in the tables represent the percentage of elements in the Pareto set of one method (in italics) that dominate over the number of elements in the Pareto set of another method. For example, the kinetic impactor dominates over the low thrust method in 16% of the cases, and over the gravity tug in 100% of the cases. The two tables show the difference in accounting for development time of the technology.

The methodology used to model and compare the deflection methods found, for example, that kinetic impact methods are not always better than low-thrust tugs, though from a theoretical point of view it may appear so. In fact the direction of the impact is rarely optimal while the thrust direction of low-thrust tugs can be steered quite efficiently; or gravity tractors are not insensitive to the morphology of the asteroid because hovering at a distance requires a detailed knowledge of the mass distribution (i.e. gravity field) of the asteroid. The conclusion of the comparison study was that nuclear stand-off explosions were the most effective on the widest range of

---

<sup>§</sup>ESA Technology Readiness Levels: 1- Basic principles observed and reported, 2- Technology concept and/or application formulated, 3- Analytical & experimental critical function and/or characteristic proof-of-concept, 4- Component and/or breadboard validation in laboratory environment, 5- Component and/or breadboard validation in relevant environment, 6- System/subsystem model or prototype demonstration in a relevant environment (ground or space), 7- System prototype demonstration in a space environment, 8- Actual system completed and “Flight qualified” through test and demonstration (ground or space), 9- Actual system “Flight proven” through successful mission operations.

Table 2: Strategy Dominance for Apophis, with no TRL applied (from [Sanchez Cuartielles et al., 2009]).

	Nuclear Interceptor	Kinetic Impactor	Low Thrust	Mass Driver	Solar Collector	Gravity Tug
<i>Nuclear Interceptor</i>	-	100	100	100	1	100
<i>Kinetic Impactor</i>	0	-	16	0	0	100
<i>Low Thrust</i>	0	98	-	0	0	100
<i>Mass Driver</i>	0	100	100	-	0	100
<i>Solar Collector</i>	100	100	100	100	-	100
<i>Gravity Tug</i>	0	1	0	0	0	-

Table 3: Strategy Dominance for Apophis, with TRL applied (from [Sanchez Cuartielles et al., 2009]).

	Nuclear Interceptor	Kinetic Impactor	Low Thrust	Mass Driver	Solar Collector	Gravity Tug
<i>Nuclear Interceptor</i>	-	100	100	100	100/98	100
<i>Kinetic Impactor</i>	7/0	-	99/39	61/54	59	100
<i>Low Thrust</i>	0	1/87	-	7/36	7/48	100
<i>Mass Driver</i>	0	99/100	100	-	0/18	100
<i>Solar Collector</i>	33/36	100	100	100	-	100
<i>Gravity Tug</i>	0	0	1/0	11/4	11/15	-

NOTE: The range of values correspond to the lower/upper limits of the assigned TRLs.

asteroids. The second best was solar sublimation, with all the other methods being an order of magnitude less effective (according to the proposed comparison criteria).

Although nuclear explosions were found to be the most effective, a subsequent study by Sanchez Cuartielles et al. (2008) demonstrated that for both nuclear explosions and kinetic impacts, the risk of a catastrophic fragmentation of the asteroid poses a significant hazard. The analysis showed that for deflection energy levels at which the nuclear explosion performs significantly better compared with other deflection methods, a fragmentation is highly possible. Due to the possible fragmentation caused by the nuclear option, the solar sublimation method appeared to be the most interesting deflection method.

#### 1.2.4 Solar sublimation

Lunan (1992) and later Melosh and Nemchinov (1993) proposed the use of a mirror (or solar concentrator) to focus solar energy onto a small part of the surface of an asteroid. The resulting heat would sublimate the surface material, creating a jet of gas and dust that would produce a low, continuous thrust. A conceptually similar idea is to use a laser beam, either powered by a nuclear reactor or solar arrays, to induce the required sublimation of the surface material. Melosh et al. compared the solar concentrator idea against the nuclear blast option showing the advantages of using

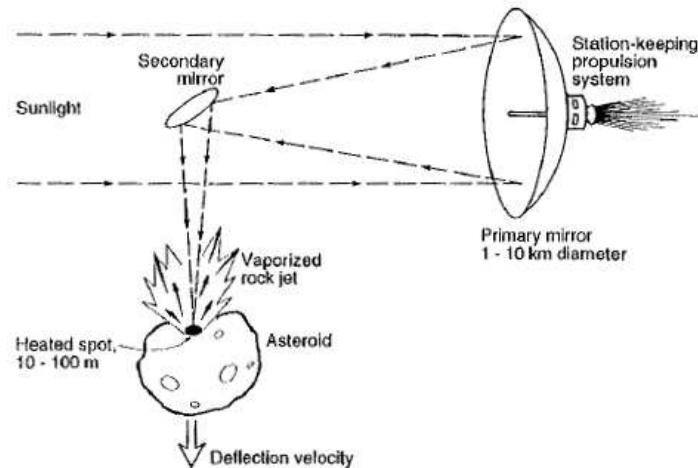


Figure 6: Illustration and caption from Melosh et al. (1994): “Schematic illustration of a solar collector deflection system. Sunlight collected by a large, light primary mirror is focused on the surface of an asteroid or comet and evaporates material from its surface. the reaction to this vapor plume changes the asteroid’s orbit. The primary mirror requires a modest station-keeping propulsion system, such as a high specific impulse solar electric system.”

the collector. However, he was proposing the use of a substantially large structure in space, a primary mirror of 1 km to 10 km in diameter focusing the light of the Sun directly on the surface of the asteroid or onto a secondary mirror used to steer the beam. Figure 6 shows an excerpt from his paper describing the idea [Melosh et al., 1994].

Kahle et al. (2006) compiled a report analysing a number of deflection concepts, and identifying a number of technological limits of the solar collector concept initially proposed by Melosh et al. In particular,

- If the light of the Sun is focused directly onto the surface of the asteroid, in order to have a high enough power density the mirror should be at relatively close distance from the asteroid, e.g. a separation distance of 1.25 km for a 630 m diameter mirror. As a consequence, the mirror should operate and manoeuvre under the effect of the irregular gravity field of the asteroid. Furthermore, at such a distance the contamination of the primary mirror, due to the ejected gasses, would be significant. A longer distance would imply a larger mirror with a consequent increased difficulty in the control of the attitude.
- If a secondary steering mirror is used, the contamination of the primary can be reduced but the secondary would suffer the full contamination problem. Kahle et al. proposed some solutions to the contamination issue but all imply a significant increase in the complexity and mass of the system.
- The deployment and control of a large mirror represents a significant technological challenge and, moreover, a single point failure for the entire mission.
- The total light pressure on the primary mirror would induce a significant force on the spacecraft requiring constant orbit control.

- The high level of solar power collected by the primary reflector would force the secondary reflector to operate at extremely high temperatures, in particular if the surface is contaminated. When this happens, absorptivity is increased, causing a further reduction in reflectivity.

All these problems can be solved if a) the light is not focused directly on the surface of the asteroid and, b) multiple smaller mirrors are used instead of a single large mirror. The idea is to use multiple mirrors of smaller dimensions and superimpose the various beams of focused light onto the same spot. The use of a collimating device, e.g. optical lens, mirrors or lasers, would also allow the placement of the collector at a farther distance from the surface of the asteroid.

The main advantages of a multi-mirror system are:

- Each spacecraft is relatively small and more easily controlled.
- The solar pressure on each spacecraft is reduced and the total power (and hence heat) on the surface of the secondary mirror is limited.
- The system is intrinsically redundant: each spacecraft does not represent a single point failure.
- The system is scalable: the formation is homogenous, therefore a larger asteroid would only require an increase in the number of spacecraft without the need for a new design and development phase.

The main challenge of implementing a multi-mirror system is to superimpose all the beams and maintain pointing with a low margin of error. The use of adaptive optics to collimate the beam gives more flexibility for the placement of the mirrors but requires the development of the control of the optics. The aim of the following study is to assess the feasibility of the deflection method, and to analyse the required technical aspects of a potential deflection mission using solar sublimation.

In the three centuries following Kepler and Newton, the world's greatest mathematicians brought celestial mechanics to such an elegant state of maturity that for several decades preceding the USSR's Sputnik in 1957, it all but disappeared from the university curriculum. [...] Not until recently did the problem exist of designing orbits subject to elaborate constraints to accomplish sophisticated mission objectives at a target planet — except possibly in the fantasy of the boldest imaginations.

*Richard H Battin (1998)*

Several possible conceptual designs are presented for the mirror-spacecraft configuration, consisting of a system that collects the radiation from the Sun, another system that converts this input power into a form suitable for sublimation, and a third system that projects the output power onto the surface of the asteroid. All these systems are related to the study of optics. For each design, the radiation from the Sun is used in a different way in order to achieve a focused spot of the asteroid surface. In particular, the device that converts the incoming power of the Sun into a form useful to sublimate the surface of the asteroid is substantially different. An introduction to the properties of the Sun and solar radiation is given, with a discussion on the implications on the conceptual optical configurations.

System mass budgets were developed for a set of representative conceptual designs in order to assess how feasible the launch of a spacecraft would be. This is also a consideration in the trade-off between the number of spacecraft versus the individual mass.

## 2.1 CONCEPTUAL DESIGN

The design of the device that uses the light of the Sun to sublimate the surface of the asteroid is a critical aspect of this deflection method. The device has to be able to concentrate a minimum power density at all times [Sanchez Cuartielles et al., 2007], therefore must have the capability to steer the beam of light towards any part of the asteroid and to control the concentration factor (or amount of light that is focused on a particular spot).

If one considers a direct projection of the light of the Sun onto the surface of the asteroid, the concentration ratio  $C_r$  of the system is the ratio of the power density at the input to the system, to that at the output. Here, the only power provided to the

system is the incoming solar radiation of the Sun, therefore while the power density changes between that received by mirror surface with that reflected onto the asteroid, the power level does not change (i.e.  $P_{solar} = P_M = P_{spot}$ ) in an ideal, lossless system. Therefore, the concentration ratio is simply a ratio of the two surface areas.

$$C_r = \frac{P_{spot}/A_{spot}}{P_M/A_M} = \frac{A_M}{A_{spot}} \quad (2.1)$$

where  $A$  is the total illuminated surface area of the mirror  $A_M$  that is *perpendicular* to the Sun, and  $A_{spot}$  the illuminated spot area on the asteroid surface. For a 3D paraboloidic mirror where the optical axis is aligned directly towards the Sun, the area  $A_M$  here would be equal not to the total physical surface area of the reflector, but to the 2D aperture area independent of the depth of the mirror.

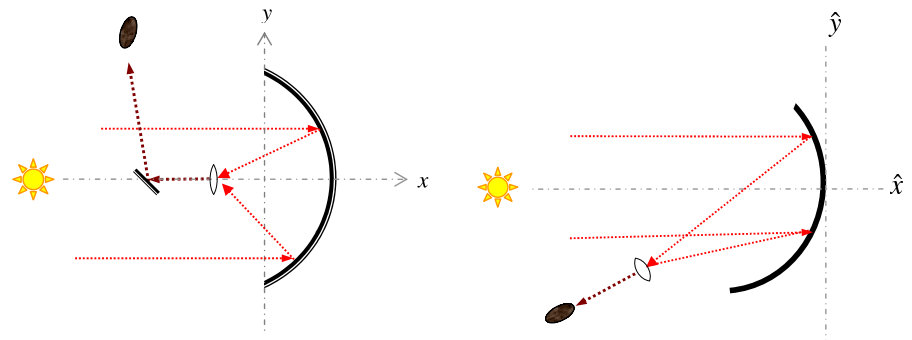
Figure 7 shows a collection of five possible designs. This is not an exhaustive list but serves to identify the basic concepts, each with substantially different technological implications. In general, each mirror-spacecraft configuration is composed of three fundamental components: a power collection unit, a power conversion unit, and a power beaming unit. Analysing the methods in Figure 7,

- (a) Fixed mirror collector, with no power conversion and optical system to collimate and steer the beam. A system of lenses directly collimate the light of the Sun, with a secondary mirror to steer the resulting beam (see Fig. 7a).
- (b) Adaptive collector, with no power conversion and direct imaging onto the surface of the asteroid. In terms of components this is the simplest concept; the complexity is in the design of the collector. Note that unlike the original concept of Melosh et al. there is no steering mirror. The steering is provided by the adaptation of the shape of the mirror (see Fig. 7b).
- (c) Dual fixed reflectors as collecting device, a laser (directly or indirectly pumped) as power conversion unit and a secondary steering mirror as the beam control system. In this case, both the laser and the secondary mirror are in the shadow of the primary mirror to help mitigate the problem of excess heat (see Fig. 7c).
- (d) Fixed mirror collector, a laser (directly or indirectly pumped) as power conversion and a secondary steering mirror as beam control system. In this case the laser is located between the primary collector and the Sun, while the steering mirror is in the shadow cone of the primary mirror (see Fig. 7d).
- (e) Large solar array as solar collector, a laser (indirectly pumped) as power conversion and a secondary steering mirror as beam control system. In this case both the laser and the secondary mirror are in the shadow cone of the primary mirror (see Fig. 7e).

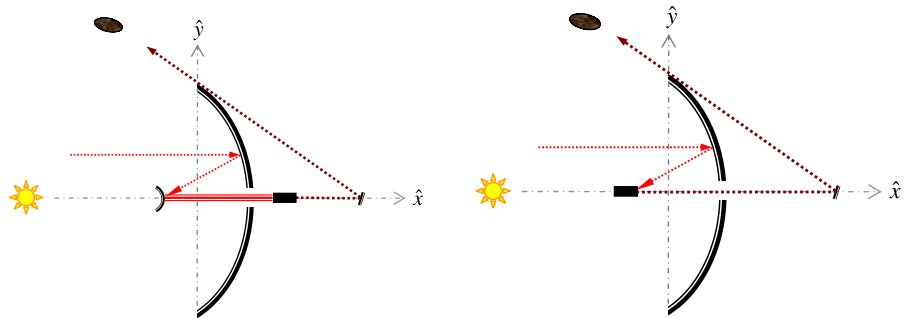
The following study explores the possible mission design for two such configurations which act as representative examples in order to derive a general answer to the feasibility of this deflection method: the dual fixed mirror plus laser option given in Fig. 7d, and the single adaptive mirror, with and without a collimator, given in Fig. 7b.

### 2.1.1 Fixed mirror configuration

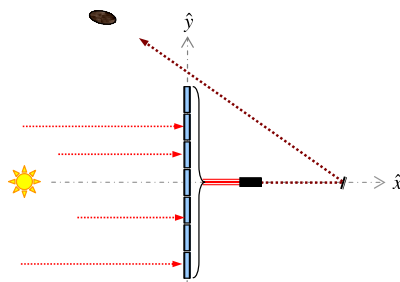
The fixed mirror configuration consists of a parabolic reflector which concentrates the reflected sunlight. This beam is then directed onto the desired spot on the surface



(a) Parabolic reflector with collimating lens, and steering mirror. (b) Direct beam using an adjustable reflector.



(c) Dual reflector system with a solar-fed laser followed by a steering mirror. (d) Single reflector with solar-pumped laser and rear directional mirror.



(e) Solar array for an indirect pumped laser system.

Figure 7: Possible configurations for the mirror assembly.

by means of a flat directional mirror. The primary parabolic mirror is held normal to the Sun to maximise the illuminated surface area, and hence power density on the surface.

As the primary reflector is symmetrical around the  $z$ -axis (i.e. the aperture is a circle), the total surface area is calculated based on the focal length  $f_\ell$  and accounting for the blockage caused by the directional mirror,

$$A_{M_1} = \iint_{\frac{d_g}{2}}^{\frac{d_{M_1}}{2}} 4 \sqrt{\left(\frac{x}{2f_\ell}\right)^2 + \left(\frac{y}{2f_\ell}\right)^2 + 1} dx dy \quad (2.2)$$

where  $d_{M_1}$  is the diameter of the aperture on the parabolic mirror,  $d_g$  is the diameter of the gap (equal to the entrance aperture of the laser assembly). The surface area integral is based on the general equation for a paraboloid,

$$z = \frac{x^2}{a^2} + \frac{y^2}{b^2} \quad (2.3)$$

and the general equation for the surface area element  $dS$  on the surface  $z = f(x, y)$  [Adams, 2000],

$$dS = \sqrt{\left(\frac{\partial z}{\partial x}\right)^2 + \left(\frac{\partial z}{\partial y}\right)^2 + 1} dA \quad (2.4)$$

Several options exist for directing the beam onto the surface of the asteroid, as seen in Fig. 7. One option is to use a lens system to collimate the beam, while another uses a laser as the collimator. Both these options are analysed in Section 2.2 on the advanced optical design.

### 2.1.2 Adaptive mirror configuration

The single mirror configuration is composed of an asymmetric, adaptive primary mirror. The shape of the primary mirror is assumed to be adaptable such that the focal point can be moved in order to steer the beam in the desired direction.

If the mirror was flat, then a local Cartesian reference frame could be defined with coordinated axes  $\mathcal{M}$  centred in the barycenter of the mirror assembly and with the axis  $\hat{x}$  perpendicular to the mirror surface. Within the same reference frame  $\mathcal{M}$ , and given: the desired position of the focal point in  $\mathcal{M}$ , the position of the centre of a mirror element with infinitesimal area  $dA_M$  and assuming a perfect reflection, the law of reflection gives,

$$\frac{dy_M}{dx_M} = \tan\left(\beta - \frac{\pi}{2} - \phi(x_M, y_M, x_f, y_f, \beta)\right) \quad (2.5)$$

where  $f_\ell = [x_f, y_f]$  is the position of the focal point,  $\beta$  is the Sun aspect angle with respect to the  $y$  axis in  $\mathcal{M}$  and  $\phi$  is the angle of reflection. Figure 8 shows the configurations of the mirror reference frame with respect to the vectors from the mirror origin (or spacecraft) to the Sun,  $\mathbf{r}_{sc/\odot}$ , to the focal point  $f_\ell$  and finally, to the asteroid  $\mathbf{r}_{sc/A}$ .

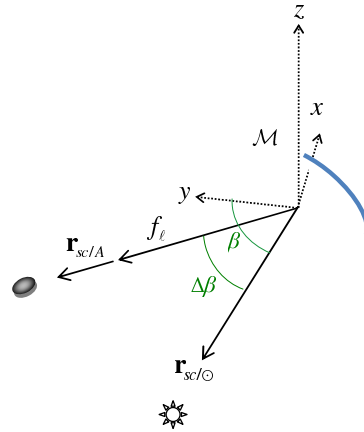


Figure 8: Definition of mirror-centric relative reference frame  $\mathcal{M}$ .

By integrating (2.5) with the initial conditions  $x_{M_0}$  and  $y_{M_0}$ , the position and attitude of each section of the mirror in the  $x^{\mathcal{M}}-y^{\mathcal{M}}$  plane can be found, given the position of the focal point and the direction of the incoming solar rays. The mirror is then considered to be symmetric with respect to the  $x^{\mathcal{M}}-y^{\mathcal{M}}$  plane such that each section of the mirror parallel to the  $y^{\mathcal{M}}-z^{\mathcal{M}}$  plane is a parabola. Equation (2.5) was coded into a Matlab<sup>®</sup> function and incorporated into an orbital dynamics model, such that for each position of the mirror with respect to the asteroid (i.e. the focal point) and for every attitude angle, a different mirror shape is generated.

Two examples are shown in Fig. 9, where the focal point is set by  $[\cos(\beta-\Delta\beta), \sin(\beta-\Delta\beta)]$  and  $x_M \in [-1, 1]$ . Both the incoming and outgoing (or reflected) rays are shown, as well as the 2D mirror shape and focal point.

## 2.2 OPTICAL SYSTEMS

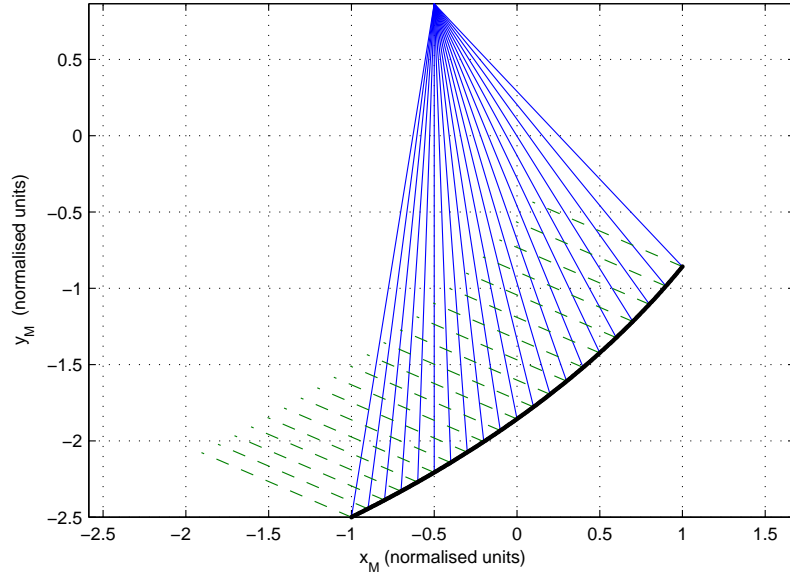
It is important to distinguish between the focusing device (or collector) and the beam generation device. The various options proposed differ in the way the power collected from the Sun is projected onto the surface of the asteroid. In particular, three different concepts are examined: direct imaging, indirect imaging through an optical system (collimating lenses) and lasers.

### 2.2.1 Solar properties

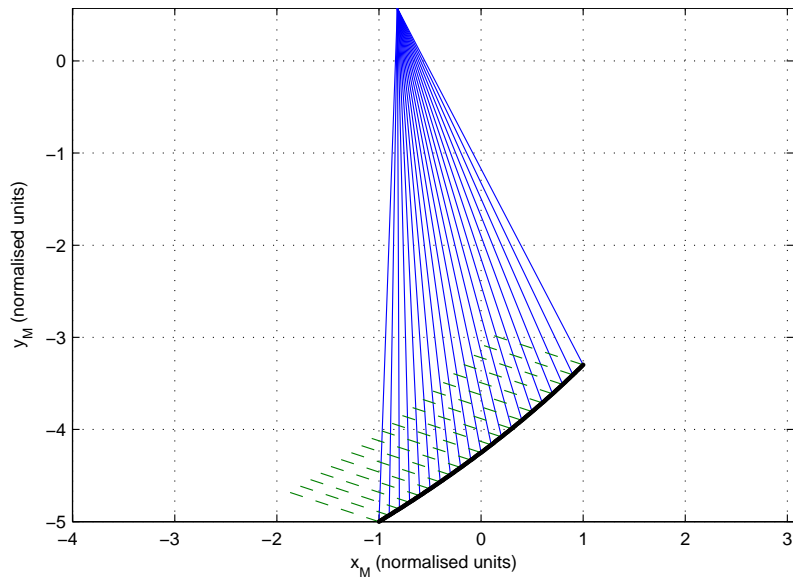
The physical angular measurement of the Sun (or *solar disk*) can be calculated by simple geometry. Given a volumetric mean radius of the Sun of  $6.9600 \times 10^5$  km, for the current orbit of Apophis the Sun has a conic half-angle of 6.2349 mrad at the NEO periapsis (0.7461 AU), and 4.2348 mrad at the NEO apoapsis (1.0986 AU).

Figure 10 shows the extra-terrestrial solar spectral irradiance for a range of wavelengths (assuming a black body temperature of 5777 K). The database used is the ASTM E-490-000\*, published by the American Society for Testing and Materials (ASTM) in 2000 based on data from spacecraft, space shuttle missions, high-altitude aircraft, rocket soundings, ground-based solar telescopes, and modelled spectral irra-

\*[www.astm.org/Standards/E490.htm](http://www.astm.org/Standards/E490.htm), link valid as of February 23, 2010.



(a)  $\beta = 155^\circ, \Delta\beta = 35^\circ$



(b)  $\beta = 160^\circ, \Delta\beta = 15^\circ$

Figure 9: Examples of a single mirror directly projecting the light of Sun onto the focal point. The green dashed lines are the Sun rays, blue lines are the reflected rays. The mirror is shown in the  $x^M$ - $y^M$  plane, with the axes normalised to one.

diance. The wavelength of visible light falls between violet (380 – 450 nm) and red (620 – 750 nm), with the peak irradiance occurring at 450.5 nm (2.2198 MHz).

The solar flux constant,  $S_0$ , is defined as the rate at which energy is received from the Sun over a unit area normal to the radiation of the Sun, taken at a mean distance of one astronomical unit. The World Radiation Centre adopted a mean solar flux

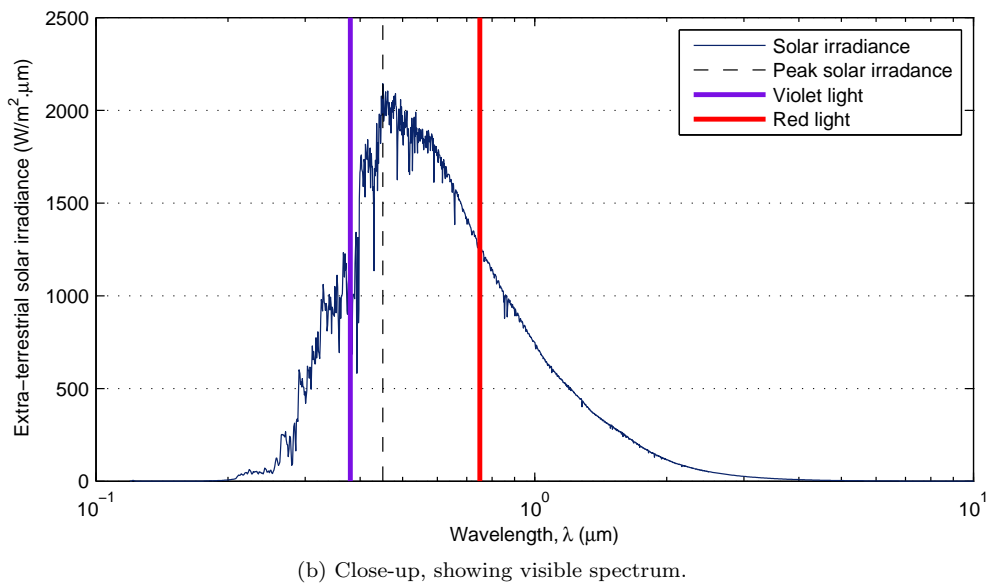
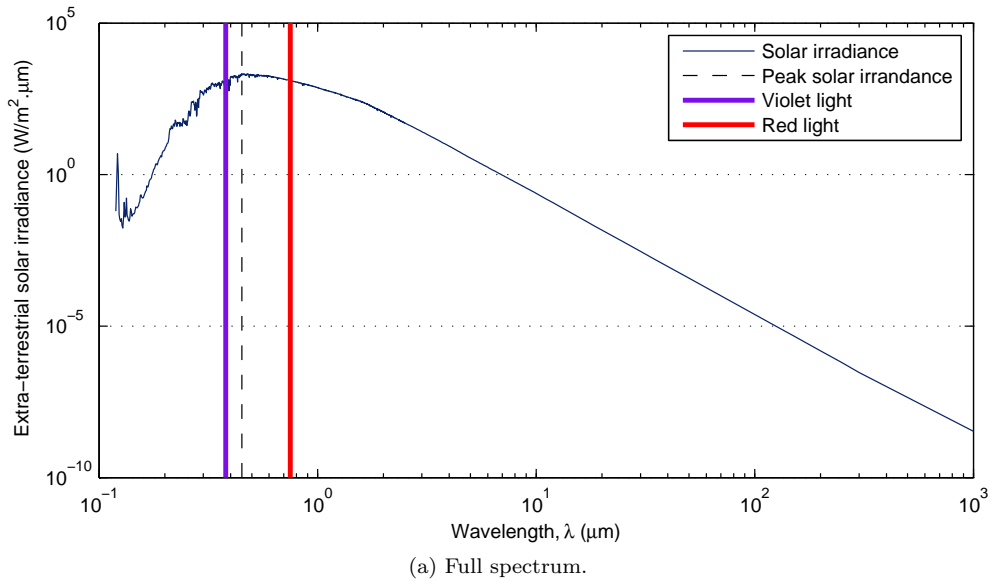


Figure 10: 2000a (2006) ASTM Standard Extraterrestrial Spectrum Reference E-490-00. Note, the integrated spectral irradiance has been made to conform to a solar constant of  $1366.1 \text{ W/m}^2$  [ASTM, 2006].

value of  $1367 \text{ W/m}^2$ , with an uncertainty of 1%, which is the one most commonly found in literature. However, as seen from Figure 11 which shows the measurements of the solar flux over a period of 25 years, that value may overestimate the amount of energy flux provided. Nevertheless, in the following the solar flux is assumed to be  $1367 \text{ W/m}^2$  and varies quadratically with the distance from the Sun,  $S(r) \propto r^{-2}$ .

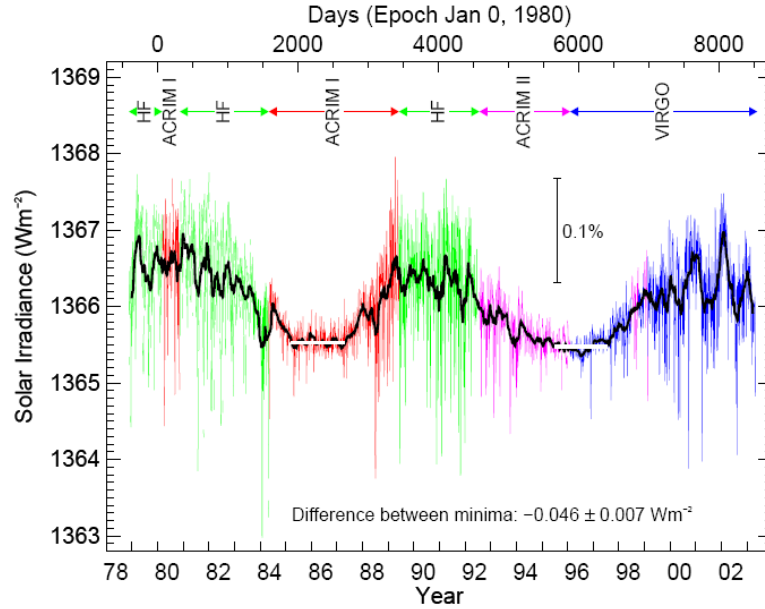


Figure 11: Composite of total solar irradiance measured by different space-based radiometers (HF on NIMBUS7, ACRIM-I on SMM, ACRIM-II on UARS, VIRGO on SOHO). The coloured lines show daily averaged values, and the black line is mean (source image from Fröhlich (2003)).

### 2.2.2 Direct imaging

The simplest design for the mirror assembly is to directly focus the sunlight onto the asteroid, essentially imaging the solar disk onto the asteroid surface. There are a number of restrictions however, given the coupled nature of the variables. The range is determined by the focal point of the mirror. Coupled with a manufacturing limit on the maximum size of the mirror, this forces the spacecraft to operate in close proximity to the surface of the asteroid, subjecting it to the largely unknown, and inhomogeneous gravity field of the NEO. In addition, issues such as contamination due to the generated debris also risk damaging the mirror surface.

The beam must also be directed towards the asteroid, since the asteroid, Sun and spacecraft are not in-line as they would be in a typical imaging system. This means that either the mirror must operate at an angle, translating into a loss of illuminated surface area, or the focal point must be raised or lowered relative to the principal optical axis.

Lastly, the spot size is determined by the concentration ratio (magnification) which is a function of the ratio of the distance between the source and the mirror ( $r_{\odot/sc}$ ), and the distance between the mirror and the image ( $r_{sc/A}$ ).

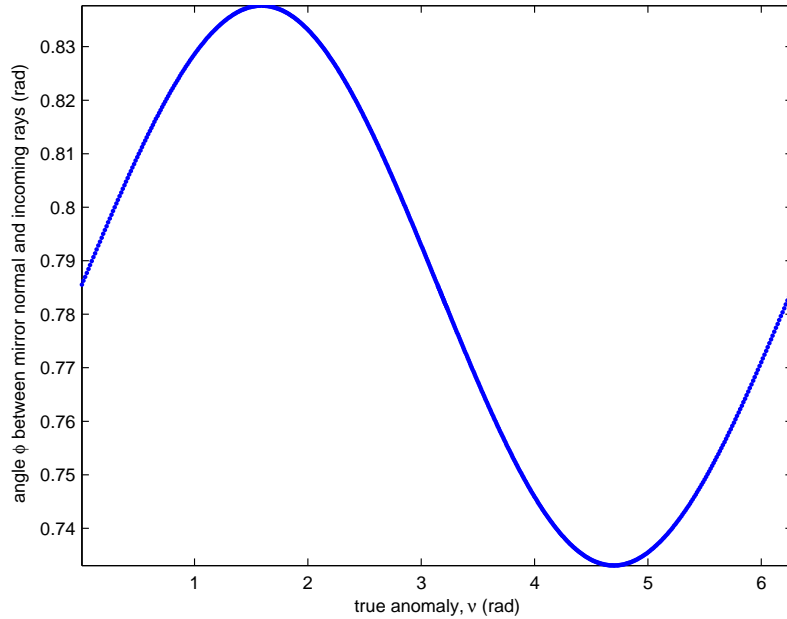


Figure 12: Angle of reflection  $\phi$ , between mirror surface normal and incoming (or outgoing) rays.

Given the equation for a  $x$ - $y$  symmetrical parabolic reflector,

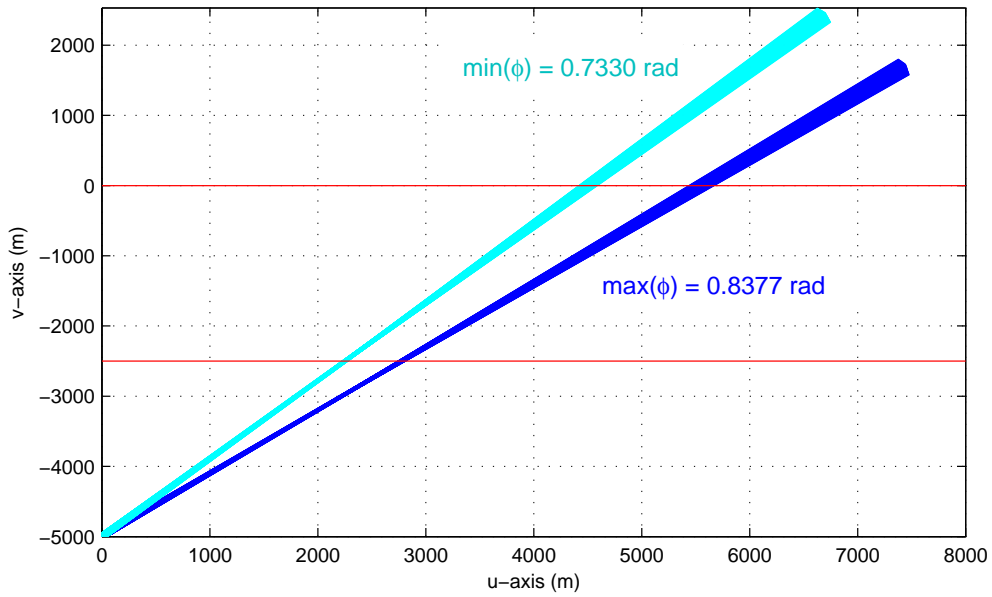
$$(z - z_0) = \frac{(x - x_0)^2}{4f_\ell} + \frac{(y - y_0)^2}{4f_\ell} \quad (2.6)$$

The angle between the Sun and one of the spacecraft in the formation is shown in Fig. 12; on average, the half-angle  $\phi$  fluctuates between 0.7 – 0.9 rads. If a parabolic mirror with a 100 m aperture diameter is rotated through the same angular range, the result is shown in Fig. 13. This is the equivalent to the change in angle the directional mirror would need, in order to keep the spot position on the asteroid constant over the one entire orbit. This difference is due to the constantly changing position of the spacecraft relative to the asteroid, and the asteroid and spacecraft relative to the Sun, as they both orbit around the Sun.

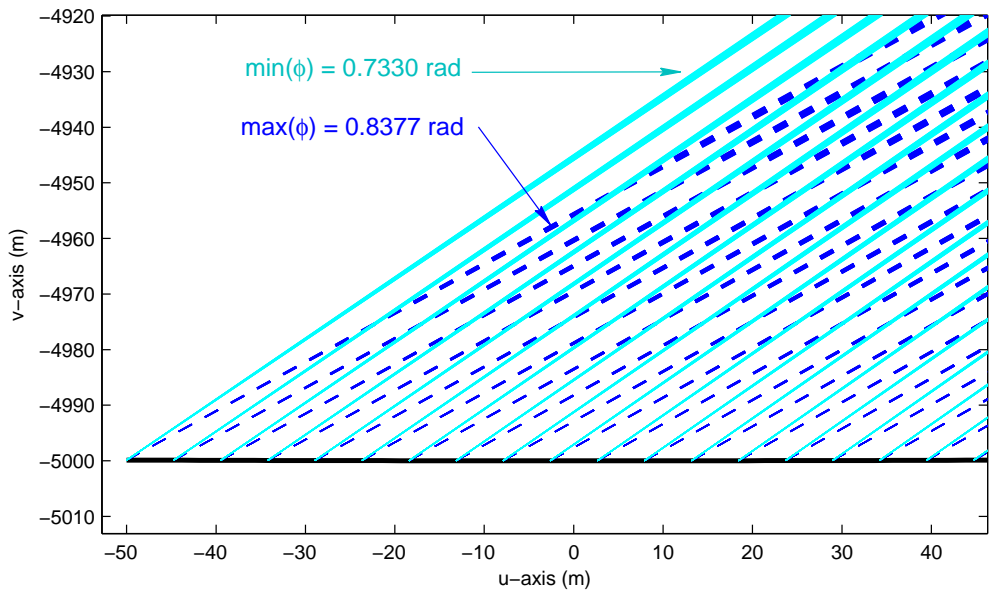
The spot size at a nominal range of 2.5 km fluctuates between 53 m at  $\min(\phi)$  to 66 m at  $\max(\phi)$ . The focal length, for a minimum image size at the nominal range, was set to 5 km. This gives a minimum concentration ratio of 2.5. This can be seen in Fig. 13, where the  $v$ -axis is the optical axis of the mirror, and  $\phi$  is the angle between that axis, and the outgoing beam. Due to the laws of reflection, the angle of incidence is equal in magnitude to the angle of reflection, but negative in sign (i.e. measured from  $+v$  towards the  $-u$ -axis). Figure 13a in particular, shows the divergence due to the solar disk as the distance away from the mirror surface increases, and the change in direction due to the variation in  $\phi$ .

For the sake of analysis, if we let  $\phi = 0$  rad, and place the focal length exactly at the asteroid ( $f_\ell \Rightarrow 2.5$  km), then the spot diameter due solely to the effect of the solar disk is 25 m (for a concentration ratio of 20).

The loss due to angle of reflection can be reduced by moving the focal point of the mirror by continually altering the shape of the reflector. This maximises the illuminated area, which allows for a greater concentration ratio. Figure 14 shows the



(a) Overview of the entire system. The reflector is designed for a focal distance of 5 km, located at the origin (0,0), with the minimum beamwidth occurring half-way, at 2.5 km (or when  $v = -2.5$ ), where the  $v$ -axis here is the optical axis of the mirror.



(b) Close-up of the above plot, at the mirror surface. Due to the long focal length relative to the mirror diameter, the parabolic mirror is essentially flat. The difference in incoming rays is due to the changing geometry between the Sun-asteroid angle, equal to  $2\phi$ .

Figure 13: Example of direct imaging of the solar disk using an 100 m diameter, fixed paraboloidal reflector, and showing the difference in beam directions and widths at the maximum and minimum angle of reflection  $\phi$ .

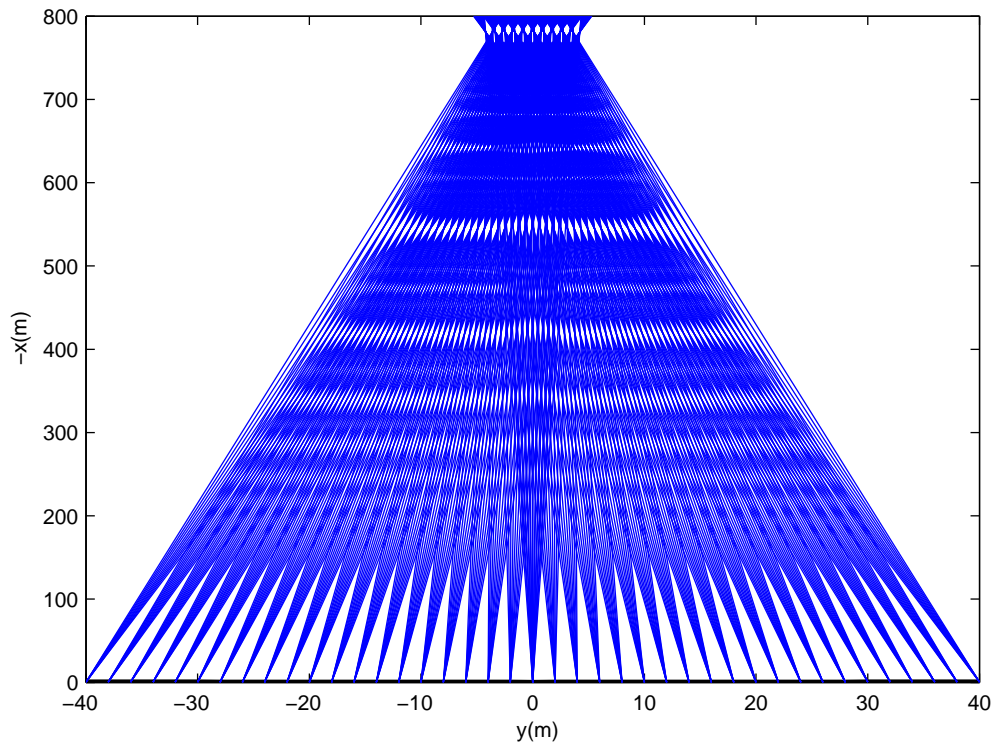


Figure 14: Direct imaging of solar disk on Apophis using an adaptive paraboloidal reflector. The mirror is located along the  $y$ -axis, and the asteroid is located at the minimum beam width, at 780 m.

result of directly focusing the solar disk on an 80 m aperture diameter reflector at a range of 780 m from the NEO. The spot diameter on the surface is 8.2 m, which would correspond to a concentration ratio of 95.

In the work of Sanchez Cuartielles et al. (2009), a system concentration ratio of 2500 was used to perform a comparison of the solar sublimation approach against other deflection methods. In other words, the power density on the surface is 2500 times greater than that provided by the solar radiation at the mirror surface.

For example, for a 1 m diameter spot size on the surface, 25 spacecraft, each with 50 m diameter mirrors would provide a system concentration ratio of 2500. The number of spacecraft and mirror size depend on the available time for the deflection action and on the distance from the asteroid. The distance from the asteroid, in turn, depends on the orbital position of the spacecraft near the asteroid that would allow the spacecraft to see the Sun and avoid any plume impingement. Note that  $C_r = 2500$  is not the minimum concentration ratio required to sublimate the surface of a NEO with a single spacecraft, simply a nominal value.

The minimum required power density of the illuminated spot is dependant on the distance from the Sun, rotational velocity of the asteroid  $w_A$ , the size of the spot, etc. As an example, considering that a point travels with a linear velocity  $v_{rot} = w_A R_A = 0.0077$  m/s (due to the rotation of the asteroid, where  $R_A$  is the radius along one axis of the asteroid) through the illuminated spot, the minimum required power density at  $r_A = 0.92$  AU is  $7.166 \times 10^5$  W/m<sup>2</sup>. This corresponds to a system concentration ratio of  $C_r = 554$  in order to induce sublimation (for a system efficiency of  $\eta_{sys} = 1$ ).

A study commissioned by NASA [Hedgepeth and Miller, 1987, 1988] in the late 1980s investigated concepts for large solar collectors, including an analysis of the effects of errors on the effective concentration ratio of space-borne paraboloidal reflectors. Starting with a perfect smooth paraboloidal reflector with aperture diameter  $d_M$ , see Fig. 15a, and assuming the same solar disk angle of  $2\varepsilon_\odot \approx 9$  mrad, the resulting image is shown on a receiver plane in Fig. 15b.

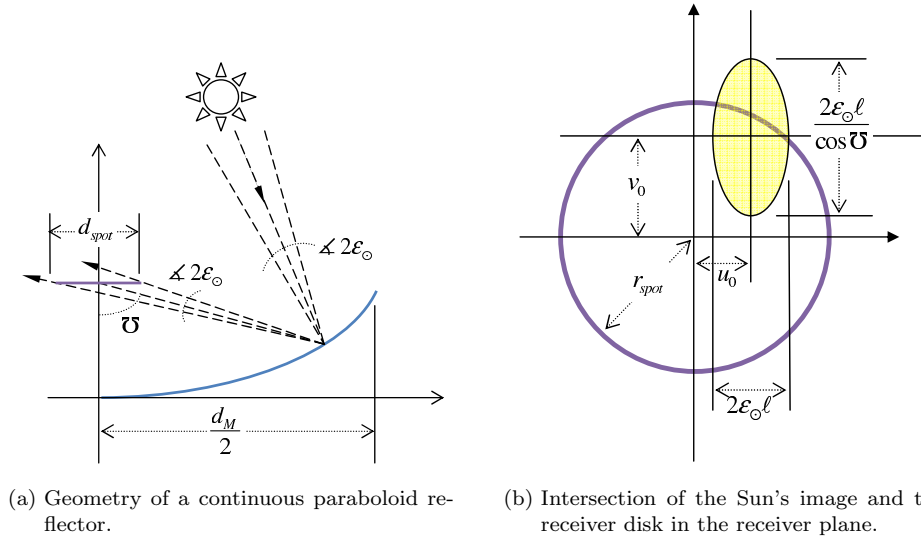


Figure 15: Analysis of the image of Sun (images from Hedgepeth and Miller (1987));  $[u_0, v_0]$  represent an offset due to geometric errors on the reflector surface at the point of reflection.

The dimensions of the image are,

$$u = 2\ell\varepsilon_\odot \quad (2.7a)$$

$$v = \frac{2\ell\varepsilon_\odot}{\cos\bar{U}} \quad (2.7b)$$

where  $\ell$  is the distance from a point on the reflector to the focal point, and  $\bar{U}$  is the angle between  $\ell$  and the optical axis of the reflector. The equations for the image do not account for any geometric errors on the structure of the reflector. The effect of any errors would be an offset in the intersection with the focal plane, altering the centre point of the elliptical image (given as  $[u_0, v_0]$  in Fig. 15b). Relating to this study, the illuminated spot on the asteroid surface is equivalent to a ‘receiver disk’ with a diameter  $d_{spot}$ . Depending on the number of spacecraft in the formation, the spot is actually a conglomerate of many beams, any errors or offset in position and the image distortion due to the elevation and azimuth angles between the mirror assembly and the Sun would result in a situation as shown in Fig. 15b. In the case of the fixed configuration, the directional mirror would have to be sized relative to the intended spot area plus a margin of error such that the majority of the beams are within the given circular area on the surface. The analysis done here accounted for the spot area and mirror or reflective areas – the diameters listed are, at least in the case of the fixed mirror configuration, the equivalent diameter assuming the area is a perfect circle.

As a first approximation, the radius of the projected image was assumed to increase linearly with the distance between the mirror and the target; the area of the collector, for a fixed concentration ratio, increases quadratically with the distance from the target. Note that as the mirror moves away from the Sun, the concentration ratio can be increased, at constant distance from the target, by keeping the size of the mirror constant and changing its curvature. Conversely, when the mirror moves toward the Sun the concentration ratio for a fixed distance and fixed size has to go down. The solar flux increases quadratically as the mirror approaches the Sun, thus compensating for the loss in concentration factor. This is also true when the mirror moves away from the Sun, therefore by changing the curvature of the mirror the total flux on the target area can be maintained constant as the mirror moves with respect to the Sun.

### 2.2.3 Collimating lens

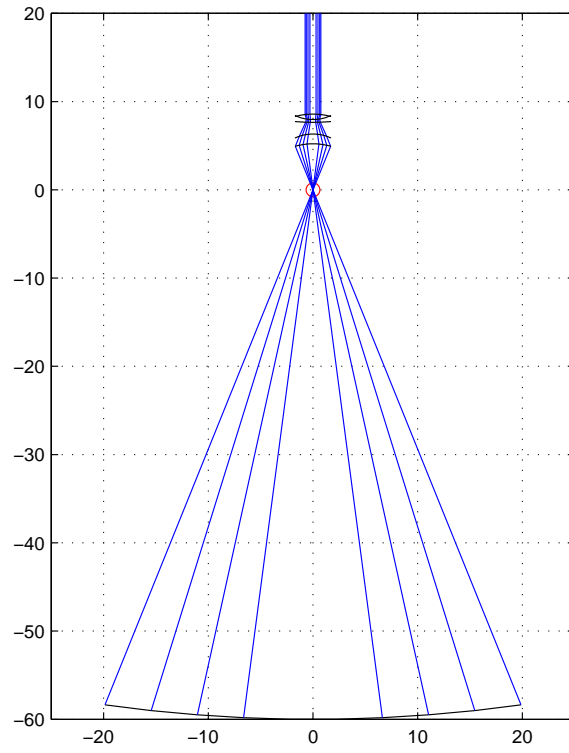
One option investigated to improve the concentration ratio was to considerably reduce the focal length to the same magnitude of the diameter, and add a lens system which minimises the divergence of the beam after the focal point of the mirror. An in-house ray tracing program was developed (in Matlab) in order to design lens systems based on an objective function. An education-version of the optical software program OSLO by SinOpt was also used to analyse the lens designs, however it was found that the Matlab code was more efficient for this analysis (due to limitations in the educational version of the software, learning curve, etc.).

A single spherical lens will always be subject to, among other errors, spherical aberrations leading to a distortion in the intersection of the beams (i.e. they do not all meet at a single point, but instead create a ‘curved envelope’ about the original focal point), or going in the other direction, the ‘collimated’ beams instead diverge.

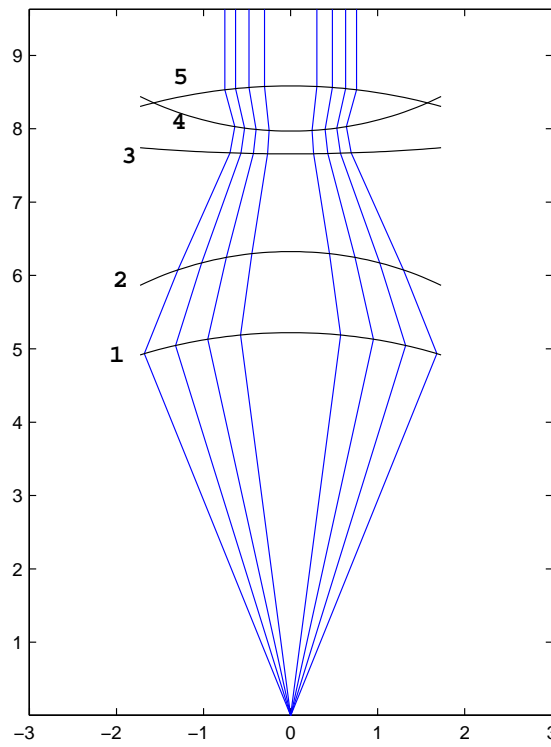
A common class of lens exist that attempt to minimise both spherical and chromatic aberrations that result from using multiple wavelengths (or frequencies) of incoming rays. The two aberrations have a similar corrective approach in that the solution attempts to bring distorted refractive/reflective rays into focus on the same plane. The distortion can be due either to the effects of different frequencies through the lens medium, or by distance from the optical axis and corresponding angle of incidence. The design for an *achromatic lens* (or achromat) uses two lenses cemented together to form a doublet. The first lens generally has a higher index of refraction, while the second has a lower index such that the aberration of one is counteracted by the second.

In this case, an optimisation was run to determine a lens systems that would collimate the output from a fixed parabolic mirror. The maximum number of lens surfaces was set to 5 (each lens having two surfaces), with the free variables set to the radius of curvature of each surface (assumed to be spherical), and the distance along the optical axis from the previous lens surface to the current surface. Figure 16 shows the resulting optimised system of lenses assuming parallel incoming rays from the Sun. The maximum angular divergence is  $5.7923 \times 10^{-5}$  rads, resulting in a spot diameter of 1.6574 m (using a reflector with an aperture diameter of 40 m and a focal length of 60 m). Table 4 gives the specific solution vector for the lens system.

When the incoming solar rays were modified to account for the size of the solar disk, the results became infeasible. As seen from Fig. 17, for the same reflector-lens configuration as above, the divergence results in a spot diameter of just over 900 m. Even when the lens system was re-optimised to account for the off-axis incoming rays, the results of the spot size are still larger than the baseline case with no lenses.

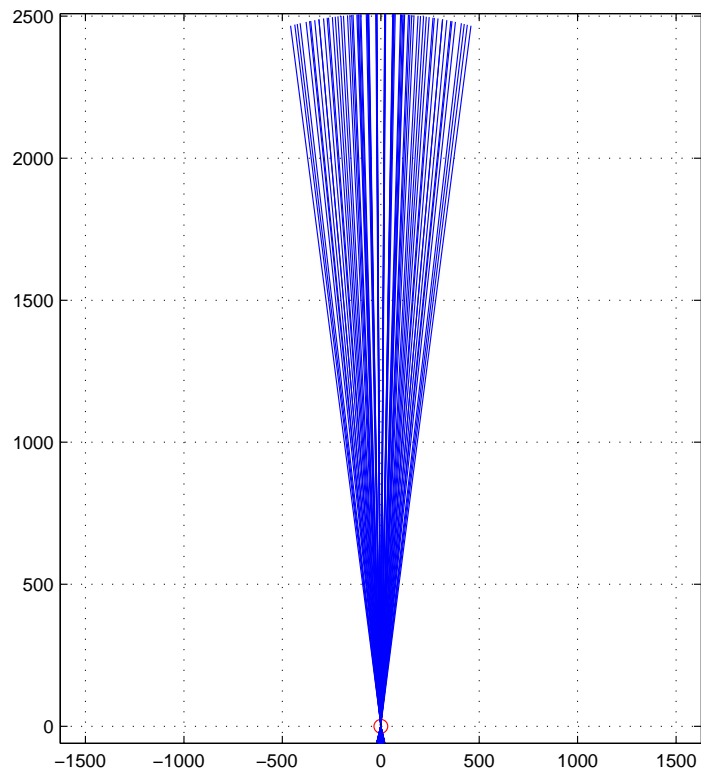


(a) Overview of system, including primary mirror, focal point, and collimating lens system.

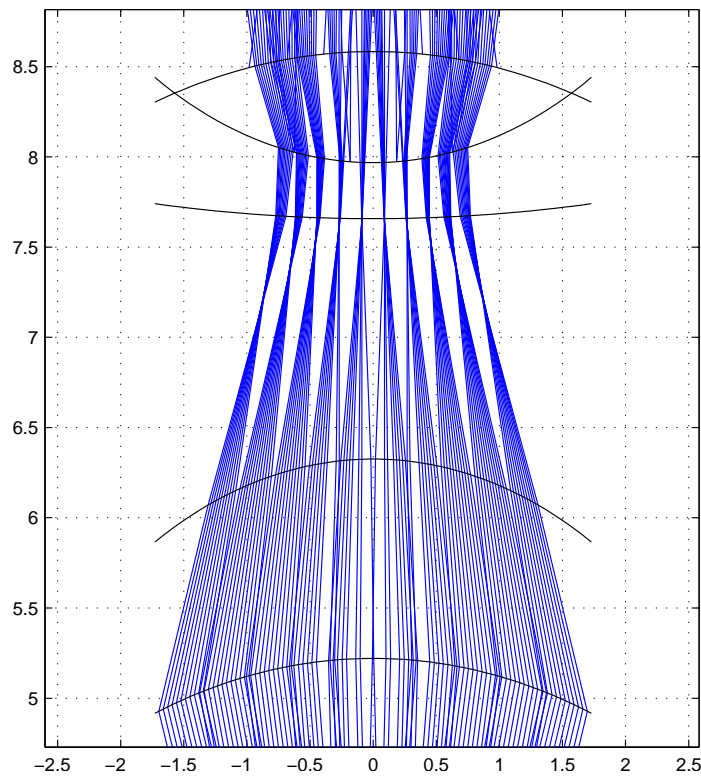


(b) Close-up of collimating lens configuration, with each surface number corresponding to Table 4.

Figure 16: Lens configuration for collimating a beam assuming parallel incoming solar rays. The axes are in metres, with the focal point of the reflector at (0,0).



(a) Overview of system, including primary mirror, focal point, and collimating lens system.



(b) Close-up of collimating lens configuration.

Figure 17: Effect of off-axis rays (accounting for the solar disk) on the lens system in Fig. 16. The axes are in metres, with the focal point of the reflector at  $(0,0)$ .

Table 4: Dimensions of lens assembly given in Figs. 16, 17.

	Surface	Radius of curvature (m)	Distance from focal point (m)	Index of refraction*, $n$
Reflector:	0	$z = \frac{R^2}{4f_\ell} - f_\ell$	-60	1.0
First lens:	1 2	5.06239 3.4792	5.220826 1.10455	1.689 1.0
Second lens:	3 4 5	-18.0540 -3.399048 5.46774	1.332166 0.310507 0.615707	1.673 1.564 1.0

\* The index of refraction listed is for the material from surface  $i$  to  $(i + 1)$ .

If the lens system worked with very little distortion, the other concern would be due to the monochromatic nature of glass lenses versus mirrors, which are frequency-independent. Superachromatic lens can focus up to four wavelengths bracketing the visible spectrum, which contains the highest energy segment of the solar spectrum, however the system would still have to account for a loss of power density due to the frequency limitation. Other, more complex options include a graded index of refraction of the material, or using slotted or notched lenses (similar in concept to a Fresnel lens, for example). However these would have to be specifically manufactured for a fixed set of angles; given the variance in the angle of incidence/reflection this poses numerous difficulties in the design. It is possible to fix the angle of incidence, and instead remove the constraint of the primary mirror to remain in-line with the Sun-pointing vector however at a cost of a decrease in available solar power (due to the shadows introduced onto the reflector surface).

#### 2.2.4 Solar-pumped laser

The concept of converting emitted radiation from the Sun, a broad-band renewable energy source, into a narrow, coherent beam is decades old [Young, 1966]. The barrier has been making the process efficient given the broad frequency band of the Sun's radiation, compared with the narrow absorption bands of most lasing crystals.

Lasers work on the premise of exciting electrons by stimulating them with the addition of photons (or quantum energy), which temporarily boost them up to a higher energy state. This stimulation continues until a population inversion exists, where there are more electrons at a higher energy state, e.g.  $E_1$  than at the lower (or original) state, e.g.  $E_0$ . The release of photons when the electrons drop back to their original base state produce an emission that has the same spectral properties of the stimulating radiation, and is therefore highly coherent. There can be any number of energy state levels and transitions, for e.g. an Nd:YAG laser has four states. The energy that is not released as part of the output emission, is instead released as heat. This means that the laser must be continually cooled, which in space means large radiators.

There are two general methods of powering the laser: *direct pumping*, where the energy is directly used to excite the laser, and *indirect pumping*, where an intermediate step is used to first convert the energy, e.g. solar radiation, into electricity.

INDIRECT PUMPING Indirect solar-pumped lasers convert the solar energy first into electricity, which is then used to power the laser. Photovoltaic cells are an obvious choice for space applications. The drawback, of course, is the addition of an electrical power generator meaning added mass, size and power requirements.

A possible solution is to use high efficiency solar arrays in conjunction with a solid state laser. Solid state lasers pumped with electric power can currently reach 60% efficiency. If the solar arrays have an efficiency of 30%, then the system would have an overall efficiency of 18%. If a pumped laser is used, then the focal point can be close to the primary mirror and a high concentration factor can be obtained with a relatively small mirror. For example, if the mirror has an area of 314 m<sup>2</sup> (equivalent to a 20 m diameter circular mirror), then the collected power at 1 AU is 429.5 kW. The solar array + laser system converts only 18% of this power, therefore only 77.3 kW is beamed to the surface to the asteroid, while the rest needs to be dissipated.

Even by placing the radiator in the shadow cone of the primary mirror and/or spacecraft, the excess power would still need to be dissipated. In steady state conditions, given a radiator of surface area  $A_R$ , the temperature of the radiator  $T_R$  would be,

$$P_{in} - P_{out} - P_{reflected} = \sigma \epsilon_R A_R T_R^4 \quad (2.8)$$

$$T_R = \left( \frac{\alpha_{SA} S_r A_M - \eta_{SA} S_r A_M - \sigma \epsilon_{SA} T_{SA}^4}{\sigma \epsilon_R A_R} \right)^{\frac{1}{4}} \quad (2.9)$$

where  $\alpha_{SA} = 0.8$  is the absorptivity of the solar converter,  $S_r$  is the solar flux at distance  $r_{\odot/sc}$ ,  $A_M$  is the area of a 20 m diameter mirror,  $\eta_{SA}$  is the efficiency of the solar converter,  $\sigma$  is the Stefan-Boltzmann constant,  $T_{sa} = 200^\circ\text{C}$  is the operating temperature of the solar converter and lastly  $\epsilon_{SA} = 0.7$ ,  $\epsilon_R = 0.9$  are the emissivity of, respectively, the solar arrays and the radiator. The solar arrays are assumed to have a surface area of 1 m<sup>2</sup>. Figure 18 shows the resulting radiator temperature versus surface area for different efficiencies  $\eta_{SA}$  of the solar array plus laser system.

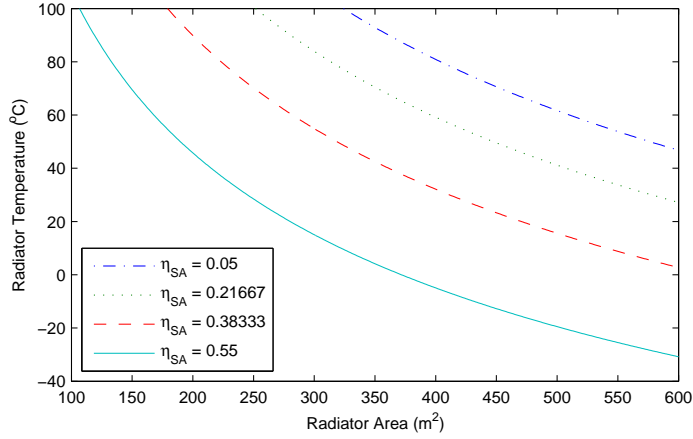


Figure 18: Radiator area vs. radiator temperature

The system would need to operate at a higher temperature than the radiator, imposing severe conditions on the solar arrays. Possible solutions include,

- the heat being dissipated through a large radiator, located in the shadow cone of the primary mirror,

- the efficiency of the solar arrays substantially increased above 30%,
- the operating temperature of the solar arrays increased above 200°C.

An alternative could be to use a solar dynamic system with a Stirling engine [Shaltens and Wong, 2007; Wua et al., 2003] (or Brayton or Rankine cycle) instead of the solar arrays. This solution would achieve a conversion efficiency of up to 38% and, more importantly, could operate at higher temperatures (up to 850°C). However, although the scalability of the system has to be considered with care, according to the current status of the research at NASA on Brayton converters [Shaltens and Mason, 1999], and considering only the mass of the receiver, Brayton engine, heat rejection and associated structures, the power conversion unit could have a specific output power of 27 W/kg. This estimation is based on the advanced technology that NASA was expecting in 1999. For the example above, the mass of the conversion unit would be about 5000 kg, with an efficiency of 34%. This mass is still unsatisfactory for a 20 m diameter mirrored spacecraft. The main problem then still exists, to make the receiver and the heat rejection system far lighter than what they are at present.

**DIRECT PUMPING** Direct solar-pumped lasers, do precisely what the name suggests: the laser is directly energised using solar radiation. Due to the mismatch between the wide-band emissions of the Sun with the narrow absorption bands of lasers, the loss of available solar power is currently rather high. Figure 19 shows the overlap between the solar spectrum, and that of the absorption bands of a common Nd:YAG lasing crystal.

### *Lasing Material*

In theory, any lasing material that can be optically pumped can also be used as a solar laser. It is not the intent of this dissertation to delve too deeply into the technical details of lasing materials, however a selection of solid-state laser materials are summarised below based on current literature [Weksler and Shwartz, 1988; Lando et al., 2003; Adbel-Hadi, 2005].

The Nd:YAG, composed of neodymium ions ( $\text{Nd}^{3+}$ ) in yttrium aluminum garnet ( $\text{Y}_2\text{Al}_5\text{O}_{12}$ ), is the most commonly used in solid-state laser for many cross-platform applications since it is relatively cheap to produce and readily available, and more importantly, has good thermal resistance, durability and lifetime. The absorption bands are relatively narrow however, and with the main peak at 1064 nm (see Fig. 19). The overlap between the Nd:YAG absorption spectrum, and the solar radiation spectrum is around 0.14 [Weksler and Shwartz, 1988]. Chromium doping, Cr:Nd:YAG can further improve the power conversion over the undoped, conventional Nd:YAG systems.

Adbel-Hadi (2005), quoted below, gives a good general description of other possible laser types:

ND:CR:GSGG has received considerable attention because of the good spectral match between the flashlamp emission and absorption of the Cr ions. The host of this laser is the Gadolinium Scandium Gallium Garnet (GSGG). An efficient energy transfer between the Cr and Nd ions results in a highly efficient Nd:laser.

ND:YLF is a good candidate for certain specialized applications, because the output is polarised, and the crystal exhibits lower thermal bi-refringence. Nd:YLF has a higher energy storage capability (due to its lower gain coefficient) compared to Nd:YAG and its output wavelength matches that

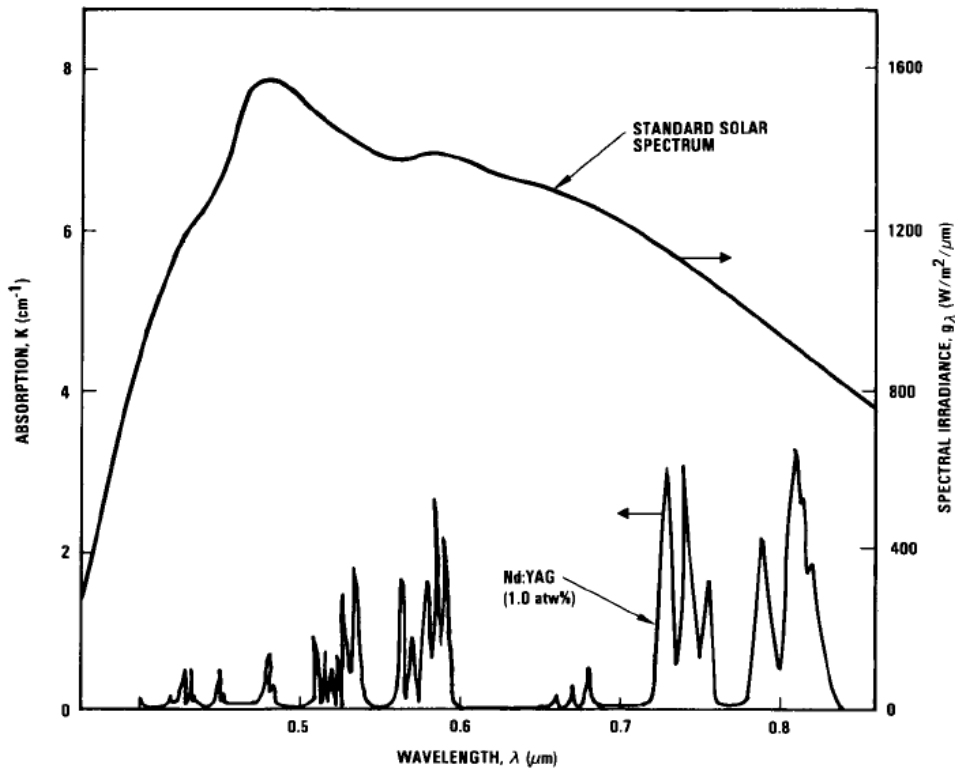


Figure 19: Nd:YAG absorption bands compared with the standard extraterrestrial solar spectrum (source image from Weksler and Schwartz (1988)).

of phosphate Nd:glass. Therefore modelocked and Q-switched Nd:YLF lasers have become the standard oscillators for large glass lasers employed in fusion research. The host YLF is the uniaxial crystal Yttrium Lithium Fluoride (YLiF<sub>4</sub>).

**ND:YVO<sub>4</sub>** The laser emission cross-sections of Nd:YVO<sub>4</sub> crystal at 1060 nm and 1340 nm are 2.7 and 18 times larger than that in Nd:YAG respectively, and the crystal has good mechanical, physical and chemical properties.

In a paper presented in 1994, Landis discussed the use of a directly solar pumped laser based on semiconductor technology [Landis, 1994]. According to Landis, the expected efficiency of directly pumped semiconductor laser would depend on the same efficiency losses of a solar cell, therefore Landis was expecting a lasing efficiency (output/input power ratio) of 35%. Such an efficiency would be one order of magnitude higher than the best YAG system, which was expected to reach 6% of overall efficiency.

Direct solar pumping would represent an interesting solution in terms of complexity of the overall system. In fact no cooling system for the photovoltaic conversion and no power transmission would be required. On the other hand the TRL of both solar cells and semiconductor lasers is far higher than the one of a directly pumped laser and an indirectly pumped laser can be expected to be operational very soon.

Furthermore, recent semiconductor laser, electrically pumped, have proven over 73% plug efficiency [nLIGHT, 2006]. A substantial increase in cells efficiency has also

to be expected. In particular, in order to achieve a 35% efficiency in direct pumping, semiconductor technology should allow the absorption of the solar spectrum over a wide range of frequencies. A high efficiency of a directly pumped laser is therefore expected to correspond to a high efficiency of solar cells. An increase of solar cell technology up to 50% [Luque et al., 2004] is reasonable, allowing an indirect pumping system to have a comparable efficiency to a 35% direct pumping system.

### 2.2.5 Discussion

From the analysis of the methods for collimation of the solar light, it is apparent that collimating the solar light at long distances is not possible with conventional optics. Though a more thorough investigation would be needed to conclude that this technological solution is not feasible, there are other solutions analysed, such as the laser, that appear promising.

From this analysis, although still preliminary in nature, the direct imaging option appears feasible. The advantage of a direct imaging system stands in its reduced number of components and the virtually zero dependence on the frequency of the light beamed on the surface of the asteroid. If the surface material has, for example, an average absorptivity of 0.7 over the visible spectrum then the material absorbs 70% of the incoming radiation. This is not true for the monochromatic beam generated by a laser since the surface material has a maximum absorption only at the certain frequencies specific to a particular laser system. The main disadvantage of a direct imaging system is that it is strongly dependent on the distance from the asteroid. For a constant concentration ratio, the size of the mirror increases with the distance from the asteroid.

The laser option has the fundamental advantage to be far less dependent on the distance from the asteroid. Therefore it allows for a more flexible beaming of the light onto the surface of the asteroid. On the other hand the number of components in the system is higher. The choice between a directly pumped system versus an indirectly pumped one is not conclusive. At this particular stage of the research in laser technology and solar cell technology the most short term solution with acceptable efficiency would be the indirect pumping. On the other hand, a 35% direct pumping laser would significantly reduce the complexity of the system. Last but not least the laser option would require a minimum knowledge of the absorption frequency of the surface material of the asteroid.

## 2.3 MASS BUDGET

In order to assess the dry mass for a single spacecraft, a range of technology levels have been assumed, from existing flight hardware (Inflatable Antenna Experiment) through to a conceptual membrane system with embedded sensing and actuation. The key driver for the mass budget is the areal density of the adaptive reflector assembly. A range of technology readiness levels (TRL) will be considered with appropriate mass margins. It will be assumed that the reflector mass includes all associated control hardware.

The spacecraft bus is assumed to be comparable to NASA’s NEAR-Shoemaker spacecraft, and is representative of a mid-sized bus operating in deep space at a solar distance of up to 2.2 AU. The dry mass of NEAR is 487 kg, therefore a 500 kg bus is used with a 10% mass margin, given the flight heritage of the NEAR spacecraft. The bus is assumed to provide power, telecommunications and attitude sensing functions. It is also assumed that the adaptive reflector is used to manage any off-set in centre-of-mass and centre-of-pressure, which would represent the primary attitude disturbance.

In addition to the adaptive reflector and bus with appropriate mass margins, a system contingency of 20% is added to provide margin for the system integration.

Three different levels of system performance are considered based on current and predicated mass density of the reflector material  $\rho_M$  [Vasile et al., 2009a].

**MASS BUDGET A** Based on Inflatable Antenna Experiment flight hardware,  $\rho_M \approx 5 \text{ kg/m}^2$  [Freeland et al., 1997]. The TRL is assumed to be 6 since flight hardware has been demonstrated, although for an RF rather than optical system. A subsystem mass margin of 10% is added. See Table 5.

**MASS BUDGET B** Based on ARISE RF Radio Telescope study  $\rho_M \approx 0.5 \text{ kg/m}^2$  [Chmielewski et al., 2000]. The TRL is assumed to be 4 since initial technology development for the ARISE mission has been undertaken. A subsystem mass margin of 15% is added. See Table 6.

**MASS BUDGET C** Based on Innovative Large-Aperture Concepts,  $\rho_M \approx 0.05 \text{ kg/m}^2$  [Bekey, 2002]. The TRL is assumed to be 2 since the adaptive membrane system is at a conceptual level, although mass estimates have been made. A subsystem mass margin of 20% is added. See Table 7.

Table 5: Mass budget A,  $\rho_M = 5 \text{ kg/m}^2$ .

Item	TRL	Area ( $\text{m}^2$ )	Mass (kg)	Margin (%)	Total (kg)
Adaptive reflector	6	3000	15000	10	16500
Bus	9		500	10	550
Contingency				20	3410
Dry Mass					20460

The spacecraft mass in Tables 5–7 does not include any additional propellant mass required at launch. From previous studies by Colombo et al. (2009) and Sanchez Cuartielles et al. (2009), a low thrust transfer to Apophis would take around 470 days, with a maximum thrust level of 0.6 N for a 3000 kg spacecraft and an  $I_{sp}$  of 3200 s. Therefore, using the rocket equation [Vallado, 2004] and assuming a low thrust

Table 6: Mass budget B,  $\rho_M = 0.5 \text{ kg/m}^2$ .

Item	TRL	Area ( $\text{m}^2$ )	Mass (kg)	Margin (%)	Total (kg)
Adaptive reflector	4	3000	1500	15	1725
Bus	9		500	10	550
Contingency				20	455
Dry Mass					2730

Table 7: Mass budget C,  $\rho_M = 0.05 \text{ kg/m}^2$ .

Item	TRL	Area ( $\text{m}^2$ )	Mass (kg)	Margin (%)	Total (kg)
Adaptive reflector	2	3000	150	20	180
Bus	9		500	10	550
Contingency				20	146
Dry Mass					876

transfer, a non-optimised propellant consumption of 40% was added to the calculated spacecraft mass.

As will be seen in Chapter 3, the orbital control of the fixed mirror configuration is around  $10^{-4} \text{ N}$  (see Section 3.6), while for the adaptive mirror case is less than  $10^{-5} \text{ N}$  (see Section 3.7) which could easily be provided with high  $I_{sp}$  FEEP engine ( $I_{sp} = 10000 \text{ s}$ ) with a negligible mass consumption compared to the transfer.

If a laser system is used instead of the direct imaging, the spacecraft is more complex and requires more elements. Four representative configurations were used:

1. Primary adaptive solar collector, solar arrays to convert the solar energy into electric power, semiconductor laser as beaming system, cooling system for solar arrays and laser (Table 8).
2. Primary parabolic (or spherical) solar collector, solar arrays to convert the solar energy into electric power, semiconductor laser as beaming system, cooling system for solar arrays and laser (Table 9).
3. Large solar arrays (standard technology) to convert the solar energy into electric power, semiconductor laser as beaming system, cooling system for solar arrays and laser (Table 10).
4. Large solar arrays (advanced technology) to convert the solar energy into electric power, semiconductor laser as beaming system, cooling system for solar arrays and laser (Table 11).

The mass of the bus and of the primary mirror are based on the previous estimation for the direct imaging system. The laser mass accounts for the mass of the semiconductor and the cavity but no optics. To compensate, a margin of 50% was added to account for the mass of casing and optical elements. The mass of the cooling system, which is generally the most massive part is computed separately.

The mass of the solar arrays in the case of the configurations with a solar collector is for a standard solar array with high efficiency, a rigid structural support and no concentrator.

The cooling system is a critical component for the laser option. If large solar arrays are used with no solar collector, the cooling system needs only to refrigerate the laser, not the solar panels. If the solar collector solution is used, the cooling process has two stages: refrigeration of the solar array, and refrigeration of the laser. The assumption here is that the laser can operate between  $0^{\circ}\text{C}$  and  $40^{\circ}\text{C}$  while the solar array cannot operate above  $100^{\circ}\text{C}$ . As the efficiency of a laser can go up to 75%, the majority of the power will need to be dissipated during the first stage since the efficiencies of solar arrays are at or below 40%.

For the mass budgets, a reference case was considered consisting of a solar collector (or equivalent large solar array) with a surface area of  $314\text{ m}^2$ , collecting a total of 429.5 kW of power at 1 AU. If the solar arrays are operating at 40% efficiency, the cooling system will have to dissipate 257.7 kW at the first stage.

The radiator is located on the shadow of the primary mirror for all cases. However, in the case of the adaptive mirror the laser has to be placed between the primary mirror and the asteroid. Therefore, the heat has to be transported from the laser/solar panel to the radiator. In order to maintain the temperature of the solar array below  $100^{\circ}\text{C}$ , the radiator has to have a total irradiating area of about  $300\text{ m}^2$  therefore comparable with the surface area of the solar collector. Note that the dissipated power is irradiated in every direction randomly and therefore does not provide an additional thrust. For any future studies, this assumption would have to be verified once a structural configuration for the radiators is defined.

To transport the heat, a dual-phase system was used, with ammonia as working fluid. A pumping system is placed in the shadow, with a mass of 3 kg per pump and a total of 10 pumps (based on the transport rate of standard pumping systems). The distance of the solar array from the surface of the primary mirror is assumed to be 2 times the aperture diameter; the diameter of the mirror is equal to 20 m, with a separation distance of 40 m. A mass density of  $0.3\text{ kg/m}^3$  was used for the pipes, and  $3\text{ g/m}^3$  for the ammonia. The system is assumed to transport 200 L of ammonia per hour, corresponding to an 8 m/s flow speed in the pipes with a Reynolds number  $Re = 150000$  and a pressure loss in the pipes of 16 bar. The radiator mass is based on advanced technology for all the configurations [Arslanturk, 2006].

In Table 9, the laser and the solar array are both in the shadow cone of the primary mirror, resulting in a simplified system with no pumps nor pipes, as there is no need to transport the heat (compared to the first case with an adaptive mirror, shown in Table 8). A secondary reflective mirror is placed such that it reflects the concentrated light through small hole in the centre of the primary mirror, through to the back of the primary where the laser and arrays are housed. The solar array and the laser are directly connected to the radiator(s). For a reflectivity of the secondary mirror of 99%, an additional radiator would be needed, attached to the secondary mirror with a total area of  $7\text{ m}^2$  (assuming an absorptivity of 0.2). The total mass of the spacecraft is lower than in the first case, along with a reduction in the overall complexity of the cooling system.

Tables 10 and 11 show the cases where no solar collector is used; the cooling system and the laser are placed in the shadow cone of the solar array. The mass of the solar arrays are taken from Carpenter and Lyons (2002) for both the standard and for the advanced technology levels. The standard technology system with large flexible solar arrays is expected to be heavier for two reasons: the overall power system, including power distribution and cabling, is larger and solar arrays need stretched lenses to increase their efficiency. The advanced system in Table 11 would be lighter and closer in mass to the system in Table 8.

The calculations performed here did not aim at an optimisation of the performances. For example, the mass of propellant required for the transfer, estimated as 40% of the dry mass, could be largely reduced. Another possibility to reduce the mass of the spacecraft is to use frequency selective mirrors. A substantial part of the mass of the spacecraft is due to the cooling system of the solar panel, which can range between 15% to 27% of the dry mass of the spacecraft for a 5 m and 10 m diameter mirror, respectively. One idea is to let the mirror absorb the part of the spectrum that the solar cells are not using.

Table 8: Adaptive primary mirror plus laser.

Component	Specific mass	Mass (kg)	Margin (%)	Subtotal (kg)	Accumulative total (kg)
Primary mirror	0.1 kg/m <sup>2</sup>	32.52	25	40.65	40.65
Laser	0.005 kg/W	601.24	50	901.86	942.51
Solar arrays	1 kg/m <sup>2</sup>	3.14	15	3.611	946.12
Cables	20% $m_{elec}$	189.22	0	189.22	1135.35
Radiator (solar array)	1.4 kg/m <sup>2</sup>	420	20	504	1639.35
Radiator (laser)	1.4 kg/m <sup>2</sup>	112	20	134.40	177.75
Pipes	0.3 kg/m	12	20	14.4	1788.15
Pumps	10×3 kg	30	20	36	1824.15
Bus	-	500	20	600	2424.15
Propellant	40% $m_{dry}$	969.66	0	969.66	3393.80
Tanks	10% $m_{fuel}$	96.97	0	96.97	<b>3490.77</b>

Table 9: Fixed primary mirror plus laser.

Component	Specific mass	Mass (kg)	Margin (%)	Subtotal (kg)	Accumulative total (kg)
Primary mirror	0.05 kg/m <sup>2</sup>	15.71	25	19.63	19.63
Directional mirror	0.1 kg/m <sup>2</sup>	0.650	25	0.813	20.45
Laser	0.005 W/m <sup>2</sup>	601.24	50	901.86	922.30
Solar arrays	1 kg/m <sup>2</sup>	3.14	15	3.611	925.92
Cables	20% $m_{elec}$	185.18	0	185.18	1111.10
Radiator (solar array)	1.4 kg/m <sup>2</sup>	420.0	20	504.0	1615.10
Radiator (laser)	1.4 kg/m <sup>2</sup>	112.0	20	134.4	1749.50
Radiator (reflective mirror)	1.4 kg/m <sup>2</sup>	9.79	20	11.76	1761.26
Bus	-	500	20	600	2361.26
Propellant	40% $m_{dry}$	944.50	0	944.50	3305.76
Tanks	10% $m_{fuel}$	94.45	0	94.45	<b>3400.21</b>

Table 10: Primary solar array plus laser, using standard solar array technology.

Component	Specific mass	Mass (kg)	Margin (%)	Subtotal (kg)	Accumulative total (kg)
Directional mirror	0.1 kg/m <sup>2</sup>	0.3251	25	0.406	0.406
Laser	0.005 kg/W	601.24	50	901.86	902.26
Solar arrays	150 kg/W	1145.22	15	1317.00	2219.26
Cables	20% $m_{elec}$	443.79	0.00	443.79	2663.11
Radiator (laser)	1.4 kg/m <sup>2</sup>	112.00	20	134.40	2797.51
Bus	-	500.00	20	600.00	3397.51
Propellant	40% $m_{dry}$	1359.01	0	1359.01	4756.52
Tanks	10% $m_{fuel}$	135.90	0	135.90	<b>4892.42</b>

Table 11: Primary solar array plus laser, using advanced solar array technology.

Component	Specific mass	Mass (kg)	Margin (%)	Subtotal (kg)	Accumulative total (kg)
Directional mirror	0.1 kg/m <sup>2</sup>	0.3251	25	0.406	0.406
Laser	0.005 kg/W	601.24	50	901.86	902.26
Solar arrays	350 kg/W	490.81	15	564.43	1466.69
Cables	20% $m_{elec}$	293.28	0	293.28	1760.03
Radiator (laser)	1.4 kg/m <sup>2</sup>	112.00	20	134.40	1894.43
Bus	-	500.00	20	600.00	2494.43
Propellant	40% $m_{dry}$	997.77	0	997.77	3492.20
Tanks	10% $m_{fuel}$	99.78	0	99.78	<b>3591.98</b>

### Discussion

As an example, based on the mass budget for the direct imaging system, a formation of 26 spacecraft with the mirror technology rated at TRL 4 would require an 80 m diameter mirror, with a mass of between 3.5 and 4.5 metric tons per spacecraft at launch. For a more reasonable formation configuration, one would need a lighter adaptive mirror, which is presently at TRL 2.

A system based on a solar pumped laser with a primary mirror of smaller size (e.g., 20 m diameter) would have a comparable mass per spacecraft for the same number of spacecraft.

It should be noted that for both the direct imaging system and for the laser system the mass is directly proportional to the surface area and therefore it is proportional to the square of the aperture of the collector. This would suggest in both cases, to opt for many smaller spacecraft rather than a single larger one. On the other hand, a small reflector in the case of a direct imaging system would also be only able to provide a low concentration factor. A complete trade off of the number of spacecrafts against the mass and size is left for future work in this area.

The TRL of the laser solution strongly depends on the TRL of the solar arrays and the laser itself. Most of the assumptions are based on current laboratory tests

in both areas (corresponding to a TRL of 4 or higher) but the overall system for space applications has still to be developed (TRL 2 – 4). The investment in the development of highly efficient lasers and solar arrays is independent of the study of asteroid deflection, and is progressing very fast due to the thousands of commercial applications.

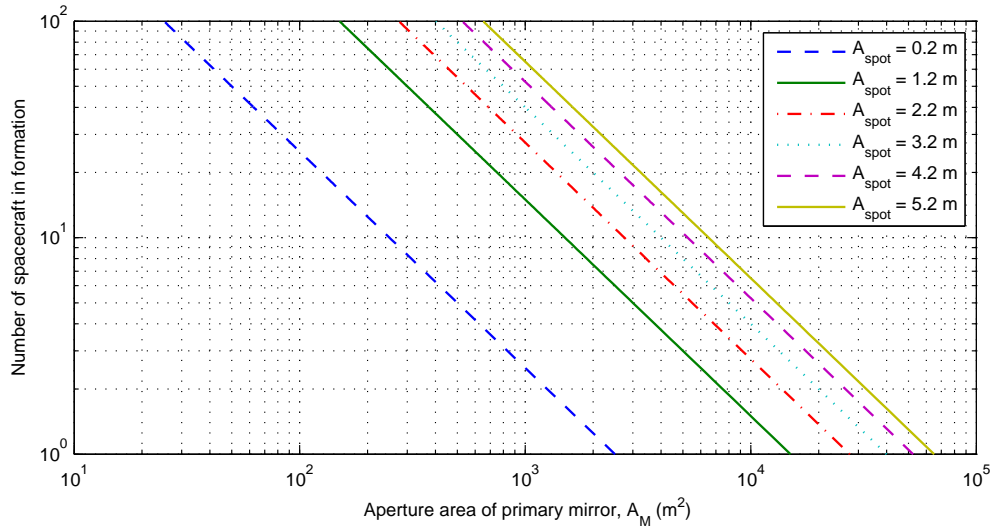
It is important to note that the mass budgets are based on systems with a total system concentration factor of 2500, to be comparable with the system analysed in the paper by Sanchez Cuartielles et al. (2009). This assumption corresponds, in the paper of Sanchez, to a deflection of over 20000 km with a single 60 m diameter mirror for 2 years operation time prior to the expected impact. If the warning time is extended from 2 to 5 years, the required concentration ratio can be reduced for the same deflection distance.

Figure 20 shows the effect of different efficiencies of the laser system (or laser plus solar arrays in the case of the indirect pumping), with the number of spacecraft as a function of the aperture area on the collector for each spacecraft. As explained previously, the concentration ratio is only a factor of the mirror surface area that is perpendicular to the incoming solar rays, not the total surface area of the reflector. Therefore, the deeper the parabola, or more tilted the mirror is with respect to the Sun, the less power the mirror will collect. Both plots in Fig. 20 assume a constant system concentration ratio of 2500, meaning each individual spacecraft has its own concentration ratio equal to the system concentration ratio, divided by the number of spacecraft. For a given illuminated area on the asteroid,  $A_{spot}$ , it is straightforward to calculate the required surface area of the mirror aperture, with a given efficiency  $\eta_{sys}$  of the ‘beaming and focusing’ system as a whole.

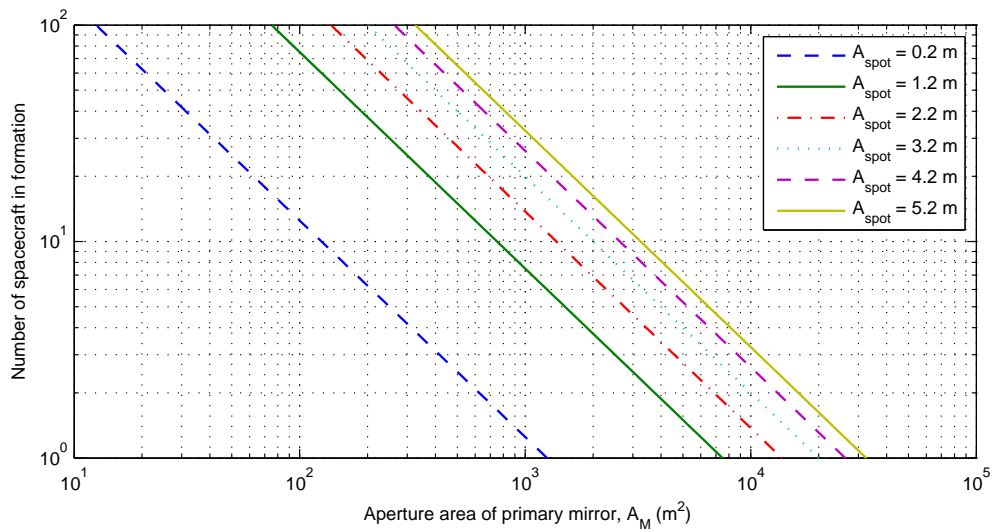
Continuing with the example above, for an equivalent total aperture area of  $\pi(60/2)^2$  (i.e., the single 60 m diameter mirror) and a system concentration ratio of 2500, and for the same spot areas in Fig. 20, the required number of spacecraft are given in Table 12.

Table 12: Required number of spacecraft for a primary aperture area of 2827 m<sup>2</sup> and a concentration ratio of 2500.

Spot area, $A_{spot}$	Number of spacecraft	
	$\eta_{sys} = 0.2$	$\eta_{sys} = 0.4$
0.2 m <sup>2</sup>	0.8841 ~ 1	0.4421 ~ 1
1.2 m <sup>2</sup>	5.3051 ~ 6	2.6526 ~ 3
2.2 m <sup>2</sup>	9.7261 ~ 10	4.8631 ~ 5
3.2 m <sup>2</sup>	14.1471 ~ 15	7.0736 ~ 8
4.2 m <sup>2</sup>	18.5680 ~ 19	9.284 ~ 10
5.2 m <sup>2</sup>	22.9890 ~ 23	11.495 ~ 12



(a) System efficiency  $\eta_{sys}$  of 20%.



(b) System efficiency  $\eta_{sys}$  of 40%.

Figure 20: Surface area of reflector versus number of spacecraft, for various concentration ratios.

Solving an optimal control problem is not easy. Pieces of the puzzle are found scattered throughout many different disciplines.

*John T. Betts (2000)*

This chapter will analyse the dynamics and control of the spacecraft in the proximity of an asteroid. The aim is to identify possible orbital solutions to place the spacecraft close enough to the asteroid to guarantee the required power density yet far enough from the debris plume, while avoiding any eclipse or occultation that may impinge on a clear line of sight between the spacecraft and the Sun.

The analysis of the spacecraft dynamics and control is one of the key points in determining the feasibility of the multi-mirror approach with solar sublimation. One of the main issues related to the use of this deflection strategy is the contamination of the mirror system due to the debris coming from the asteroid. The relative motion of the spacecraft with respect to the asteroid also imposes some severe constraints on the control of the projected beam.

Two different ways of positioning and controlling the spacecraft in the proximity of the asteroid are presented: closed formation and artificial equilibrium points.

### 3.1 BACKGROUND

The following section presents some necessary background on the various concepts, definitions and theorems used in the analysis of the dynamics and control. An introduction to spacecraft formation flying is given, along with a more mathematical description of the general equations governing formation dynamics.

#### 3.1.1 *Introduction to formation flying*

The exact definition of spacecraft formation flying is subjective. Mauro (2005) in his PhD dissertation, for example, defined it as:

A group of spacecraft which orbit maintaining a certain configuration which is characterized by small relative distances with respect to the orbit radius.

while Adams et al. (1996) out of Stanford University, gave a more general definition:

The coordinated motion control of a group of vehicles where the vehicle positions relative to each other are important. These vehicles may be groups of trucks, aircraft, spacecraft, or mobile robots.

It is this small relative distance between spacecraft that is often used to distinguish spacecraft formation flying from spacecraft constellation design – such as the Walker

delta constellation [Walker, 1984] used by the US global positioning system (GPS), see Fig. 21a. This is not always true however, as many ‘formation flying’ missions today are designed with spacecraft separated by hundreds or even millions of kilometres from each other. The distinction aside, a spacecraft formation can often be thought of as the equivalent of one, large virtual spacecraft with one overall mission.

The benefits of a formation of spacecraft versus a single large spacecraft are, for the most part, common sense. In the environment of space, where no maintenance, refuelling or upgrading are possible, the spacecraft simply must work. Redundancy is paramount. With formations, the risk of a malfunction or failure is decreased by dividing the work among several spacecraft – this increases redundancy, and decreases the complexity (and generally mass) of each individual spacecraft. There is also a potential savings in cost as well, as the production of many smaller, identical spacecraft drives down the manufacturing cost versus the production of one large, specialised spacecraft.

The disadvantage of a formation however, is a drastic increase in the complexity of the design. With so many spacecraft in close proximity, very accurate control of the absolute and relative position of each spacecraft is required. From an user point of view, the formation should act as the equivalent of a single spacecraft. Where a single spacecraft will follow only one orbit, in a formation each individual spacecraft must be able to track its own course as well as the formation as a whole. Moreover, in cases with small relative separation distances, issues like collision avoidance and thruster plume avoidance must be accounted for in the mission design.

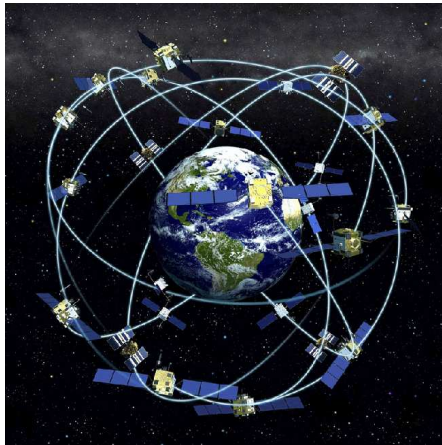
With all this complexity however, the concept of a formation, versus a single spacecraft, opens up a wealth of new applications. Virtual or sparse antennas with diameters up to 10 km are now possible [Bekey, 2002]. For fields such as interferometry or Earth observation, a large antenna means higher gain and smaller beamwidth, ergo the ability to see farther and in more detail. A formation also allows the measurement of gravitational and/or magnetic fields by tracking the relative drift of each spacecraft in the formation. The joint ESA-NASA mission LISA\* (Laser Interferometer Space Antenna) is an example of this technology, with the mission objective to measure low frequency gravitational waves by precisely monitoring the relative movement between three spacecraft placed 5 million miles apart.

Other proposed missions using formation flying are NASA’s Terrestrial Planet Finder (TPF) project [Beichman et al., 1999; Lawson, 2001], with a proposed infrared interferometer based on a fixed formation of small telescopes (Fig. 21e). ESA has a similar mission planned, under their Cosmic Vision programme [Fridlund, 2004]: “Darwin is a flotilla of four or five spacecraft that will search for Earth-like planets and analyse their atmospheres for the chemical signature of life. One spacecraft will be a central communications hub. The other three will function as light collectors, redirecting light beams to the hub spacecraft<sup>†</sup>” (Fig. 21b). PROBA-3 (PROject for OnBoard Autonomy) is another planned ESA technology demonstrator for various guidance, navigation and control (GNC) algorithms developed for formation flying. Already in operation (2000–2009), although not without many problems along the way, is the Cluster mission (Fig. 21c). “Cluster is constituted of four identical spacecraft that fly in a tetrahedral configuration. The separation distances between the spacecraft will be varied between 600 km and 20 000 km, according to the key scientific regions<sup>‡</sup>.” Other NASA missions include DART (Demonstration of Autonomous Rendezvous

\*<http://lisa.nasa.gov/>, link valid as of February 23, 2010.

<sup>†</sup><http://www.esa.int/science/darwin>, link valid as of February 23, 2010.

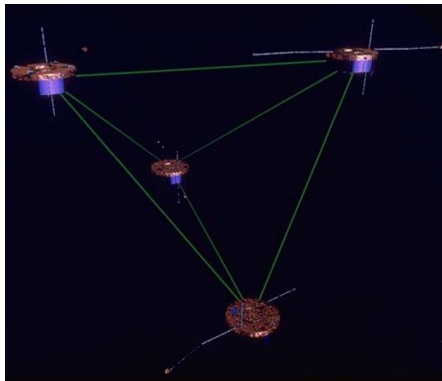
<sup>‡</sup><http://sci.esa.int/cluster>, link valid as of February 23, 2010.



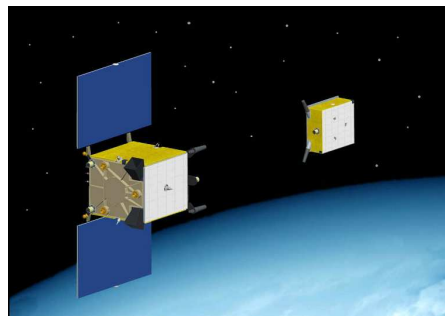
(a) GPS Walker configuration (image courtesy of NOAA).



(b) Darwin mission (image courtesy of ESA).



(c) Cluster mission (image courtesy of ESA).



(d) PRISMA technology demonstrator (image from DLR).



(e) NASA TPF interferometer (image courtesy of NASA).

Figure 21: Formation flying missions.

Technology) launched in 2005, which incidentally collided with the rendezvous spacecraft, MMS (Magnetosphere Multiscale Mission) a 4-spacecraft formation in a closely spaced tetrahedral configuration currently in the preliminary design stage, as well as conceptual designs like SIRA (Solar Imaging Radio Array) and MAXIM (Micro-Arcsecond X-ray Imaging Mission) which envisions a large interferometer to image a black hole, with up to 33 spacecraft flying in formation with a precision of 20 nanometres, plus a detector spacecraft 500 kilometres behind the mirrors. Other agencies also investigated formation flying, for example the now-defunct TechSat21 project developed by the US Air Force [Das and Cobb, 1998; Burns et al., 2000], plus numerous smaller technology demonstrators such as the Swedish PRISMA mission (Fig. 21d), which should be launched in 2010 to test GNC algorithms [Persson et al., 2005; Gill et al., 2007].

Over the past decade, many authors and scholars have compiled reviews on the subject. Scharf and his team at JPL/CalTech presented a comprehensive survey of spacecraft formation flying guidance [Scharf et al., 2003] and control [Scharf et al., 2004] methods. Alfriend and Yan (2005) published a paper on the evaluation and comparison of basic relative motion theories, including the effect of modelling errors. In addition, there are PhD and Masters' dissertations which present more detailed background and comparisons of the various techniques for planet orbiting formation designs [Sai Vaddi, 2003; Roberts, 2005; Mauro, 2005; Sengupta, 2006]. In this study, only those related to deep space formations are studied, and therefore do not include any of the gravitational  $J_2$  terms, gravity gradient, atmospheric drag and other orbital perturbations related to orbits in or near the atmospheres of planets.

There are three typical configurations used in spacecraft formation flying: leader-follower, virtual structure and behavioural. These configurations encompass both the dynamics and control of the formation, as one directly affects the requirements of the other. Along with recent applications to space-specific research, many of the papers and work done originated within the field of robotics, and to a lesser degree the control of multiple aircraft and unmanned aerial vehicles (UAV) [Schultz and Parker, 2002].

**LEADER-FOLLOWER** Leader-follower is very much like it sounds. One spacecraft is designated as the leader, with the remaining spacecraft trailing behind, offset typically by a time interval. Several of the leader-follower tracking techniques studied include: leader tracking, nearest neighbour tracking and barycentre tracking [Wang and Hadaegh, 1996]. Adaptive control laws have also been developed to account for such problems as mechanical limitations of devices in space, and common space disturbances. A good description of a leader-follower design for a Earth-orbiting formation is given in [Kapila et al., 1999]; Kristiansen and Nicklasson (2009) also published a review on feedback control methods for leader-follower configurations. This type of formation flying is also known as 'chief-deputy', or occasionally as 'master-slave'.

**VIRTUAL STRUCTURE** Virtual structures are defined as "a collection of elements [...] which maintain a (semi) rigid geometric relationship to each other and to a frame of reference" [Tan and Lewis, 1997]. These elements are typically robots, or in this case, individual spacecraft in a formation. Beard et al. (2001), who has written a number of papers on formation and robotic control, sums up the approach nicely:

In the virtual structure approach, there are three main steps: first, the desired dynamics of the virtual structure are defined, second, the motion of the virtual structure is translated into the desired motion for each agent, and finally, tracking controls for each spacecraft are derived.

The virtual structure approach has been used, for example, in study of tethered spacecraft formations [Blake and Misra, 2008; Pizarro-Chong and Misra, 2008].

**BEHAVIOURAL** Last, but not least, is behavioural control. The basic idea is that various desired behaviours are associated to a spacecraft, for example collision/plume avoidance or formation keeping, with a certain priority, or weight, attached to each. The resultant placement and control for the spacecraft are a combination of these specific behavioural algorithms [Scharf et al., 2004]. Behavioural control is a reactive type of control, acting as a middle layer between the high level mission objectives and goals, and the bottom physical layer controlling the thrusters and hardware.

This is a relatively nascent field, with the majority of the work within the scope of spacecraft formation flying done in the past decade. Arkin [Arkin, 1998; Balch and Arkin, 1998] is a benchmark reference for behavioural control for ground-based robotics. Applying to this formations, Lawton (2000) for example, a protegee under Beard, wrote his doctorate thesis focusing on the development of a behaviour based control strategy based on "the coupled dynamics approach to formation flying", including feedback within the control laws. McInnes et al. [McInnes, 1995; McQuade et al., 2002; Badawy and McInnes, 2009] has published numerous papers on behaviour control using a potential field method.

### 3.1.2 Proximal motion

In a Keplerian two-body dynamical system, the motion of an orbit can be described by the equation,

$$\ddot{\mathbf{r}} = -\frac{\mu}{r^3}\mathbf{r} \quad (3.1)$$

This can be extended to the case of the proximal motion of body  $D$  relative to body  $C$  in inertial space (nominally corresponding to the standard nomenclature of chief  $C$  and deputy  $D$  formations),

$$\ddot{\mathbf{r}}_C = -\frac{\mu}{r_C^3}\mathbf{r}_C \quad (3.2)$$

$$\ddot{\mathbf{r}}_D = -\frac{\mu}{r_D^3}\mathbf{r}_D = -\frac{\mu}{r_D^3} \begin{bmatrix} r_C + x \\ y \\ z \end{bmatrix} \quad (3.3)$$

Proximal motion, in this context, is generally described in the Hill frame – a local, rotating reference frame measured in the radial  $\hat{\mathbf{x}}$ , transverse  $\hat{\mathbf{y}}$  and normal  $\hat{\mathbf{z}}$  directions defined in (3.4). The normal is defined as parallel to the angular momentum vector  $\mathbf{h}$  of the spacecraft.

$$\hat{\mathbf{x}} = \hat{\mathbf{r}} = \frac{\mathbf{r}}{r} \quad (3.4a)$$

$$\hat{\mathbf{y}} = \hat{\mathbf{h}} \wedge \hat{\mathbf{r}} \quad (3.4b)$$

$$\hat{\mathbf{z}} = \frac{\mathbf{h}}{h} \quad (3.4c)$$

Figure 22 gives a visual representation of this reference coordinate system. Typically the Hill frame is centred on the chief spacecraft, with the motion of the deputy spacecraft described relative to the chief, however the Hill frame is valid for any object, virtual or not.

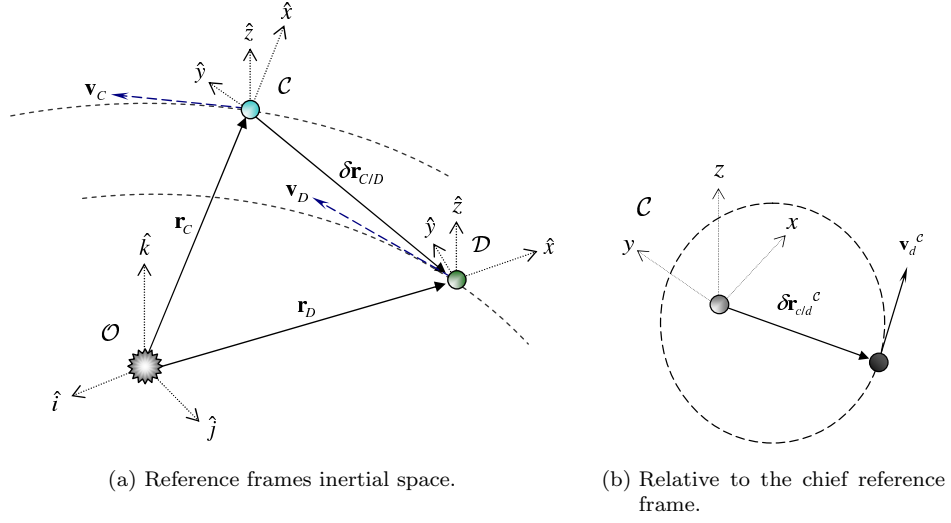


Figure 22: Hill reference frames for a chief-deputy spacecraft formation.

Integrating (3.2) and (3.4), the exact nonlinear relative equations of motion are,

$$\ddot{x} = 2\dot{\nu} \left( \dot{y} - y \frac{\dot{r}_c}{r_c} \right) + x\dot{\nu}^2 + \frac{\mu}{r_c^2} - \frac{\mu}{r_D^3} (r_c + x) \quad (3.5a)$$

$$\ddot{y} = -2\dot{\nu} \left( \dot{x} - x \frac{\dot{r}_c}{r_c} \right) + y\dot{\nu}^2 - \frac{\mu}{r_D^3} y \quad (3.5b)$$

$$\ddot{z} = -\frac{\mu}{r_D^3} z \quad (3.5c)$$

where  $\nu$  is the true anomaly. The relative motion between two spacecraft, both in closed orbits (i.e. circular or elliptical), can be solved either by numerically integrating (3.5) or by analytical means.

One set of analytical equations [Vadali et al., 2002; Sai Vaddi, 2003] is based on the general coordinate frame identities in (3.4),

$$x = \frac{\delta \mathbf{r}^T \cdot \mathbf{r}}{r} \quad (3.6a)$$

$$y = \frac{\delta \mathbf{r}^T \cdot (\mathbf{h} \wedge \mathbf{r})}{\|\mathbf{h} \wedge \mathbf{r}\|} \quad (3.6b)$$

$$z = \frac{\delta \mathbf{r}^T \cdot \mathbf{h}}{h} \quad (3.6c)$$

$$\dot{x} = \frac{\delta \dot{\mathbf{r}}^T \cdot \mathbf{r} + \delta \mathbf{r}^T \cdot \dot{\mathbf{r}}}{r} - \frac{(\delta \mathbf{r}^T \cdot \mathbf{r})(\mathbf{r}^T \cdot \dot{\mathbf{r}})}{r^3} \quad (3.6d)$$

$$\dot{y} = \frac{\delta \dot{\mathbf{r}}^T (\mathbf{h} \wedge \mathbf{r}) + \delta \mathbf{r}^T (\dot{\mathbf{h}} \wedge \mathbf{r} + \mathbf{h} \wedge \dot{\mathbf{r}})}{\|\mathbf{h} \wedge \mathbf{r}\|} - \frac{\delta \mathbf{r}^T (\mathbf{h} \wedge \mathbf{r})(\mathbf{h} \wedge \mathbf{r})^T (\dot{\mathbf{h}} \wedge \mathbf{r} + \mathbf{h} \wedge \dot{\mathbf{r}})}{\|\mathbf{h} \wedge \mathbf{r}\|^3} \quad (3.6e)$$

$$\dot{z} = \frac{\delta \dot{\mathbf{r}}^T \cdot \mathbf{h} + \delta \mathbf{r}^T \cdot \dot{\mathbf{h}}}{h} - \frac{(\delta \mathbf{r}^T \cdot \mathbf{h})(\mathbf{h}^T \cdot \dot{\mathbf{h}})}{h^3} \quad (3.6f)$$

where the relative position vector from the chief to the deputy is given by,

$$\delta\mathbf{r} = \mathbf{r}_D^C - \mathbf{r}_C^C = x\hat{\mathbf{x}} + y\hat{\mathbf{y}} + z\hat{\mathbf{z}} \quad (3.7a)$$

$$\|\delta\mathbf{r}^C\| = \delta r = \sqrt{x^2 + y^2 + z^2} \quad (3.7b)$$

Note that  $\mathbf{r} = \mathbf{r}_C$  and  $\mathbf{r}_D$  are the vectors from the central body (e.g., the Sun) to the chief or deputy spacecraft, measured in the Hill reference frame of the chief  $\mathcal{C}$  (not the inertial reference frame).

A number of simplified linearised equations exist as well. The most widely-used are the Clohessy-Wiltshire (HCW) equations developed in 1960 [Clohessy and Wiltshire, 1960], based in part on work done by Hill in 1878.

$$\ddot{x} = 2n\dot{y} + 3n^2x \quad (3.8a)$$

$$\ddot{y} = -2n\dot{x} \quad (3.8b)$$

$$\ddot{z} = -n^2z \quad (3.8c)$$

Negating the secular terms by setting  $y_0 \Rightarrow -2x_0n$  and solving analytically, the equations become,

$$x(t) = \frac{\dot{x}_0}{n} \sin nt + x_0 \cos nt \quad (3.9a)$$

$$y(t) = \frac{2\dot{x}_0}{n} \cos nt - 2x_0 \sin nt - \frac{2\dot{x}_0}{n} + y_0 \quad (3.9b)$$

$$z(t) = \frac{\dot{z}_0}{n} \sin nt + z_0 \cos nt \quad (3.9c)$$

where  $n$  is the mean motion, equal here to the rotational velocity since the orbit is circular. These equations form the basis for formation flying design, however are only valid for orbits that are perfectly circular ( $e = 0$ ) and where, in the inertial frame, the relative distance between the two spacecraft is orders of magnitude less compared to the orbital radius from the central body ( $\delta r \ll r$ ). As can be seen from (3.8), they account for gravitational, Coriolis and centripetal accelerations. For more information, many text books such as Vallado (2004) for example, give more detailed deviations of these equations. The other drawback of the HCW equations is that they were originally derived for short-term spacecraft rendezvous, not long term orbital propagation.

Since the paper of Clohessy and Wiltshire, several authors have extended their work to: elliptical orbits [Carter and Humi, 1987; Inalhan et al., 2002; Wang and Yang, 2003], additional perturbations such as the  $J_2$  effect for Earth-centric orbits [Schweighart and Sedwick, 2002; Sengupta, 2006] or Halo orbits [Scheeres et al., 2003], and higher-order terms [Karlgaard and Lutze, 2003; Mitchell and Richardson, 2003; Kassin et al., 2005] just to name a few. Notwithstanding the well-known equations of Lawden (1963) and Tschauner and Hempel (1965) who were the first to independently extend the HCW equations to the elliptical orbit reference case.

An alternate form of representing orbital motion are Keplerian elements,

$$\mathbf{k} = [a, e, i, \Omega, \omega, \nu] \quad (3.10)$$

where  $a$  is the semi-major axis, or a maximum distance from the geometric centre of the orbit to a point along the orbital path,  $e$  is the eccentricity which is a measure of the circularity of the orbit ( $e = 0$  being a perfect circle and  $e > 1$  being a hyperbola),  $i$  is the inclination of the orbital plane,  $\Omega$  and  $\omega$  are angles determining the location of

the line of intersection between the orbital plane and the reference plane, and orbital plane and periapsis respectively, and lastly  $\nu$  is the true anomaly. The latter term is the only time-varying parameter, and represents the angle between the periapsis of the orbit (the location of the minimum distance from the focal point to the orbit path) and the actual location of the spacecraft at that point in time relative to the focal point of the orbit.

The general equations of motion given in (3.5) can be linearly mapped from Cartesian Hill coordinates to a set of orbital elements by means of a transformation matrix  $\mathbf{F}$  [Schaub and Junkins, 2003].

$$\mathbf{X} = [\mathbf{F}(\mathbf{k})] \cdot \delta\mathbf{k} \quad \Leftrightarrow \quad \delta\mathbf{k} = [\mathbf{F}^{-1}(\mathbf{k})] \cdot \mathbf{X} \quad (3.11)$$

where  $\mathbf{X}(t) = [x, y, z, \dot{x}, \dot{y}, \dot{z}]$  is the state vector containing the position and velocity components of the spacecraft in the Hill reference frame at a given time, and  $\delta\mathbf{k}(t) = \mathbf{k}_D - \mathbf{k}_C = [\delta a, \delta e, \delta i, \delta\Omega, \delta\omega, \delta\nu]$  is the set of orbital element differences between the chief orbital element set  $\mathbf{k}_C$  and the deputy  $\mathbf{k}_D$ . Appendix A lists the full set of equations for the two matrices  $\mathbf{F}$  and  $\mathbf{F}^{-1}$ . This research follows the research done by Schaub (2004), Alfriend and Junkins et al. on orbital element differences, however other researchers also developed similar methods in parallel, for example Wei (2002).

Using the equations (3.11) above, a set of linearised equations for the relative orbital motion can be developed in order to propagate the state vector of the spacecraft forward in time. The equations of motion can be rearranged to use the true anomaly as the variable parameter instead of time. Indeed, using the rate of change of a central angle is preferable when working with periodic orbits, rather than simply propagating forward for a set amount of time (typically equal to the period of the orbit).

A set of equations for the linearised relative motion, represented by matrix  $\mathbf{F}$  in (3.11), have been developed based on the true anomaly of the chief at time  $t$  [Schaub and Alfriend, 2002],

$$x(\nu) = \frac{r}{a}\delta a + ae\frac{\sin\nu}{\eta}\delta M - (a\cos\nu)\delta e \quad (3.12a)$$

$$y(\nu) = \frac{r}{\eta^3}(1 + e\cos\nu)^2\delta M + r\delta\omega + r\frac{\sin\nu}{\eta^2}(2 + e\cos\nu)\delta e + (r\cos i)\delta\Omega \quad (3.12b)$$

$$z(\nu) = r(\sin\theta\delta i - \cos\theta\sin i\delta\Omega) \quad (3.12c)$$

$$\dot{x}(\nu) = \frac{\dot{r}}{a}\delta a + \frac{ae\dot{\nu}\cos\nu}{\eta}\delta M + (a\dot{\nu}\sin\nu)\delta e \quad (3.12d)$$

$$\begin{aligned} \dot{y}(\nu) &= \frac{1}{\eta^3}(\dot{r}(1 + e\cos\nu)^2 - 2r\dot{\nu}e(1 + e\cos\nu)\sin\nu)\delta M + \dot{r}\delta\omega \\ &+ \frac{1}{\eta^2}(\dot{r}\sin\nu(2 + e\cos\nu) + r\dot{\nu}\cos\nu(2 + e\cos\nu) - r\dot{\nu}\sin^2\nu)\delta e + (\dot{r}\cos i)\delta\Omega \end{aligned} \quad (3.12e)$$

$$\dot{z}(\nu) = \dot{r}(\sin\theta\delta i - \cos\theta\sin i\delta\Omega) + r(\dot{\nu}\cos\theta\delta i + \dot{r}\sin\theta\sin i\delta\Omega) \quad (3.12f)$$

where  $\eta = \sqrt{1 - e^2}$  and  $\theta = \nu + \omega$  is the true latitude.

Kepler's second law states that for a closed orbit "a spacecraft will sweep out equal areas in equal time" [Vallado, 2004]. For an elliptical orbit, the true anomaly is not linearly varying with time as the velocity of the spacecraft is constantly changing depending on the position relative to the central body. Kepler's equation introduces

an alternate angular measurement of the position of the spacecraft, the mean anomaly  $M$ , based on the mean angular velocity,  $n$ .

$$M = \int_{t_0}^{t_i} n dt = \sqrt{\frac{\mu}{a^3}} (t_i - t_0) \quad (3.13)$$

The mean anomaly corresponds to a uniform angular motion on an equivalent circle of radius equal to the semi-major axis,  $a$ , of the elliptical orbit. The relationship between the true  $\nu$ , mean  $M$  and eccentric  $E$  anomaly is as follows,

$$\tan \frac{\nu}{2} = \sqrt{\frac{1+e}{1-e}} \tan \frac{E}{2} \quad (3.14)$$

$$M = E - e \sin E \quad (3.15)$$

Figure 23 shows the geometric relations. Note that  $M$  has no geometric representation, it is a mathematical construct only. By replacing the difference in true anomaly with the difference in mean anomaly,  $\delta M$ , the equations can be written in a form which is more convenient when looking for periodic solutions.

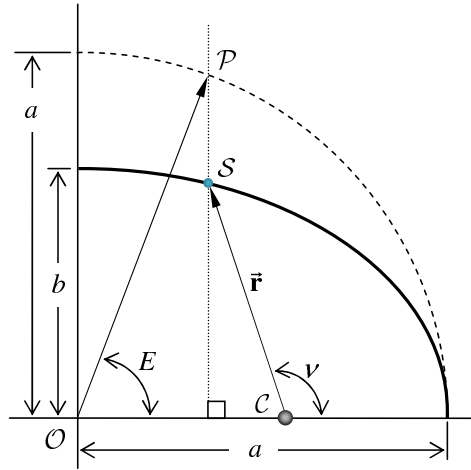


Figure 23: Geometric representation of the true  $\nu$  and eccentric  $E$  anomalies of an elliptical Keplerian orbit. Note that the mean anomaly  $M$  is a mathematical quantity only, not a physical one. The semi-major  $a$  and semi-minor  $b$  axes of the ellipse are shown along with the radius vector  $\mathbf{r}$  from the central body  $C$  to the spacecraft  $S$ . The point  $P$  is on a reference circle with radius  $a$  measured from the geometric centre of the ellipse  $O$ . The eccentricity of an ellipse is given by  $\sqrt{a^2 - b^2}/a$ .

In order to minimise the required station-keeping of the spacecraft, a bounded, or periodic, orbit is advantageous. The bounded orbit is essentially one that will return to the same position after a fixed period of time and thus, not need any external control to maintain the spacecraft in the orbit. The conditions of periodicity are such that the period of the formation orbit must be equal to the period of the NEO in order not to incur any drift. This is done by setting the difference in semi-major axes equal to zero since the equation for the period of an orbit is a function of only the semi-major axis and gravitational constant,  $\mu$ .

By setting  $\delta a = 0$ , the variation of the mean anomaly  $\delta M$  becomes constant with time. A periodic orbit can be found for almost any point in space surrounding the

chief orbit. However, as in the case of any space mission, there are several mission-specific requirements that restrict the choice of the operational orbit, such as being in close proximity to the surface.

$$\delta a = 0 = \begin{bmatrix} \frac{2a}{r} \left( 2 + \frac{3a}{r} e \cos \theta \cos(2\omega) \right) + \frac{2ea \tan \theta}{r \cos(2\omega)} \sin \theta \\ \frac{a \tan \theta}{r \cos(2\omega)} \left( 2 \left( 1 + \frac{2ae}{r} \cos \theta \cos(2\omega) \right) - e \sin \theta \right) \\ 0 \\ 2a^2 e \sin \theta \\ \frac{2ar}{h} \left( 1 + \frac{2a}{r} e \cos \theta \cos(2\omega) \right) + \frac{ae \tan \theta}{r \cos(2\omega)} \sin \theta \\ 0 \end{bmatrix} \begin{bmatrix} x \\ y \\ z \\ \dot{x} \\ \dot{y} \\ \dot{z} \end{bmatrix} \quad (3.16)$$

Equation (3.16) also demonstrates the difference in complexity, and the obvious benefit of switching from the Cartesian Hill frame to an orbital element set. Given initial conditions for the  $x$  and  $y$  positions, and the radial velocity  $\dot{x}$ , it is possible to rearrange (3.16) to find the required transversal, or along-track, velocity  $\dot{y}$  for a periodic orbit. As can be seen from the equation, the calculation is independent of the out-of-plane elements,  $z$  and  $\dot{z}$ .

Once the complete set of initial conditions are determined, the orbit can be propagated forward. As mentioned earlier, using the Cartesian Hill coordinates requires the integration of 6 time-varying parameters. By switching to an orbital element set, there is only one time-dependant parameter,  $\nu$ , that can be integrated over the angular range  $[0, 2\pi]$ .

A state-transition matrix,  $\Phi_{\mathbf{X}}$ , can also be used to determine the position of the formation spacecraft at any given point in time [Gim and Alfriend, 2003]. The matrix determines the sensitivity of the state vector  $\mathbf{X}$  at time  $t$  relative to the initial state vector at  $t_0$ .

$$\Phi_{\mathbf{X}}(t, t_0) = \left[ \frac{\partial \mathbf{X}(t)}{\partial \mathbf{X}(t_0)} \right] = \mathbf{F}(t) \left[ \frac{\partial \delta \mathbf{k}(t)}{\partial \delta \mathbf{k}(t_0)} \right] \mathbf{F}^{-1}(t_0) \quad (3.17)$$

The state vector of the spacecraft can then be determined by,

$$\mathbf{X}(t) \approx [\Phi_{\mathbf{X}}(t, t_0)] \mathbf{X}(t_0) \quad (3.18)$$

The implementation and full set of equations can be found in Appendix A.1.

### 3.2 ASTEROID DEFLECTION MODEL

The asteroid 99942 Apophis was chosen as a test case based on its popularity. Compared to other near Earth objects, Apophis has a relatively high probability of impacting the Earth in April 2036, although the actual cumulative impact probability is low, only  $2.2 \times 10^{-5}$  [NASA Near Earth Object program, 2009a]. Whether the asteroid will impact the Earth is contingent upon the asteroid's fly-by of Earth in 2029. During that event Apophis could pass through a gravitational keyhole, a precise region in space no more than about 400 m across, which would set up future resonant impacts starting on 13 April 2036.

As with nearly all NEOs, the orbital data for Apophis has been gained from Earth-based observations, which are limited based on the visibility of the asteroid from the astronomy station, availability of the station, etc. [Chesley, 2005]. As a result, the present knowledge of the orbit of Apophis is not good enough to provide an accurate

long term prediction of its evolution. This underlines the need for longer term measurements from a space-based platform [Schweickart, 2005]. Table 13 gives the orbital and physical data of the asteroid used in this study, and, if known, the estimated uncertainty [NASA Near Earth Object program, 2009a]. The physical dimensions are estimated using an ellipsoidal model for the asteroid, based on the observed magnitude of 19.7, where  $a_1 \leq b_1 \leq c_1$  are the three radii along the three orthogonal axes (see Fig. 24) [Delbò et al., 2007]. Figure 25 shows the orbit of Apophis relative to the nearby planets.

Table 13: Estimated and observed orbital and physical properties of Apophis 99942 [NASA Near Earth Object program, 2009a].

Element		Measured Value	Uncertainty, $1\sigma$
Semi-major axis	$a_A$	0.922438 AU	$2.3613 \times 10^{-8}$
Eccentricity	$e_A$	0.191204	$7.6074 \times 10^{-8}$
Inclination	$i_A$	3.331420 deg	$2.0238 \times 10^{-6}$
RAAN	$\Omega_A$	204.442505 deg	0.00010721
Argument of periapsis	$\omega_A$	126.404227 deg	0.00010632
Period	$T_A$	323.596917 d	$1.2426 \times 10^{-5}$
Mean motion	$n_A$	1.112495 deg/d	$4.2718 \times 10^{-8}$
Mass	$m_A$	$2.7 \times 10^{10}$ kg	
Gravitational constant	$\mu_A$	$1.801599 \times 10^{-9}$ km <sup>3</sup> /s <sup>2</sup>	
Physical dimensions	$a_1, b_1, c_1$	191 m, 135 m, 95 m	60
Rotational velocity	$w_A$	$5.8177 \times 10^{-5}$ rad/s	
Albedo	$\varsigma_A$	0.33	0.08

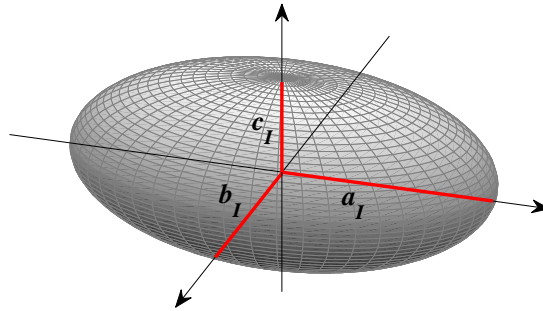
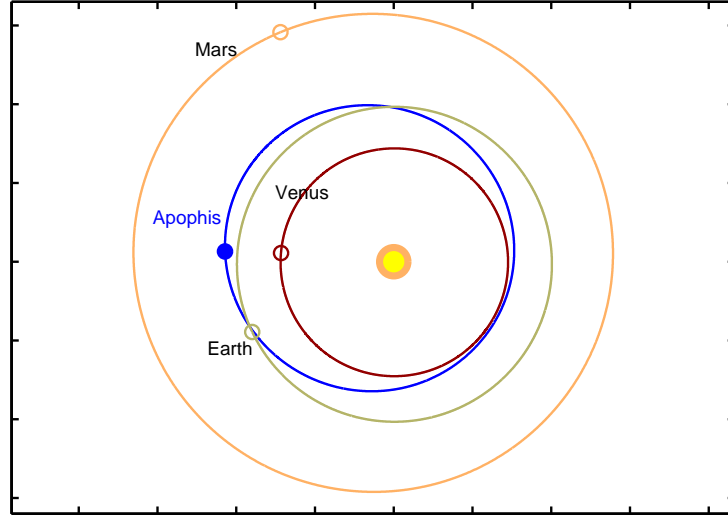
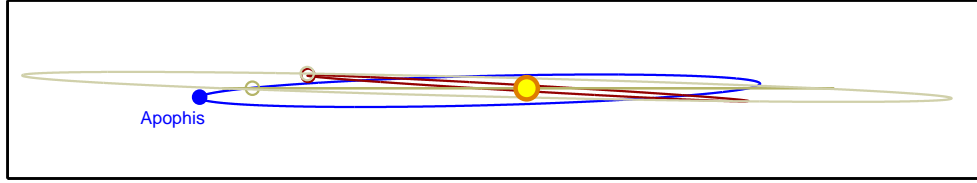


Figure 24: Ellipsoid model used for the asteroid, with  $a_1$ ,  $b_1$  and  $c_1$  giving the radial dimensions.

The minimum orbital intersection distance (MOID) is defined as the separation distance at the closest point between two orbits, e.g. Apophis and the Earth. The deviation distance is defined here as the difference in  $r_A$  between the original, un-deviated orbit and the deviated orbit at  $t_{\text{MOID}}$  [Colombo et al., 2009] (see Fig. 26). Non-linear equations were derived for determining the difference in  $r_A$  are expressed



(a) View of the ecliptic plane



(b) Inclination difference between the orbits

Figure 25: Orbit of the NEO Apophis, compared to the orbits of the Mars, Earth and Venus.

as a function of the ephemeris in the Hill reference frame  $\mathcal{A}$  (equal to chief reference frame  $\mathcal{C}$  in Fig. 22) centred on the asteroid, with  $\Delta\mathbf{k}$  giving the difference in Keplerian parameters between the undeviated and deviated orbit.

The deflection formulas used in the study by Colombo et al. (2009), also shown in (3.12), are based on proximal motion kinematics with a first order approximation contingent on  $\delta r \ll r_A$ . Since the distance  $\Delta r_{dev}$  between the undeviated ( $A_0$ ) and deviated ( $A_{dev}$ ) asteroid orbits can be of the order up to the Earth-Moon distance, the approximations start to lose accuracy at large distances. Moreover, the linearised proximal motion equations do not account for any out of plane motion, e.g. the inclination of the orbit.

Therefore, a general set of nonlinear equations was derived in terms of the orbital element differences (see Appendix A.1 for the full derivation) [Maddock and Vasile, 2008a].

$$\Delta\mathbf{r}_{dev} = r_{A_{dev}} \Psi - \begin{bmatrix} r_{A_0} \\ 0 \\ 0 \end{bmatrix} \quad (3.19)$$

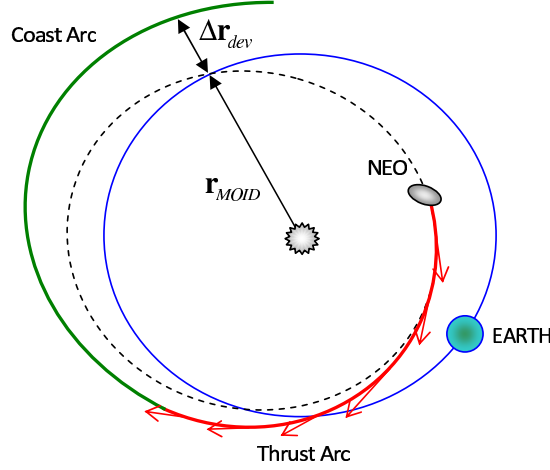


Figure 26: Definition of deviation distance at the MOID.

$$\Psi = \begin{bmatrix} \xi \cos(\theta_{A_0} + \Delta\theta) + \sin(\theta_{A_0} + \Delta\theta) (\varrho \sin \theta_{A_0} - \cos(i_{A_0} + \Delta i) \sin \Delta\Omega \cos \theta_{A_0}) \\ -\zeta \cos(\theta_{A_0} + \Delta\theta) + \sin(\theta_{A_0} + \Delta\theta) (\varrho \cos \theta_{A_0} + \cos(i_{A_0} + \Delta i) \sin \Delta\Omega \sin \theta_{A_0}) \\ -\cos(\theta_{A_0} + \Delta\theta) \sin \Delta\Omega \sin i_{A_0} + \varpi \sin(\theta_{A_0} + \Delta\theta) \end{bmatrix}$$

where

$$\varpi = \cos i_{A_0} \sin(i_{A_0} + \Delta i) - \cos \Delta\Omega \cos(i_{A_0} + \Delta i) \sin i_{A_0} \quad (3.20a)$$

$$\varrho = \sin i_{A_0} \sin(i_{A_0} + \Delta i) + \cos \Delta\Omega \cos(i_{A_0} + \Delta i) \cos i_{A_0} \quad (3.20b)$$

$$\xi = \cos \Delta\Omega \cos \theta_{A_0} + \cos i_{A_0} \sin \Delta\Omega \sin \theta_{A_0} \quad (3.20c)$$

$$\zeta = \cos \Delta\Omega \sin \theta_{A_0} - \cos i_{A_0} \sin \Delta\Omega \cos \theta_{A_0} \quad (3.20d)$$

The deviation vector  $\Delta \mathbf{r}_{dev} = \mathbf{r}_{A_{dev}} - \mathbf{r}_{A_0}$  is from the undeviated to the deviated orbit, in the relative  $\{r-t-h\}$  Hill frame of the undeviated orbit where  $\Psi$  is the coordinate system transformation matrix.

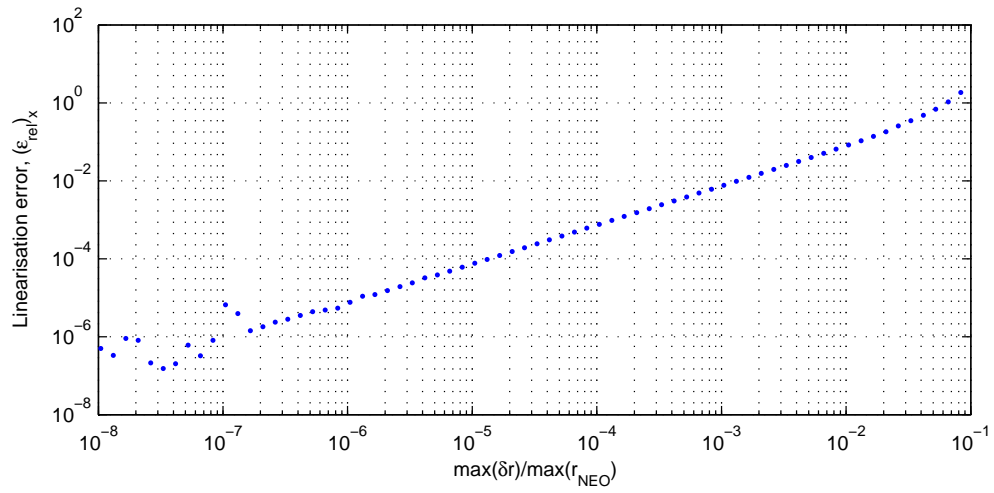
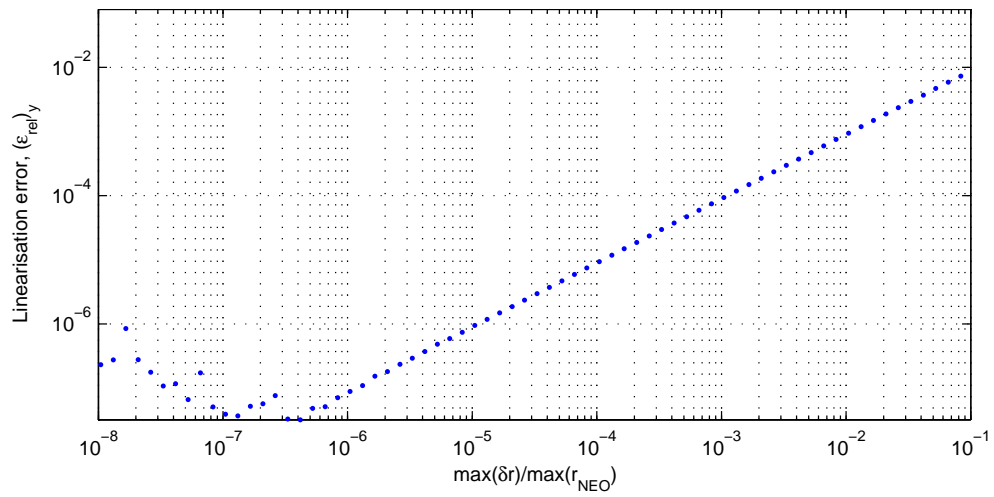
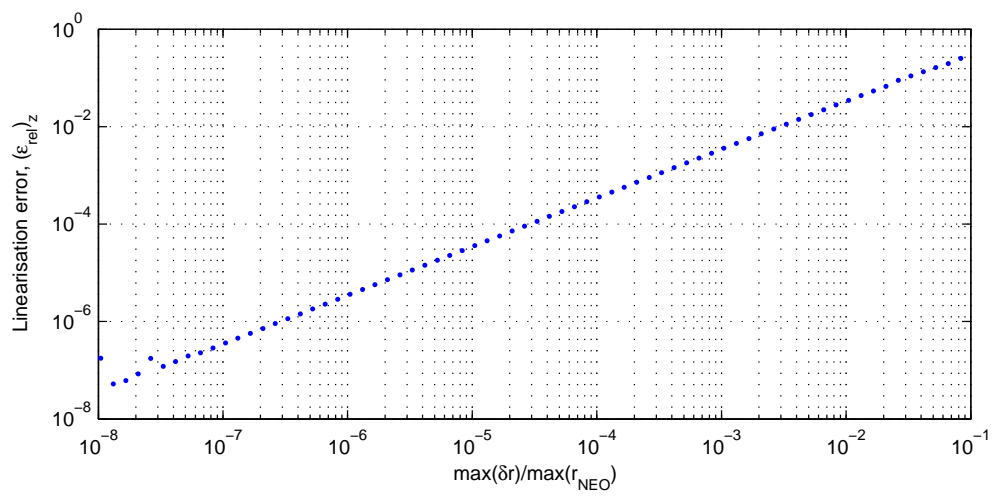
Figure 27 illustrates the error introduced by the linearisation of the equations in (3.12), compared with the nonlinear equations in (3.19). The error was calculated for each of the  $x$ ,  $y$  and  $z$  components, against the ratio of the relative distance, and the distance from the central body. The largest values for both  $\delta r$  and  $r$  over one full orbit were used for the comparison. The relative error was determined by,

$$\varepsilon_{rel} = \frac{\max |\delta r^N - \delta r^L|}{\delta r_{max\Delta}^N} \quad (3.21)$$

where  $\delta r^N$ ,  $\delta r^L$  are the relative distances calculated using the nonlinear and linear forms respectively, and  $\delta r_{max\Delta}^N$  is the value of  $\delta r^N$  when  $(\max |\delta r^N - \delta r^L|)$  is true.

Examining the figures, for a small ratio such as 1 km: 1 AU (or  $\delta r/r \approx 10^{-8}$ ), the error is negligible, around  $10^{-6}$  for all axes. However, at a  $\delta r$  around the Earth-Moon distance, i.e.  $\delta r/r \approx 10^{-3}$ , the errors start to impact the accuracy of the calculations, with the relative error in the  $x$  and  $z$  directions both around 0.01.

The change in the orbital parameters in (3.19) are calculated by numerically integrating the Gauss planetary equations in (3.23) [Battin, 1999] using an applied

(a) Relative error along the radial direction,  $x$ .(b) Relative error along the transverse direction,  $y$ .(c) Relative error along the normal/out-of-plane direction,  $z$ .Figure 27: Relative error between the linear and nonlinear forms of the proximal motion equations as a function of the ratio of the maximum  $\delta r/r$ .

thrust vector operating solely in the tangential direction  $\mathbf{u} = \mathbf{u}_{dev}$ , and induced by the sublimation method.

$$\Delta \mathbf{k} = \mathbf{k}_{A_{dev}} - \mathbf{k}_{A_0} = \int_{t_0}^{t_i} \frac{d\mathbf{k}(\mathbf{u}_{dev})}{dt} dt \quad (3.22)$$

where the rate of change of elements  $\dot{\mathbf{k}}$  are given by,

$$\frac{da}{dt} = \frac{2a^2 v}{\mu} u_v \quad (3.23a)$$

$$\frac{de}{dt} = \frac{1}{v} \left( 2(e + \cos \nu) u_v - \frac{r \sin \nu}{a} u_n \right) \quad (3.23b)$$

$$\frac{di}{dt} = \frac{r \cos \theta}{h} u_h \quad (3.23c)$$

$$\frac{d\Omega}{dt} = \frac{r \sin \theta}{h \sin i} u_h \quad (3.23d)$$

$$\frac{d\omega}{dt} = \frac{1}{ev} \left( 2 \sin \nu u_v + \left( 2e + \frac{r}{a \cos \nu} \right) u_n \right) - \frac{r \sin \theta \cos i}{h \sin i} u_h \quad (3.23e)$$

$$\frac{d\nu}{dt} = \frac{h}{r^2} - \frac{1}{ev} \left( 2 \sin \nu u_v + \left( 2e + \frac{r}{a} \cos \nu \right) u_n \right) \quad (3.23f)$$

$$\frac{dM}{dt} = n - \frac{\sqrt{ap}}{eav} \left( 2 \sin \nu \left( 1 + e^2 \frac{r}{p} \right) u_t + \frac{r \cos \nu}{a} u_n \right) \quad (3.23g)$$

given,

$$p = a(1 - e^2) \quad (3.24)$$

$$h = \sqrt{p\mu} \quad (3.25)$$

$$v = \sqrt{\frac{2\mu}{r} - \frac{\mu}{a}} \quad (3.26)$$

$$n = \sqrt{\frac{\mu}{a^3}} \quad (3.27)$$

where  $n$  is the mean orbital motion, and  $\mathbf{u} = [u_v, u_n, u_h]$  the applied control components in the tangential direction, also equal to NEO velocity unit vector ( $u_v$ ), normal to the tangent within the orbital plane ( $u_n$ ), and in the direction of angular momentum ( $u_h$ ).

Note that two different forms of Gauss equations are used within the dynamics and control simulations: the set described here in  $\{v-n-h\}$  coordinates, and an alternate

form using the radial-transverse-normal directions  $\{r-t-h\}$ , given below. This second form is more suitable when dealing with Hill frame dynamics.

$$\frac{da}{dt} = \frac{2a^2}{h} \left( e \sin \nu u_r + \frac{p}{r} u_t \right) \quad (3.28a)$$

$$\frac{de}{dt} = \frac{1}{h} u_t (p \sin \nu u_r + ((p+r) \cos f + re)) \quad (3.28b)$$

$$\frac{di}{dt} = \frac{r \cos \theta}{h} u_h \quad (3.28c)$$

$$\frac{d\Omega}{dt} = \frac{r \sin \theta}{h \sin i} u_h \quad (3.28d)$$

$$\frac{d\omega}{dt} = \frac{1}{he} (-p \cos \nu u_r + (p+r) \sin \nu u_t) - \frac{r \sin \theta \cos i}{h \cos i} u_h \quad (3.28e)$$

$$\frac{d\nu}{dt} = \frac{h}{r^2} + \frac{1}{eh} (p \cos \nu u_r - (p+r) \sin \nu u_t) \quad (3.28f)$$

$$\frac{dM}{dt} = n + \frac{1}{a^2 en} ((p \cos \nu - 2re) u_r - (p+r) \sin \nu u_t) \quad (3.28g)$$

In both these cases, the third axis is measured in the same direction, parallel to the angular momentum vector  $\mathbf{h}$ . The conversion between the two reference systems is,

$$\begin{bmatrix} \hat{r} \\ \hat{t} \end{bmatrix} = \frac{h}{pv} \begin{bmatrix} e \sin \nu & -(1+e \cos \nu) \\ 1+e \cos \nu & e \sin \nu \end{bmatrix} \begin{bmatrix} \hat{v} \\ \hat{n} \end{bmatrix} \quad (3.29)$$

Colombo et al. (2009) determined that the change in angular location, in this case given by the mean anomaly, is calculated at the MOID by,

$$\Delta M = \int_{t_0}^{t_i} \frac{dM}{dt} dt + n_{A_0} (t_0 - t_{\text{MOID}}) + n_{A_i} (t_{\text{MOID}} - t_i) \quad (3.30)$$

This is used to propagate the equations of motion for the asteroid forward to the location of the original MOID, in order to calculate the total deflection distance achieved.

The thrust produced by the deflection method is a direct function of the rate of the expelled surface matter,  $\dot{m}_{exp}$  [Sanchez Cuartielles et al., 2009].

$$\frac{dm_{exp}}{dt} = 2v_{rot} \int_{y_0}^{y_{max}} \int_{t_{in}}^{t_{out}} \frac{1}{H} \left( P_{in} - Q_{rad} - Q_{cond} \sqrt{\frac{1}{t}} \right) dt dy \quad (3.31)$$

where  $[t_{in}, t_{out}]$  is the duration for which a point is illuminated,  $[y_0, y_{max}]$  are the limits of the vertical illuminated surface area (i.e. orthogonal to the direction of rotation of the asteroid),  $H$  is the enthalpy of sublimation and  $v_{rot}$  is the linear velocity of a point as it travels through the illuminated spot area. The spot area for the simulation is assumed to be flat (i.e. 2D), such that the velocity as an infinitesimal point moves through it, is linear. In reality, the area under the spot would be irregular, at best a small area of an ellipse.

The input power due to the solar concentrators is given by,

$$P_{in} = \eta_{sys} C_r (1 - \zeta_A) \frac{S_0}{r_{\odot/A}^2} \quad (3.32)$$

where  $\zeta_A$  is the albedo of the asteroid,  $(S_0/r_{\odot/A}^2)$  is the solar flux at the mirror surface (see Section 2.2.1),  $\eta_{sys}$  is the system efficiency, and  $C_r$  is the concentration ratio in

(2.1). The heat losses due to black-body radiation and conduction loss are defined, respectively, as,

$$Q_{rad} = \sigma \epsilon_{bb} T^4 \quad (3.33)$$

$$Q_{cond} = (T_{subl} - T_0) \sqrt{\frac{c_A \kappa_A \rho_A}{\pi t}} \quad (3.34)$$

where  $\sigma$  is the Stefan-Boltzmann constant,  $\epsilon_{bb}$  is the black body emissivity,  $T$  is the temperature and  $c_A$ ,  $\rho_A$  and  $\kappa_A$  are, respectively, the heat capacity, density and thermal conductivity of the asteroid. For the asteroid Apophis,  $c_A = 750$  J/kg·K based on the average value for silicate materials,  $\kappa_A = 2$  W/K/m and  $\rho_A = 2600$  kg/m<sup>3</sup> [Remo, 1994]. The sublimation temperature assumed is that for forsterites,  $T_{subl} = 1800$  K [Wang et al., 1999], with  $T_0$  set to 278 K.

Based on the duration of time an infinitesimal ‘point’ spends under the spot beam, the minimum power density required to sublimate changes. Figure 28 shows the relationship between time duration of illumination, and the minimum power density for a 1 m diameter spot.

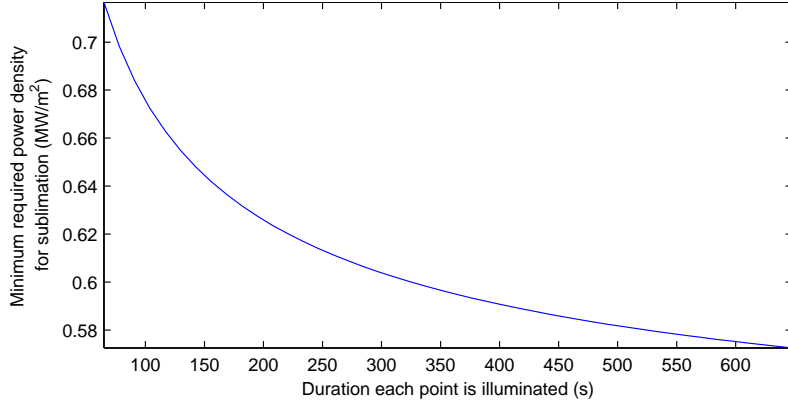


Figure 28: Amount of time a point spends under the spot beam on the asteroid surface versus minimum required power density level for sublimation, for a nominal 1 m diameter spot.

Finally, the induced acceleration  $\mathbf{u}_{dev}$  can be determined by,

$$\mathbf{u}_{dev} = \frac{\Lambda \bar{v}_{exp} \dot{m}_{exp}}{m_{A_i}} \cdot \hat{\mathbf{v}}_A \quad (3.35)$$

where  $\hat{\mathbf{v}}_A$  is direction of velocity vector of the NEO,  $\Lambda \simeq \left(\frac{2}{\pi}\right)$  is the scattering factor assuming the debris plume is uniformly distributed over a half-sphere, and the remaining mass of the asteroid  $m_{A_i} = m_A(t_i)$  is calculated by numerically integrating (3.31). The average velocity of the expelled debris is modelled using the Maxwell-Boltzmann distribution for particles of an ideal gas,

$$\bar{v}_{exp} = \sqrt{\frac{8k_B T_{subl}}{\pi M_{Mg_2SiO_4}}} \quad (3.36)$$

where  $k_B$  is the Boltzmann constant, and  $M_{Mg_2SiO_4}$  is the molecular mass of forsterite.

This induced acceleration is used with the Gauss equations in (3.23) in order to determine the change in the NEO orbit due to the solar sublimation.

For further information on the development of the thermal model, please see Sanchez Cuartielles et al. (2009).

### 3.3 FUNNEL ORBIT DYNAMICS

For the orbit of the spacecraft, an initial solar orbit was set equal to that of the asteroid under study, Apophis. A spatial offset was introduced relative to the position of the asteroid at an arbitrary initial time,  $t_0$ . This offset acts like a periodic disturbance, in which the period of the oscillation is equal to that of the orbital period around the Sun. The end result is a relatively small formation orbit, which in turn orbits around the Sun. From a kinematic point of view, the concept is similar to the orbit of the Moon; the Moon orbits about a central point, the Earth, which in turn both orbit as a system around the Sun. The formation orbit can be thought of as an orbit around the Sun with a small offset in the initial position  $\delta\mathbf{r}_0$  and velocity  $\delta\mathbf{v}_0$ .

#### 3.3.1 Optimisation of the initial state vector

A relative periodic orbit can be found for almost any point in space surrounding the chief orbit. However, in the case of most space missions, there are several specific requirements and conditions that restrict the choice of orbit. As such, an optimiser was used to determine the optimal initial state vector based on a set of objectives and constraints.

The dynamics of the funnel orbits are defined by the initial state vector containing the element set  $\delta\mathbf{k}(t_0)$ . All the elements in the set are constant throughout the orbit (time-invariant), so  $\delta\mathbf{k}(t_0) = \delta\mathbf{k}(t_i) = \delta\mathbf{k}$ .

The state vector is defined as either,

$$\xi_x = [\delta r_x \quad \delta r_y \quad \delta r_z \quad \delta v_x \quad \delta v_z] \quad (3.37)$$

with  $\delta v_y$  calculated in order to guarantee the periodicity of the orbit, or,

$$\xi_k = [\delta e \quad \delta i \quad \delta \Omega \quad \delta \omega \quad \delta M] \quad (3.38)$$

with  $\delta a \Rightarrow 0$  to guarantee the periodicity of the orbit.

Optimal formation design problems were developed for the two different test missions: a NEO tracking mission, and a NEO deviation mission. For the deflection mission case, two different sets of objective functions were used.

The design of a formation made up of  $n$  spacecraft, all with optimal orbital characteristics, requires the identification not only of the global minimum but also of  $(n-1)$  additional, feasible local minima within a given search domain (each solution represents one orbit for one spacecraft, thus for a  $n$ -spacecraft formation,  $n$  solutions are needed). It is expected that for almost every position on the orbit, i.e. every instant of time, there are several optimal solution vectors that locally minimise the objective function(s). Therefore, a characterisation of the search space is required in order to find not only the global optimum but also a set of local optima with a value of the objective function close to the one of the global solution. For multiobjective optimisation problems, this requires the identification of a set of feasible Pareto optimal solutions for the set of objective functions.

The optimiser used here, EPIC, was developed by Vasile [Vasile, 2008; Maddock and Vasile, 2008a], and employs a hybrid behavioural-search approach that stores all the feasible solutions. Appendix B describes the background information on the optimisation procedure.

*Tracking mission*

For a tracking mission, it is beneficial that the spacecraft remain at a constant distance from the asteroid in order to get the most accurate measurements possible. At the same time, it is desirable to see the asteroid from different angles. Therefore the problem is to design a periodic orbit that minimises the difference between the minimum and the maximum distance from the centre of the asteroid.

$$J_{T1} = \left| \max_{\nu}(\delta r) - \min_{\nu}(\delta r) \right| \quad (3.39)$$

Another desirable property of the formation would be to bring the plane of the orbit as close to the NEO as possible without crossing into the sphere of influence of the asteroid. This is implemented by minimising the difference between the maximum distance at any point in the formation orbit, and a predetermined minimum distance  $r_{lim}$ . In this case, as the spacecraft is to fly as close to the asteroid as possible, the minimum distance is set equal to the radius of the sphere of influence of the asteroid.

$$J_{T2} = \left| r_{lim} - \max_{\nu}(\delta r) \right| \quad (3.40)$$

subject to the constraint:

$$C_{ineq} = \min_{\xi \in D} (\delta r - r_{lim}) > 0 \quad (3.41)$$

The constraint is added to reduce the effects of the nonlinear gravity field of the asteroid on the spacecraft. The radius of the sphere of influence is approximated by [Battin, 1999],

$$r_{lim} \Rightarrow r_{soi} \approx r_c \left( \frac{m_A}{m_{\odot}} \right)^{\frac{2}{5}} \quad (3.42)$$

since the mass of each object differs by an order of magnitude,  $m_{sc} \ll m_A \ll m_{\odot}$ .

Due to the dependant nature of the two objective functions, the optimisation can be run as a single objective optimisation. The overall objective function  $J_T$  is simply a sum of the two equations (3.39) and (3.40),

$$\min_{\xi \in D} J_T = \min_{\xi \in D} (J_{T1} + J_{T2}) \quad (3.43)$$

The dependency was verified both by examining the dynamics, and by monitoring the two objective function values independently for a number of runs. In over 500 runs using a local SQP optimiser from Matlab `fmincon` with a multi-start approach for the start condition, the two values for  $J_{T1}$  and  $J_{T2}$  were almost identical, differing only after the tenth significant digit.

A number of boundary conditions were set for each element in Cartesian state vector  $\xi_x$  to reduce the search space, and improve the computation speed. The position components were limited to  $\delta \mathbf{r} \in [-5, +5]$  km, and the velocity values to  $\delta v_x, \delta v_z \in [-100, 100] \times 10^{-9}$  km/s. As the relative velocity values are quite small compared to the position, the two velocity components were scaled up by a factor of  $10^9$ .

This first optimisation was run over a period of 30 days, starting on 3693.5 MJD2000 (or 01 January 2010). EPIC was run with a total of 10 agents exploring the search space. The number of subdomains for the first run was limited to 5 and the maximum number of function evaluations per subdomain was set to 10000.

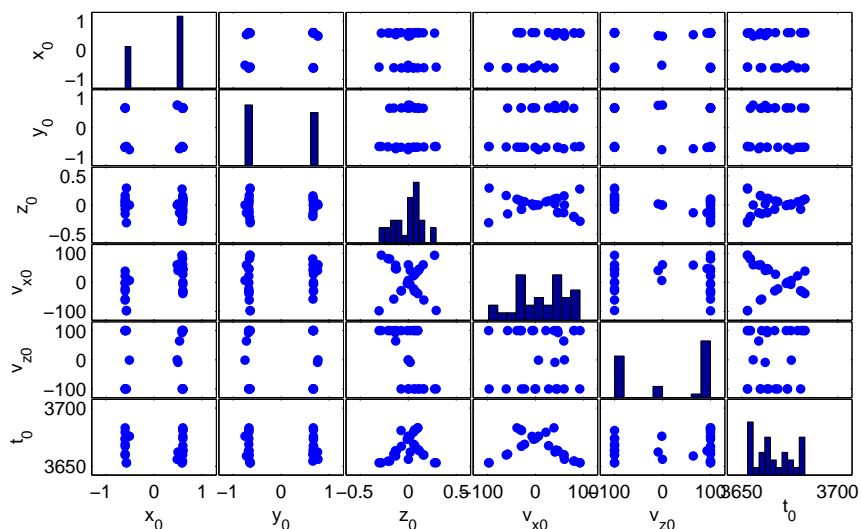


Figure 29: The cross-comparison of the best 30 solutions of  $\xi_x$  found using EPIC. The distances are measured in km, velocities in  $10^{-9}$  km/s and time in MJD2000.

Figure 29 shows the distribution of the minima at the end of the search. Each element in the solution vector, i.e.  $[x_0, y_0, z_0]$ ,  $[v_{x_0}, v_{z_0}]$  and  $t_0$ , are plotted against each of the other remaining five elements for all the solutions in a given set. The diagonal shows the normalised distribution of that element within the solution set. In Fig. 29, it can be clearly seen that for all the solutions, the values of  $x_0$  and  $y_0$  fall into two main groupings. The two groups can be said to be independent of time since for every value of  $t_0$  in the solution set, the values of  $x_0$  will only fall into one of two values (plus or minus a small margin). By comparison, when  $x_0, y_0$  are compared against  $v_{z_0}$ , they form six distinct clusters. This means that there are clear sets of values for these three variables that satisfy the objective function.

Looking at the velocities, the initial radial velocity  $v_{x_0}$  forms a cross pattern with the two out-of-plane elements ( $z_0, v_{z_0}$ ), meaning they are all closely coupled with each other. Finally, examining the last row/column showing the time, it can be seen that a feasible minima can be found for almost every point in time within the search space. Although, as seen from the normalised distribution of  $t_0$ , some initial times are more favourable to finding optimal minima than others.

From this search, it is simple to find the smallest objective function value and extract the optimal initial state vector for the orbit, and starting date. Figure 30 shows the resulting formation orbit. The optimised initial state vector at  $t_0 = 3653.0$  MJD2000 is,

$$\mathbf{X}_0^{opt} = \begin{bmatrix} x_0 = 575.44 \text{ m} \\ y_0 = 646.62 \text{ m} \\ z_0 = 304.15 \text{ m} \\ \dot{x}_0 = 9.738e-5 \text{ m/s} \\ \dot{y}_0 = -3.517e-4 \text{ m/s} \\ \dot{z}_0 = -1.00e-4 \text{ m/s} \end{bmatrix} \Leftrightarrow \delta \mathbf{k}_0^{opt} = \begin{bmatrix} \delta a = 0 \text{ m} \\ \delta e = -0.0884 \\ \delta i = 1.564 \text{ rad} \\ \delta \Omega = -2.347 \text{ rad} \\ \delta \omega = -23.62 \text{ rad} \\ \delta \nu_0 = 0.468 \text{ rad} \end{bmatrix} \times 10^{-7}$$

A by-product of the equations of motion is that the closer the orbit is to the asteroid, the more normal the orbital plane becomes relative to the asteroid velocity vector. Conversely, the farther away the formation orbit is from the chief point, the larger the semi-major axis and the more parallel the orbital plane.

In Fig. 30, the period of the formation orbit is equal to the time it takes for the asteroid to make one complete revolution about the Sun. The final orbit has a slight deviation from the desired orbital plane, on the order of 300 km. This orbit provides a relatively consistent distance from the surface of the asteroid and provides good coverage of the surface.

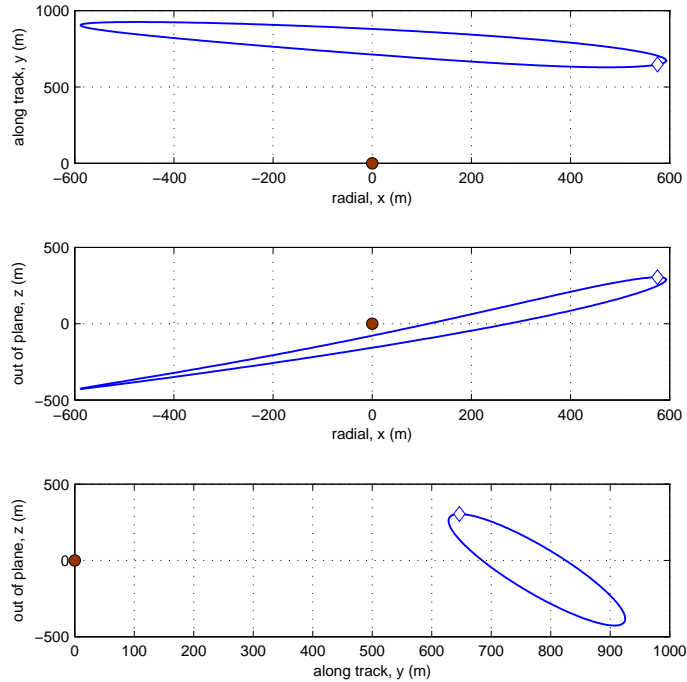


Figure 30: Orthographic view of the optimal formation orbit, including the initial state vector (shown as a diamond), and location relative to Apophis (shown as a brown circle).

Note from Fig. 29, that along the  $t_0$  coordinate the distribution is almost continuous. This evidence confirms the fact that an optimal configuration exists for every position along the orbit. It also suggests that there exists a globally optimal position along the orbit that gives the minimum for both objective functions. A second optimisation was conducted extending the bounds of  $t_0$  to 1 Earth year, from 01 January – 31 December 2010. The period of Apophis is slightly less than that of Earth; 323.6 days. By searching for a full year, one can see the effect of the orbital position of the asteroid on the initial state vector, see Fig. 31.

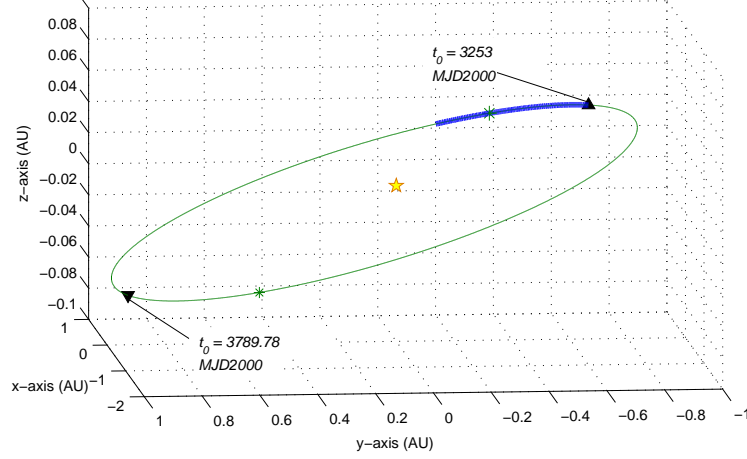


Figure 31: Orbit of Apophis showing the optimal  $t_0$  for the two solutions (shown as black triangles). The apoapsis and periapsis are also shown for reference (green stars) with the first solution near the periapsis, and the second solution near the apoapsis. The first search space for  $t_0$  is shown in blue (bold).

The optimal initial state vector is given below for  $t_0 = 3789.76$  MJD2000, and the resulting formation orbit in Fig. 32.

$$\mathbf{X}_0^{opt} = \begin{bmatrix} x_0 = -529.88 \text{ m} \\ y_0 = -664.10 \text{ m} \\ z_0 = 468.73 \text{ m} \\ \dot{x}_0 = -1.000e-4 \text{ m/s} \\ \dot{y}_0 = 1.95e-4 \text{ m/s} \\ \dot{z}_0 = -9.99e-5 \text{ m/s} \end{bmatrix} \iff \delta \mathbf{k}_0^{opt} = \begin{bmatrix} \delta a = 0 \text{ m} \\ \delta e = 0.038 \\ \delta i = -1.701 \text{ rad} \\ \delta \Omega = 8.389 \text{ rad} \\ \delta \omega = -40.92 \text{ rad} \\ \delta \nu_0 = -0.755 \text{ rad} \end{bmatrix} \times 10^{-7}$$

A more extensive optimisation was performed, with EPIC set to run with a total of 20 agents exploring the search space. The number of subdomains was set to 14 and the maximum number of function evaluations per subdomain was set to 60000 (see Appendix B for more explanation on the equations and design of EPIC). Although the result was quite good, achieving a value of the objective function of 2.93, it was found that by re-optimising locally with an SQP method (`fmincon`), the value of the best solution could be further improved to 2.8997. The tolerance on the constraint was set equal to  $10^{-6}$ , or 0.00000044%, which was deemed acceptable especially considering that the equation for the sphere of influence is an approximation.

Figure 33 shows a cross-comparison between the different elements of the solution vector for 2182 possible solutions (or the total number of solutions generated from 10 independent runs). Note that the intent was not to minimise the number of function evaluations or convergence time to the best value.

Figure 34 shows the variation in objective function  $J_T$  across all the runs. It is clear that there are intervals where the value of the objective function is relatively constant. This is reflected by either only fractional changes in the orbital element differences in  $\xi$ , or is due to symmetry around the  $y$ -axis of the asteroid. Figure 35 shows the values of the corresponding solution vector elements as the value of the objective function increases. The *solution index number* refers to the ranking of the solution vector  $\xi_T$

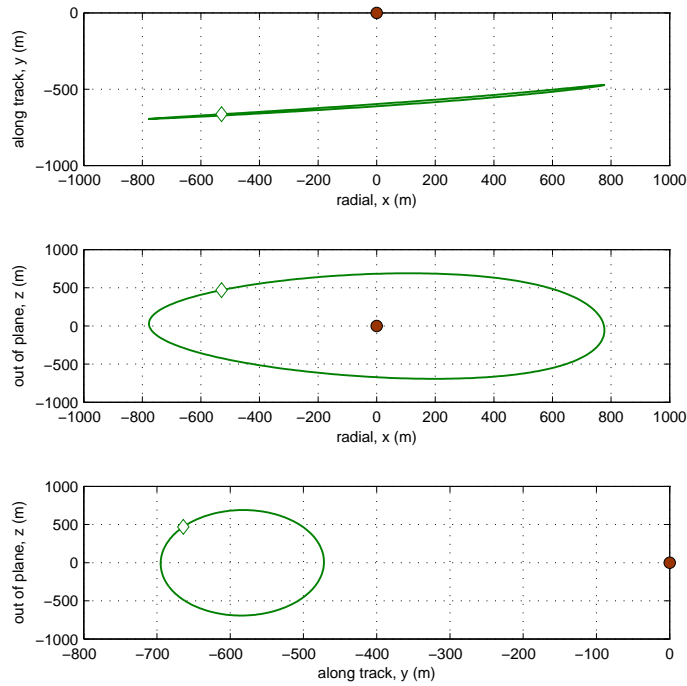


Figure 32: Orthographic view of the formation orbit optimised over an 1 year period, showing the initial state vector (shown as a diamond), and location relative to Apophis (shown as a brown circle).

relative to increasing values of  $J_T$  (the optimal value for  $\min(J_T)$  has a solution index number of 1).

Figures 36–38 show the three groupings, or ‘families’, of optimal orbits. Within the same family, the difference in objective function is almost zero while the differences in orbit geometry are significant. In particular,

FAMILY A Four types of small symmetric orbits, inclined with respect to the  $x$ - $y$  plane (see Fig. 36),

FAMILY B Two types of symmetric orbits that are slightly inclined with respect to the  $x$ - $y$  plane (see Fig. 37),

FAMILY C Two types of large symmetric orbits, inclined with respect to the  $x$ - $y$  plane and encircle the asteroid (see Fig. 38).

In the three orthographic views, the top figure of the  $x$ - $y$  plane shows the view looking ‘down’ on the ecliptic plane. The second plot in the  $x$ - $z$  plane is from the point-of-view of the asteroid looking out at the formation, and the lastly  $y$ - $z$  plot is the view looking from the Sun. For each of the diagrams, the asteroid is located at the centre point (0, 0) and the small circle on each orbit represents the position of the spacecraft at a specific point in time. The corresponding values for Figs. 36 – 38 of the objective function and solution vectors are given in Table 14.

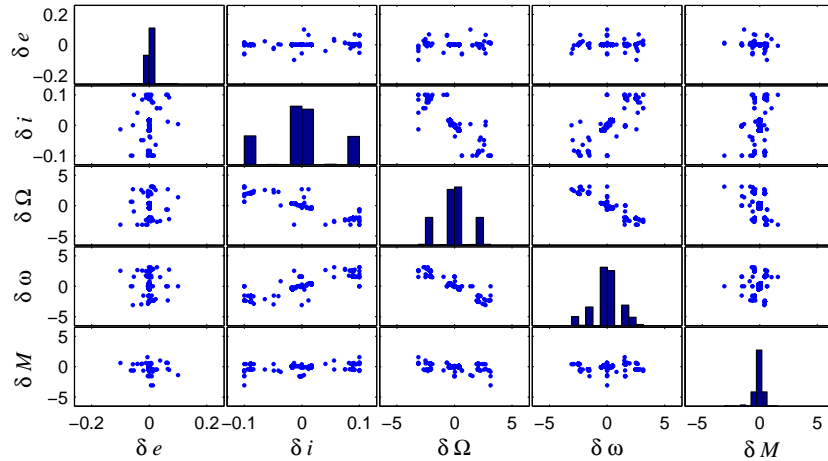


Figure 33: Cross-comparison of the solution vector  $\xi_T$  for the SOO using EPIC.

As can be seen, the spatial separation among the spacecraft flying on the second family of orbits is very small. Such a small separation is not ideal for tracking measurements in the case where multiple spacecraft are tracking through triangulation. In the first family of orbits however, four spacecraft can be placed each with good visibility and good separation. By exploiting the symmetry of the second family another two spacecraft can be added; with a possibility to add a further four spacecraft using the orbits from family C.

Table 14: Values for the best results for each family of objection function  $J_T$  and the corresponding solution vector  $\xi_k$ .

Objective function:	$J_T$	2.8997	45.5922	80.4110
Solution vector:	$\delta e$	$1.3629 \times 10^{-9}$	$7.2294 \times 10^{-8}$	$4.0447 \times 10^{-7}$
	$\delta i$	0.01671	0.0006949	-0.08853
	$\delta \Omega$	-0.3908	-0.005114	2.0699
	$\delta \omega$	0.3070	-0.07934	-1.6261
	$\delta M$	-0.08197	-0.08289	-0.4342

NOTE: all values in the solution vector are scaled by an additional factor of  $10^{-7}$ .

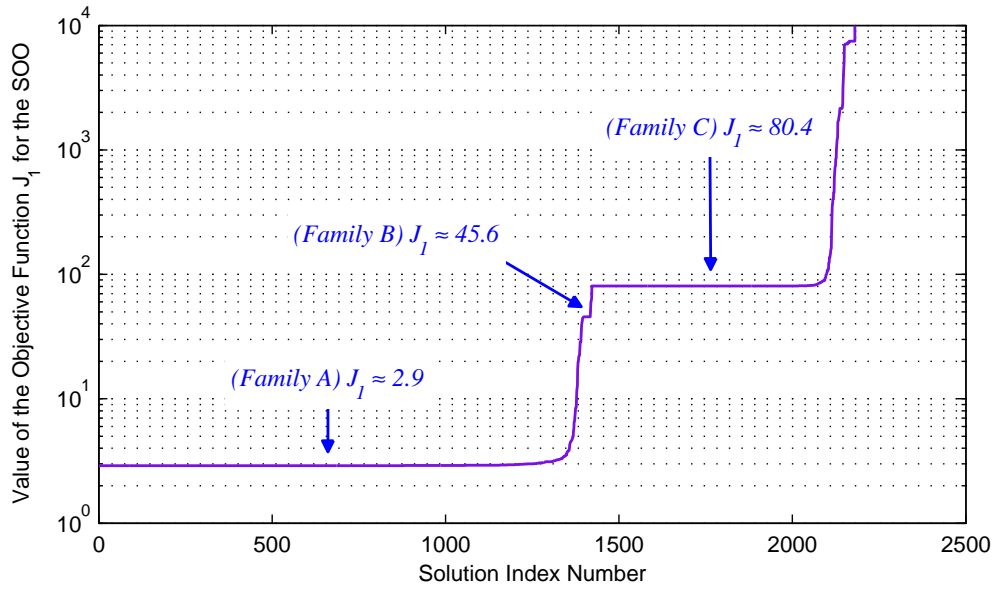


Figure 34: Range of all optimised values for the objective function  $J_T$  from all runs.

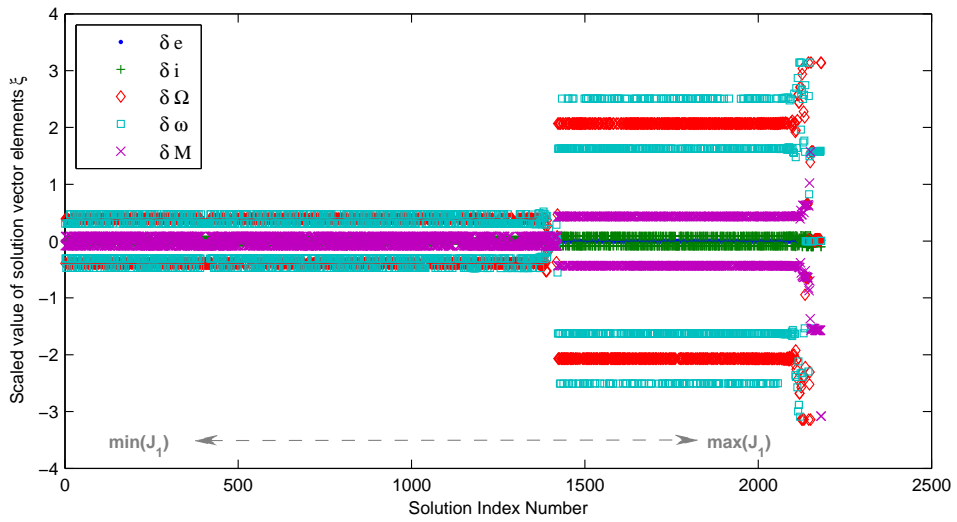


Figure 35: Comparison of the values for the solution vector  $\xi_k$  for each of the results of the optimisation.

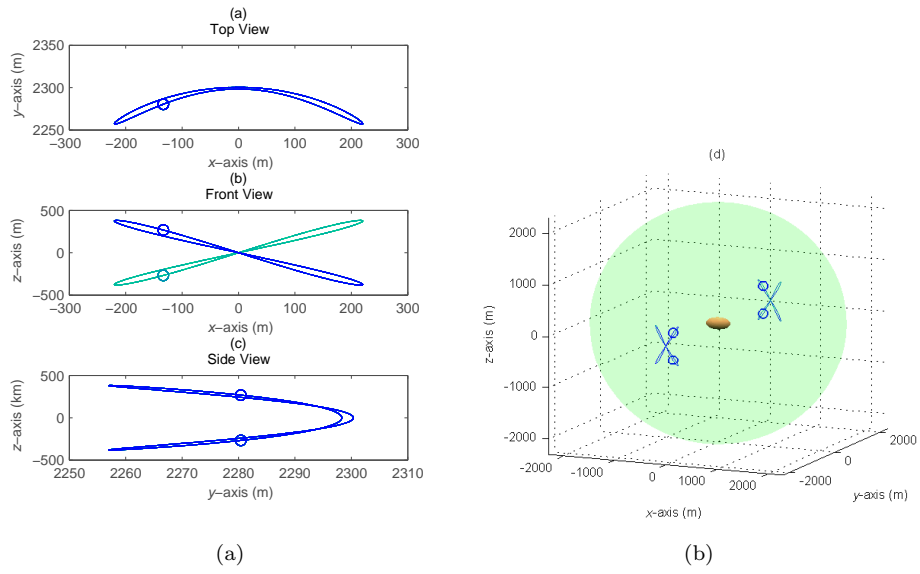


Figure 36: Orbital geometry of solutions from family A,  $J_T \approx 2.9$ .

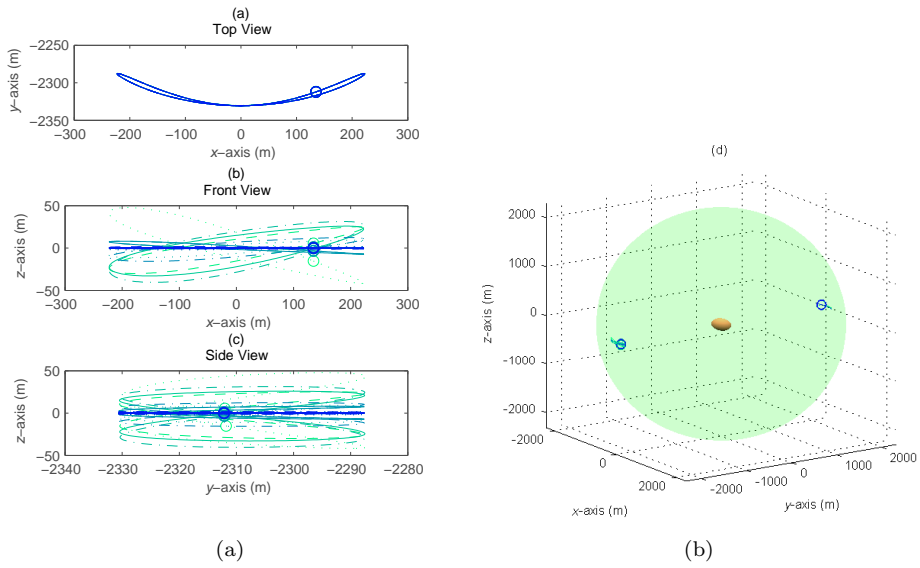


Figure 37: Orbital geometry of solutions from family B,  $J_T \approx 45.6$ .

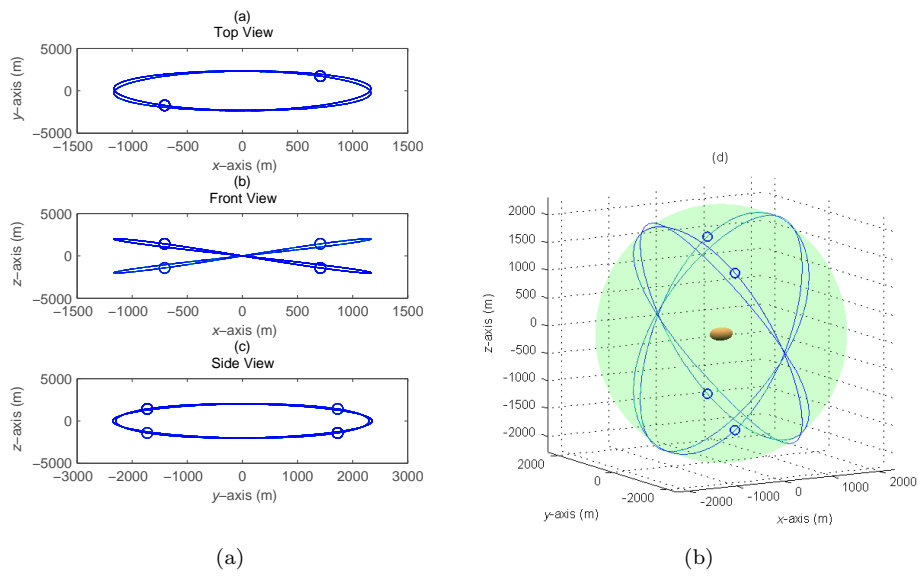


Figure 38: Orbital geometry of solutions from family C,  $J_T \approx 80.4$ .

### NEO Deflection Mission

In order to deflect an asteroid, the spacecraft have to maintain their relative position with respect to the asteroid in order to keep the required power density on the same spot of the surface of the asteroid. Therefore, the formation orbits have to be periodic and in close proximity with low excursion in the relative distance from the asteroid. On the other hand the spacecraft should avoid, as much as possible, the irregular regions of the gravity field close to the asteroid and avoid any impingement with the plume of debris and gas coming from the sublimation of the surface material.

If the optimal thrust direction that maximises the deviation is along the unperturbed velocity vector of the asteroid, [Colombo et al., 2009] then the exhaust gases will flow in the same general direction as the  $y$ -axis of the local Hill reference frame. Therefore, the size of the formation orbits projected in the  $x$ - $z$  plane should be maximal (see Fig. 39).

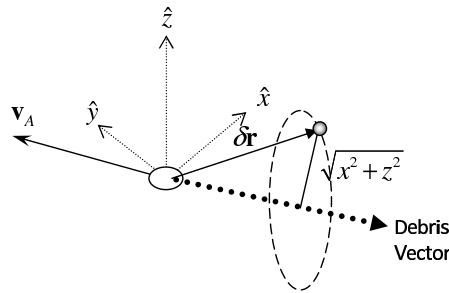


Figure 39: Illustration of debris plume relative to the desired spacecraft formation orbit.

This is an approximation in the case of Apophis since the orbit is elliptical. The flight path angle, i.e., the angular difference between the velocity vector of the asteroid, and the orbit tangential vector  $\hat{y}$ , ranges between  $\pm 0.1922$  rad throughout an orbit.

All the requirements on the formation orbits can be formulated in mathematical terms as a multi-objective optimisation problem,

$$\min_{\delta \mathbf{k} \in D} \min_{\nu} J_{D1} = \delta r \quad (3.44)$$

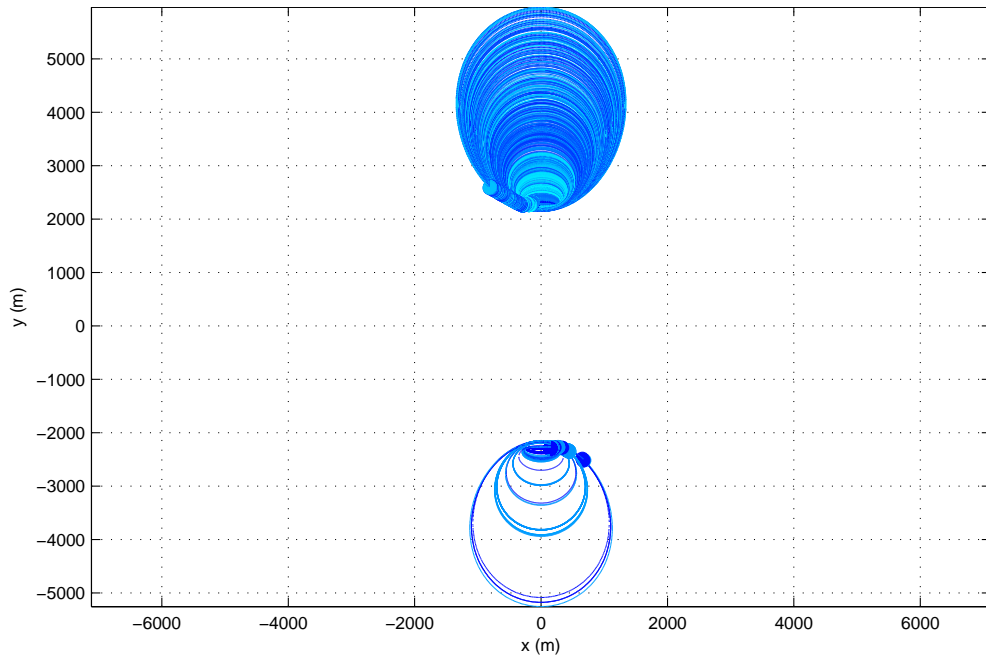
$$\min_{\delta \mathbf{k} \in D} \min_{\nu} J_{D2} = -\sqrt{x^2 + z^2} \quad (3.45)$$

subject to the same inequality constraint on the minimum allowable  $\delta r$  given in (3.41).

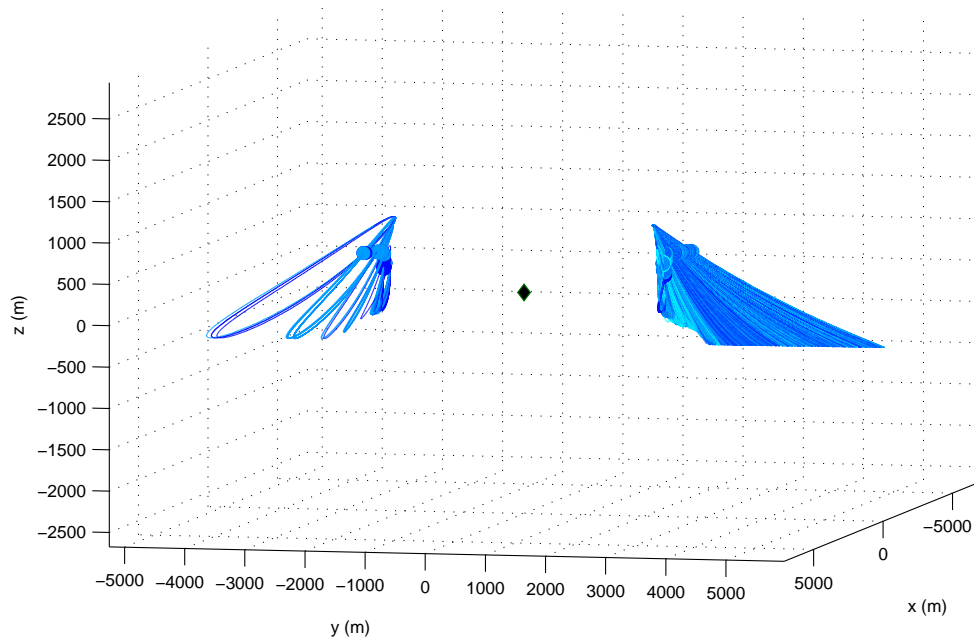
An alternate approach for generating orbits is based on minimising the requirements for the flat pointing mirror in the spacecraft mirror assembly. The first objective function is used to minimise the required control accuracy of the spot beam positioning, by optimising the required angular response of the controller. In other words, the larger the conic angle of the spot beam, the easier it will be for the controller to maintain the same position on the asteroid, and the less affected it would be by small errors in the pointing.

The angular resolution required for the spot beam can be characterised by the following angle,

$$\sin \vartheta_{spot} = \frac{d_{spot}/2}{\delta r} = \frac{d_{Mdir} \sin \phi}{2\delta r} \quad (3.46)$$



(a)



(b)

Figure 40: Overview of all Pareto-optimal orbits for objective functions  $J_{D1}$  and  $J_{D2}$ . The initial state is shown as a circle on the orbits, with the asteroid located in the centre of the Hill frame.

which is a direct function of the distance of the spacecraft from the asteroid. Therefore, the first objective function  $J_{D3}$  for the deflection mission is the same as the one given in (3.39). The mirror  $M_{dir}$  in (3.46) is the smaller directional mirror.

The second objective is to limit the variation in the Sun-spacecraft-asteroid half angle  $\phi$  in order to minimise the requirements on the attitude control system. Given,

$$\phi = 2 \arccos \left( \frac{\langle \delta \mathbf{r}, \mathbf{r}_{\odot/s} \rangle}{\delta r_{\odot/s}} \right) \quad (3.47)$$

the second objective function is defined as,

$$\min_{\xi \in D} J_{D4} = \max(\phi) - \min(\phi) \quad (3.48)$$

As with the tracking mission, a number of boundary conditions were set to restrict the search space and improve the speed of the search. Given the small relative distance between the spacecraft and the asteroid, in the order of 1 – 10 km, the values of the  $\delta \mathbf{k}$  parameters will be very small, in the order of  $0 \pm 10^{-7}$ . Due to these very small expected values, the inputs were scaled up closer to unity for the optimisation process. Table 15 lists the upper and lower boundaries imposed on optimisation of the solution vector  $\xi$ .

Table 15: Boundaries on search space for the initial state vector  $\xi_k$ .

Element in Initial State Vector	Lower Bound	Upper Bound
Difference in Eccentricity, $\delta e$ ( $10^{-7}$ )	-0.1	0.1
Difference in Inclination, $\delta i$ ( $10^{-7}$ rad)	-0.1	0.1
Difference in RAAN, $\delta \Omega$ ( $10^{-7}$ rad)	$-\pi$	$\pi$
Difference in Argument of periapsis, $\delta \omega$ ( $10^{-7}$ rad)	$-\pi$	$\pi$
Difference in Mean anomaly, $\delta M$ ( $10^{-7}$ rad)	$-\pi$	$\pi$

Through the previous optimisation of the single objective function  $J_T$ , three families of formation orbits were identified (see Figs. 36–38) each with different characteristics and values of the objective function  $J_T$ . Families A and B were both very close to the asteroid and are particularly interesting for a deflection mission as they provide an advantageous position from which the sunlight can be focused on the surface of the asteroid. Moreover the Sun-spacecraft-Asteroid angle  $\phi$  is nearly the same for all the spacecraft, which allows all the spacecraft to have similar attitude control. Starting from the solutions of the first Family A, the whole set of Pareto optimal solutions was computed that minimise, at the same time  $J_{D3}$  and  $J_{D4}$ . EPIC was run for 40000 function evaluations with 20 agents and no domain decomposition.

Figure 41 shows a cross-comparison between the different elements of the solution vector for the whole Pareto set. Figure 42 shows the optimal Pareto front for the multi-objective optimisation (MOO). The best group of solutions of the single objective case would be in the upper left part of the Pareto front, all with a very similar value for the objective function  $J_{D4}$ .

Figure 43 shows the orbit with the objective function  $J_{D3}$  minimised. This represents the formation orbit closest to the asteroid and with the minimum difference between the closest point and the farthest point from the asteroid. By comparison, Fig. 44 shows the orbit minimising the second objective function,  $J_{D4}$ . The spacecraft moves back and forth along an orbit which is stretched in the direction of the

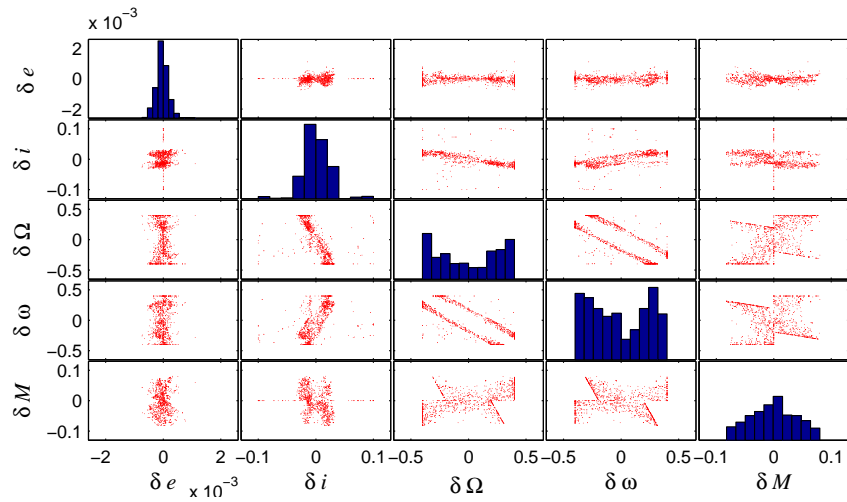


Figure 41: Cross comparison of the solution vector  $\xi$  for the MOO using EPIC.

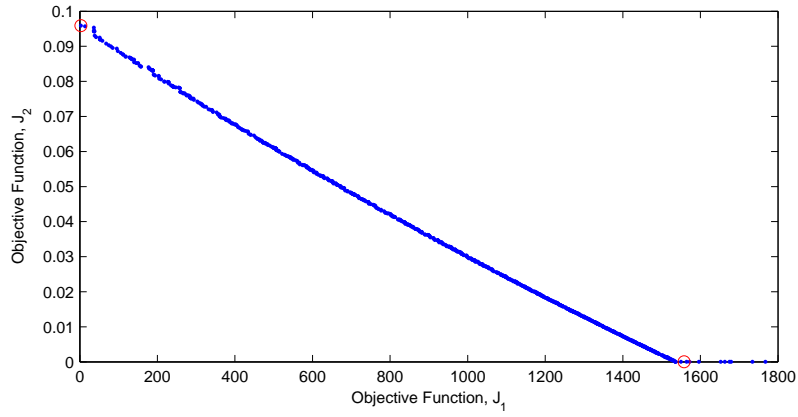


Figure 42: Optimal Pareto front for MOO illustrating the trade-off in accuracy of the beam. The red circles represent the two solution points given in Table 16.

$y$  axis and, as such, only requires minute adjustments in the directional mirror. Table 16 shows the corresponding values for the objective functions and state vector. Note that for the latter solution, although the difference between the farthest point and the closest point is higher than for the former solution, the whole trajectory on average, is still quite close to the asteroid.

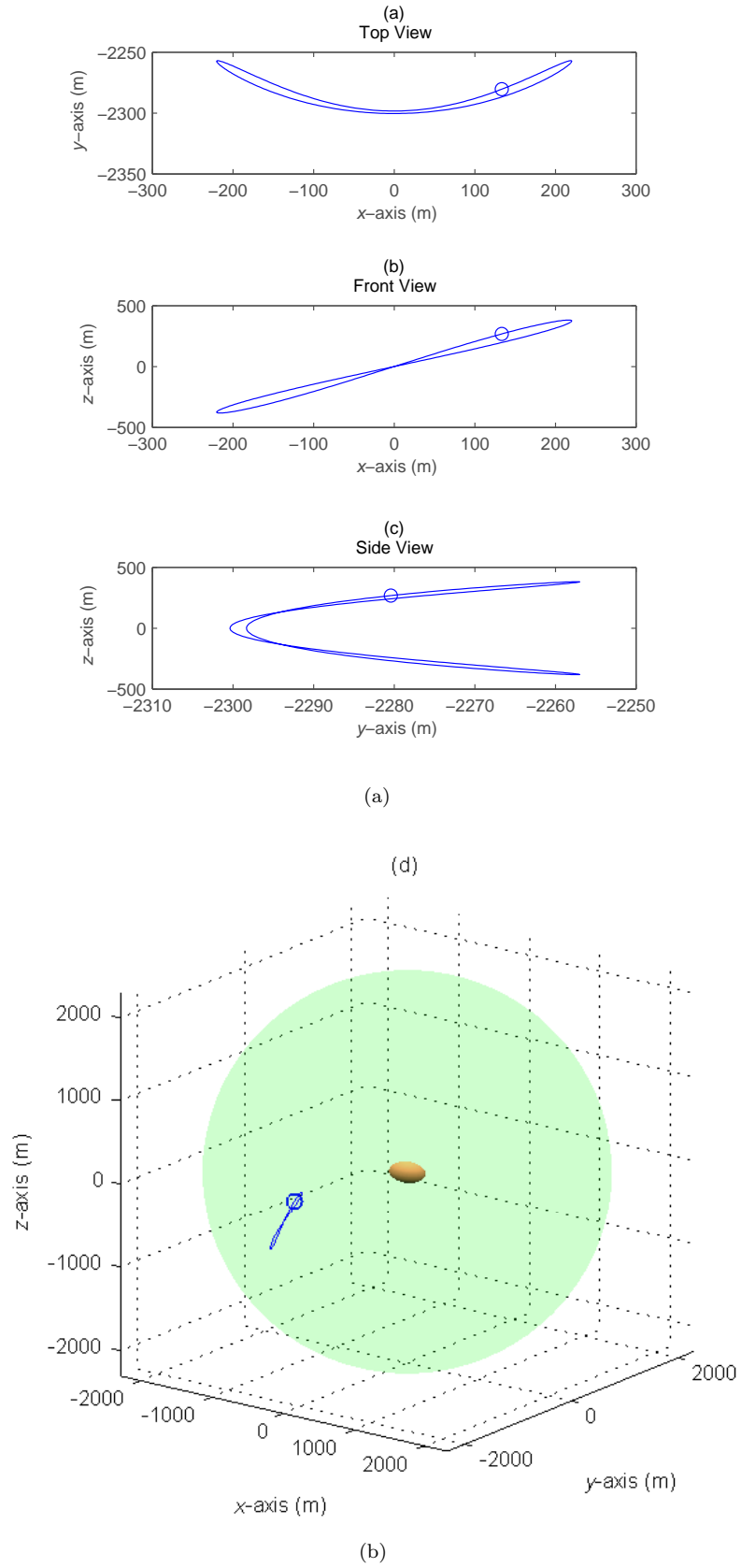


Figure 43: Formation orbit minimising the  $J_{D3}$  value.

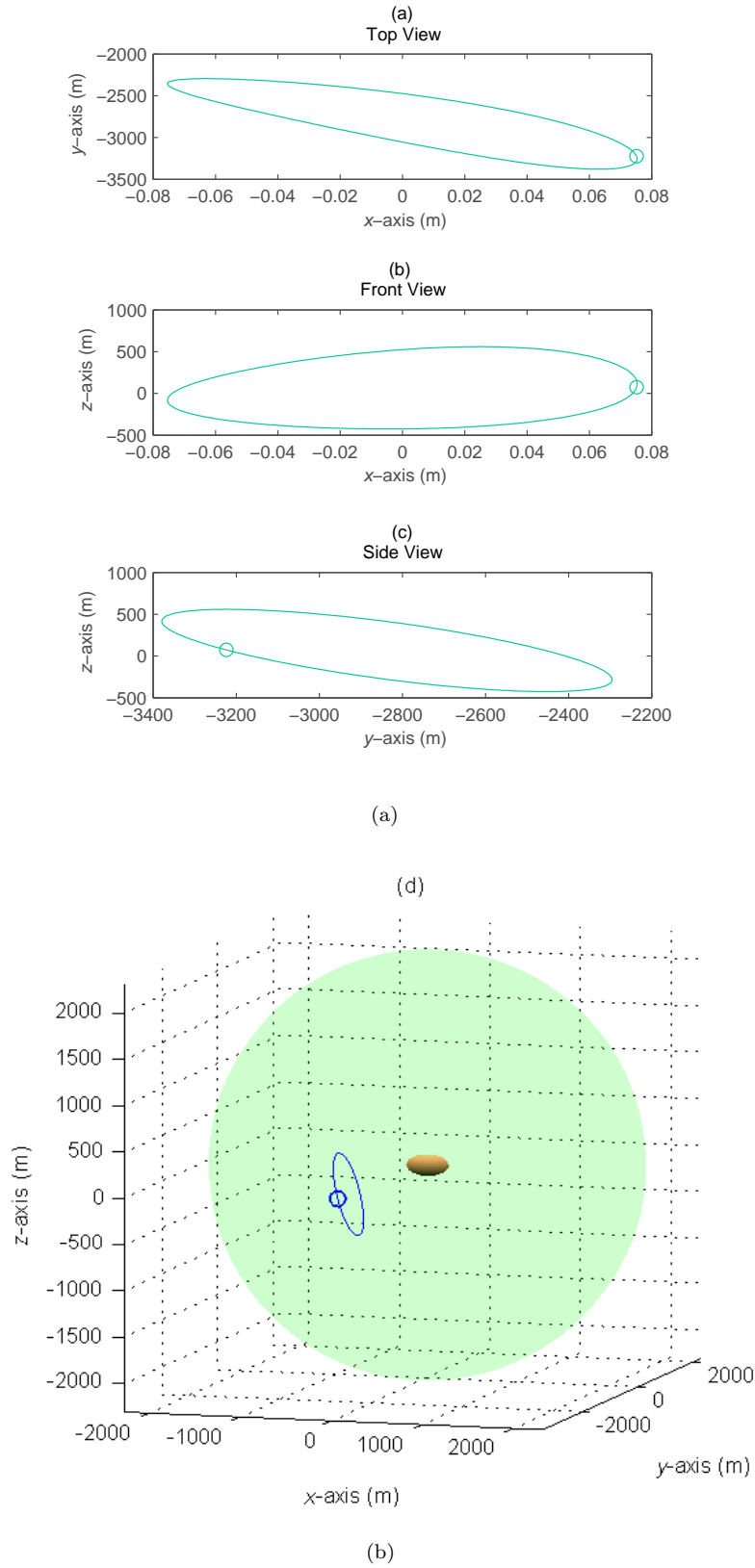


Figure 44: Formation orbit minimising the  $J_{D4}$  value.

Table 16: Values for the objective functions and solution vector  $\xi_k$  for the end limits of the Pareto front for the MOO.

		Value with optimal $J_{D3}$	Value with optimal $J_{D4}$
Objective function:	$J_{D3}$	2.8997	1558.01
	$J_{D4}$	0.095905	$2.7719 \times 10^{-5}$
Solution vector:	$\delta e$	$1.3629 \times 10^{-9}$	$4.5655 \times 10^{-6}$
	$\delta i$	0.01671	-0.03557
	$\delta \Omega$	-0.3908	0.09568
	$\delta \omega$	0.3070	-0.3011
	$\delta M$	-0.08197	$-1.5409 \times 10^{-5}$

NOTE: all values in the solution vector are scaled by an additional factor of  $10^{-7}$ .

## 3.4 ARTIFICIAL EQUILIBRIUM POINTS

If solar pressure and the gravity field of the asteroid are taken into account in the dynamics, then the mirrors can be designed such that the two forces are in equilibrium, with the spacecraft hovering at a fixed location and distance from the asteroid using the single-mirror configuration to control the beam. These points, called here *artificial equilibrium points* (AEP), are in fact static points where the forces are momentarily balanced, or in equilibrium. It should be noted these are not in dynamic equilibrium in which the spacecraft could remain indefinitely at a fixed point in space, due to the constantly changing forces at work.

Considering a perfectly spherical and homogenous gravity field of the asteroid, the dynamics of the mirror are governed by the following set of equations, based on (3.5),

$$\ddot{x} = 2\dot{v}\left(\dot{y} - y\frac{\dot{r}_A}{r_A}\right) + x\dot{v}^2 + \frac{\mu_\odot}{r_A^2} - \frac{\mu_\odot}{\delta r^3}(r_A + x) - \frac{\mu_A}{\delta r^3}x + \frac{F_{s_x}(x, y, z)}{m_{sc}} + \frac{F_{u_x}}{m_{sc}} \quad (3.49a)$$

$$\ddot{y} = -2\dot{v}\left(\dot{x} - x\frac{\dot{r}_A}{r_A}\right) + y\dot{v}^2 - \frac{\mu_\odot}{r_{sc}^3}y - \frac{\mu_A}{\delta r^3}y + \frac{F_{s_y}(x, y, z)}{m_{sc}} + \frac{F_{u_y}}{m_{sc}} \quad (3.49b)$$

$$\ddot{z} = -\frac{\mu_\odot}{r_{sc}^3}z - \frac{\mu_A}{\delta r^3}z + \frac{F_{s_z}(x, y, z)}{m_{sc}} + \frac{F_{u_z}}{m_{sc}} \quad (3.49c)$$

where  $m_{sc}$  is the estimated mass of the spacecraft,  $\mathbf{F}_{SRP} = [F_{s_x}, F_{s_y}, F_{s_z}]$  is force due to the solar radiation pressure and  $\mathbf{F}_u = [F_{u_x}, F_{u_y}, F_{u_z}]$  is the control force. Given the principle of the AEPs to balance the solar pressure and gravitational forces, the system is therefore,

$$2\dot{v}\left(-y\frac{\dot{r}_A}{r_A}\right) + x\dot{v}^2 + \frac{\mu_\odot}{r_A^2} - \frac{\mu_\odot}{r_{sc}^3}(r_A + x) - \frac{\mu_A}{\delta r^3}x + \frac{F_{s_x}(x, y, z, \beta, f_\ell)}{m_{sc}} = 0 \quad (3.50a)$$

$$-2\dot{v}\left(-x\frac{\dot{r}_A}{r_A}\right) + y\dot{v}^2 - \frac{\mu_\odot}{r_{sc}^3}y - \frac{\mu_A}{\delta r^3}y + \frac{F_{s_y}(x, y, z, \beta, f_\ell)}{m_{sc}} = 0 \quad (3.50b)$$

$$-\frac{\mu_\odot}{r_{sc}^3}z - \frac{\mu_A}{\delta r^3}z + \frac{F_{s_z}(x, y, z, \beta, f_\ell)}{m_{sc}} = 0 \quad (3.50c)$$

The third equation (3.50c) is always satisfied if the mirror is in the  $x_M$ - $y_M$  plane. Considering that the mirror has to constantly reflect the light onto the surface of the asteroid, if the mirror is flat the only possible equilibrium configuration is with the asteroid-mirror direction aligned with the spacecraft-Sun direction. If the mirror is not flat, then the position vector  $\delta\mathbf{r}$ , solar aspect angle  $\beta$  and focal distance  $f_\ell$  can be determined, such that the vector  $\mathbf{F}_{SRP}$  is aligned with the asteroid-mirror direction (see Fig. 45, or Fig. 8 on pg. 18). The angle  $\beta$  also represents the attitude angle of the mirror reference frame with respect to the Hill reference frame centred in the asteroid  $\mathcal{A}$ , considering that all the solar rays are parallel to the Sun-Asteroid vector.

Figure 46 illustrates the angular misalignment between the force vector due to the solar pressure, and the spacecraft-asteroid direction (ideally, they should be in-line). The angle  $\beta$  is determined by the direction of the incoming light impacting on the mirror, while  $\Delta\beta$  is the angle between the incoming light and the direction of the focal point of the mirror (see Fig. 45). The direction of the focal point identifies the pointing direction of the beam, which should be in the direction of the asteroid.

By setting  $\beta = \pi/2$ , it can be seen that the only artificial equilibrium points are along the Sun-asteroid direction. In this case however, the mirror would be in shadow

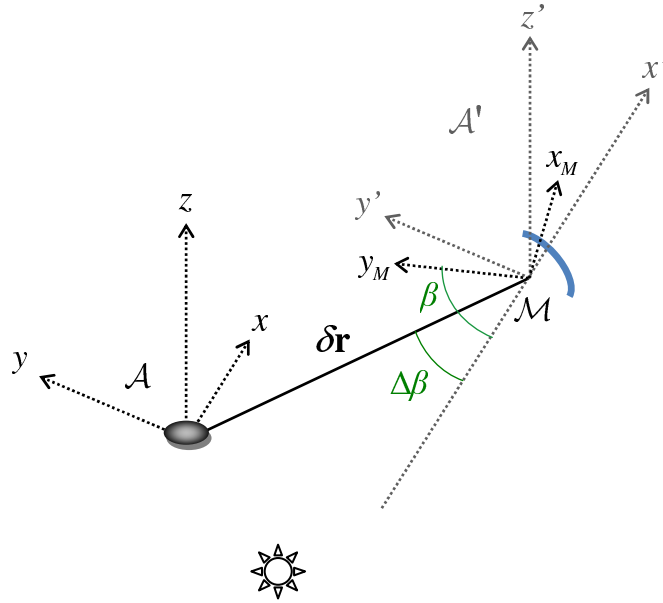


Figure 45: Definition of mirror-centric relative reference frame  $\mathcal{M}$ . The reference frame  $\mathcal{A}'$  is the translated from the barycenter of the asteroid to that of the mirror, with  $\mathcal{A}' \parallel \mathcal{A}$ .

and therefore no equilibrium points can exist along that direction. For higher values of  $\beta$ , equilibrium points can exist at higher angular distances from the radial direction.

For example, for  $\beta = 139^\circ$  the mirror can be placed at  $\delta \mathbf{r} = [1.3699, 0.48225, 0]$  km, which is about  $20^\circ$  from the radial direction; Fig. 47 shows the level of acceleration acting on the spacecraft. Only one quadrant of the Hill frame is shown here:  $\{+x, -y\}$ , since the solutions in the  $\{+x, +y\}$  quadrant are symmetric. There are no solutions in the other two quadrants as in the  $-x$  direction, the back of the mirror would be blocking the sunlight.

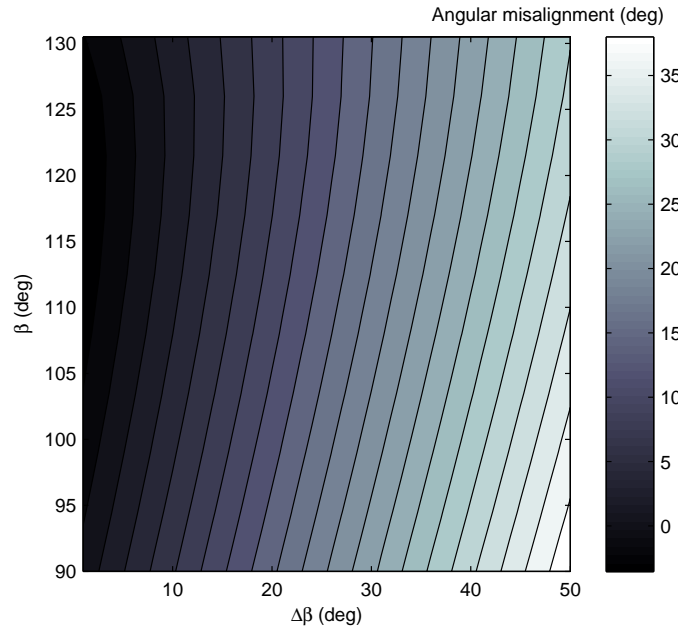
This artificial equilibrium point offers a good location for projecting the light of the Sun on the side of the asteroid along the  $y$  direction, and away from the plume of gases. Assuming that the optical system can produce a collimated light beam with negligible divergence, and that the beam is projected at the intersection of the surface of the asteroid with the  $y$ -axis, then the two extreme points of the beam which intersect the surface of the asteroid can be calculated. At this intersection, the spot size can be easily computed given the beam size and the elevation over the  $y$ -axis.

Figure 48 shows, for a beam size between 0.5 and 1 m in diameter, the increase in spot size due to an elevation of  $70^\circ$  along the  $y$ -axis and  $20^\circ$  from the radial  $x$ -axis is still limited.

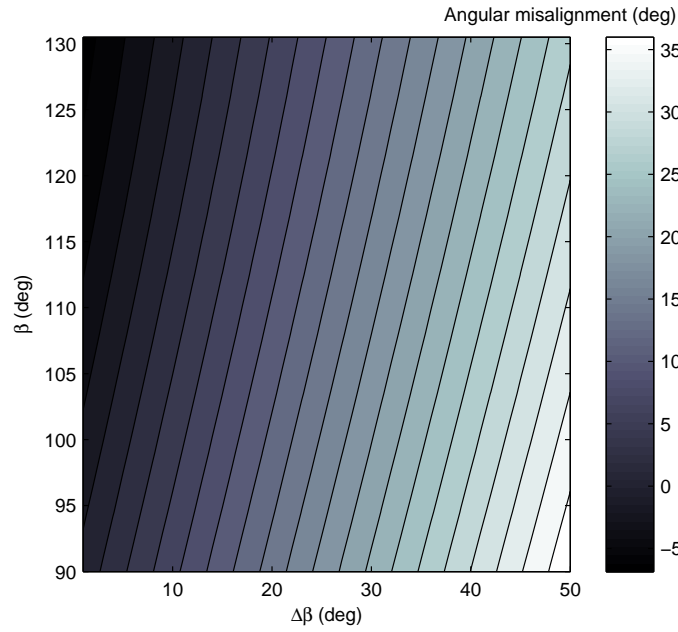
Figure 49 shows the variation of the position of the AEPs for various mirror sizes (given here by the total reflective surface area due to the irregular shape of the mirror surface).

It should be noted that due to the movement of the asteroid along the orbit, the AEPs are not at a single, fixed position since the modulus of the solar force varies with the inverse of the square of the distance from the Sun.

These results identify AEPs in the case of a perfectly spherical asteroid only. The actual shape of Apophis however, as well as most other asteroids, cannot be consid-



(a) Angular misalignment, for a focal distance equal to  $1L$ ,  $y_M \in [-1, 1]$  and  $x_{M_0} = -1$ .



(b) Angular misalignment, for a focal distance equal to  $5L$ ,  $y_M \in [-2, 2]$  and  $x_{M_0} = -4.5$ .

Figure 46: Angular misalignment between the position vector  $\delta \mathbf{r}$  and the direction of net force due to solar pressure, where the focal point is given by  $[L \cos(\beta - \Delta\beta), L \sin(\beta - \Delta\beta)]$  where  $L$  is the projection of the mirror shape onto the  $y^M$  axis.

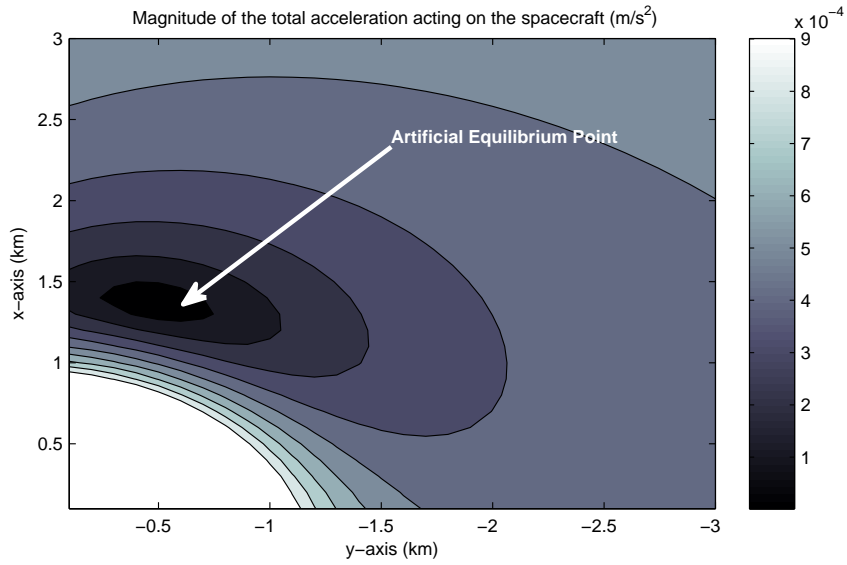


Figure 47: Example of AEP at 20° from the radial direction.

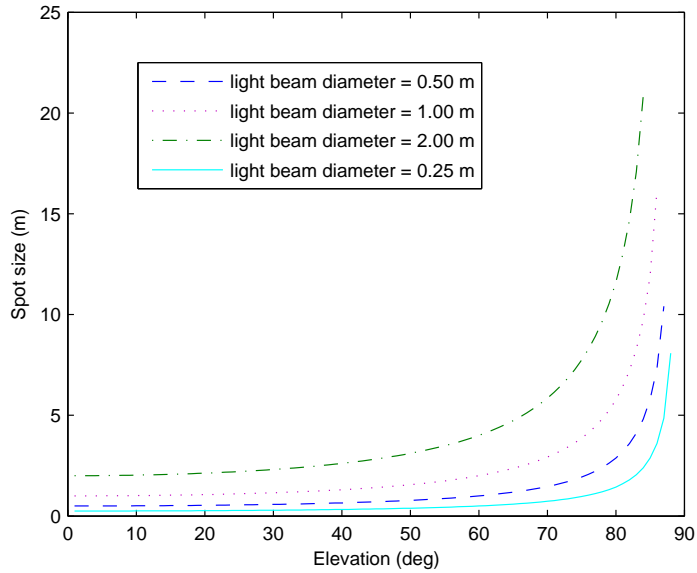


Figure 48: Increase in the spot size as a function of the elevation above the  $y$  axis.

ered spherical. Consistent with studies by other authors [Hu and Scheeres, 2002], the asteroid was modelled as an ellipsoid with semi-axes  $a_1$ ,  $b_1$  and  $c_1$  (see Table 13 and Fig. 24). The smallest semi-axis  $c_1$  is assumed to be along the  $z$ -axis of the asteroid Hill frame  $\mathcal{A}$  with the asteroid is rotating around the  $z$ -axis with angular velocity  $w_A$ .

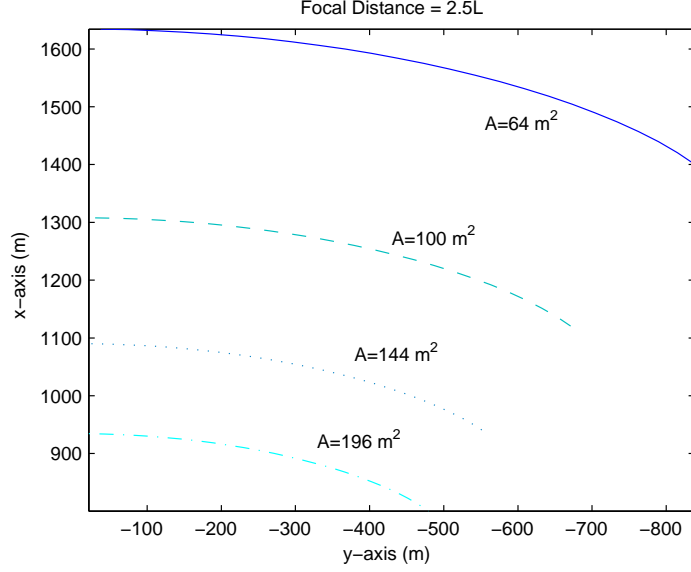


Figure 49: Artificial equilibrium points for different mirror sizes.

The gravity field of the asteroid can be expressed as the sum of a spherical field plus a second-degree and second-order field [Hu and Scheeres, 2002; Rossi et al., 1999],

$$U_{20+22} = \frac{\mu_A}{\delta r^3} \left( C_{20} \left( 1 - \frac{3}{2} \cos^2 \gamma \right) + 3C_{22} \cos^2 \gamma \cos 2\kappa \right) \quad (3.51)$$

where the harmonic coefficients  $C_{20}$  and  $C_{22}$  can be expressed as a function of the semi-axes,

$$C_{20} = -\frac{1}{10}(2c_1^2 - a_1^2 - b_1^2) \quad (3.52a)$$

$$C_{22} = \frac{1}{20}(a_1^2 - b_1^2) \quad (3.52b)$$

where  $\kappa$  is defined as,

$$\kappa = \arctan\left(\frac{y}{x}\right) + w_A t$$

and  $\gamma = 0$  since only the in-plane motion is considered.

The equations for the orbital dynamics of the spacecraft can therefore be expressed as,

$$2\dot{v}\left(-y\frac{\dot{r}_A}{r_A}\right) + x\dot{v}^2 + \frac{\mu_\odot}{r_A^2} - \frac{\mu_\odot}{r_{sc}^3}(r_A + x) - \frac{\mu_A}{\delta r^3}x + \frac{F_{s_x}(x, y, z, \beta, f_\ell)}{m_{sc}} + \frac{\partial U_{20+22}}{\partial x} = 0 \quad (3.53a)$$

$$-2\dot{v}\left(-x\frac{\dot{r}_A}{r_A}\right) + y\dot{v}^2 - \frac{\mu_\odot}{r_{sc}^3}y - \frac{\mu_A}{\delta r^3}y + \frac{F_{s_y}(x, y, z, \beta, f_\ell)}{m_{sc}} + \frac{\partial U_{20+22}}{\partial y} = 0 \quad (3.53b)$$

$$-\frac{\mu_\odot}{r_{sc}^3}z - \frac{\mu_A}{\delta r^3}z + \frac{F_{s_z}(x, y, z, \beta, f_\ell)}{m_{sc}} + \frac{\partial U_{20+22}}{\partial z} = 0 \quad (3.53c)$$

Note that even in this case (3.53c) is satisfied for  $z = 0$ . If the actual shape of the asteroid is considered, the AEP position is no longer moving along a rectilinear line but is now spiralling around the line, as shown in Fig. 50.

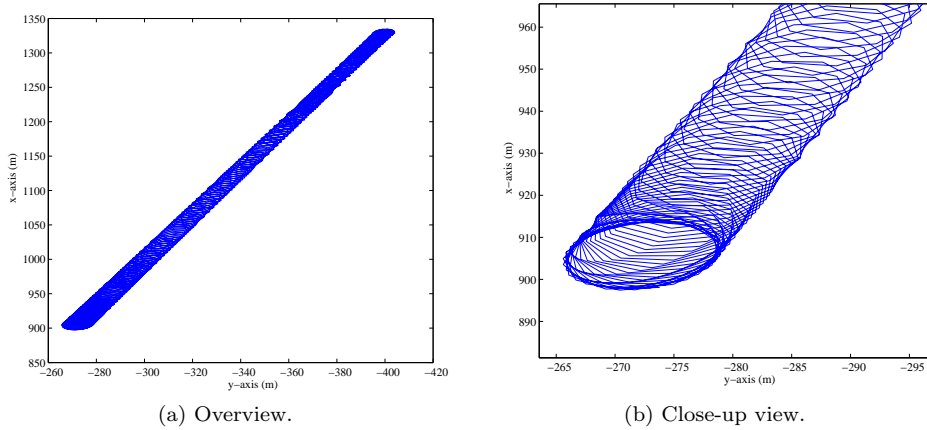


Figure 50: Variation of the equilibrium points with the true anomaly for a mirror of surface area  $A_M = 196 \text{ m}^2$ , and using an ellipsoidal model for the asteroid.

### 3.4.1 AEP in three dimensional space

The initial analysis considered a two dimensional motion with a high concentration ratio, or short focal distance and small mirror size. As a consequence, the elevation angle from the  $y$ -axis and distance from the centre of the asteroid, were limited. In fact at low elevation angles, equilibrium points may exist only for high solar aspect angles. However, for short focal distances, high curvature of the mirror and high solar aspect angles, the edges of the mirror were shadowing part of the mirror surface.

If the direct imaging concept is used, then the focal point is set equal to the position of the asteroid, causing the mirror shape to be almost flat. This removes the limitation on the elevation angle and on the solar aspect angle. Furthermore, an increase in the surface area implies a higher solar pressure and therefore a demand for a closer positioning of the mirror with respect to the asteroid.

The distance from the asteroid can be determined for different surface areas and different spacecraft masses by integrating,

$$dF = \frac{\mu_A}{\delta r^2} - P_r \sigma_M \frac{A_M}{m_{sc}} = 0 \quad (3.54)$$

where  $P_r$  is the solar pressure at a distance  $r_{sc}$  from the Sun given by,

$$P_r = \frac{S_0}{c} \left( \frac{r_{AU}}{r_{sc}} \right)^2 = P_0 \left( \frac{r_{AU}}{r_{sc}} \right)^2 \quad (3.55)$$

and  $S_0$  is the solar flux,  $c$  is the speed of light,  $\mu_A$  is given in Table 13,  $\sigma_M$  is the coefficient of reflectivity of the mirror,  $A_M$  is the perpendicular surface area, and  $r_{sc}$  and  $r_{AU}$  are the distance between the Sun and spacecraft, and the Sun and the Earth (1 AU) respectively.

For a distance of  $r_{sc} = 1 \text{ AU}$ , (3.54) gives the curves in Figs. 51a and 51b for a spacecraft mass of 1000 kg and 2000 kg respectively, where the curve labelled with  $r - Sp$  shows the line of equilibrium between the gravity attraction and solar pressure for each distance and surface area. On the same graph, the curves were plotted at constant concentration factors in the range [20, 200]. The two plots shows that for

a low concentration factor the surface area of the mirror is small and therefore the distance from the asteroid can be high. On the other hand, for high concentration factors the surface area of the mirror is high and the distance from the asteroid must be low to have a balance between gravity and solar pressure.

The situation works concurrently, for a shorter distance from the asteroid would imply little space to place multiple mirrors while larger distances would allow for multiple spacecraft. Conversely, a larger distance implies bigger mirrors. As a consequence, with a constant concentration factor, the number of spacecraft that can be placed on the surface of a sphere centred on the asteroid is linear depending on the distance from the asteroid. For example, a concentration factor of 2000 and an arc of  $60^\circ$  on each side of the  $y$ - $z$  plane, would accommodate 5 spacecraft, each with an edge length of 288 m (assuming a square shape). If the concentration factor is reduced to 100, then it is possible to accommodate 22 spacecraft, each with an edge length of 64 m.

The distance from the asteroid is also limited by the size of the asteroid, the extension of the plume and the shadow projected by the asteroid. In Fig. 51, moving away from the boundary line where the forces are balanced (i.e.  $F_{srp} = F_{grav}$ ) along a curve with constant concentration factor, the distance from the asteroid increases causing the solar pressure to dominate the gravitational attraction. An alternative approach would be to compensate for the unbalanced force with a low thrust propulsion system.

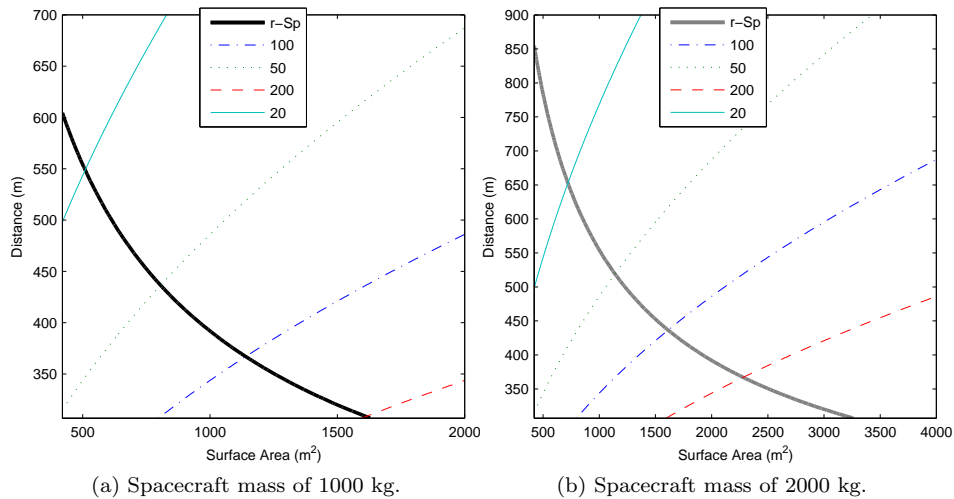


Figure 51: Balance between solar pressure and gravity forces for different concentration ratios, where  $r$ - $Sp$  denotes the line where the two forces are in balance,  $\Sigma F = 0$ .

Figure 52 shows the strategy in the two dimensional case (i.e.  $x$ - $y$  plane only). Assuming an elevation of  $60^\circ$ , the plume can flow into a ‘cone’ with an angular extension of up to  $120^\circ$ . Higher elevations are limited by the shadow projected by the asteroid. Furthermore the plume partially shadows the mirrors, which limits the maximum number of spacecraft. Note that the spacecraft can either lead or lag the asteroid (as in Fig. 52), but not both. The strategy in Fig. 52 is based on the assumption that thrusting along the  $y$ -axis is optimal for this deflection method; see Colombo et al. (2009); Vasile et al. (2009b); Song et al. (2007) for further reference on the optimality

of deflection methods. Thrusting along the  $x$ -axis would solve a number of problems and would allow placing the spacecraft along both the positive and negative  $y$  axis. By comparison, thrusting in the  $x$  direction is suboptimal for long warning times [Colombo et al., 2009; Song et al., 2007] and requires a higher level of thrust.

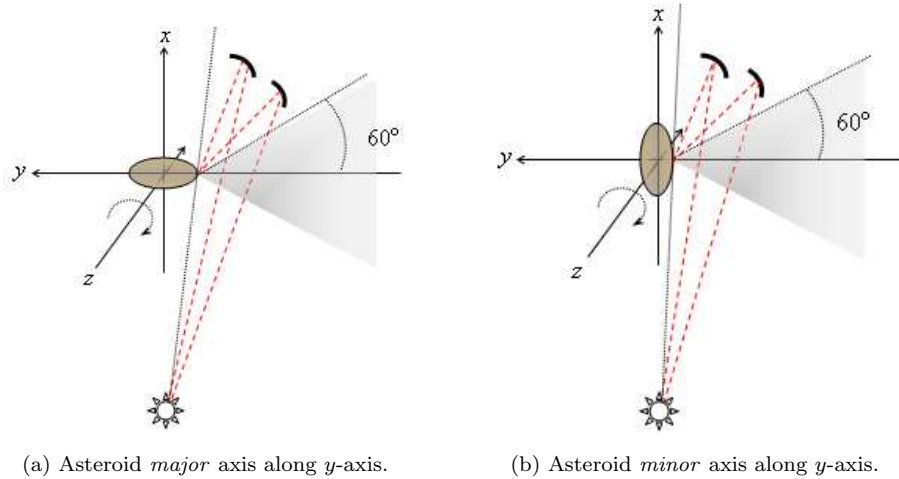


Figure 52: Spacecraft configuration with respect to the asteroid.

Figure 53 instead shows the strategy in the three dimensional case. The spacecraft are clear of the plume and can be placed on both sides (along the  $z$  axis) at any elevation angle outside the shadow region produced by the asteroid. High elevation angles would lead to a elongation of the spot area on the surface of the asteroid which, would reduce the power density, albeit perhaps by only a small percent. This would be a consideration to account for in further work on this topic.

The other interesting aspect is that the concentration factor is proportional to the inverse of the square of the distance from the Sun, therefore as the spacecraft moves toward the Sun, the power collected increases and the concentration factor decreases, while moving away from the Sun the concentration factor increases and the power of the Sun light decreases. The product of the two remains constant therefore, even if the curvature of the mirror is altered, the power density on the surface of the asteroid remains constant.

The approach used to design the mirror in three dimensions is similar to the one used in two dimensions. A local mirror reference frame  $\mathcal{M}$  is defined (see Fig. 54), with the position of the light source given by  $(x_{\odot}, y_{\odot}, z_{\odot})$  and the focal point,  $(x_f, y_f, z_f)$ . For each point  $(x, y, z)$ , the direction of the normal vector  $\hat{\mathbf{n}}$  is defined such that a ray coming from the Sun is reflected onto the focal point. For each surface element, the magnitude of the solar force in the mirror reference frame  $F_M$  is given by,

$$\mathbf{F}_M = 2\sigma_M P_r \int_{A_M} \cos^2 \phi \hat{\mathbf{n}} dA \quad (3.56)$$

where  $\phi$  is the angle of reflection, and  $P_r$  is the solar pressure at a distance  $r_{\odot/sc}$  from the Sun. The force vector in the mirror reference frame  $\mathcal{M}$  is then transformed to the local spacecraft reference frame  $\mathcal{S}$  through the rotation matrix  $\mathbf{Q}(\mathbf{q})$ ,

$$\mathbf{F}_{sc} = \mathbf{Q}(\mathbf{q})\mathbf{F}_M \quad (3.57)$$

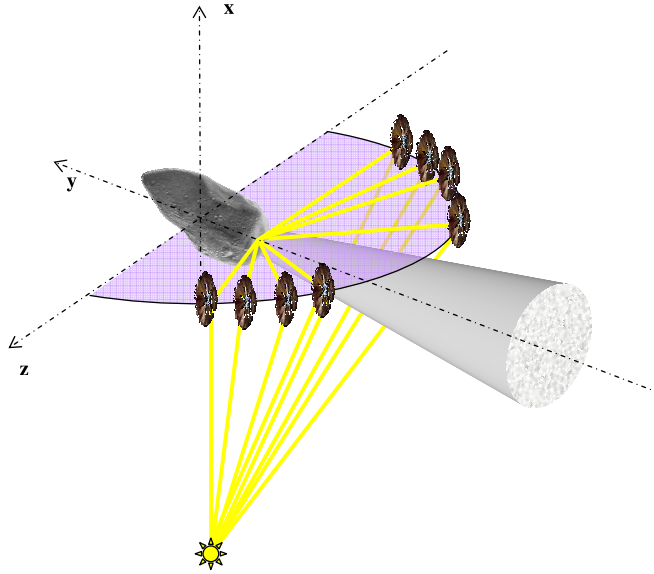


Figure 53: Conceptual spacecraft configuration using AEPs in three dimensions.

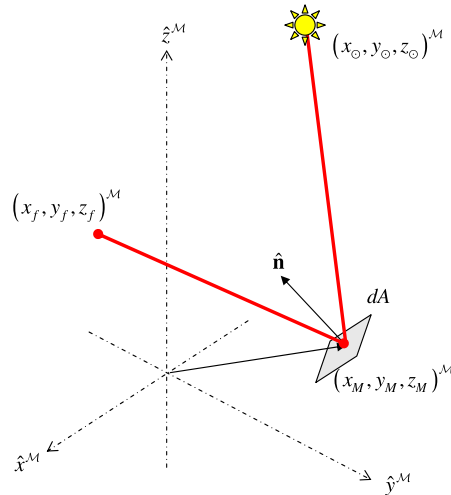


Figure 54: Reference frame for the three dimensional mirror design.

For each position of the mirror in the spacecraft-centric Hill reference frame  $\mathcal{S}$ , the goal is to find the correct attitude and shape of the mirror that allows for an equilibrium state between the gravity force and solar pressure force.

Figure 55 shows two possible mirror shapes and positions; showing both the incoming and reflected rays as a result of the surface shape. For both figures,  $\beta = 130^\circ$  and  $\Delta\beta = 20^\circ$ , with the focal point located at  $[\sin \beta, \cos(\frac{\pi}{2} - \Delta\beta) \cos \beta, \sin(\frac{\pi}{2} - \Delta\beta) \cos \beta]$ .

Regions of equilibrium exist also in the 3D case, but for viable values of the concentration factor for direct imaging, they are too close to the asteroid. A possible solution would be to move away from the equilibrium positions and use a low-thrust system to compensate for the solar pressure (the dominant component in this case).

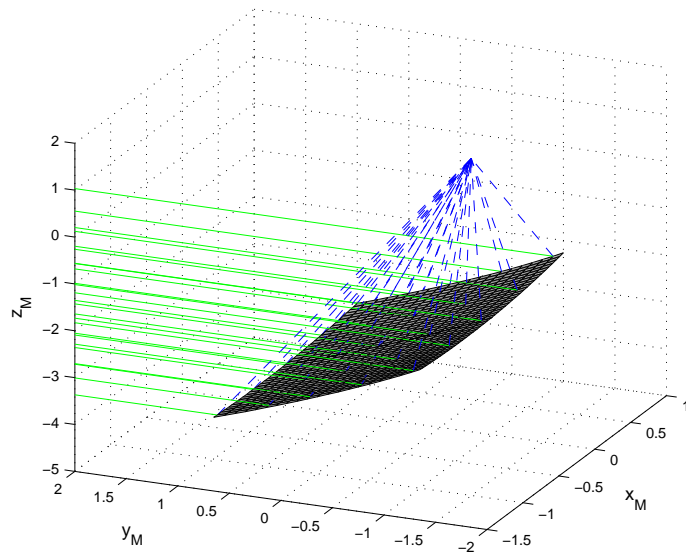
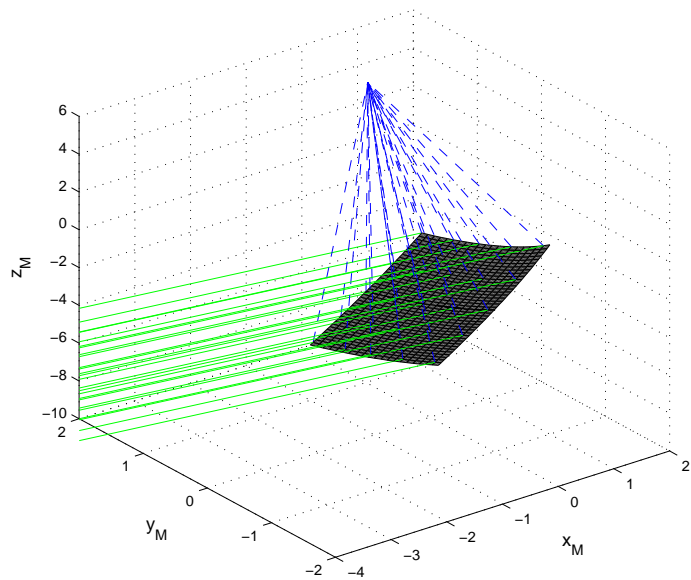
(a) Attitude,  $q = [0.75, 0.75, 0.75, 0.75]$ .(b) Attitude,  $q = [2, 1, 0, 1]$ .

Figure 55: Example of a single 3D mirror projecting the light of Sun onto a focal point. Green lines are the Sun rays, blue lines are the reflected rays. The mirror is represented in the mirror reference frame  $\mathcal{M}$ , with the axes in normalised units.

The other possibility is to use a solar pumped laser, similar to that in the fixed mirror design. If a solar pumped laser solution is adopted, then smaller mirrors can be used and the analysis of the 2D case is valid.

### 3.5 PERTURBATIONS

In the case of the two-body problem, as in the case of the funnel orbits, only the gravitational effect of the Sun was accounted for in the equations. However, there are many other forces that act on the spacecraft and affect the orbit. The two main sources are the pressure from the solar radiation on the surface of the spacecraft, and in particular on the large surface area of the primary mirror, and the gravitational effects from the asteroid. The two perturbations are modelled in the following section for the fixed mirror case.

#### 3.5.1 Solar radiation pressure

Solar radiation pressure (SRP) acts on every surface area exposed to either the Sun and/or the focused beam. For the fixed mirror configuration in Fig. 56, this includes: the primary reflector ( $M_1$ ), the secondary reflector ( $M_2$ ), the laser ( $L$ ), the directional mirror ( $M_3$ ), and the solar panels. The spacecraft body and radiators are both blocked by the primary mirror.

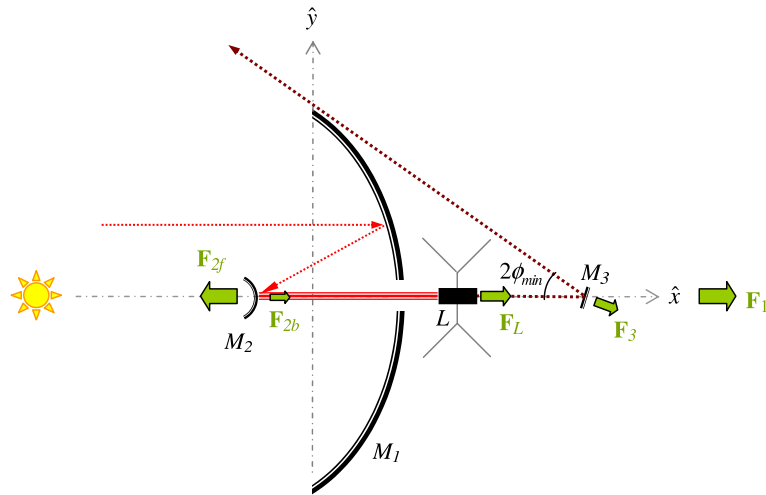


Figure 56: Vectors of solar radiation pressure on a fixed mirror configuration.

The force from the solar radiation pressure on the primary reflector is given by,

$$\mathbf{F}_1 = 2P_r A_{M_1} \sigma_{M_1} \cdot \hat{\mathbf{r}}_{\odot/sc} \quad (3.58)$$

where  $\sigma$  is the coefficient of reflectivity of the surface,  $A_{M_1}$  is the illuminated surface area perpendicular to the Sun (i.e. the area of the aperture), and  $P_r$  is the solar power at distance  $r_{sc}$  from the Sun, given in (3.55).

The secondary reflector is exposed to both direct sunlight (on the ‘back’ of the mirror), and the focused light from the primary reflector.

$$\mathbf{F}_2 = (2P_r \sigma_{M_2} A_{M_2} - F_1 \sigma_{M_2}) \cdot \hat{\mathbf{r}}_{\odot/sc} \quad (3.59)$$

In order to help balance the forces on the mirror, the coefficient of reflectivity on the back is the set the same as the front, meaning that both sides are equally reflective.

The focused beam from the second mirror is fed directly into the laser assembly,

$$\mathbf{F}_L = \left(\frac{1}{2} F_1 \sigma_{M_2}\right) \sigma_L \cdot \hat{\mathbf{r}}_{\odot/sc} \quad (3.60)$$

The output of the laser is then directed onto the asteroid by means of a small directional mirror,

$$\mathbf{F}_3 = \eta_L F_L \sigma_{M_4} \cos^2 \phi \cdot \hat{\mathbf{n}}_M \quad (3.61)$$

where  $\eta_L$  is the efficiency of the laser.

Lastly, the pressure on the solar panels powering the spacecraft must be accounted for,

$$\mathbf{F}_{sp} = P_r A_{sp} \sigma_{sp} \cdot \hat{\mathbf{r}}_{\odot/sc} \quad (3.62)$$

The total acceleration on the spacecraft due to SRP is then,

$$\mathbf{u}_{srp} = \frac{\mathbf{F}_1 + \mathbf{F}_2 + \mathbf{F}_L + \mathbf{F}_3 + \mathbf{F}_{sp}}{m_{sc}} \quad (3.63)$$

The equations for the solar pressure given in (3.58) – (3.62) can be rewritten in terms of the orbital elements of the asteroid, and the orbital element differences  $\delta \mathbf{k}$ . All the equations are relative to the  $\mathcal{S}$  Hill frame. Given,

$$\begin{aligned} \cos^2 \phi = \frac{1}{2\delta r} & \left( \delta r - r_A + r_{sc} \cos(\theta_A + \delta\theta) (\cos(-\delta\Omega) \cos \theta_A + \cos i_A \sin \delta\Omega \sin \theta_A) \right. \\ & + r_{sc} \left( \cos(i_A + \delta i) \cos \theta_A \sin \delta\Omega + (\cos i_A \cos(i_A + \delta i) \cos(-\delta\Omega) \right. \\ & \left. \left. + \sin i_A \sin(i_A + \delta i)) \sin \theta_A \right) \sin(\theta_A + \delta\theta) \right) \end{aligned} \quad (3.64)$$

where  $\phi$  is the angle of reflection from the optical axis of the mirror (normal to the surface), and  $\theta = \nu + \omega$  is the true latitude.

The unit vector  $\hat{\mathbf{n}}_M$  gives the direction of the net force due to the SRP on the directional mirror  $M_3$ ,

$$\hat{\mathbf{n}}_M = \frac{\mathbf{n}_M}{\|\mathbf{n}_M\|} \quad (3.65)$$

$$\mathbf{n}_M = \left[ \begin{array}{l} -r_A (\cos(\delta\theta - \theta) \sin \delta\Omega \sin i + \varpi \sin(\delta\theta - \theta)) \left( \sqrt{\frac{2\Gamma}{\delta r}} + 2(r_{sc} + r_A \varrho \cos \theta + r_A \zeta \sin \theta) \right) \\ r_A (\cos i \cos(\delta\theta - \theta) \cos \theta \sin \delta\Omega + \xi \cos \theta \sin(\delta\theta - \theta) - \varrho \sin \theta) \\ -\sqrt{\frac{\Gamma}{2\delta r}} (r_{sc} + r_A \varrho \cos \theta + r_A \zeta \sin \theta) \end{array} \right]^S \quad (3.66)$$

where  $\varpi$ ,  $\xi$ ,  $\varrho$ ,  $\zeta$  are defined in (3.20), and

$$\begin{aligned} \Gamma = \delta r + r_{sc} - r_A & \left( \cos \delta\Omega \cos(\delta\theta - \theta) \cos \theta \right. \\ & \left. + \cos(\delta i - i) \cos \theta \sin \delta\Omega \sin(\delta\theta - \theta) + \zeta \sin \theta \right) \end{aligned} \quad (3.67)$$

### 3.5.2 Third body effects

Since the effects of the asteroid's gravity field after a certain distance are relatively linear [Sanchez Cuartielles et al., 2007], and much less compared to those due the solar radiation pressure, the asteroid is treated, as a first approximation, as a point mass with  $\mu_A = 1.8016e-9 \text{ km}^3/\text{s}^2$ . The acceleration due to a third body is given by [Vallado, 2004],

$$\ddot{\mathbf{r}}_{\odot/sc} = -\frac{\mu_{\odot}\mathbf{r}_{\odot/sc}}{r_{\odot/sc}^3} + \mu_A \left( \frac{\delta\mathbf{r}}{\delta r^3} - \frac{\mathbf{r}_{\odot/A}}{r_{\odot/A}^3} \right) \quad (3.68)$$

assuming  $m_{\odot} \gg m_A \gg m_{sc}$ . Adding the perturbing acceleration due to the asteroid, the perturbing control vector becomes,

$$\mathbf{u}_{pert} = \begin{bmatrix} \frac{F_1 + F_2 + F_L + F_{sp}}{m_{sc}} + \frac{F_3}{m_{sc}}\hat{n}_x + \mu_A \left( \frac{\delta r_x}{|\delta r|^3} - \frac{r_{sc} + \delta r_x}{|r_A|^3} \right) \\ \frac{F_3}{m_{sc}}\hat{n}_y + \mu_A \left( \frac{\delta r_y}{|\delta r|^3} - \frac{\delta r_y}{|r_A|^3} \right) \\ \frac{F_3}{m_{sc}}\hat{n}_z + \mu_A \left( \frac{\delta r_z}{|\delta r|^3} - \frac{\delta r_z}{|r_A|^3} \right) \end{bmatrix}^S \quad (3.69)$$

Figures 57 – 60 show the forces acting on the spacecraft due to the solar radiation pressure and third body effects from Apophis. Formation orbit  $\delta\mathbf{k}_{5/1}$  from Table 17 was used as the representative case. The spacecraft mass was set to 2000 kg, for a 20 m diameter primary mirror with a 5 m focal length, a 1 m diameter secondary and tertiary mirrors, and solar arrays of dimensions  $8 \times 2$  m.

As expected, the SRP is dominant in the radial direction given that all the mirrors are positioned such that they directly face the Sun, with the force normal in the positive  $x$  direction. There is a small component in the  $y$ , and to an even lesser degree the out of plane  $z$  due to the directional mirror which is angled towards the asteroid. It is interesting to compare the difference in magnitude between Figs. 57c and 57d, which show the forces acting on either side of the directional mirror. The focused light exerts a force, in this case a factor of  $10^3$  greater than the pressure from the Sun. The oscillation in the SRP is due to the elliptical orbit, and shows the effect of even a relatively small eccentricity of 0.191 will change the force by 1.2 mN.

The perturbations introduced by the asteroid, modelled as a point source, is relative small compared to the SRP. It does not follow the same trend however, with the dominant direction being along the  $y$  axis. The gravitational force still contributes to the overall perturbations, as seen in Figure 60 along the  $y$  axis. Examining the effect on the orbital parameters in Fig. 61, only the semi-major axis is affected by any tangible amount. However, while the perturbations seem small, on the order of  $10^{-7}$  it is important to remember that the orbital differences that the control would need to maintain are on the same order of magnitude.

## 3.6 FUNNEL CONTROL

While the dynamical design of the artificial equilibrium points accounts for the additional perturbations, the funnel formation design does not. Instead, a control law is required to compensate not only for the solar pressure and third body effects, but also for the constantly changing orbit of the asteroid. The aim of the control law is to match the relative orbital parameters to those determined by the funnel orbits, using

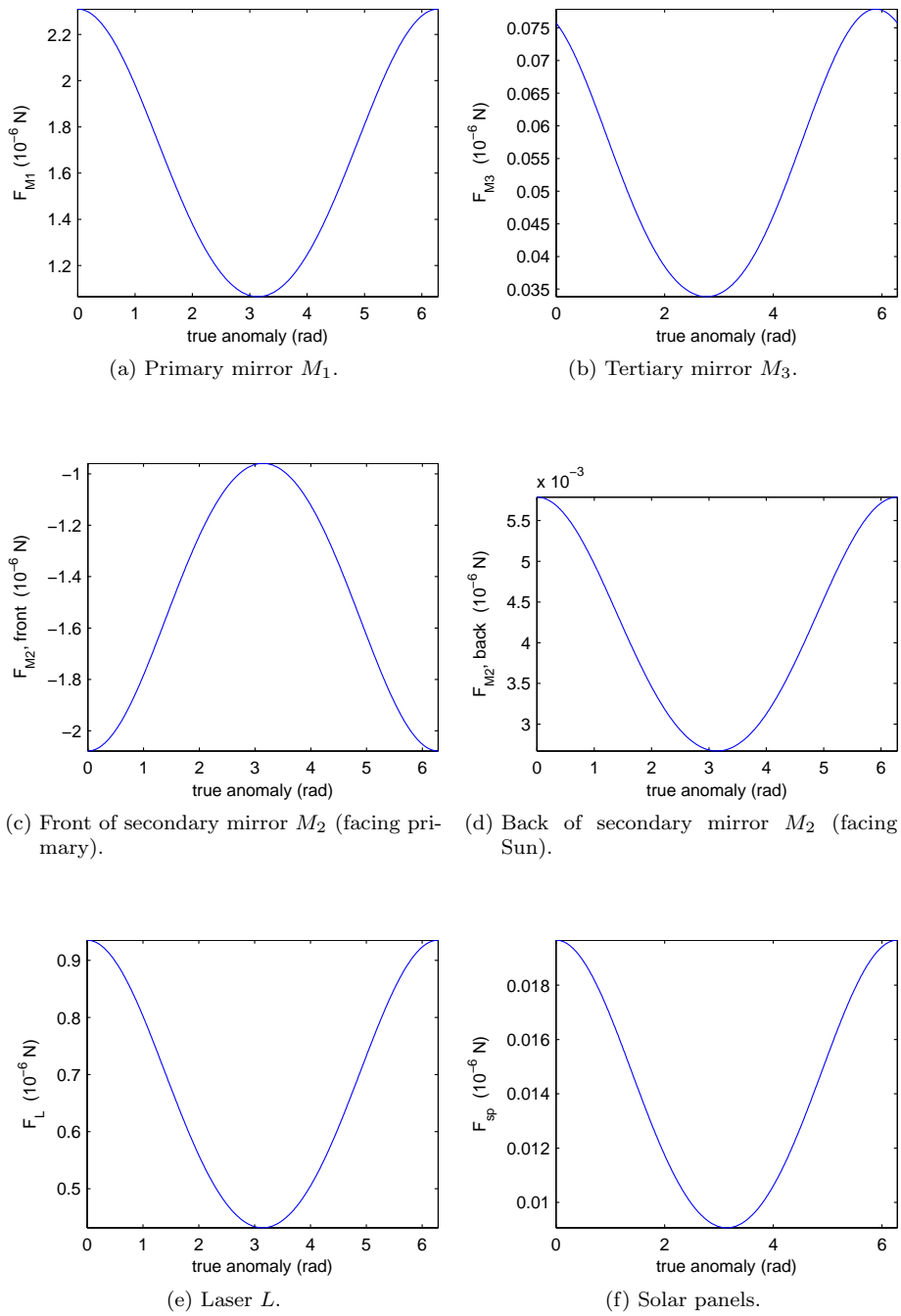
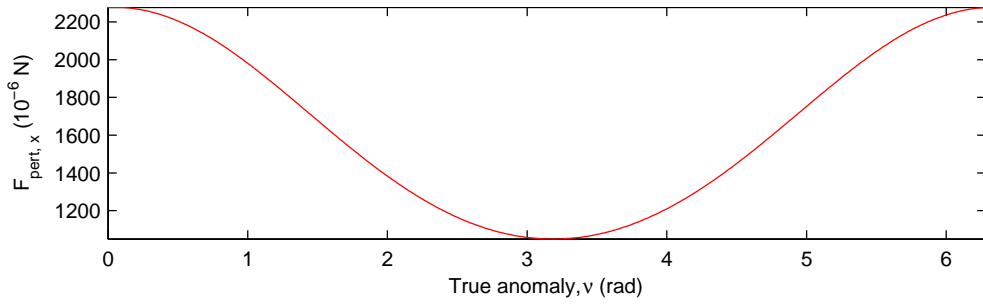
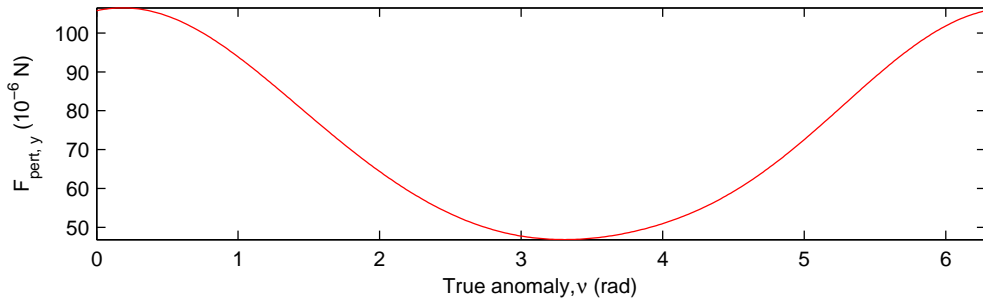


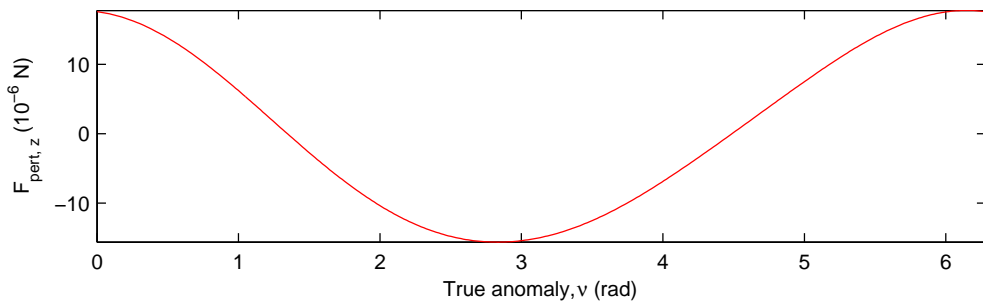
Figure 57: Force due to solar radiation pressure on the various surfaces of the spacecraft.



(a) Radial component.

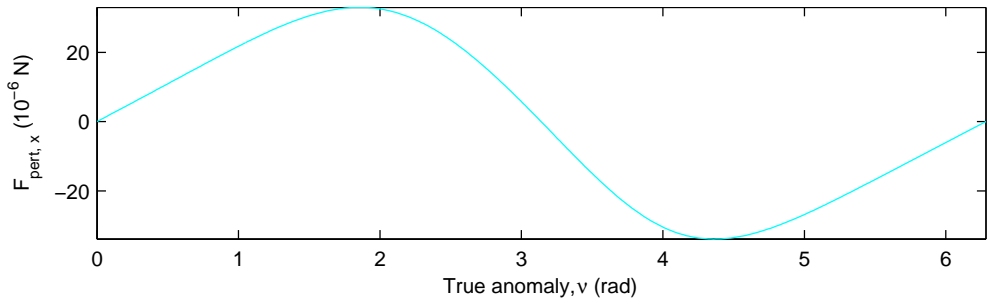


(b) Transverse component.

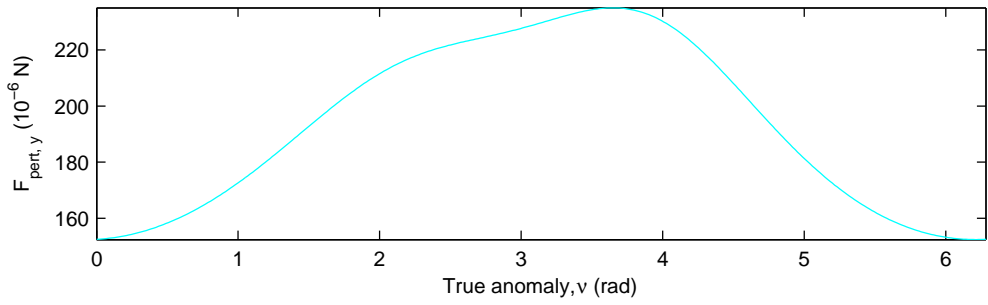


(c) Normal component.

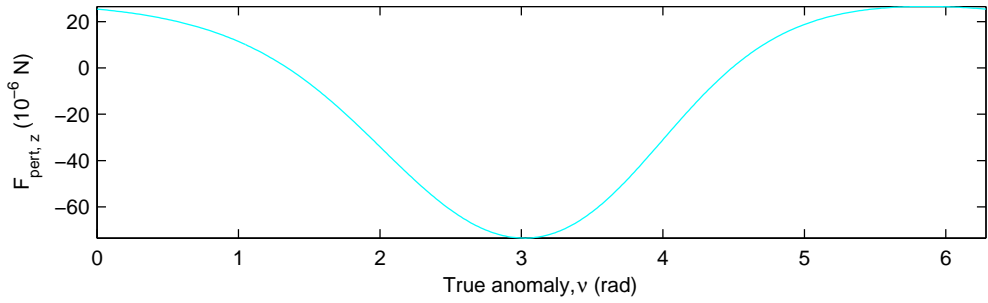
Figure 58: Total force due to solar radiation pressure.



(a) Radial component.

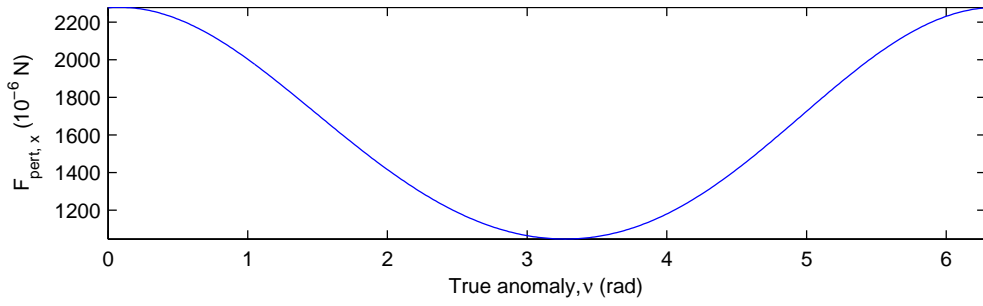


(b) Transverse component.

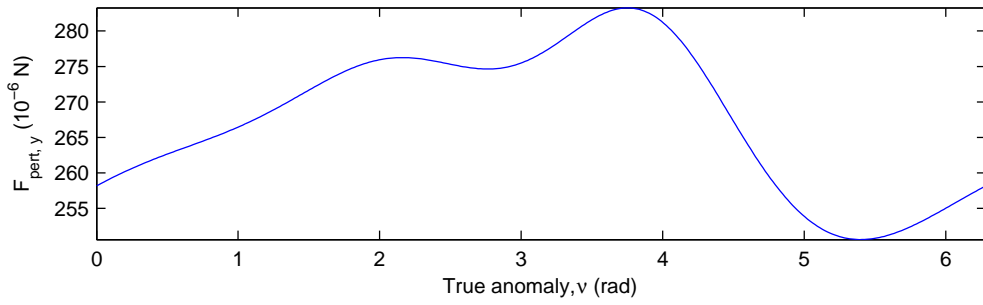


(c) Normal component.

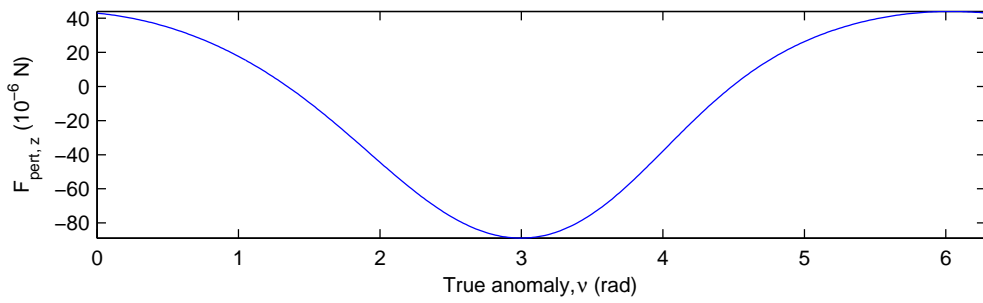
Figure 59: Force due to third body effects from the NEO.



(a) Radial component.



(b) Transverse component.



(c) Normal component.

Figure 60: Total perturbing force acting on the spacecraft.

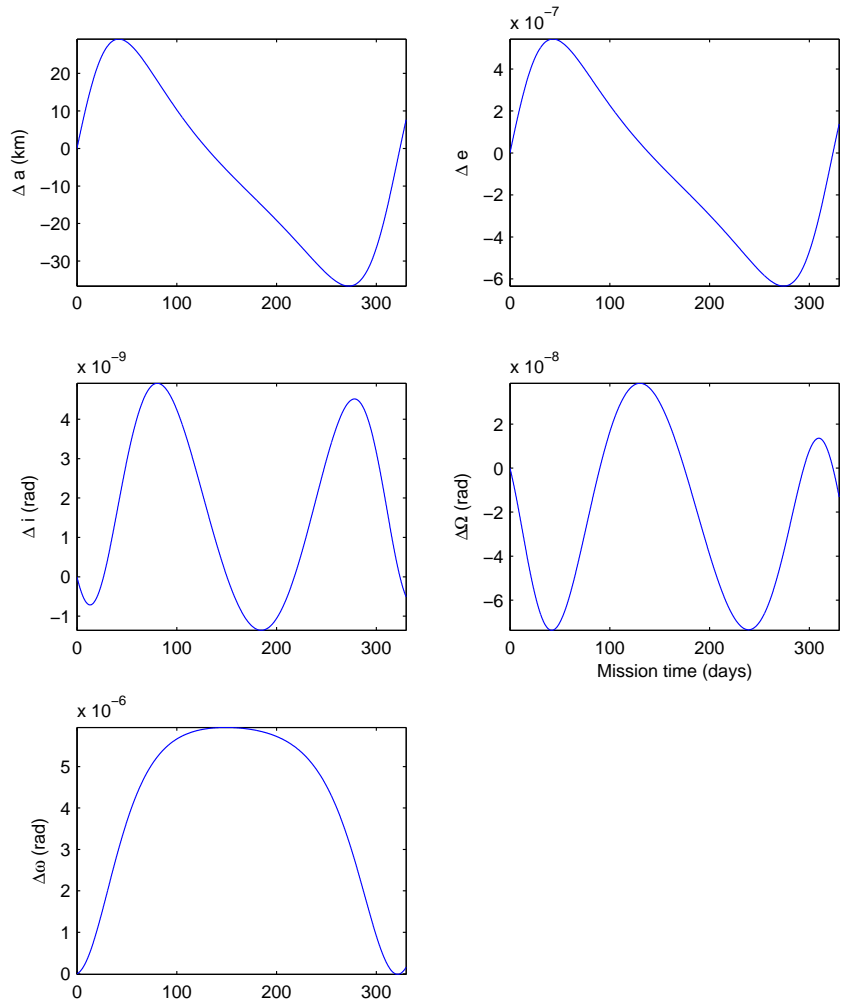


Figure 61: Effect of total perturbing acceleration on the spacecraft orbit parameters.

as feedback the measured position and velocity of the spacecraft relative to the NEO since these values are needed for the tracking and deviation the asteroid.

### 3.6.1 Proximity-quotient control law

The initial approach was to use the proximity-quotient, or  $Q$ -law, originally developed by Petropoulos (2003) for the restricted two-body problem. The  $Q$ -law is based on a Lyapunov feedback control law, and calculates the optimal in-plane and out-of-plane thrust angles  $(\alpha, \beta)$  based on the proximity to the target orbit (i.e. the difference in the static Keplerian parameters) and the current location of the spacecraft on the orbit (i.e. true anomaly). The thrust vector here is assumed to the net direction of thrust applied by the spacecraft, which is modelled here as a simple point mass. It is not the intent to delve into what or how the thrust would be applied.

Appendix C contains a detailed description and discussion of the work done on implementing  $Q$ -law, and a full listing of all the derivations and equations required.

The control law function is give by,

$$Q = \sum_{\delta \mathbf{k}} W_k \left( \frac{k_i - k_T}{\dot{k}(\alpha_{max}, \beta_{max}, \nu_{max})} \right)^2 \rightarrow \min(\dot{Q}) \quad (3.70)$$

where  $\dot{k}$  is given by the Gauss equations (3.28), setting the in-plane thrust angle  $\alpha = \alpha_{max}$ , the out-of-plane thrust angle  $\beta = \beta_{max}$ , and the orbital location  $\nu = \nu_{max}$  that give the maximum rate of change for each of the following elements:  $a, e, i, \Omega$  and  $\omega$ .

In this case, the control acceleration  $\mathbf{u}$  is given by,

$$u_r = \frac{\bar{\Gamma}}{m_{sc}} \sin \alpha \cos \beta \quad (3.71)$$

$$u_t = \frac{\bar{\Gamma}}{m_{sc}} \cos \alpha \cos \beta \quad (3.72)$$

$$u_h = \frac{\bar{\Gamma}}{m_{sc}} \sin \beta \quad (3.73)$$

where  $\bar{\Gamma}$  is the maximum thrust that can be applied to the spacecraft, which when divided by the spacecraft mass gives the applied acceleration (in order to feed into the Gauss equations). The  $Q$ -law is constructed assuming that the thrust level is either on, or off. No partial thrust can be applied, although since it can be turned on and off over very short intervals of time, this can be somewhat approximated.

The  $Q$ -law was developed to provide a first-guess solution for transfers between orbits, not point-to-point, so the mean anomaly  $M$  (or true anomaly  $\nu$ ) was left as a free variable. The equations were updated to include the target  $M$  term, and account for SRP and third body effects in the Gauss equations  $\dot{\mathbf{k}}$  required for this test case [Maddock and Vasile, 2008b].

### 3.6.2 Orbital maintenance control law

There were a number of issues that arose when using the adapted  $Q$ -law for the orbital maintenance of the funnel orbits. The first was due to the high degree of accuracy needed to maintain the funnel orbits. The difference in Keplerian orbital elements between the NEO and the spacecraft are on the order of  $10^{-7}$ , and need to remain

constant even as the NEO deviates. This resulted in a lot of ‘chatter’ (over-shooting) around the target orbital elements, due to strong dependance on the time step  $\delta t$  and the magnitude of the control (which employed on-off shooting). Even at very small time steps, the magnitude of the over-shooting was too large for the system requirements. The effects of the perturbations are also relatively large, on the scale of mN in the radial direction (see Fig. 61) and need to be compensated on a continuous basis.

An alternative approach was therefore developed to deal with these mission-specific limitations. The first was to switch from minimising only with respect to the thrust angles, to minimising with respect to the components  $[u_r, u_t, u_h]$ , which has the benefit of finding the optimal magnitude for the thrust, as well as the required angles. A new  $Q^*$  function was created,

$$Q^* = \sum_{j=1}^6 W_j \left( \Delta k_{T,j} - \int_0^{\delta t} \frac{dk_j}{dt} dt \right)^2 \quad (3.74)$$

where  $\Delta \mathbf{k}_T = (\mathbf{k}_i - \mathbf{k}_T)$  is the desired variation of the orbital parameters in the time interval  $\delta t$ . The function  $Q^*$  is then minimised with respect to the control components  $[u_r, u_t, u_h]$  every  $\delta t$  units of time.

#### Least-squares solution

It can be assumed that over very small time steps, the rate of change of orbital parameters given by the Gauss equations is constant. If so, then the control function can be directly solved by,

$$\sum W_j \left( \Delta k_{T,j} - \frac{dk_j}{dt} \delta t \right)^2 \quad (3.75)$$

Inherently, if the desired change in the  $j^{\text{th}}$  element ( $k_{i,j} - k_{T,j}$ ) is negative, then the rate of change is positive, and vice versa. As such, the control equation will always have a single minimum. Therefore there is no need to minimise the time derivative.

The solution for the control vector  $\mathbf{u}_c$  is found by using an ordinary least squares fitting to the linear systems of equations,  $\mathbf{A} \mathbf{u}_c = \mathbf{b}$ . In our case, the matrix  $\mathbf{A}$  is set equal to the Gauss equations,

$$\frac{d\mathbf{k}}{dt} = \mathbf{A} \cdot \mathbf{u}_c \quad (3.76)$$

$$\begin{bmatrix} \dot{a} \\ \dot{e} \\ \dot{i} \\ \dot{\Omega} \\ \dot{\omega} \\ \dot{M}^* \end{bmatrix} = \begin{bmatrix} \frac{2a^2 e \sin \nu}{h} & \frac{2a^2 p}{hr} & 0 \\ \frac{p \sin \nu}{h} & \frac{(p+r) \cos \nu + re}{h} & 0 \\ 0 & 0 & \frac{r \cos \theta}{h} \\ 0 & 0 & \frac{r \sin \theta}{h \sin i} \\ -\frac{p \cos \nu}{he} & \frac{(p+r) \sin \nu}{he} & -\frac{r \sin \theta \cos i}{h \sin i} \\ \frac{p \cos \nu - 2re}{e\sqrt{a\mu}} & -\frac{(p+r) \sin \nu}{e\sqrt{a\mu}} & 0 \end{bmatrix} \begin{bmatrix} u_r \\ u_t \\ u_h \end{bmatrix} \quad (3.77)$$

The actual Gauss equation for  $dM/dt$  also includes a term for the mean motion  $n$  to account for the rotation around the Sun. In this case however, the control does not need to compensate for the nominal motion of the orbit, just those induced by the perturbations and deviation of the asteroid. The mean motion is added to  $M^*$

after each iteration of the simulation control loop, where  $M_i = M^* + n_{sc}\delta t$  (since the nominal rate of the change of the mean anomaly is linear).

The matrix  $\mathbf{b}$  is solved by,

$$\mathbf{b} = \frac{\mathbf{k}_T - \mathbf{k}_i}{\delta t} - \mathbf{A}(\mathbf{u}_{pert}) \quad (3.78)$$

Again, this is equivalent to minimising the quadratic function

$$\sum W_j(\Delta k_j - \Delta k_{T,j})^2$$

where  $\Delta k_j$  is the change of the  $j^{\text{th}}$  orbital element over time  $\delta t$ , and  $\Delta k_{T,j}$  is the desired change.

#### *Integration approach*

An integration approach can also be used with the same control function  $Q^*$  in (3.74) which numerically integrates the Gauss equations to determine  $\Delta k_{i,j}$ .

$$\Delta k_{i,j} = \int_0^{\delta t} \frac{dk_j}{dt} dt \quad (3.79)$$

The least-squares approach provides a computationally faster solution (for the same time step) but is less accurate, especially over larger time steps. To see the effect of the linear assumption, Fig. 62 shows the variation of the orbital elements of Apophis over one full orbit. The control acceleration was set to  $10^{-9}$  km/s<sup>2</sup> in all directions (equivalent to  $u = 1.732e-9$  km/s<sup>2</sup>,  $\alpha = \frac{\pi}{4}$  rad and  $\beta = \arctan(\cos \alpha) \approx 0.6155$  rad).

#### *Simulation results*

The algorithm loop for computing the control is as follow,

STEP 1: Identify starting conditions for spacecraft: the number of spacecraft  $n_{sc}$ , the initial state vector  $\delta \mathbf{k}_0$ , the mass-in-orbit of each spacecraft  $m_{sc}$  kg, the aperture diameter  $d_M$ , depth and illuminated surface area for the parabolic mirror  $A_M$  and spot on the NEO  $A_{spot}$ .

STEP 2: Identify starting conditions for NEO Apophis: time and true anomaly at calculated MOID,  $t_{MOID}$  and  $\nu_{MOID}$ , time when the spacecraft starts the deviation action (i.e. solar sublimation)  $t_0$ , target deviation distance  $\Delta r_{devT}$ , initial mass of asteroid  $m_A$  kg, and initial orbital parameters  $k_{A_0}$ .

STEP 3: Initial target elements are set equal to initial starting position,  $\mathbf{k}_T = \mathbf{k}_i = \mathbf{k}_0$ .

STEP 4: Determine optimal control vector  $\mathbf{u}_c = [u_{c_r}, u_{c_t}, u_{c_h}]$  solving the linear system of equations  $\mathbf{A}\mathbf{u}_c = \mathbf{b}$  given in (3.76)–(3.78) by the method of ordinary least squares fitting, given:  $\mathbf{k}_i, \mathbf{k}_T, \delta \mathbf{k}, m_{A_i}$ .

STEP 5: Propagate spacecraft forward by time step  $\delta t$  using Gauss equations with input  $\mathbf{u} = \mathbf{u}_c + \mathbf{u}_{pert}$ .

STEP 6: Update  $\mathbf{k}_i$

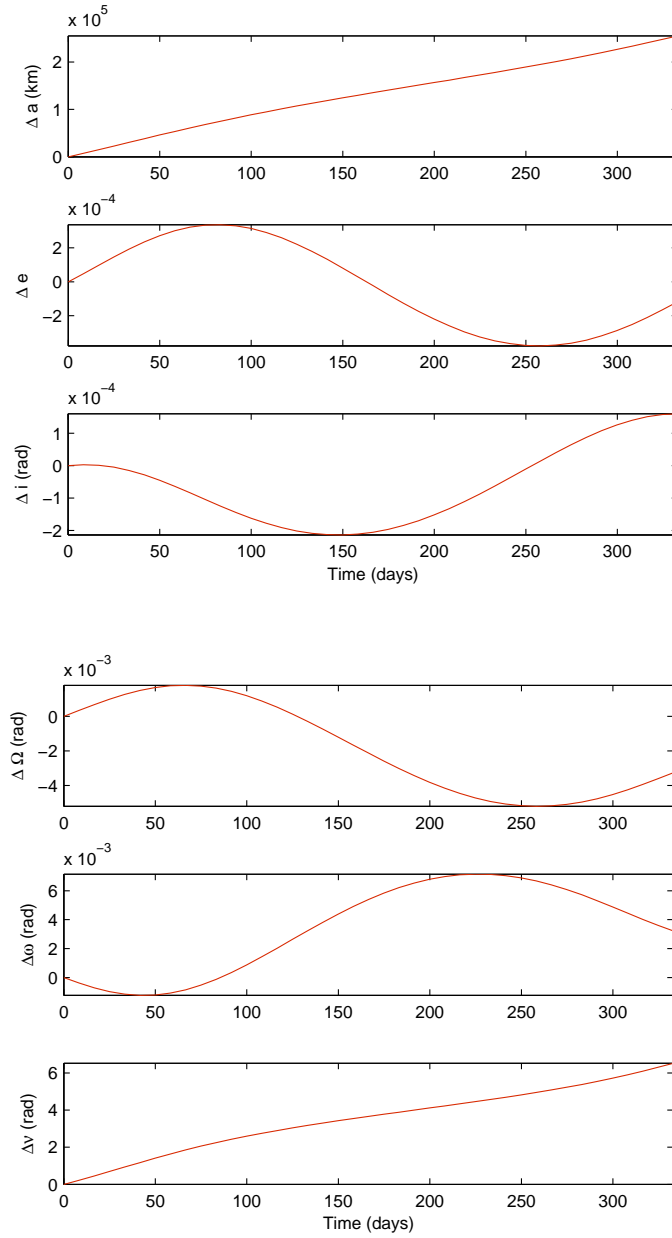


Figure 62: Variation in the orbital elements over one orbit of Apophis.

STEP 7: Propagate asteroid forward by time step  $\delta t$  using Gauss equations with input  $\mathbf{u} = \mathbf{u}_{dev}$ .

STEP 8: Update  $\mathbf{k}_A$ ,  $m_{A_i}$  and  $\delta\mathbf{k}_i = \mathbf{k}_i - \mathbf{k}_A$ .

STEP 9: Update target vector to reflect the deviated orbit of Apophis,  $\mathbf{k}_T = \mathbf{k}_A + \delta\mathbf{k}_0$ .

STEP 10: Calculate achieved deviation distance  $\Delta r_A$ . If  $\Delta r_A \geq \Delta r_{devT}$ , then stop; otherwise repeat from Step 4.

Simulations were run using both the least squares and integration method control loop, each with time steps  $\delta t = [1, 10, 60]$  s, using the five test orbits chosen out of the set of Pareto optimal funnel solutions (see Table 17 and Fig. 63). A 20 spacecraft formation was used ( $n_{sc} = 20$ ), however all the spacecraft were assigned the same set of orbital elements  $\delta\mathbf{k}$ , meaning they were in essence co-located. While this is an unrealistic assumption in practice, the purpose of this simulation was to test the control of a spacecraft. The number of spacecraft in the formation only affects the NEO deviation distance, not the control. The reason it was included is to simulate the deviations to the orbit of the NEO when the sublimation process occurs. It is important to note that the control is not trying to coordinate the movement of the formation, but simply to ensure that each single spacecraft follows its target orbit.

Table 17: Test case formation orbits,  $\delta\mathbf{k}$  parameters.

Spacecraft	$\delta e$	$\delta i$	$\delta\Omega$	$\delta\omega$	$\delta M$
$\delta\mathbf{k}_{5/1}$	$1.0000 \times 10^{-11}$	$-6.6861 \times 10^{-9}$	$-5.0000 \times 10^{-8}$	$4.4815 \times 10^{-8}$	$2.5043 \times 10^{-8}$
$\delta\mathbf{k}_{5/2}$	$3.3323 \times 10^{-12}$	$-3.7934 \times 10^{-9}$	$-4.7308 \times 10^{-8}$	$4.9561 \times 10^{-8}$	$1.5711 \times 10^{-8}$
$\delta\mathbf{k}_{5/3}$	$6.1028 \times 10^{-13}$	$-1.3168 \times 10^{-8}$	$-4.9986 \times 10^{-8}$	$2.8846 \times 10^{-8}$	$4.4166 \times 10^{-8}$
$\delta\mathbf{k}_{5/4}$	$-8.5308 \times 10^{-13}$	$-2.0467 \times 10^{-9}$	$-2.4000 \times 10^{-8}$	$3.0878 \times 10^{-8}$	$9.9775 \times 10^{-9}$
$\delta\mathbf{k}_{5/5}$	$-6.8000 \times 10^{-12}$	$-1.4403 \times 10^{-9}$	$-2.1705 \times 10^{-8}$	$3.0000 \times 10^{-8}$	$8.4145 \times 10^{-9}$

NOTE:  $\delta a = 0$  for all test orbits.

The thrust leg of the mission was started 13 April 2031 – 5 years before the first potential impact. The required thrust duration is 552.30 days to reach a deviation distance of 384400 km (equal to the Earth-Moon distance) in 2036. The mass of the spacecraft was set to 2000 kg.

The initial parameters for the asteroid Apophis are given in Table 13, with  $t_{\text{MOID}} = 13252.06736$  MJD2000 and  $\nu_{\text{MOID}} = -2.690855$  rad. These are needed for the calculation of the deflection distance, not directly for the control. The primary mirror has an aperture diameter of 20 m (corresponding to a focal length of 5 m), and a spot area of  $\pi(0.5)^2$  m<sup>2</sup>. The efficiency of all the mirrors was set to 90%, including the front and back of the secondary mirror. This was done in order to help balance the SRP exerted on the second mirror. The laser efficiency was set to 25%. The total area of the solar panels was set to 16 m<sup>2</sup>, with an efficiency of 30%.

Figures 64 – 69 show the change in Keplerian elements, position vector and thrust profile for the integration method required for a single spacecraft in the formation; Figs. 70 and 75 show the same for the least squares method. Only the figures for the orbit  $\delta\mathbf{k}_{5/1}$  are shown here; the remaining figures are included in Appendix D.

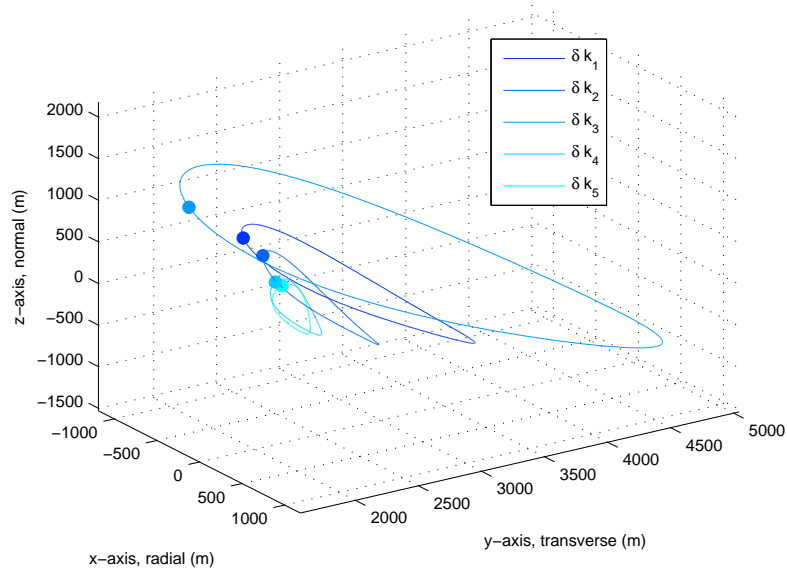


Figure 63: Formation orbits for test cases, shown in the Hill reference frame  $\mathcal{A}$  relative to Apophis, located at  $(0,0)$ . The initial position at  $t_0$  is shown as a solid circle on the orbit.

### 3.6.3 Discussion

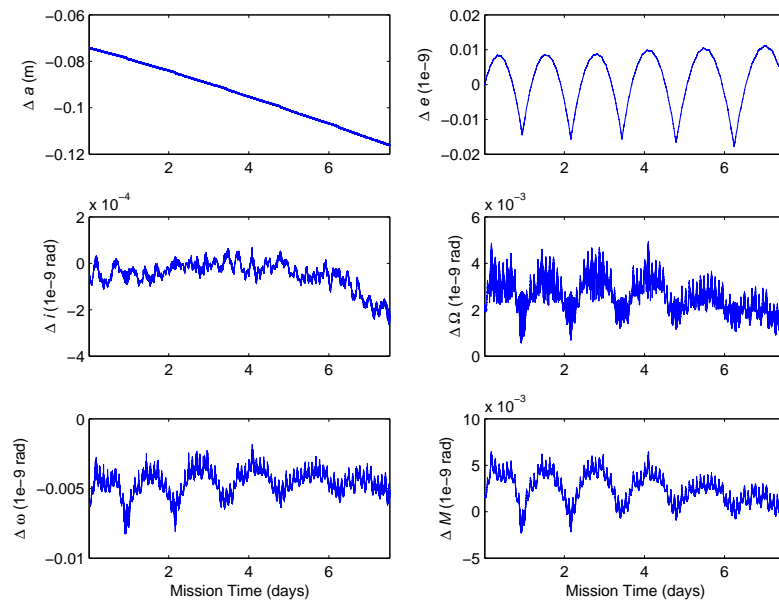
For both the integration and least squares approach, the simulations run with a time step  $\delta t = 60$  s do not converge to the target values, and end up diverging to orbits that are impractical and not feasible for the deflection mission and spacecraft design. In the case of the least squares law, the control acts like an underdamped system, where the parameters are oscillating with the same period as the NEO Apophis (323 days). The longer the duration of the mission, the larger the deviations to which the control law seems unable to compensate for. For all the simulations, there was no upper limit placed on the solution values for the thrust level.

In most of the simulations, there occurs periods of large quick variations in the thrust where the system is overcompensating resulting in chatter around the target parameters. This chatter can be seen in the plots of the variation of the Keplerian parameters and thrust levels, but due to the low level are too small to be seen in the Hill reference frame components.

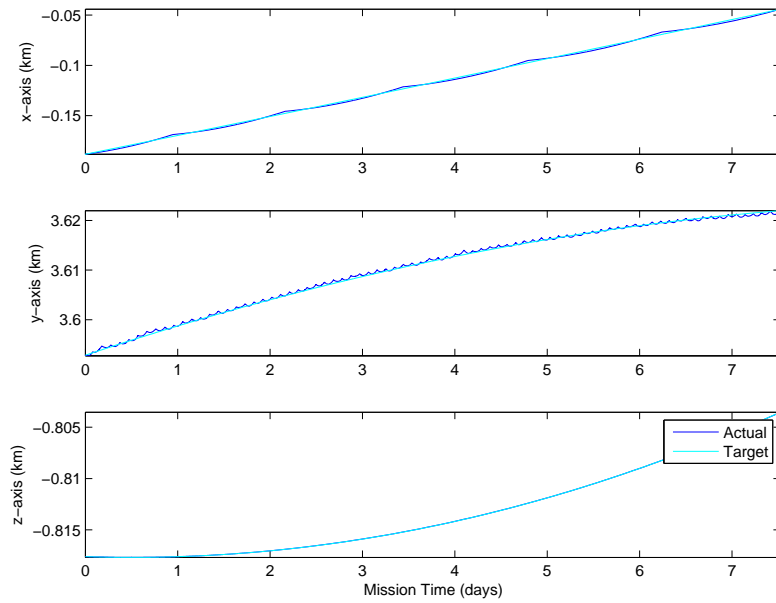
As seen in Section 3.5, the perturbations are mainly in the  $x$ - $y$  plane of the Hill coordinate system, so as expected, the divergence, if any, occurs predominantly in these two axes. The out of plane motion, either in the  $z$  axis or in the inclination, RAAN and in part in the argument of periapsis are much better controlled than the semi-major axis, for example.

For the smaller time steps of  $\delta t = 1, 10$  s, both methods are able to control the various perturbations and track the target orbit parameters with a relatively high degree of accuracy, on the order of 0.001 – 1%. As expected, the least squares is faster to simulate (in terms of computational time), but with slightly larger errors than those of the integration. The oscillations, for example in the control of the eccentricity in Fig. 64 are due to the rotational period of the NEO (30 hrs in the case of Apophis) which

alters the distance between the spacecraft and the NEO, increasing and decreasing the third body perturbations.



(a) Variations in the orbital element differences.



(b) Variations in the Hill frame components.

Figure 64: Integration control law for spacecraft formation  $\delta \mathbf{k}_{5/1}$  at time step of  $\delta t = 1$  s using the fixed mirror configuration with a system efficiency of 25%.

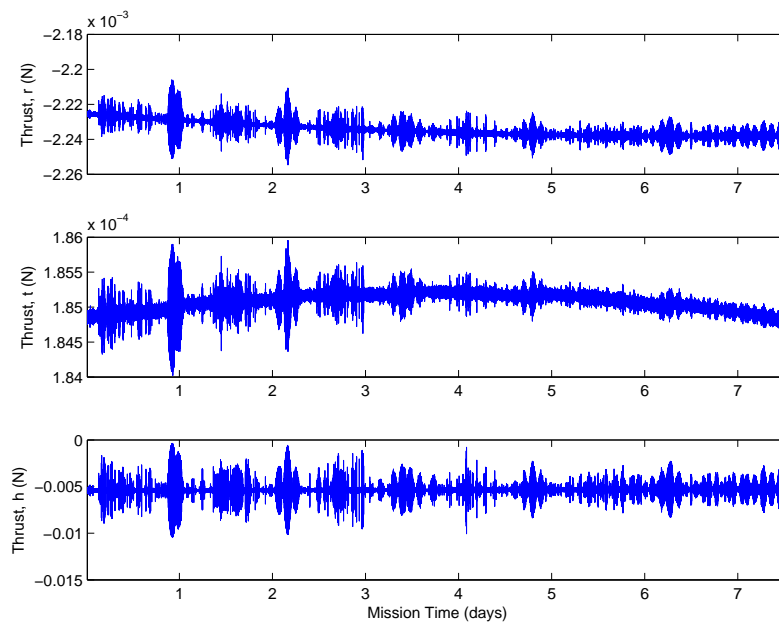
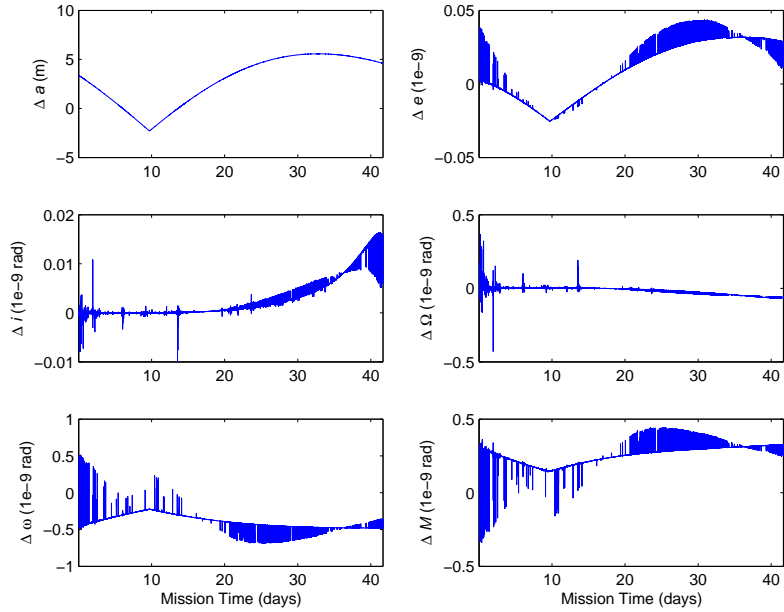
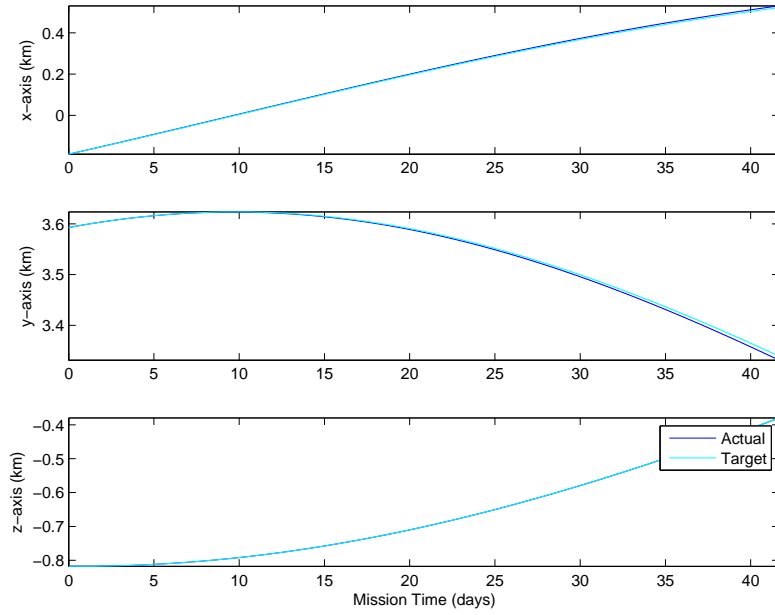


Figure 65: Integration control law for spacecraft formation  $\delta \mathbf{k}_{5/1}$  at time step of  $\delta t = 1$  s using the fixed mirror configuration with a system efficiency of 25%.



(a) Variations in the orbital element differences.



(b) Variations in the Hill frame components.

Figure 66: Integration control law for spacecraft formation  $\delta \mathbf{k}_{5/1}$  at time step of  $\delta t = 10$  s using the fixed mirror configuration with a system efficiency of 25%.

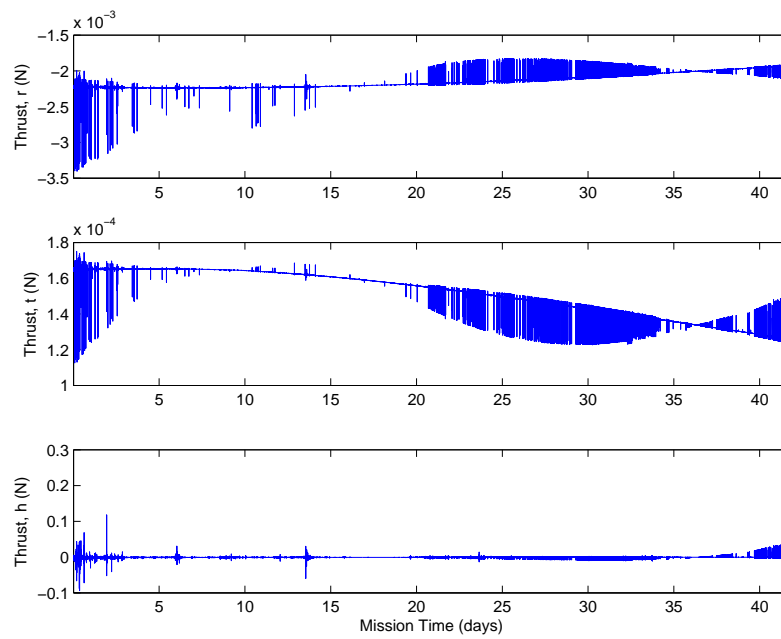
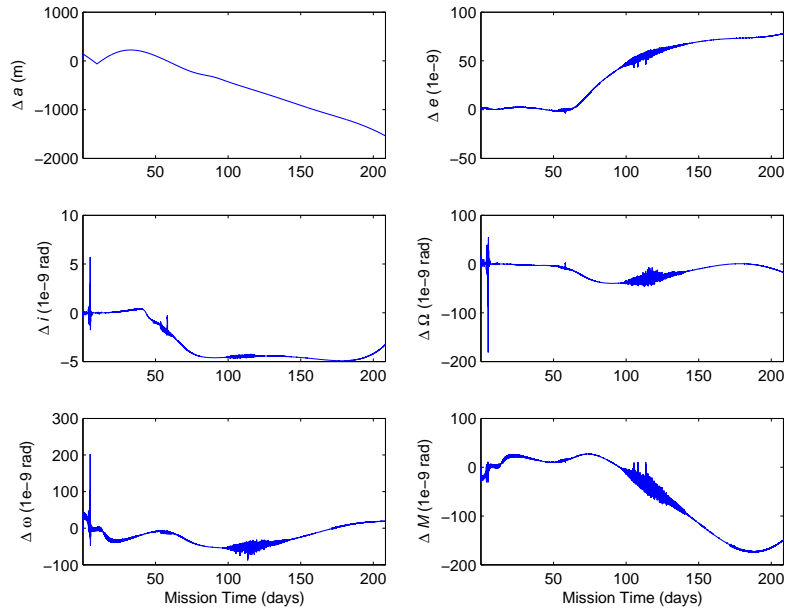
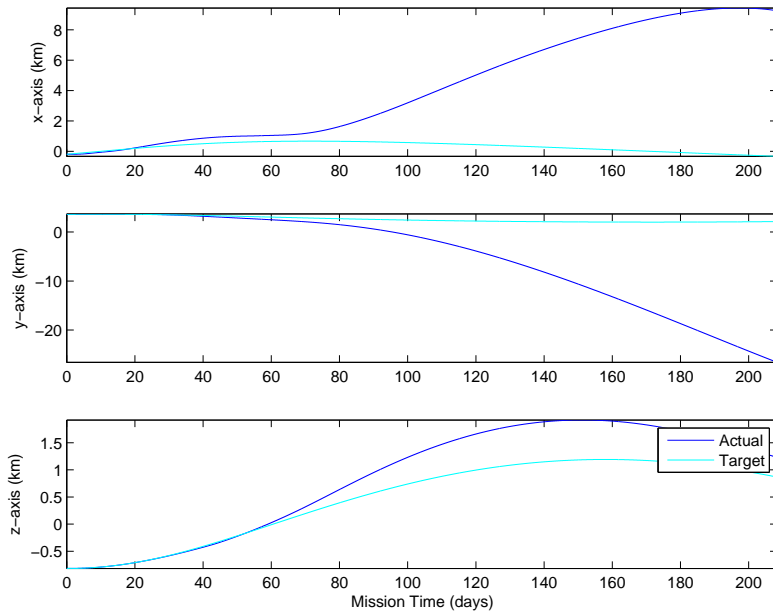


Figure 67: Integration control law for spacecraft formation  $\delta\mathbf{k}_{5/1}$  at time step of  $\delta t = 10$  s using the fixed mirror configuration with a system efficiency of 25%.



(a) Variations in the orbital element differences.



(b) Variations in the Hill frame components.

Figure 68: Integration control law for spacecraft formation  $\delta \mathbf{k}_{5/1}$  at time step of  $\delta t = 60$  s using the fixed mirror configuration with a system efficiency of 25%.

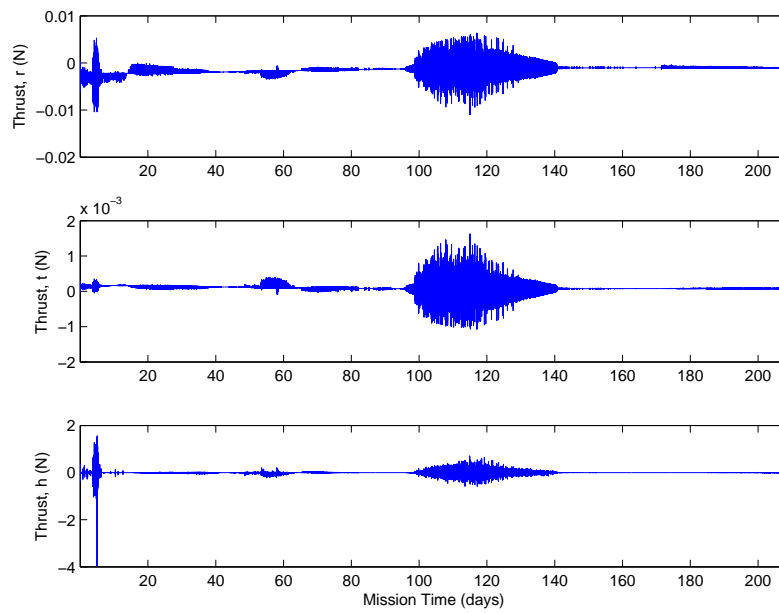
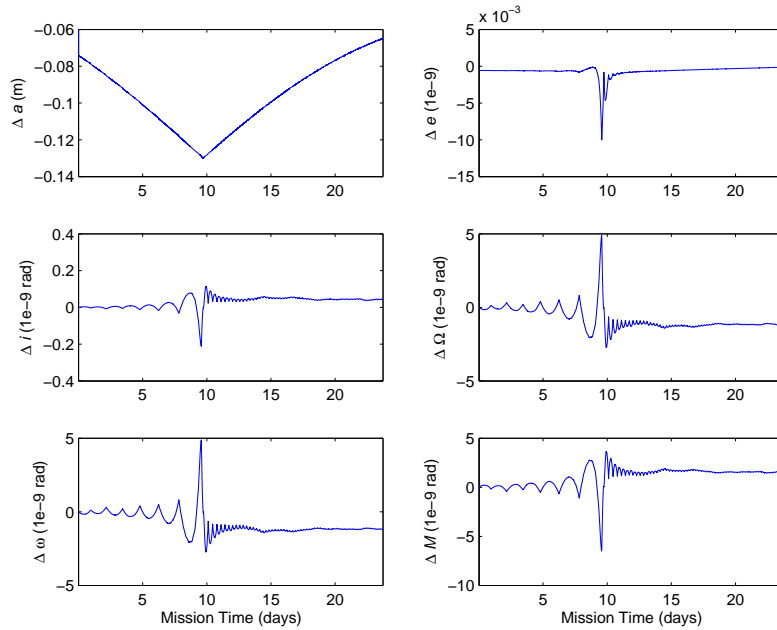
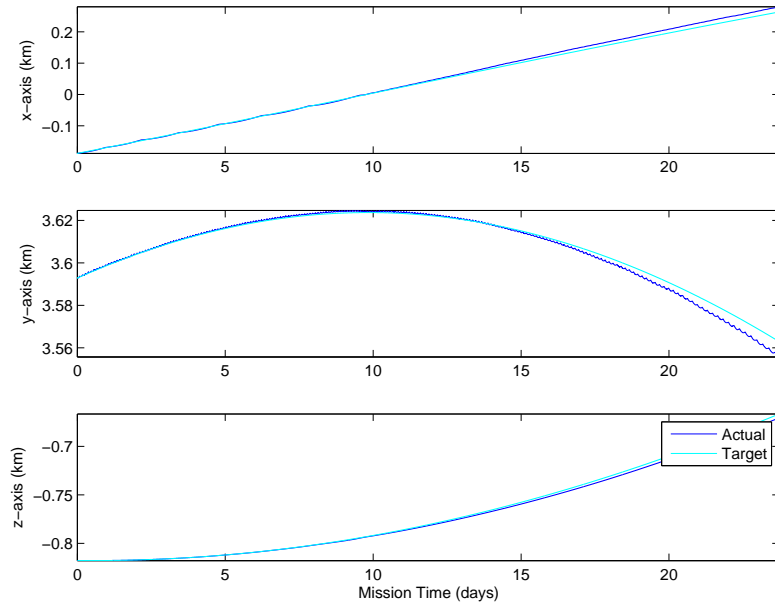


Figure 69: Integration control law for spacecraft formation  $\delta \mathbf{k}_{5/1}$  at time step of  $\delta t = 60$  s using the fixed mirror configuration with a system efficiency of 25%.



(a) Variations in the orbital element differences.



(b) Variations in the Hill frame components.

Figure 70: Least squares control law for spacecraft formation  $\delta \mathbf{k}_{5/1}$  at time step of  $\delta t = 1$  s using the fixed mirror configuration with a system efficiency of 25% and weights,  $W = [1e-6, 1e6, 1, 1, 1, 1]$ .

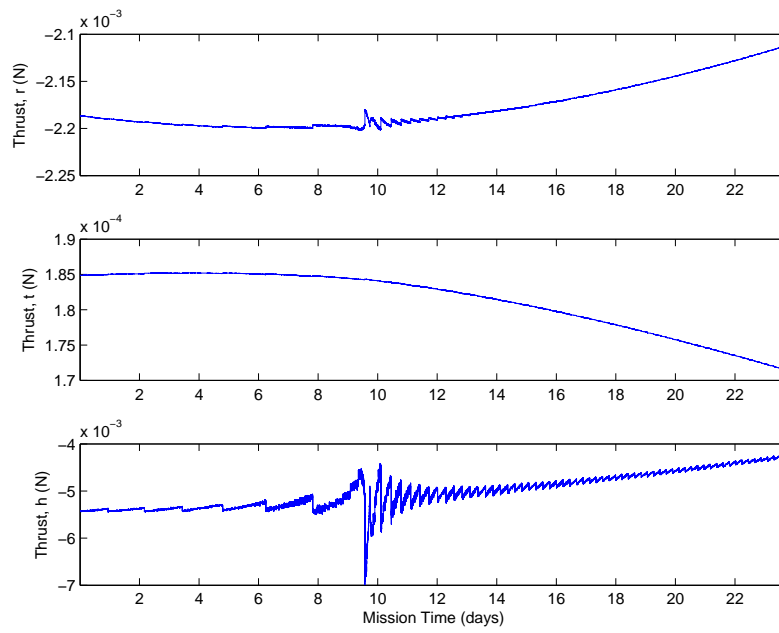
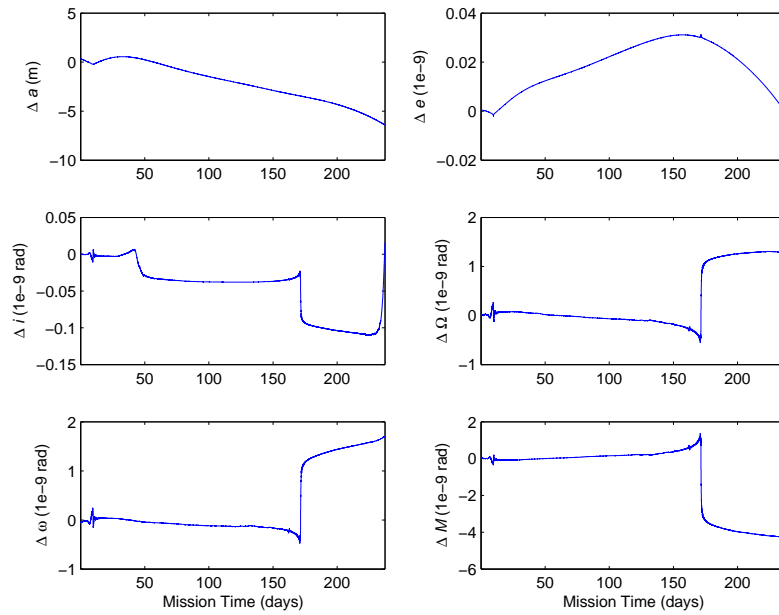
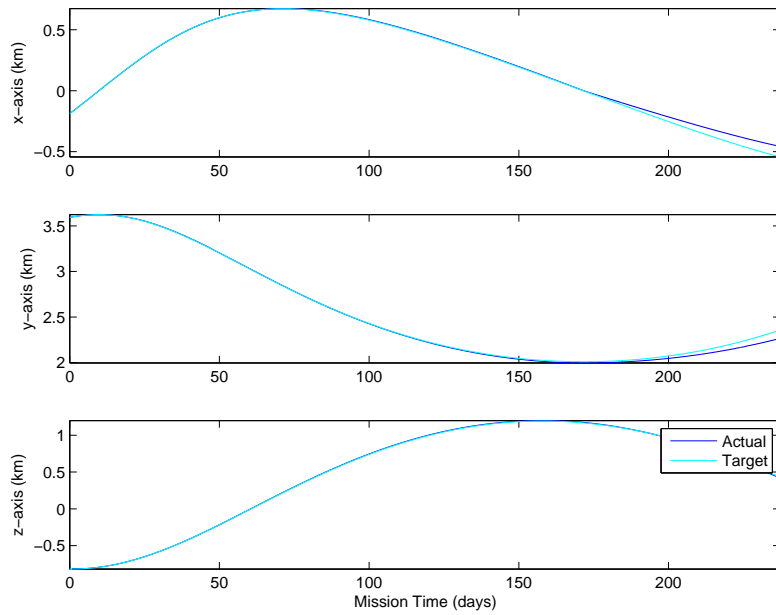


Figure 71: Least squares control law for spacecraft formation  $\delta \mathbf{k}_{5/1}$  at time step of  $\delta t = 1$  s using the fixed mirror configuration with a system efficiency of 25% and weights,  $W = [1e-6, 1e6, 1, 1, 1, 1]$ .



(a) Variations in the orbital element differences.



(b) Variations in the Hill frame components.

Figure 72: Least squares control law for spacecraft formation  $\delta \mathbf{k}_{5/1}$  at time step of  $\delta t = 10$  s using the fixed mirror configuration with a system efficiency of 25% and weights,  $W = [1e-6, 1e6, 1, 1, 1, 1]$ .

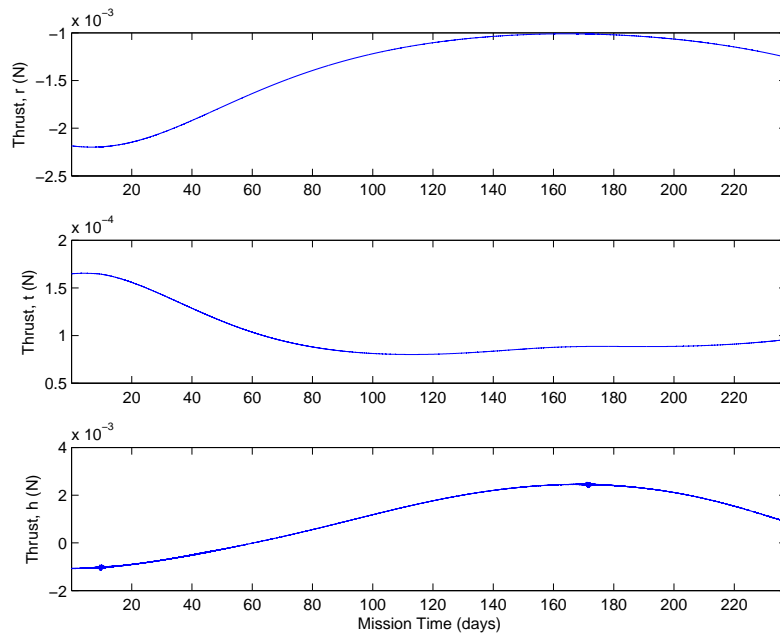
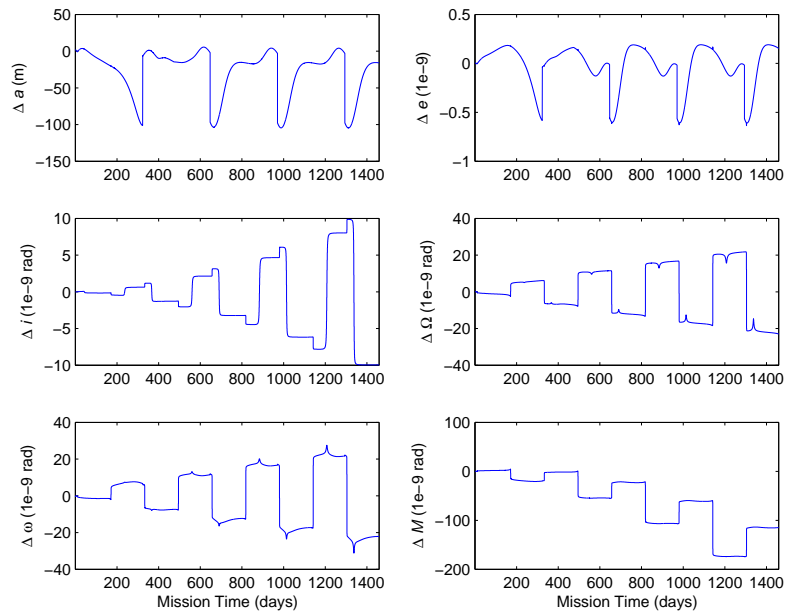
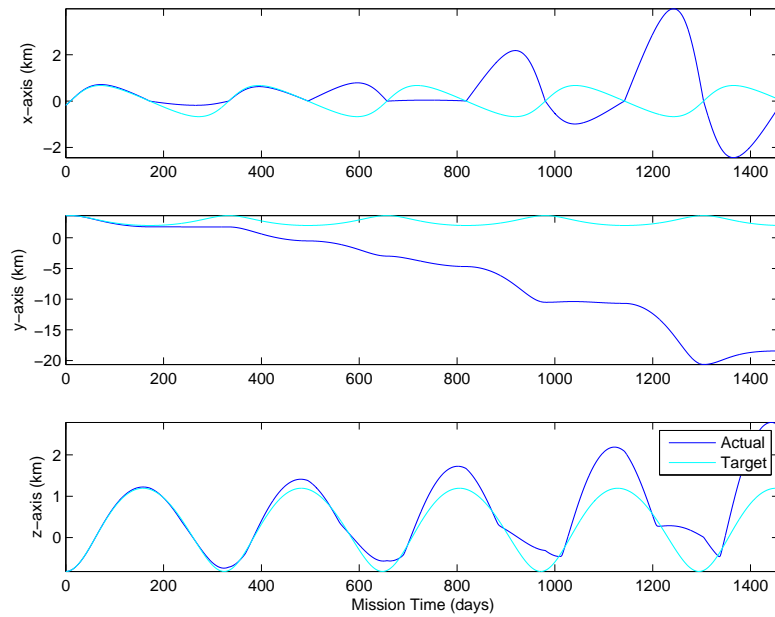


Figure 73: Least squares control law for spacecraft formation  $\delta \mathbf{k}_{5/1}$  at time step of  $\delta t = 10$  s using the fixed mirror configuration with a system efficiency of 25% and weights,  $W = [1e-6, 1e6, 1, 1, 1, 1]$ .



(a) Variations in the orbital element differences.



(b) Variations in the Hill frame components.

Figure 74: Least squares control law for spacecraft formation  $\delta \mathbf{k}_{5/1}$  at time step of  $\delta t = 60$  s using the fixed mirror configuration with a system efficiency of 25% and weights,  $W = [1e-6, 1e6, 1, 1, 1, 1]$ .

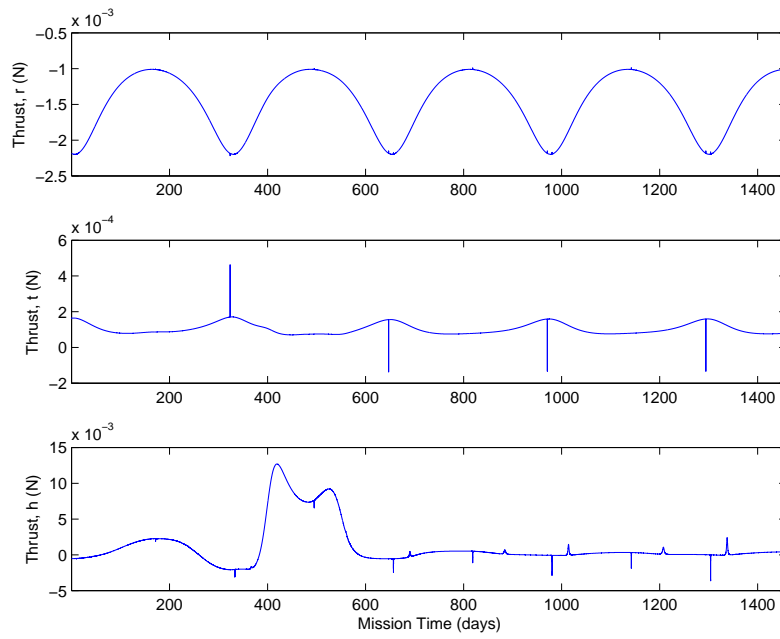


Figure 75: Least squares control law for spacecraft formation  $\delta \mathbf{k}_{5/1}$  at time step of  $\delta t = 60$  s using the fixed mirror configuration with a system efficiency of 25% and weights,  $W = [1e-6, 1e6, 1, 1, 1, 1]$ .

3.7 CONTROL OF AEPS

Two strategies were studied to maintain the orbital position of the mirror: the first directly compensates for the solar pressure and gravity attraction with an active control, whereas the second option allows the spacecraft to oscillate along the radial direction, effectively chasing the artificial equilibrium points. Both of these approaches are based on a model of the adaptive mirror with a collimating laser. A Lyapunov-based controller is also simulated for the case of direct imaging laser with an adaptive mirror.

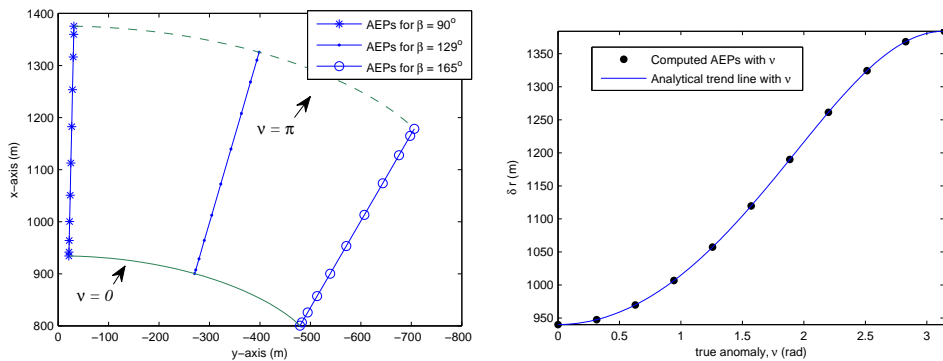
3.7.1 Adaptive mirror with laser

Solar pressure depends on the distance from the Sun, therefore, if the size of the mirror is constant, as the asteroid moves around the Sun, the force acting on the spacecraft changes with the true anomaly  $\nu$ . As a consequence, the position of the equilibrium points changes with time unless the orbit of the asteroid is circular.

Once the shape and orientation of the mirror are defined, the total force acting on the mirror assembly can be computed by integrating the following expression over the surface of the mirror  $A_M$ :

$$\mathbf{F}_{\text{SRP}} = 2\sigma_M P_r \int_{A_M} \cos^2 \phi \hat{\mathbf{n}} dA \tag{3.80}$$

where  $\sigma_M$  is the efficiency of the mirror, or coefficient of reflectivity, and  $P_r$  is the solar pressure at a distance  $r_{\odot/sc}$  from the Sun.



(a) Position of the equilibrium points over a full orbit of the asteroid Apophis. (b) Variation of the position of the AEP for a mirror attitude of  $129^\circ$ , over half an orbit.

Figure 76: Variation of the equilibrium points with the true anomaly for  $A_M = 196 \text{ m}^2$ .

Figure 76a shows, for different attitudes of the mirror, the position of the equilibrium points over a full orbit of the asteroid Apophis. Figure 76b instead shows the variation of the position of the AEP for a particular attitude of the mirror, over half

an orbit. The black dots represent the computed position of the equilibrium points for an angle  $\beta = 129^\circ$  while the continuous line is given by the following equations,

$$x_{\text{AEP}} = \delta r_{\text{AEP}_0} \cos \epsilon_0 \left( \frac{1 + e \cos \nu_0}{1 + e \cos \nu} \right) \quad (3.81a)$$

$$y_{\text{AEP}} = \delta r_{\text{AEP}_0} \sin \epsilon_0 \left( \frac{1 + e \cos \nu_0}{1 + e \cos \nu} \right) \quad (3.81b)$$

where

$$\epsilon_0 = \arctan \left( \frac{y_{\text{AEP}}(\nu_0)}{x_{\text{AEP}}(\nu_0)} \right)$$

is the angular position of the AEP at  $\nu = \nu_0$ .

Then, the distance of the AEP from the asteroid varies with the following law,

$$\delta r_{\text{AEP}} = \delta r_{\text{AEP}_0} \frac{1 + e \cos \nu_0}{1 + e \cos \nu} \quad (3.82)$$

Since the AEPs are moving a spacecraft placed at an AEP would depart toward the asteroid or away from the asteroid depending on the initial true anomaly  $\nu$ . In particular, for the true anomaly  $\nu \in [0, \pi]$  the spacecraft would fall toward the asteroid, while for  $\nu \in [\pi, 2\pi]$  the spacecraft would escape along a radial direction.

In order to chase the AEPs the spacecraft has to move with the same kinematics, the following conditions are placed on the velocity and acceleration,

$$\frac{dx_{\text{AEP}}}{dt} = \frac{d(\delta r_{\text{AEP}})}{dt} \cos \epsilon \quad (3.83a)$$

$$\frac{dy_{\text{AEP}}}{dt} = \frac{d(\delta r_{\text{AEP}})}{dt} \sin \epsilon \quad (3.83b)$$

$$\frac{d^2 x_{\text{AEP}}}{dt^2} = \frac{d^2(\delta r_{\text{AEP}})}{dt^2} \cos \epsilon \quad (3.84a)$$

$$\frac{d^2 y_{\text{AEP}}}{dt^2} = \frac{d^2(\delta r_{\text{AEP}})}{dt^2} \sin \epsilon \quad (3.84b)$$

with

$$\frac{d(\delta r_{\text{AEP}})}{dt} = \frac{(\delta r_{\text{AEP}})^2 e \dot{\nu} \sin \nu}{\delta r_{\text{AEP}_0} (1 + e \cos \nu_0)} \quad (3.85)$$

$$\frac{d^2(\delta r_{\text{AEP}})}{dt^2} = \frac{e \delta r_{\text{AEP}}}{\delta r_{\text{AEP}_0} (1 + e \cos \nu_0)} (2 \delta \dot{r}_{\text{AEP}} \dot{\nu} \sin \nu + \delta r_{\text{AEP}} \dot{\nu}^2 \cos \nu + \delta r_{\text{AEP}} \ddot{\nu} \sin \nu) \quad (3.86)$$

Equations (3.83) and (3.84) represent an imposed shape to the motion of the spacecraft. If (3.81), (3.83) and (3.84) are substituted back into the dynamic equations in (3.53) and solving for the controls, it is possible to get the thrust components required to follow the prescribed kinematics.

Figure 77 presents an example of the required thrust profile to maintain a fixed position for an AEP computed at the perihelion. By comparison, Fig. 78 shows the required control profile to allow the spacecraft to drift, following the motion of the AEP for different values of the true anomaly. Both examples assume a spherical gravity model for the asteroid.

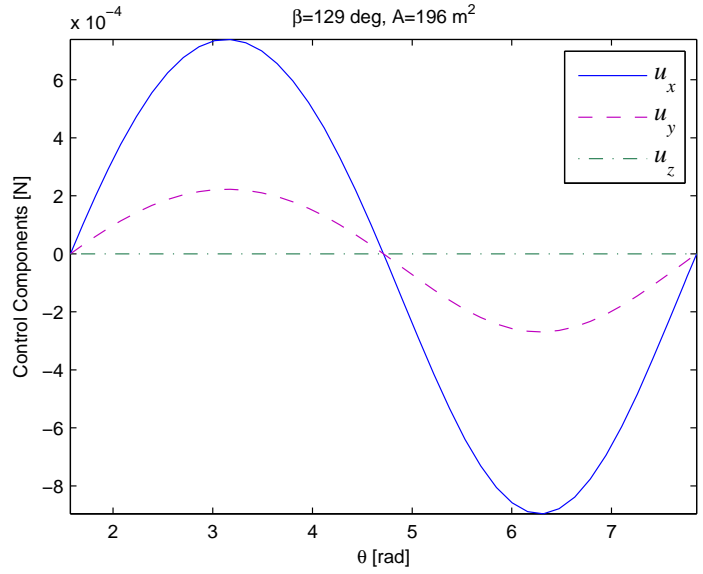


Figure 77: Control profile for orbit maintenance for ( $A = 196 \text{ m}^2$ ,  $\beta = 139^\circ$ ,  $\nu_0 = \pi$ ) maintaining a fixed position in the Hill frame

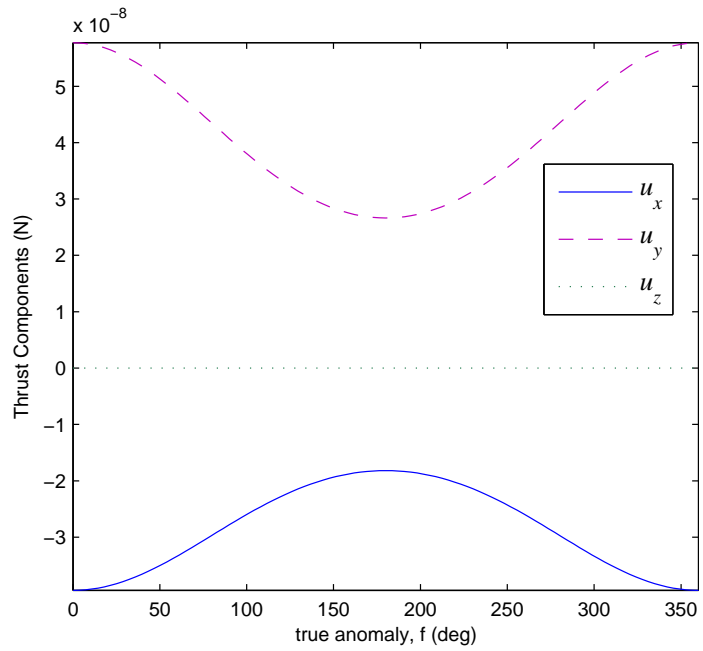


Figure 78: Control profile for orbit maintenance for ( $A = 196 \text{ m}^2$ ,  $\beta = 139^\circ$ ) following the motion of the AEP.

As can be seen the control capability required to maintain a fixed position is greater than the one required to chase the AEP. A possible scenario, therefore, is that the formation can be distributed around the asteroid at different angles of  $\epsilon$ , with the mirrors oscillating along the radial directions. As can be seen from the figures, the control authority required to maintain the position of an AEP is several orders of

magnitude higher, though still very small, than what is required to chase the AEP. Figure 79, instead, shows the required control profile to follow the motion of the AEP computed for a spherical asteroid when the gravity field for an elongated body is considered.

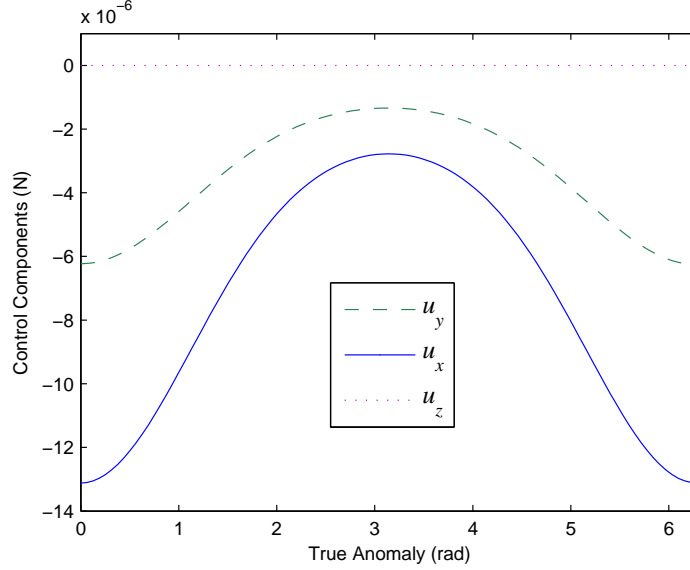


Figure 79: Control required to follow the AEP motion originally computed assuming a spherical asteroid (see Fig. 78) for a non-spherical asteroid.

### 3.7.2 Adaptive mirror with direct imaging

For a direct reflection of the light onto the NEO surface, the vector from the mirror to the focal point is parallel to the mirror-asteroid direction, with a magnitude roughly equal to the distance between the mirror and the asteroid. For such a long focal distance, the resulting mirror is almost flat.

Assuming a perfect reflection, the force  $\mathbf{F}_{srp}$  is,

$$\mathbf{F}_{srp} = 2A_M P_0 \left( \frac{r_{AU}}{r_{sc}} \right)^2 \cos^2 \phi \begin{bmatrix} \cos \phi \\ \sin \phi \\ 0 \end{bmatrix} \quad (3.87)$$

where  $P_0 = 4.562 \times 10^{-6} \text{ kg}\cdot\text{s}^2/\text{m}$  is the solar pressure at 1 AU, and  $\phi$  is the angle of reflection.

$$\phi = \frac{1}{2} \arctan \left( \frac{y_{AEP}}{x_{AEP}} \right) \quad (3.88)$$

Given these equations, the force due to solar pressure cannot be aligned with the asteroid-mirror direction. Therefore in order to maintain the spacecraft position relative to the asteroid, it is necessary to have an active control system. Moreover, the modulus of the solar pressure is a function on the distance from the Sun, therefore the active control will also need to compensate for the variation in solar pressure along the orbit.

A Lyapunov control function can be formulated, assuming (1) the centrifugal and Coriolis forces are negligible compared to solar pressure, and (2) the gravity of the asteroid and any non-spherical terms in the gravity field expansion result in only a small perturbation.

$$V = \frac{1}{2}\delta v^2 + \frac{1}{2}k \left( (x - x_{\text{AEP}})^2 + (y - y_{\text{AEP}})^2 + (z - z_{\text{AEP}})^2 \right) \quad (3.89)$$

where  $\delta \mathbf{r}_{\text{AEP}} = [x_{\text{AEP}}, y_{\text{AEP}}, z_{\text{AEP}}]$  are the coordinates of the artificial equilibrium point at which the mirror should be placed. Consistent with Lyapunov stability, if there exist a control  $\mathbf{u}$  such that  $dV/dt < 0$ , then the mirror can be placed at or in the proximity of the artificial equilibrium point. A possible control is given by,

$$\mathbf{u} = - \left( -\frac{\mu_A}{\delta r^3} \delta \mathbf{r} + \frac{\mathbf{F}_{srp}}{m_{sc}} \right) - k(\delta \mathbf{r} - \delta \mathbf{r}_{\text{AEP}}) - c_d \delta \mathbf{v} \quad (3.90)$$

With the derivative of the Lyapunov function  $V$ ,

$$\frac{dV}{dt} = \delta \mathbf{v}^T \delta \dot{\mathbf{v}} + k(\delta \mathbf{r} - \delta \mathbf{r}_{\text{AEP}})^T \delta \mathbf{v} \quad (3.91a)$$

$$= \delta \mathbf{v}^T \left( -\frac{\mu_A}{\delta r^3} \delta \mathbf{r} + \frac{\mathbf{F}_{srp}}{m_{sc}} - \left( -\frac{\mu_A}{\delta r^3} \delta \mathbf{r} + \frac{\mathbf{F}_{srp}}{m_{sc}} \right) \right) \quad (3.91b)$$

$$- k(\delta \mathbf{r} - \delta \mathbf{r}_{\text{AEP}}) - c_d \delta \mathbf{v} + k(\delta \mathbf{r} - \delta \mathbf{r}_{\text{AEP}})^T \delta \mathbf{v} \\ = -c_d \delta \mathbf{v}^T \delta \mathbf{v} < 0 \quad (3.91c)$$

where  $\delta \mathbf{v} = [\dot{x}, \dot{y}, \dot{z}]$  is the velocity of the spacecraft in the asteroid Hill reference frame  $\mathcal{A}$ .

The control (3.90) can be introduced into the full dynamic model in (3.53) to validate the earlier assumptions that the perturbations given by centrifugal, Coriolis forces and aspherical gravity field are negligible.

The Lyapunov controller is applied to two cases: the first fixes the position of the AEP and maintains the spacecraft at that one location. The second allows the spacecraft to follow the same oscillatory motion of the AEPs, where at different instants of time during the asteroid orbit, a different AEP location is chosen along the asteroid-mirror line.

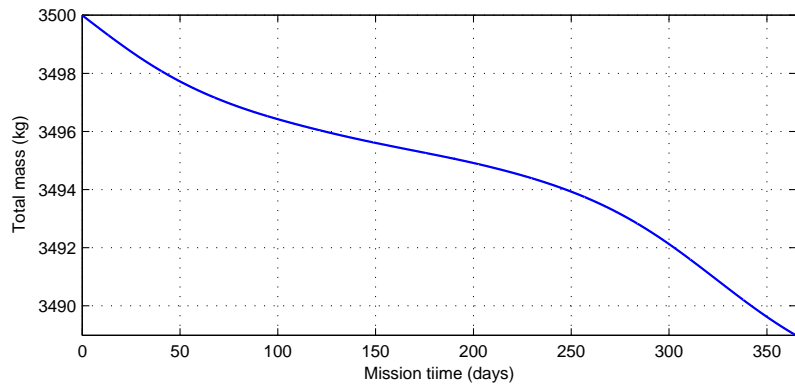
In particular, AEPs are selected such that,

$$\delta \mathbf{r}_{\text{AEP}} = \frac{d_{spot}/2}{\epsilon_{\odot}} \frac{r_{sc}}{r_{AU}} \begin{bmatrix} \cos \epsilon_{\text{AEP}} \\ \sin \epsilon_{\text{AEP}} \\ 0 \end{bmatrix} \quad (3.92)$$

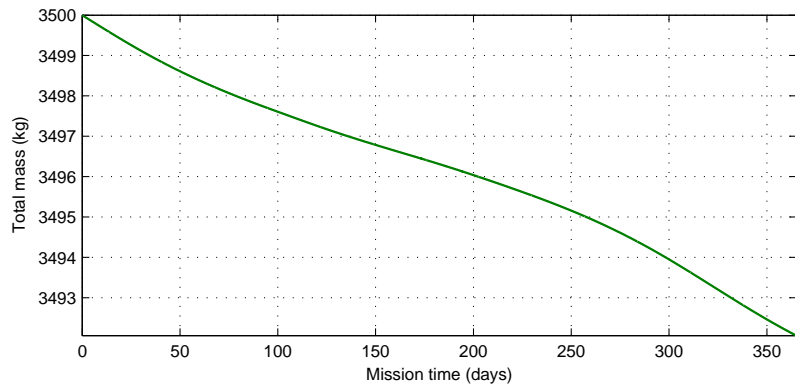
where  $d_{spot}$  is the desired diameter of the illuminated spot and  $\epsilon_{\odot} = 4.53$  mrad is the angular radius of the Sun at one AU (see Section 2.2.1).

Figure 81 shows that the controller is able to maintain the mirror in close proximity to the radial direction, effectively chasing the position of the AEP. Figures 82 and 80 represent the modulus of the thrust and the mass consumption for a one year of operation of a 3.5 metric ton spacecraft, carrying a mirror with an aperture diameter of 65 m. The required peak thrust is below 13 mN, with a total mass consumption of 4.5 kg assuming an engine  $I_{sp}$  of 4500 s. The elastic coefficient  $k$  for both cases is  $10^{-6}$  while the dissipative coefficient  $c_d$  was set to  $10^{-5}$ .

The second strategy maintains a constant concentration ratio, compensating for the variation in the Sun-asteroid distance (due to the elliptical orbit of Apophis). In



(a) Fixed position.

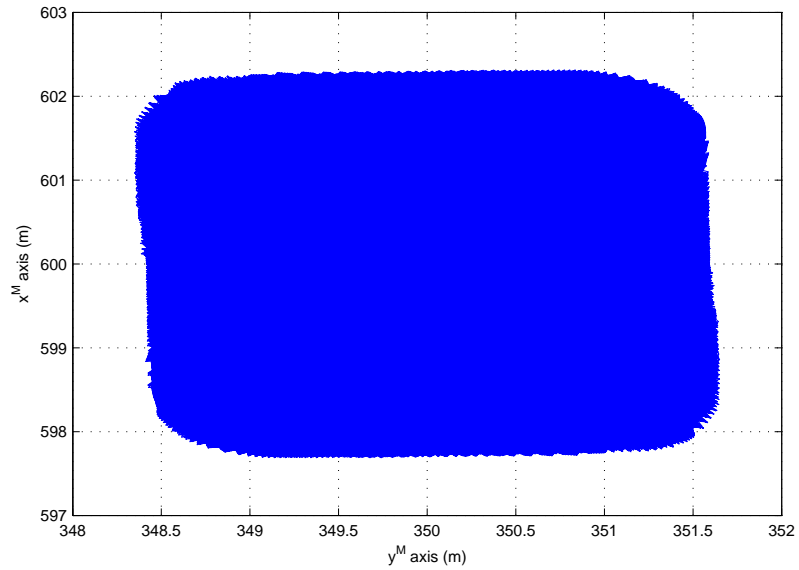


(b) Variable position.

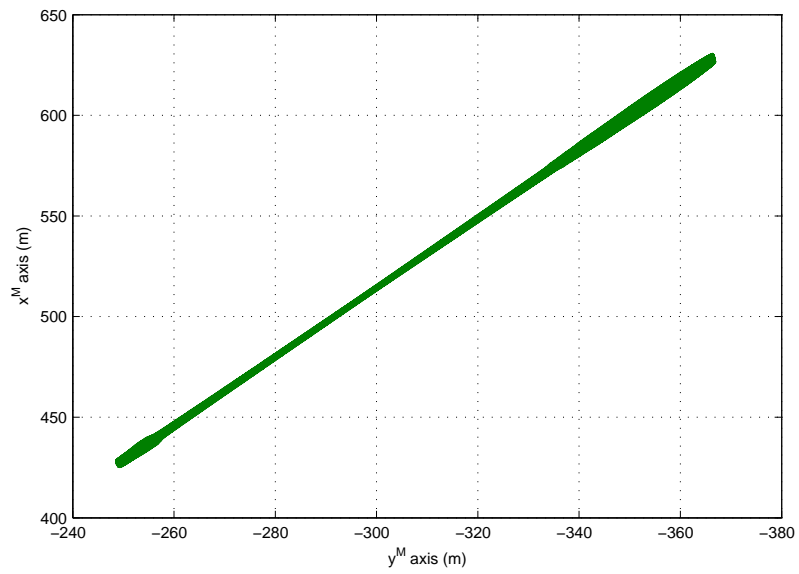
Figure 80: Spacecraft mass after fuel consumption for Lyapunov controlled AEPS.

order to maintain a constant  $C_r$ , the focal length has to be modified according to the angular diameter of the Sun.

These figures demonstrate that with a very small electric propulsion system, the mirror position can be maintained at the desired proximity to the asteroid.

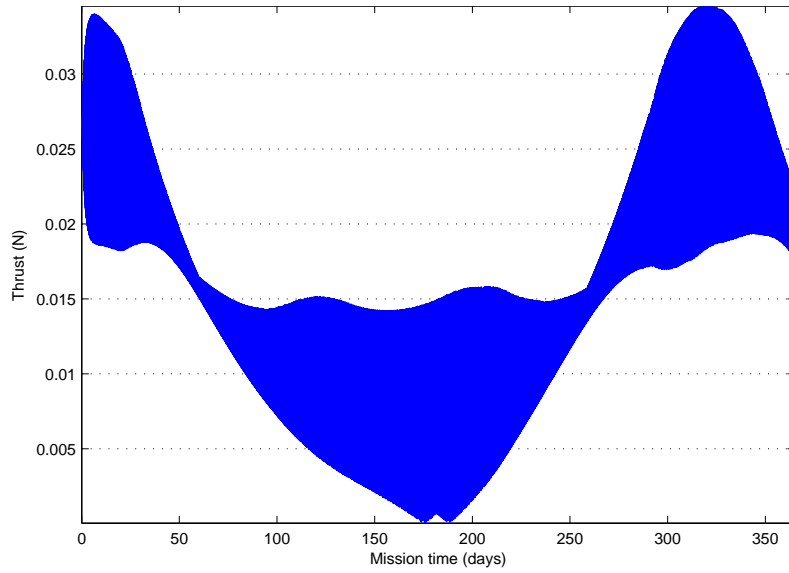


(a) Fixed position.

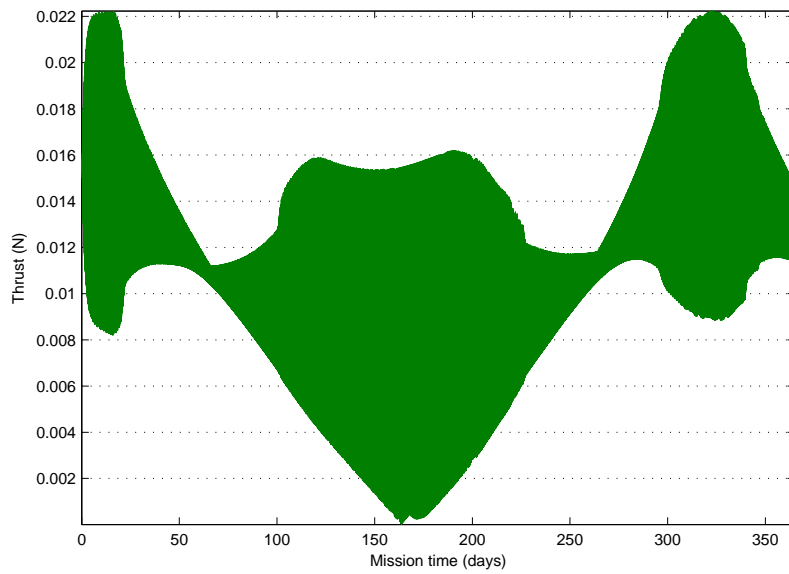


(b) Variable position.

Figure 81: Variation in position over one orbit shown in the local mirror reference frame, for Lyapunov controlled AEPs.



(a) Fixed position.



(b) Variable position.

Figure 82: Thrust magnitude for Lyapunov controlled AEPs.

The use of a single mirror implies a number of difficulties in the control of the orbit and attitude of the spacecraft and in the overall system design. On the other hand, the use of multiple mirrors will require pointing control of the beams in order to maintain the superposition. The navigation strategy has two goals: (a) to coordinate the pointing control of all the spacecraft in order to intersect the beams and hit the same spot on the surface of the asteroid, and (b) to estimate the position of the asteroid during the deflection manoeuvre.

#### 4.1 INTRODUCTION

A number of systems, such as the control, require knowledge of the position and velocity of the asteroid relative to the spacecraft in the formation. It is assumed that the inertial position and velocity of each spacecraft are known from ground measurements. Furthermore, it is assumed that each spacecraft can measure its attitude with a star tracker. In order to determine the location of the asteroid, an onboard camera is used to first determine the angular direction of the asteroid. Using the formation, the range can then be determined by triangulation. The same technique can be used to coordinate the steering of all the beams in order to target the same spot on the surface of the asteroid.

A preliminary analysis of the relative orbit determination of the spacecraft with respect to the asteroid is presented for the fixed mirror case, as it is the most critical one. The single mirror design maintains a fixed angular separation between the spacecraft-asteroid vector and the spacecraft-Sun vector, therefore the beaming direction is constant with respect to time and does not need to be controlled.

Previous studies have addressed different approaches towards navigation in the proximity of minor bodies, e.g. Kubota et al. (2003); Xiangyu et al. (2004), with particular attention to the problem of landing. For this application, the requirements are substantially different and therefore some of the strategies that could be found in the literature cannot be used. On the other hand, a wide range of navigation techniques using, e.g., radar, lidar and other instruments have been already developed for past and future missions and are expected to be used for this application as well.

#### 4.2 COORDINATE TRANSFORMATION

The directional cosine matrix  $\mathbf{D}$ , quaternions  $\mathbf{q}$  and Euler angles  $[\mathbf{e}, \psi]$  can all be used interchangeably for conversion from one coordinate system to another [Wie, 1998].

$$q_1 = e_1 \sin\left(\frac{1}{2}\psi\right) = \frac{1}{4q_4}(D_{23} - D_{32}) \quad (4.1a)$$

$$q_2 = e_2 \sin\left(\frac{1}{2}\psi\right) = \frac{1}{4q_4}(D_{31} - D_{13}) \quad (4.1b)$$

$$q_3 = e_3 \sin\left(\frac{1}{2}\psi\right) = \frac{1}{4q_4}(D_{12} - D_{21}) \quad (4.1c)$$

$$q_4 = \cos\left(\frac{1}{2}\psi\right) = \pm \frac{1}{2}\sqrt{1 + D_{11} + D_{22} + D_{33}} \quad (4.1d)$$

where  $D_{ij}$  is entry in the  $i^{\text{th}}$  row,  $j^{\text{th}}$  column of the matrix  $\mathbf{D}$ .

Of particular interest, is the rotational matrix  $\mathbf{D}_{\mathcal{O}/\mathcal{S}}$  that translates a vector from the heliocentric inertial reference frame  $\mathcal{O}$  to the spacecraft-centric reference frame  $\mathcal{S}$ .

$$\mathbf{D}_{\mathcal{O}/\mathcal{S}} = \begin{bmatrix} \frac{\mathbf{r}_x}{r} & \frac{(\mathbf{h} \wedge \mathbf{r})_x}{\|\mathbf{h} \wedge \mathbf{r}\|} & \frac{\mathbf{h}_x}{h} \\ \frac{\mathbf{r}_y}{r} & \frac{(\mathbf{h} \wedge \mathbf{r})_y}{\|\mathbf{h} \wedge \mathbf{r}\|} & \frac{\mathbf{h}_y}{h} \\ \frac{\mathbf{r}_z}{r} & \frac{(\mathbf{h} \wedge \mathbf{r})_z}{\|\mathbf{h} \wedge \mathbf{r}\|} & \frac{\mathbf{h}_z}{h} \end{bmatrix}^{-1} \quad (4.2)$$

where  $\mathbf{r} = \mathbf{r}_{\mathcal{O}/sc}$ ,  $\mathbf{v} = \mathbf{v}_{\mathcal{O}/sc}$  are position and velocity vectors from the Sun to a given spacecraft in the inertial  $\mathcal{O}$  frame, and the angular momentum  $\mathbf{h} = \mathbf{r}_{\mathcal{O}/sc} \wedge \mathbf{v}_{\mathcal{O}/sc}$ .

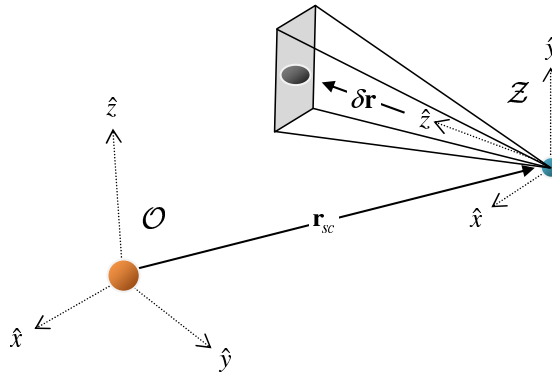


Figure 83: Camera reference frame  $\mathcal{Z}$  shown in inertial frame (not to scale).

The other reference frame required is the relative camera reference frame  $\mathcal{Z}$ , defined with the  $z$ -axis along the camera boresight (i.e. pointing direction of the camera), and the  $x$ - $y$  axes composing the image plane (see Fig. 83). For the navigation simulation, the local  $y^{\mathcal{Z}}$ -axis was nominally set parallel to the angular orbital momentum of the spacecraft. Figures 84 – 86 show the quaternions for three of the test orbits, along with the rotational angle  $\psi$  from (4.1) which in this case represents the angle between the intended  $z$  axis of the mirror reference frame, expressed in the inertial reference frame. This is equal to elevation angle of the vector  $\delta\hat{\mathbf{r}}^{\mathcal{O}}$  in spherical coordinates.

The five test orbits used here are the same as in the control simulations, and are given in Table 17 (on pg. 97) and Figure 63 (on pg. 98).

#### 4.3 SIMULATION MODEL

The first step is to correctly locate the asteroid, using a nominal lead spacecraft. Each spacecraft should have a basic idea of the region of space in which the asteroid should be located, however even in the worst cast where no region is known, a wide-coverage scan/search procedure can be implemented. Once the asteroid is in view of the camera, the camera aligns the calculated centre of the asteroid with the boresight of the camera (i.e. the origin (0,0) on the camera image plane). This is repeated for a second camera, in order to triangulate the location of the asteroid. Figure 87 illustrates this concept.

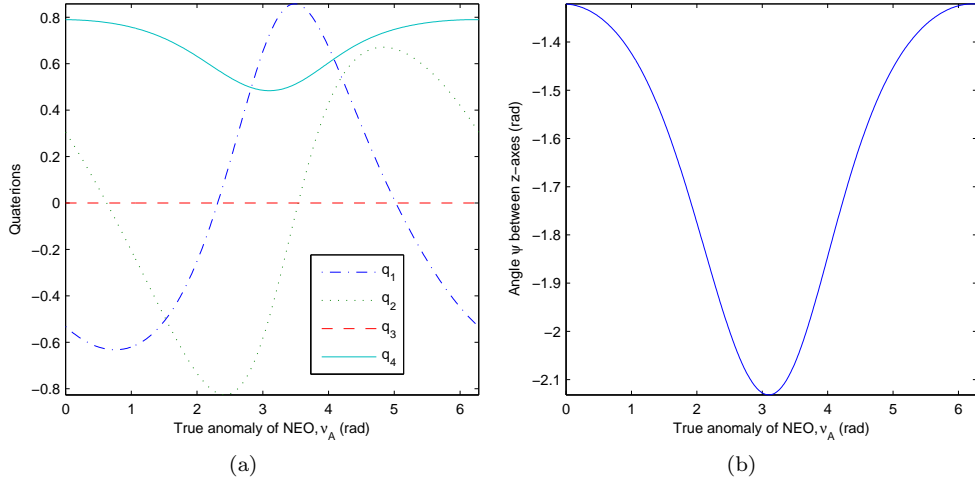


Figure 84: Quaternions and rotational angle  $\psi$  for transformation from inertial  $\mathcal{O}$  to camera  $\mathcal{Z}$  reference frame, for orbit  $\delta \mathbf{k}_{5/1}$ .

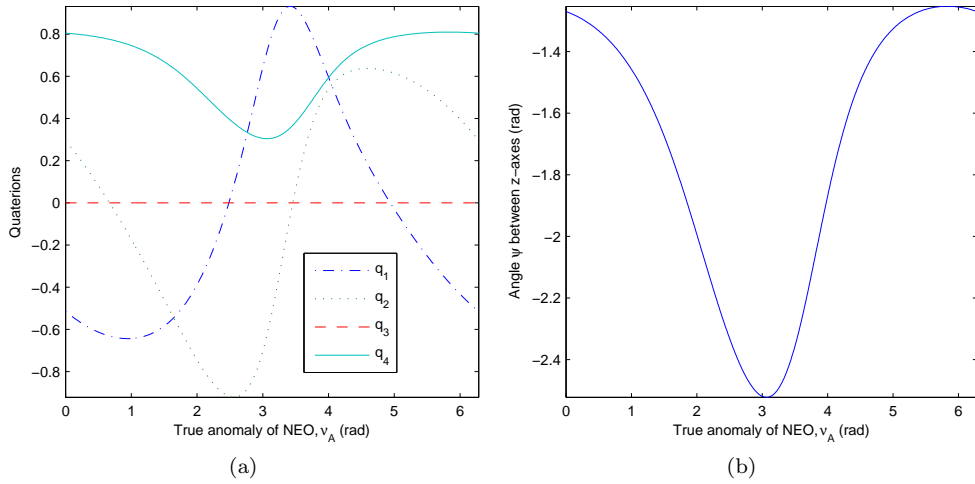


Figure 85: Quaternions and rotational angle  $\psi$  for transformation from inertial  $\mathcal{O}$  to camera  $\mathcal{Z}$  reference frame, for orbit  $\delta \mathbf{k}_{5/3}$ .

The asteroid is modelled as a series of discrete points composing a hollow ellipsoid, since we are only interested in the surface boundaries of the image (see Fig. 88a). The physical dimensions used to model Apophis are given in Table 13 (on pg. 51).

In Fig. 88a,  $[u, v, w]$  are the axes of inertia of a rotating ellipsoid. As not much is known about the rotational characteristics of Apophis, the smallest radius,  $w$  here, was nominally aligned with the direction of orbital momentum ( $\hat{z}^S$ ) with the asteroid rotating about  $w$  in the  $u$ - $v$  plane. Depending on the geometry of the spacecraft and camera, the points are projected onto the image plane and discretised according to the given pixel size, to account for the errors introduced by rasterisation.

A simple equation was used that estimates the average horizontal and vertical pixel locations within the asteroid image on the camera plane. If we defined a set  $\mathbf{p}$  of

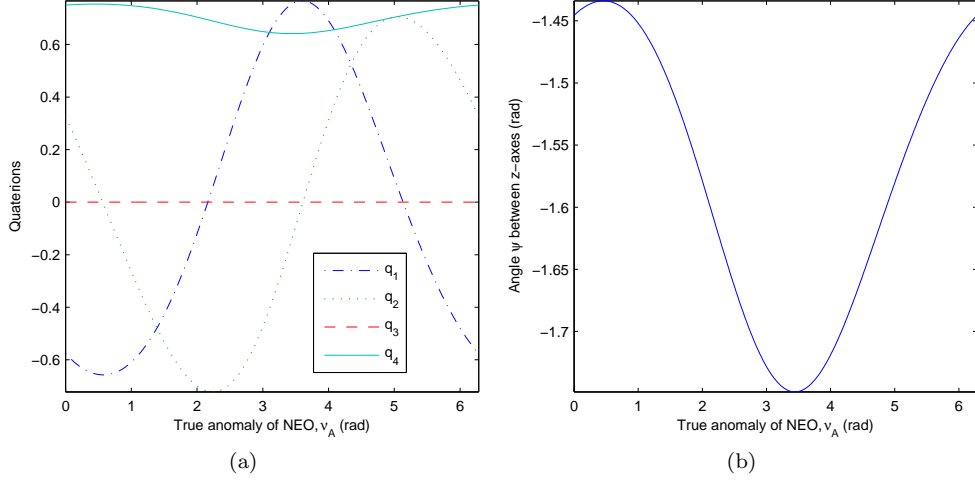


Figure 86: Quaternions and rotational angle  $\psi$  for transformation from inertial  $\mathcal{O}$  to camera  $\mathcal{Z}$  reference frame, for orbit  $\delta\mathbf{k}_{5/5}$ .

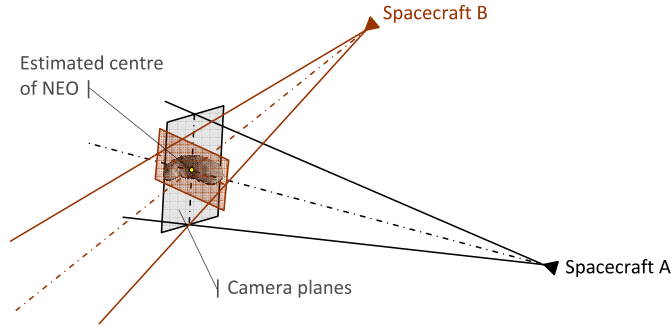


Figure 87: Navigation strategy using on-board cameras.

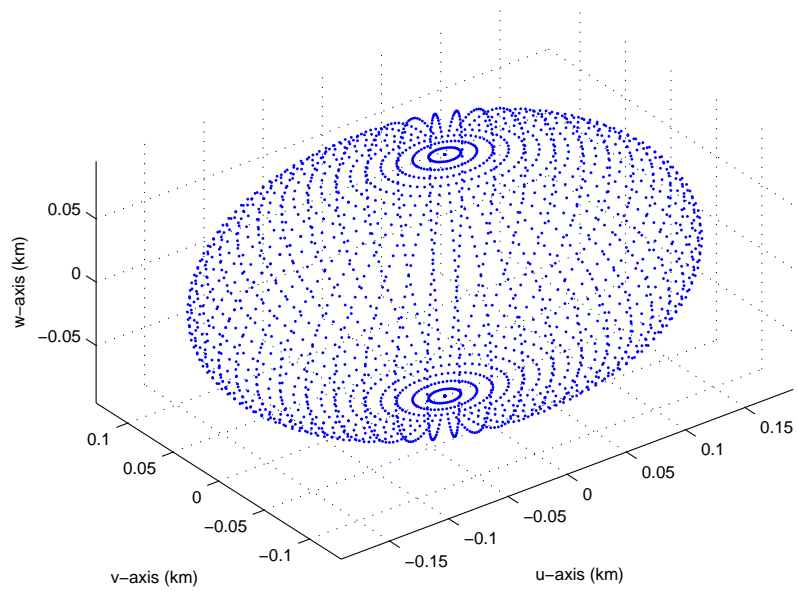
points on the surface of the NEO in 3D mapped onto the discretised 2D camera (or image) plane, then the estimated centre of the asteroid is defined as,

$$\begin{cases} \min \mathbf{p}_x^{\mathcal{Z}} + \frac{1}{2} (|\max \mathbf{p}_x^{\mathcal{Z}} - \min \mathbf{p}_x^{\mathcal{Z}}|) \\ \min \mathbf{p}_y^{\mathcal{Z}} + \frac{1}{2} (|\max \mathbf{p}_y^{\mathcal{Z}} - \min \mathbf{p}_y^{\mathcal{Z}}|) \end{cases} \quad (4.3)$$

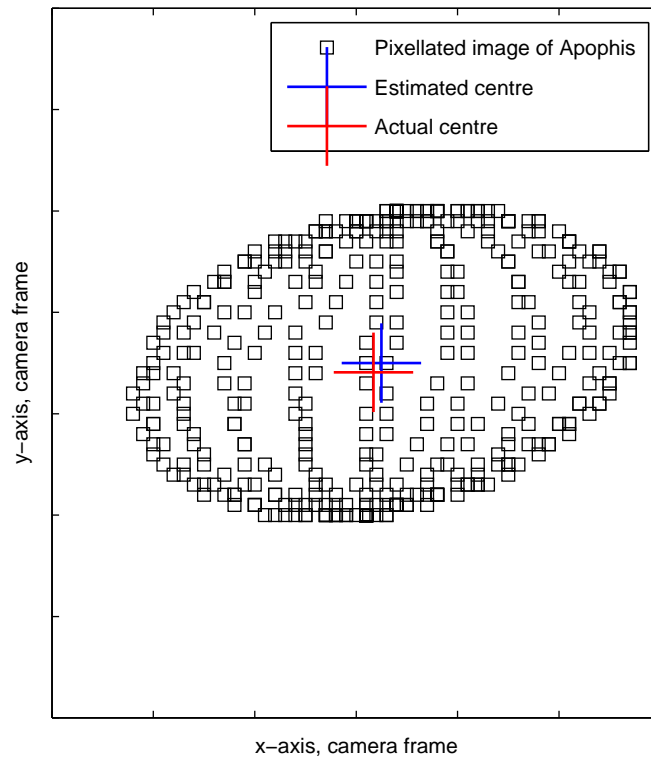
For this study, the approximation is sufficient however a more advanced algorithm is clearly necessary for future studies due to a number of sources of errors, such as the distortion of the image due to high elevation angles. Clipping errors are also a factor, since the vector of points  $\mathbf{p}$  given by the camera only contains those seen within the field-of-view (FOV) of the camera. For the simulation, the camera is designed with specification such that the entire asteroid can be contained with the FOV of the camera.

The estimation of the centre gives the angles – spacecraft-relative azimuth and elevation – required by the mirror pointing system, however the range is still outstanding.

If each camera is aligned with the centre of the image on the estimated centre of the asteroid, then all the cameras should be pointing along the spacecraft-asteroid vector. Logically then, the intersection point(s) of these beams will create the spot area. For



(a) Model of Apophis as a set of discrete surface points of an ellipsoid with dimensions  $R_u = 190.92$  m,  $R_v = 135.0$  m,  $R_w = 95.46$  m. [Delbò et al., 2007]



(b) Camera image view of the asteroid Apophis. The pixel size in this plot was enlarged to  $10 \times 10$  m in order to see the effects of rasterisation on the object.

Figure 88: Asteroid representations for navigation simulation.

this simulation, the centre of the NEO was used; in future studies, this should be adjusted to cross on the surface instead, accounting for the changes in range due to rotation.

The spacecraft-asteroid vector (i.e. from the camera to the centre of the NEO) in the inertial reference frame can be written in parametric form as,

$$\mathbf{x} = \mathbf{g}t + \mathbf{x}_0 \begin{cases} x = g_x t + x_0 \\ y = g_y t + y_0 \\ z = g_z t + z_0 \end{cases} \quad (4.4)$$

From a simulation point of view, with the angles determined, the only remaining factor to solve is  $t_a$  and  $t_b$  (corresponding to two nominal spacecraft,  $a$  and  $b$ ). This can be solved by a minimisation function (in this case `fminbnd` in Matlab) where  $t_a$  is the free variable. Fixing the direction of camera pointing vector  $z_a^{\mathcal{O}}$ , the intersection point is moved until the  $z_b^{\mathcal{O}}$  camera vector is aligned with the estimated centre of the asteroid from spacecraft  $b$ . Once  $\mathbf{x}$ ,  $\mathbf{x}_0$  and  $t$  are known, the parameter  $\mathbf{g}$  can be determined by solving the system of equations.

Measurement errors were introduced on the position estimate of the spacecraft in inertial space, and the attitude determination each spacecraft. Table 18 lists the three different sets of errors used in the simulations, depending on the accuracy of the onboard devices.

Table 18: Errors on positional and angular measurements.

		Error set A	Error set B	Error set C	Error set D
Position	m	0	5	100	1000
Angle	deg	0	0.003	0.01	0.001

The camera parameters are given in Table 19. For ease of simulation, all the parameters, such as the CCD matrix are assumed to be square, e.g.  $800 \times 800$  px instead of the more common  $600 \times 800$  px. Three different cameras configurations were used, representing good (A), poor (B), and optimal (C) which was used for testing only. The focal length is calculated by simple trigonometry,

$$f_l = \frac{ccd \times l_{px}}{\tan(fov)} \quad (4.5)$$

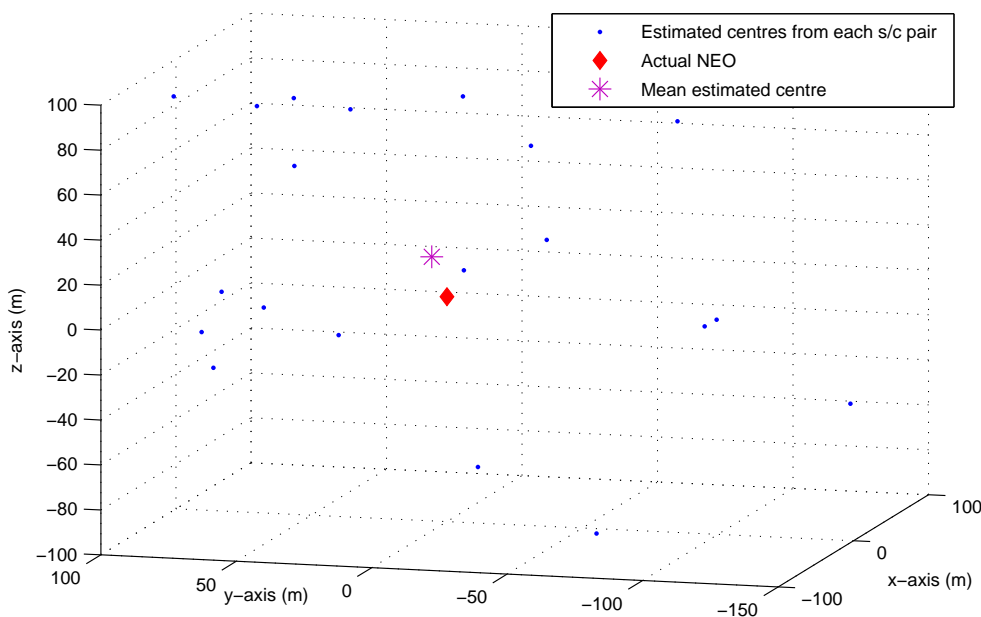
The variables are defined in Table 19. For reference, Apophis subtends a half-angle of 76.146 mrad, as seen from a distance of 2.5 km (the minimum distance from the formation).

To compensate for the errors introduced by rasterisation and pointing errors, the intersection points were calculated for each pair of spacecraft. Figure 89 shows the differences between the estimated centres determined by each spacecraft-pair combination relative to the actual centre, located at  $(0, 0)$ . A 5-spacecraft formation was used, giving 20 estimated values for the centre of the NEO in inertial space, with camera A and error set B, taken at a nominal true anomaly of  $\nu = 20^\circ$ .

Figures 90 – 100 show the mean and standard deviation of the set of estimated centres relative to the actual centre of Apophis in the heliocentric inertial reference frame  $\mathcal{O}$ , over one full orbit, for each camera and error set using the five-spacecraft formation given previously. Table 20 summaries the results.

Table 19: Parameters of on-board camera (all dimensions are assumed square).

		Camera A	Camera B	Camera C
Total field-of-view ( $fov$ )	deg	10	20	10
Pixel size ( $l_{px}$ )	m	$5 \times 10^{-7}$	$9 \times 10^{-6}$	$1 \times 10^{-12}$
CCD array dimensions ( $ccd$ )	pixels	1768	800	8000
Focal length ( $f_\ell$ )	m	$2.5067 \times 10^{-3}$	$9.8909 \times 10^{-3}$	$2.0417 \times 10^{-7}$

Figure 89: Positions of the estimated centres relative to the actual centre of Apophis with camera A and error set B, taken at a nominal true anomaly  $\nu = 20^\circ$ .

## 4.4 DISCUSSION

The method shown for the navigation works in principle provided that the position of the spacecraft is known with good accuracy. Although an accuracy of 1 km in position has to be expected for a single spacecraft in deep space, a formation can improve this accuracy by combining the intersatellite position measurements with the position measurement based on other navigation approaches. The use of intersatellite measurements, in fact, would filter out all position errors with opposite sign. A substantial improvement in the estimation of the position of the spacecraft was theoretically proven for the mission LISA in a recent study by Chung (2006).

Furthermore, note that the algorithm used to isolate the centre from the 2D image plane is overly simplistic and does not use measurements over long arcs. In addition, for the orbits chosen, the spacecraft are often in close proximity to each other, reducing the accuracy of the differential measurements. This can be seen when the standard deviation of the measurements increases around the periapsis.

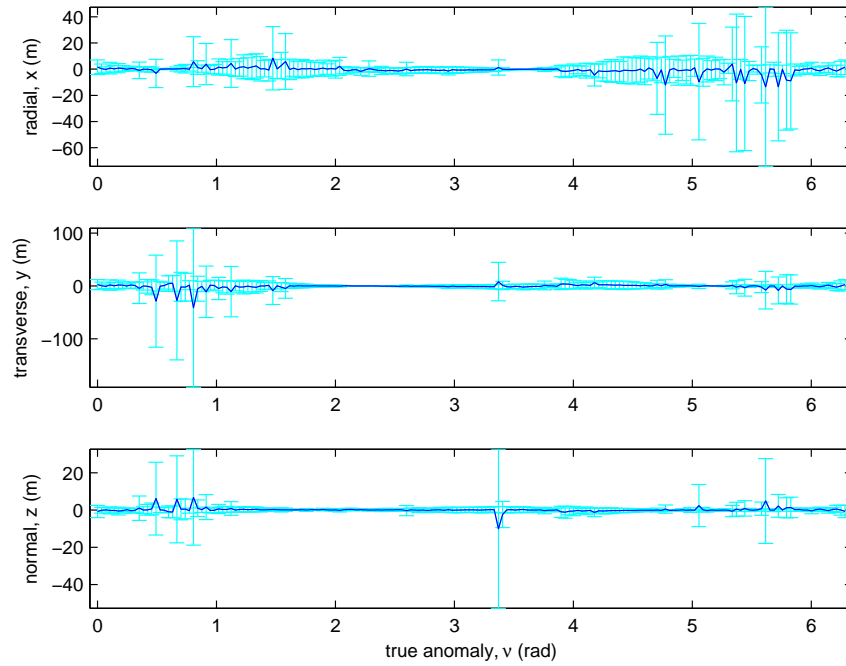
A more selective analysis of spacecraft orbits would certainly improve the estimation. The simulations assumed that the asteroid was a geometric object with no

Table 20: Error range statistics on the estimation of the NEO inertial position, for the 5 spacecraft formation.

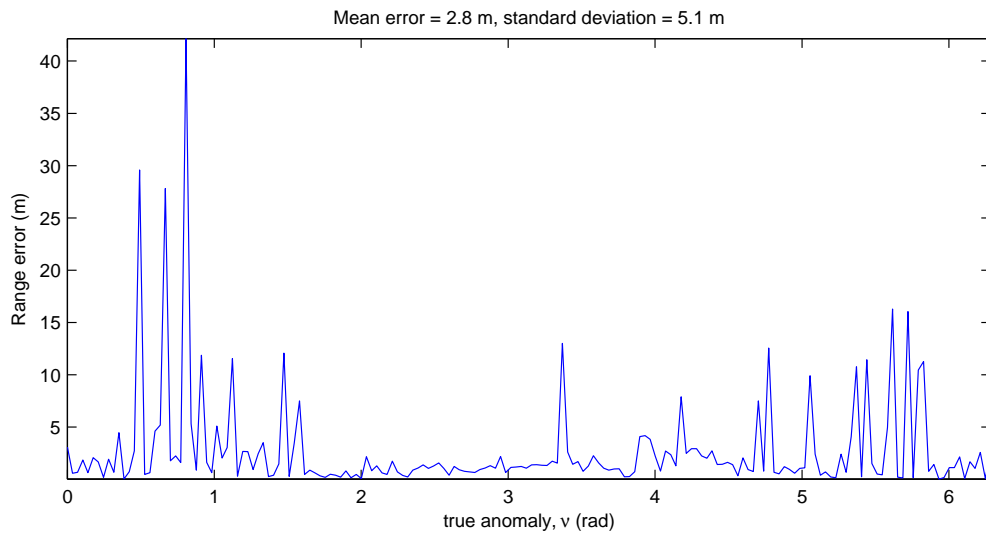
Camera	Error set	Range error (m)			
		Minimum	Maximum	Mean	Standard deviation
A	A	0.038741	42.144	2.7655	5.075
	B	0.39318	42.561	3.172	4.9803
	C	3.2068	47.556	20.936	8.9259
	D	15.345	482.42	211.65	88.157
B	A	0.093827	74.272	13.015	15.291
	B	0.47067	74.552	13.106	15.182
	C	4.9653	85.625	25.411	14.178
	D	23.193	598.64	211.02	97.729
C	A	0.04022	11.43	1.0995	1.2739
	B	0.32809	12.086	1.6174	1.2267
	C	4.4508	47.886	20.343	8.6189

irregularities in the surface beyond those introduced by rasterisation. Moreover, the NEO will be partially in shadow, or eclipse, which the algorithm will have to compensate for. Therefore, the irregular shape of the asteroid should be known in advance or better the ellipsoid enveloping the true shape of the asteroid should be known in advance.

Lastly, if the laser option is considered the quality of the beam needs to be controlled during the operations. Existing studies and patents [Bennett, 2005] suggest that this is feasible with an evolution of current technology.

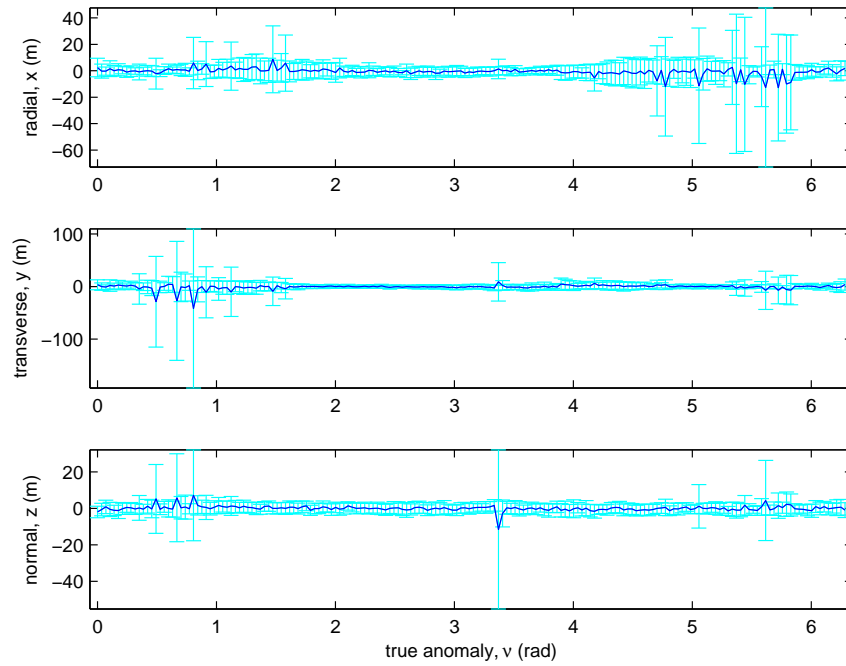


(a) Error on centre estimate in Hill frame components.

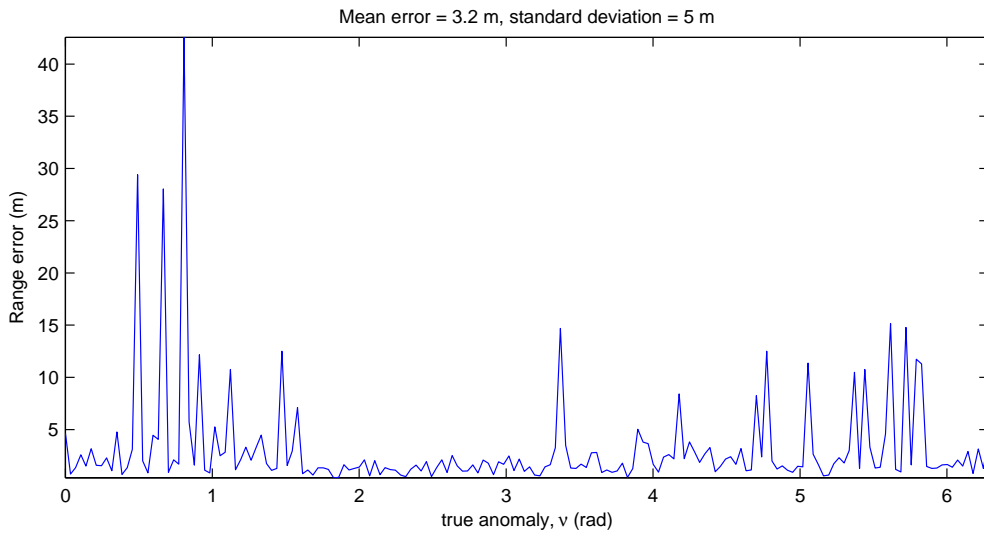


(b) Error on distance.

Figure 90: Mean and standard deviation (shown as error bars) of estimated centres relative to the actual centre of Apophis in the heliocentric inertial reference frame  $\mathcal{O}$ , over one full orbit using 5 spacecraft each with camera A, error set A (no errors).

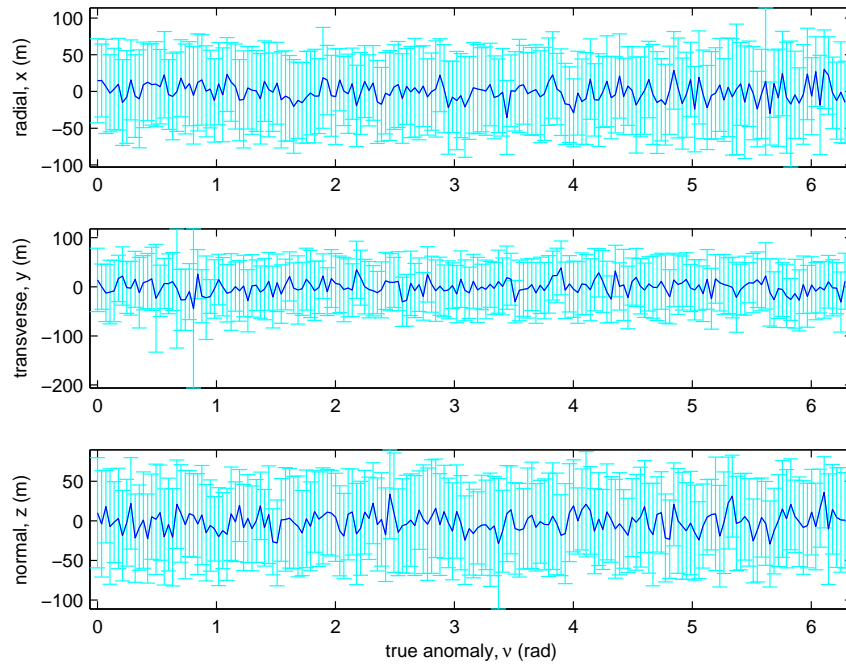


(a) Error on centre estimate in Hill frame components.

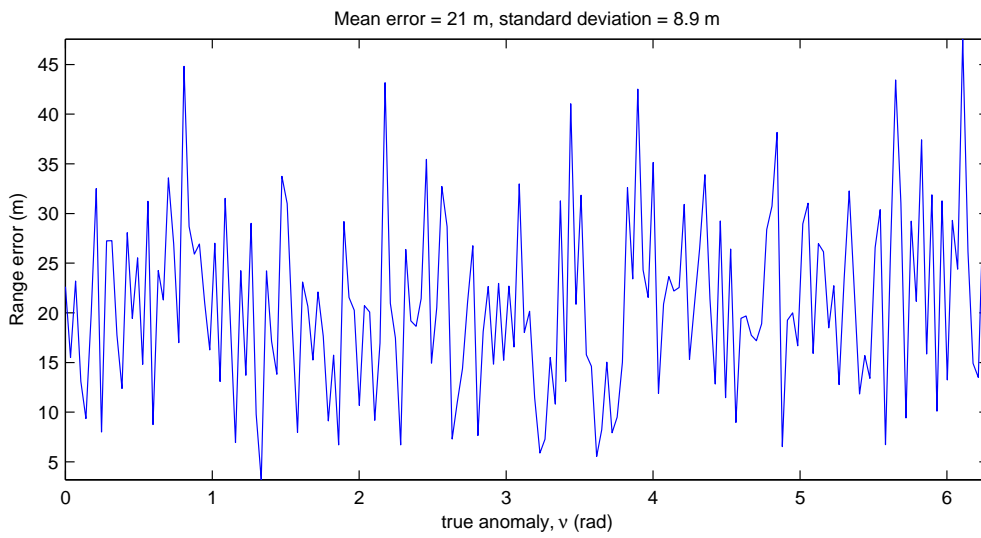


(b) Error on distance.

Figure 91: Mean and standard deviation (shown as error bars) of estimated centres relative to the actual centre of Apophis in the heliocentric inertial reference frame  $\mathcal{O}$ , over one full orbit using 5 spacecraft each with camera A, error set B.

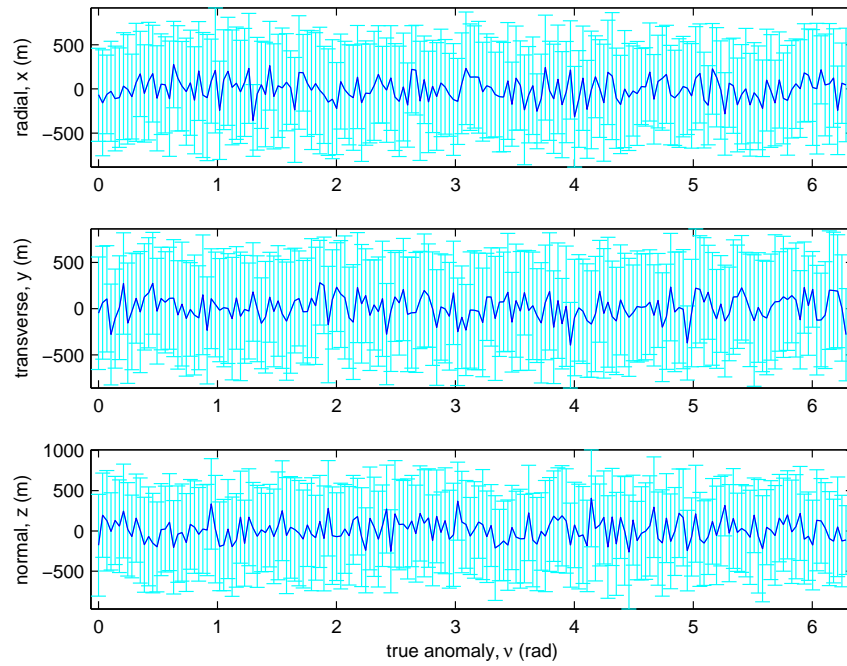


(a) Error on centre estimate in Hill frame components.

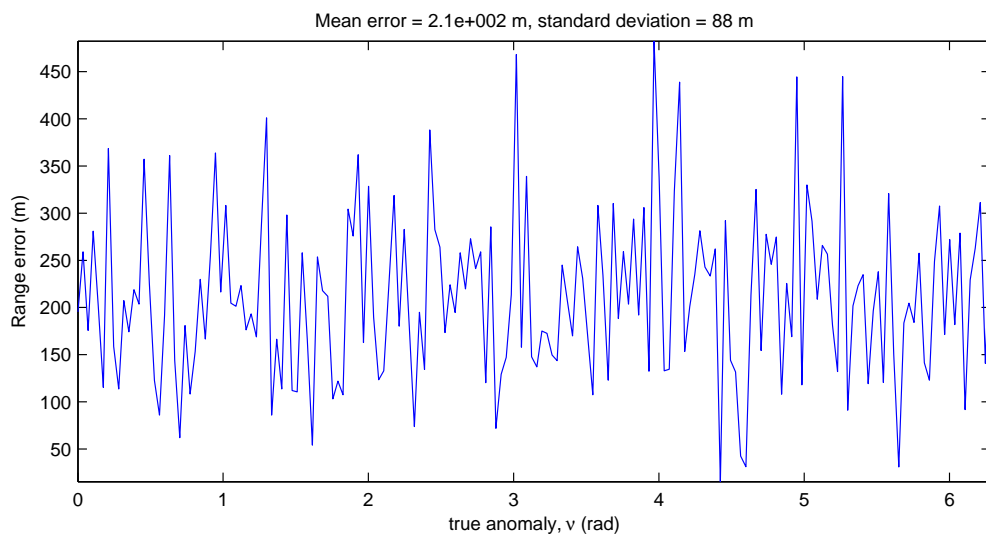


(b) Error on distance.

Figure 92: Mean and standard deviation (shown as error bars) of estimated centres relative to the actual centre of Apophis in the heliocentric inertial reference frame  $\mathcal{O}$ , over one full orbit using 5 spacecraft each with camera A, error set C.

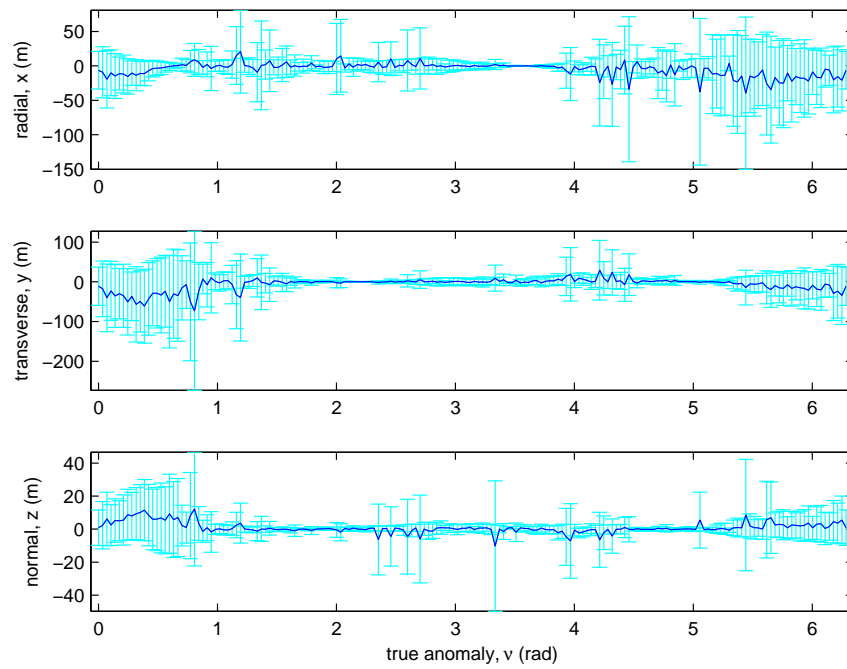


(a) Error on centre estimate in Hill frame components.

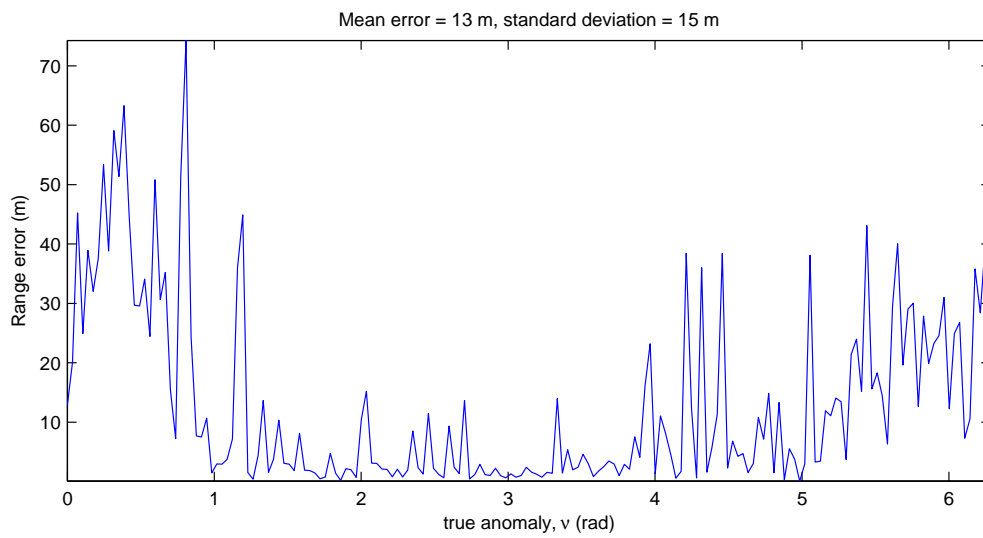


(b) Error on distance.

Figure 93: Mean and standard deviation (shown as error bars) of estimated centres relative to the actual centre of Apophis in the heliocentric inertial reference frame  $\mathcal{O}$ , over one full orbit using 5 spacecraft each with camera A, error set D.

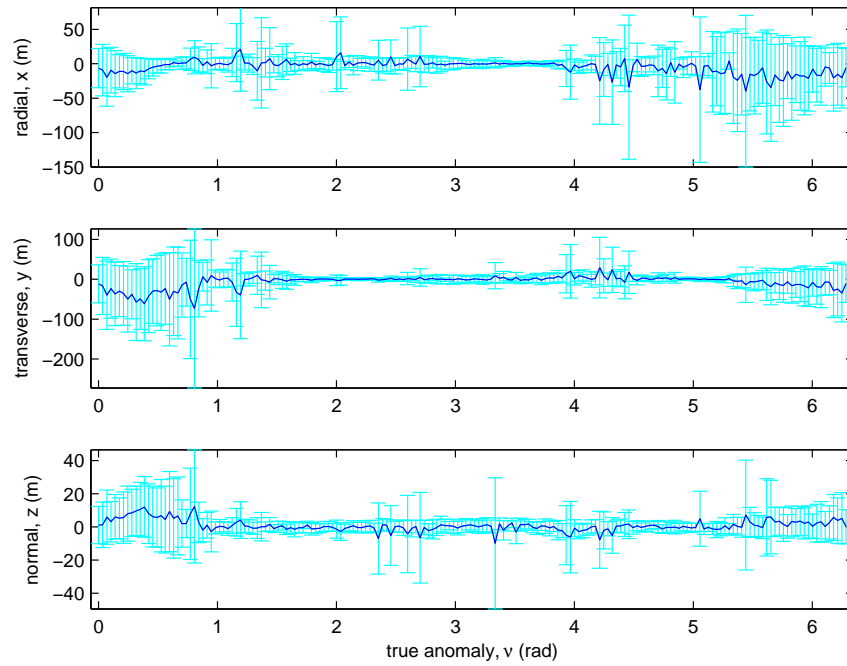


(a) Error on centre estimate in Hill frame components.

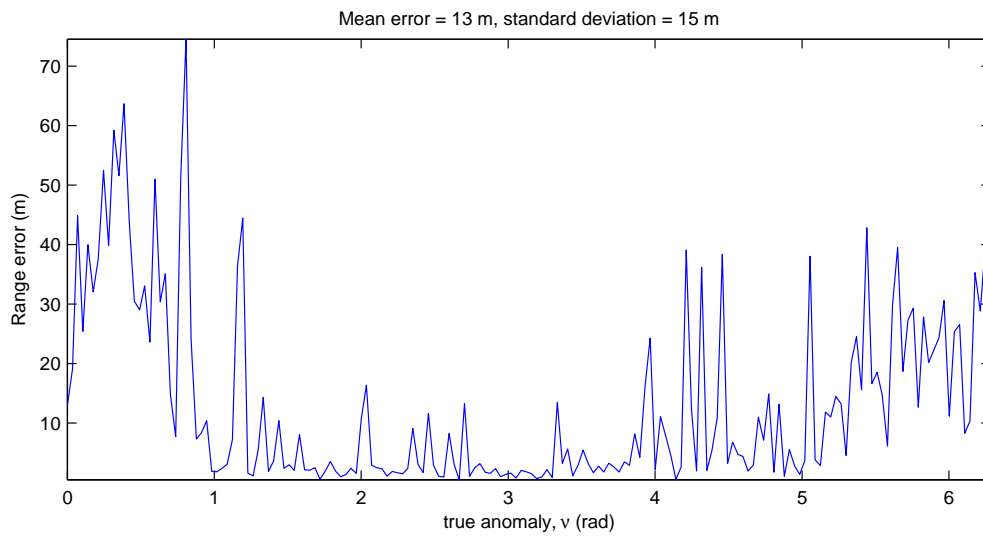


(b) Error on distance.

Figure 94: Mean and standard deviation (shown as error bars) of estimated centres relative to the actual centre of Apophis in the heliocentric inertial reference frame  $\mathcal{O}$ , over one full orbit using 5 spacecraft each with camera B, error set A (no errors).

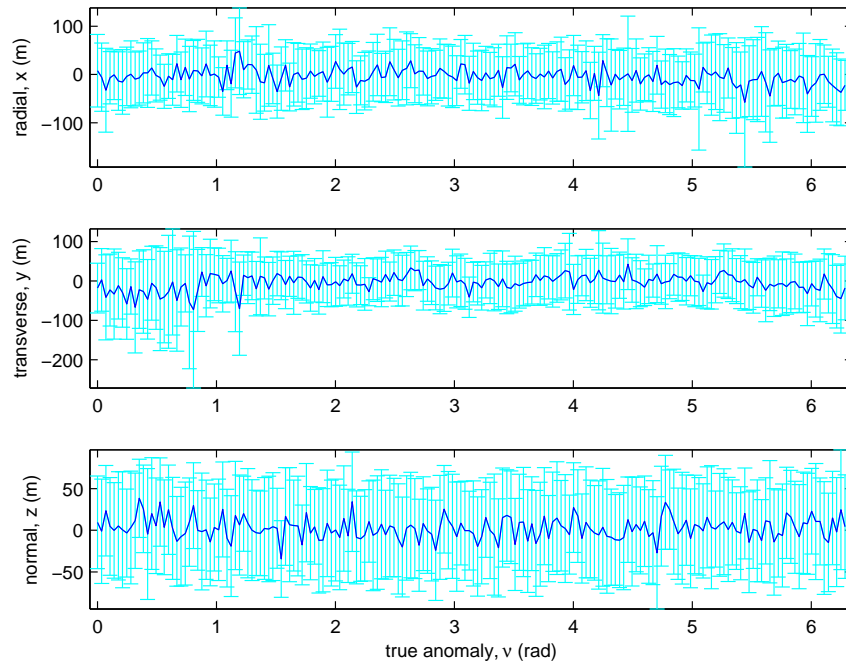


(a) Error on centre estimate in Hill frame components.

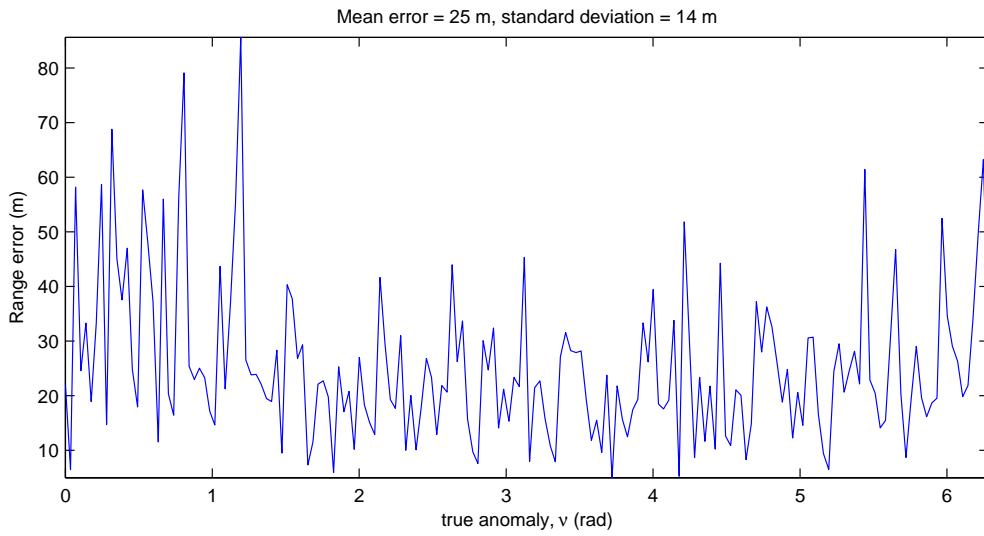


(b) Error on distance.

Figure 95: Mean and standard deviation (shown as error bars) of estimated centres relative to the actual centre of Apophis in the heliocentric inertial reference frame  $\mathcal{O}$ , over one full orbit using 5 spacecraft each with camera B, error set B.

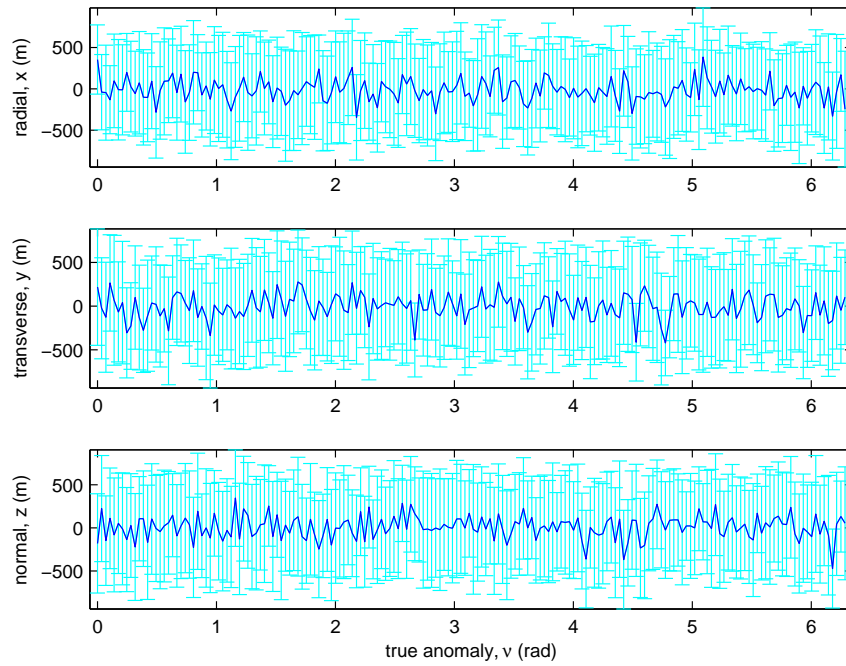


(a) Error on centre estimate in Hill frame components.

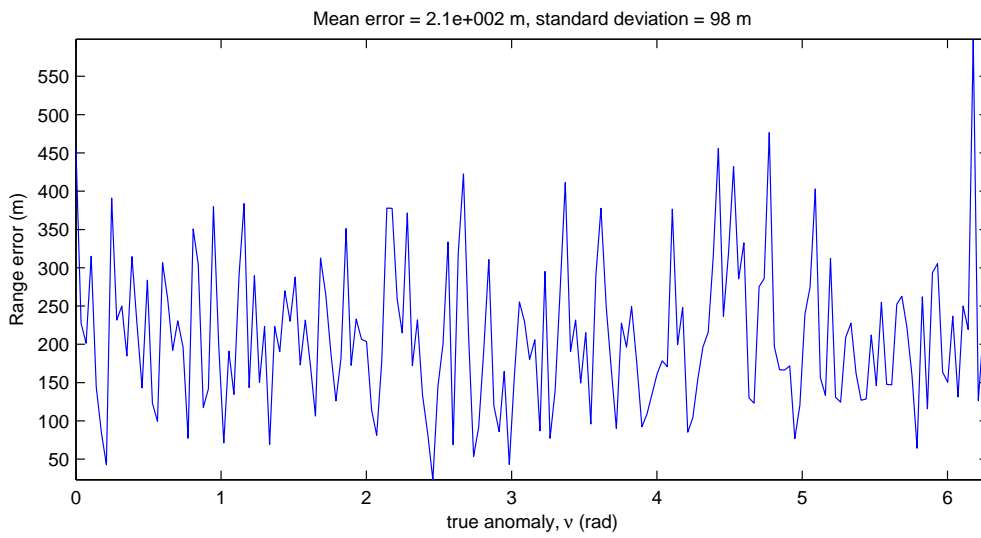


(b) Error on distance.

Figure 96: Mean and standard deviation (shown as error bars) of estimated centres relative to the actual centre of Apophis in the heliocentric inertial reference frame  $\mathcal{O}$ , over one full orbit using 5 spacecraft each with camera B, error set C.

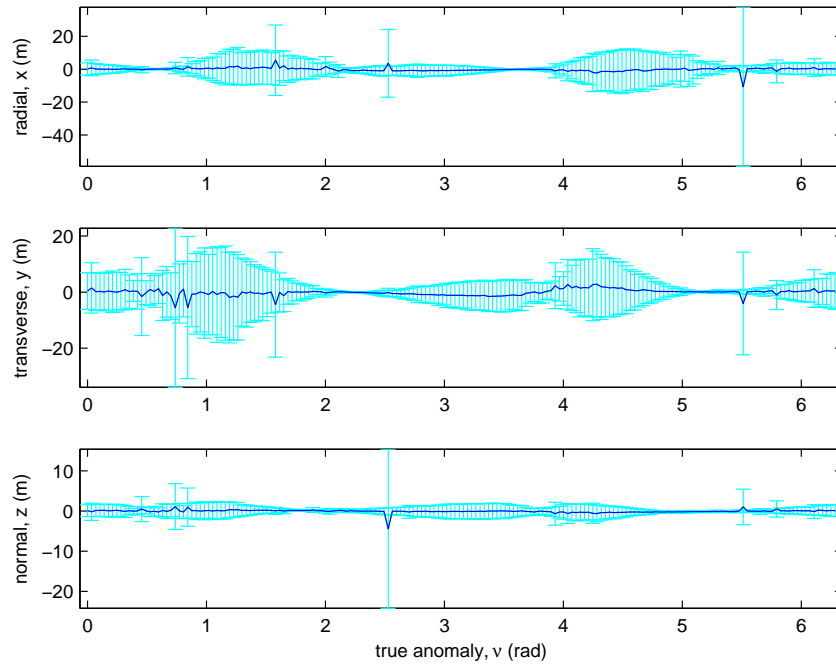


(a) Error on centre estimate in Hill frame components.

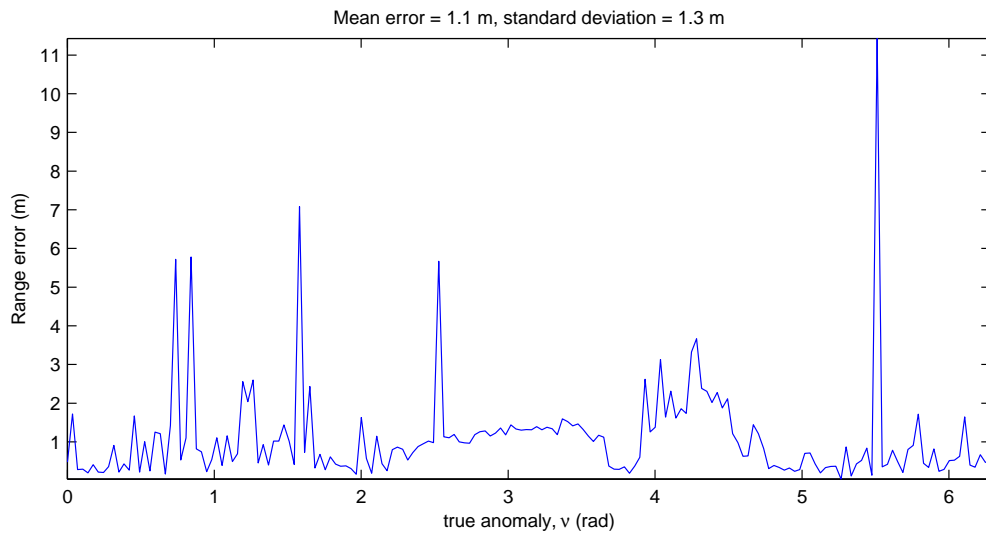


(b) Error on distance.

Figure 97: Mean and standard deviation (shown as error bars) of estimated centres relative to the actual centre of Apophis in the heliocentric inertial reference frame  $\mathcal{O}$ , over one full orbit using 5 spacecraft each with camera B, error set D.

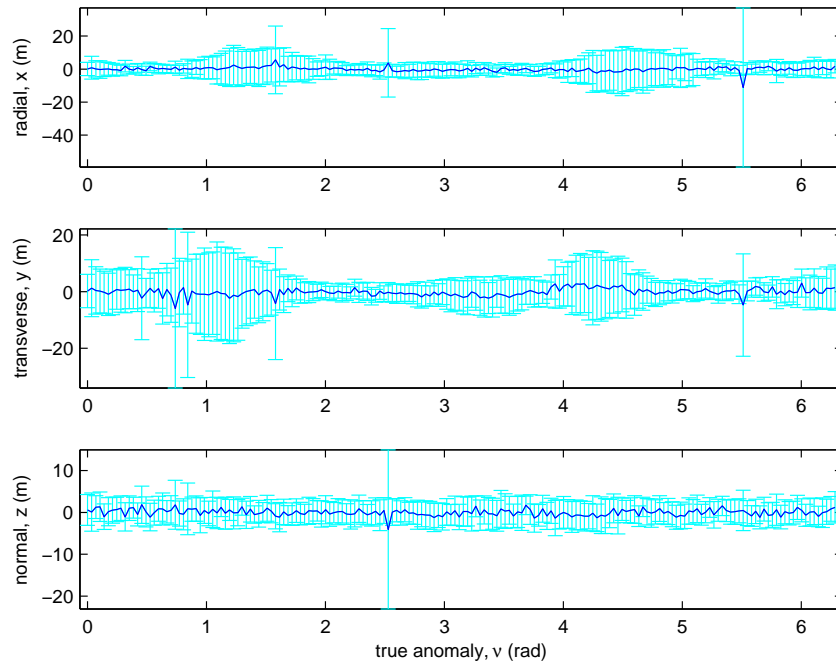


(a) Error on centre estimate in Hill frame components.

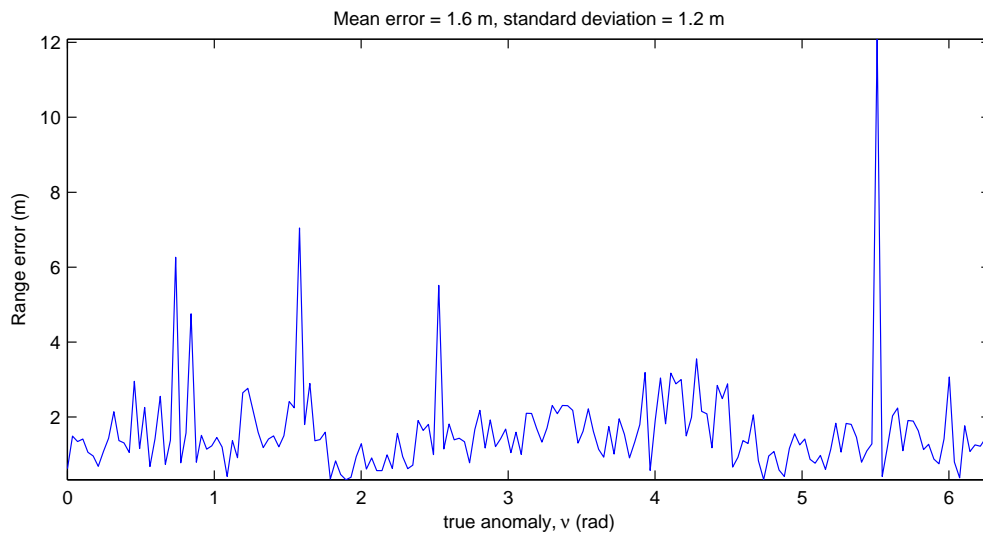


(b) Error on distance.

Figure 98: Mean and standard deviation (shown as error bars) of estimated centres relative to the actual centre of Apophis in the heliocentric inertial reference frame  $\mathcal{O}$ , over one full orbit using 5 spacecraft each with camera C, error set A (no errors).

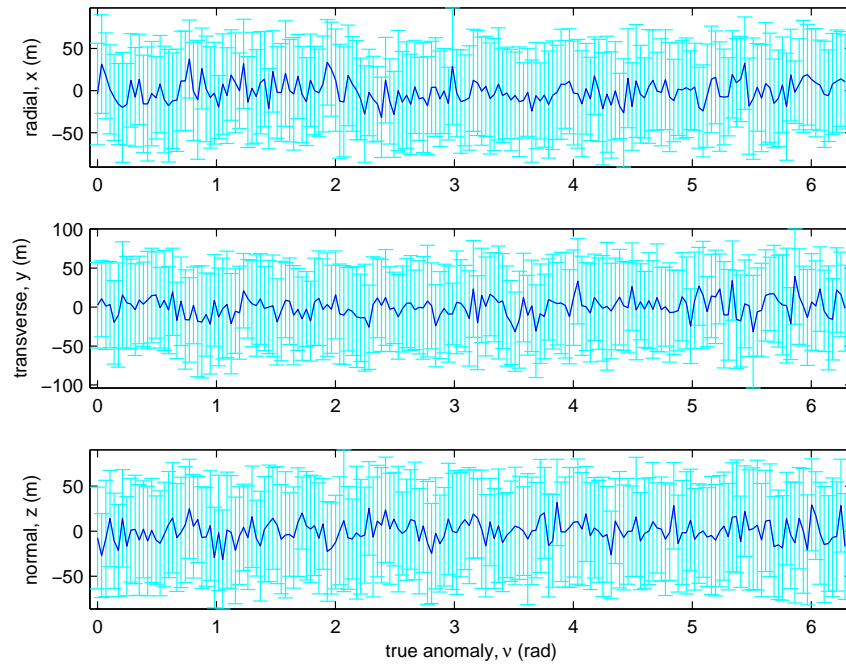


(a) Error on centre estimate in Hill frame components.

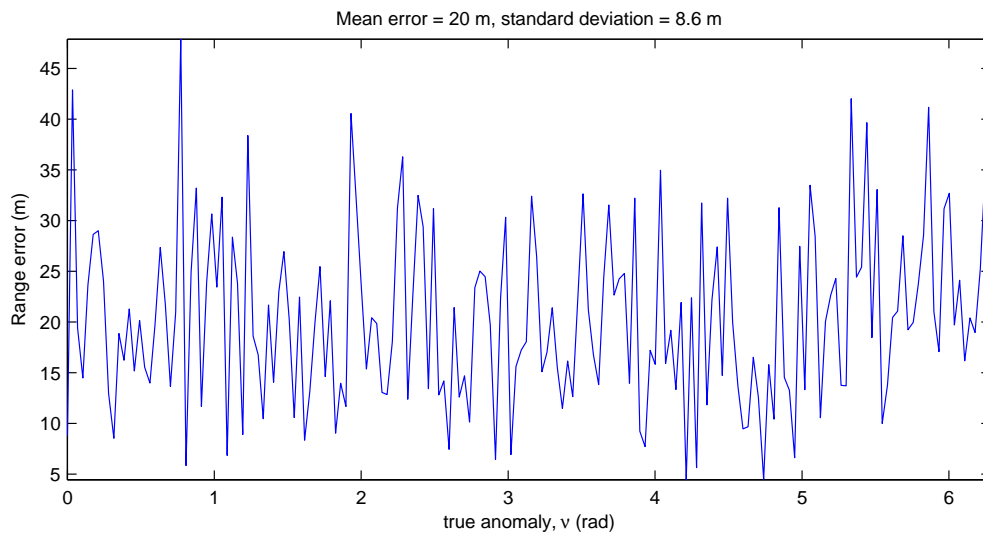


(b) Error on distance.

Figure 99: Mean and standard deviation (shown as error bars) of estimated centres relative to the actual centre of Apophis in the heliocentric inertial reference frame  $\mathcal{O}$ , over one full orbit using 5 spacecraft each with camera C, error set B.



(a) Error on centre estimate in Hill frame components.



(b) Error on distance.

Figure 100: Mean and standard deviation (shown as error bars) of estimated centres relative to the actual centre of Apophis in the heliocentric inertial reference frame  $\mathcal{O}$ , over one full orbit using 5 spacecraft each with camera C, error set C.

The dinosaurs became extinct because they didn't have a space program. And if we become extinct because we don't have a space program, it'll serve us right!

*Larry Niven*

This chapter ties together the simulation models developed previously for the asteroid, orbital dynamics and deflection method. In order to reduce the simulation time, the control law was removed. A number of free variables exist in the design of the mission: the number of spacecraft in the formation  $n_{sc}$ , the warning time  $t_{warn}$  and thrust duration  $t_{thrust}$  or target deflection distance, the concentration ratio  $C_r$ , size/surface area of the mirrors or spacecraft mass, and system efficiency depending on the design used.

### 5.1 SIMULATION RESULTS

Figures 102–103 provide an estimation of the required operation time, along the  $x$  axis, against the concentration ratio for different warning times (i.e., time from the beginning of the deflection operation to the date of the forecasted impact) and two different estimated masses of Apophis for each of the two systems. The warning times are given as multiples of the orbital period of the NEO ( $T_A = 323.5599$  days) instead of Earth years, such that the starting true anomaly is always the same. Due to the eccentricity of the orbit of Apophis, the effect of the thrust on the deflection distance changes depending on the orbital location.

Figure 104 show the differences in required thrust time for a set of warning times between 4–6  $T_A$ , or 1294–1941 days prior to the  $t_{MOID}$  on 13 April 2036 (64796.56736 MJD). The thrust duration is plotted against both the true anomaly of the NEO at the start of the thrust segment (Fig. 104a), and the warning time (Fig. 104b).

Figure 105 shows the total expelled mass, from  $\dot{m}_{exp}$  in (3.31), versus a fixed value of the ‘system’ concentration ratio, i.e. the number of spacecraft times the concentration ratio of each individual spacecraft. It is clearly shown in the plot that for a larger number of spacecraft (e.g., 5) with a smaller individual concentration ratio, a greater thrust and hence deflection can be achieved. Figure 105 also shows that below a given number of spacecraft and a given concentration ratio (lower left corner of the plot), deviating the asteroid is not possible. The power density is too low and the sublimation process does not start.

Figures 106 – 124 show the achieved deflection distance at the MOID with the Earth in 2036 ( $t_{MOID} = 13252.06736$  MJD2000) versus a given number of spacecraft, concentration ratios, different warning  $t_{warn}$  and thrusting times  $t_{thrust}$ , a fixed aperture diameter of the primary mirror ( $d_M$ ) and system power efficiency ( $\eta_{sys}$ ). In the case of the laser system, the efficiency is set to 25%, whereas for the direct imaging, a

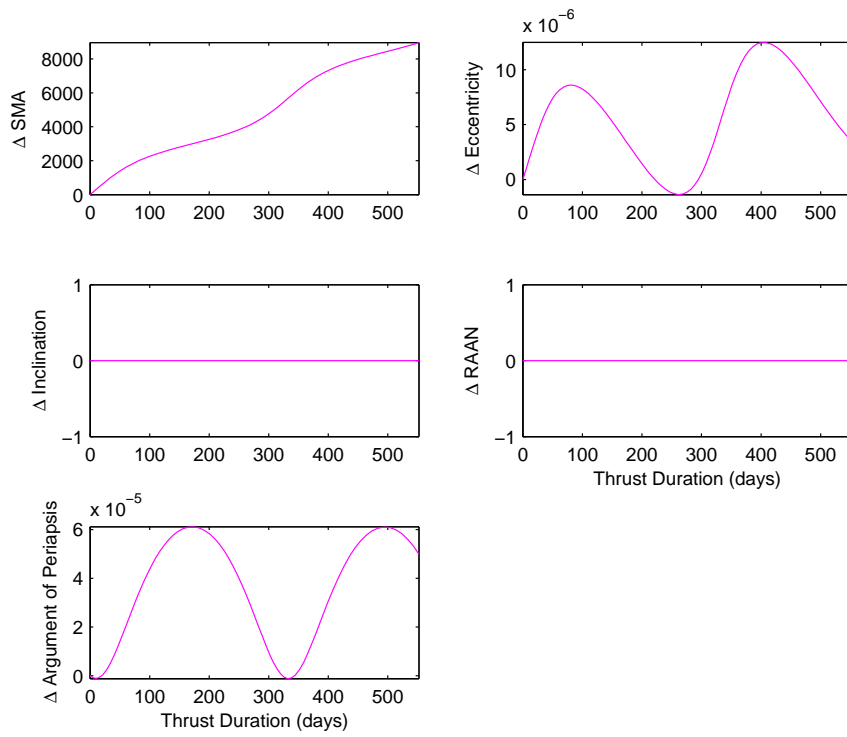


Figure 101: Deviation of Keplerian elements for Apophis, with a warning time of 5 years before the 2036 potential impact for a deviation distance of 384400 km in 2036.

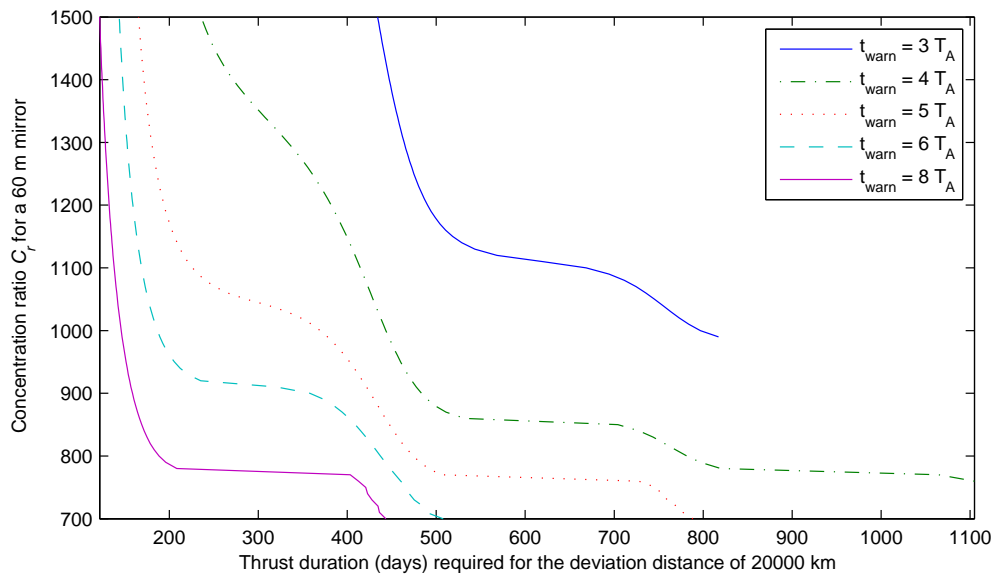
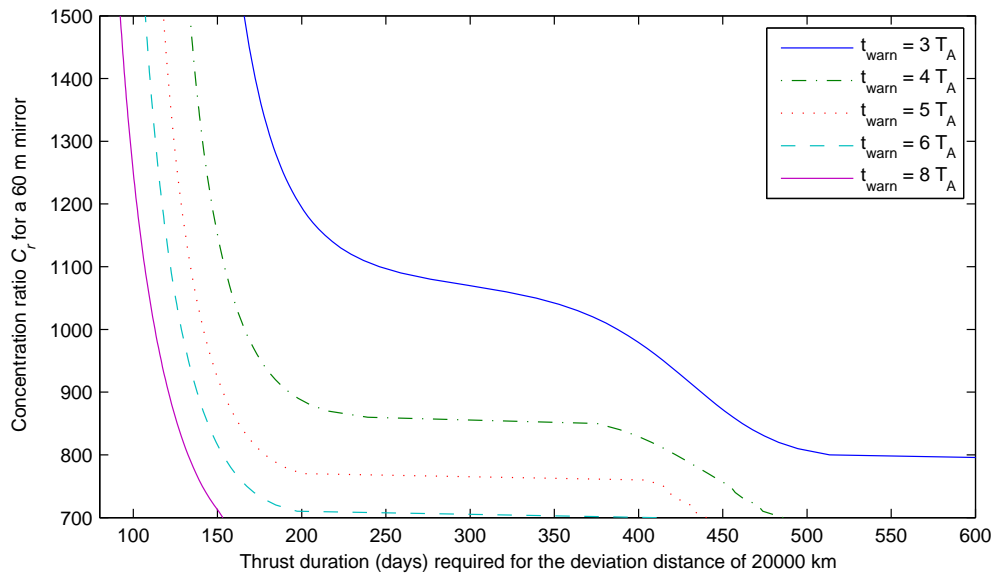


Figure 102: Concentration ratio vs required thrust time for a single 60 m diameter mirror using direct imaging to achieve a deflection of 20000 km at the 2036 MOID.

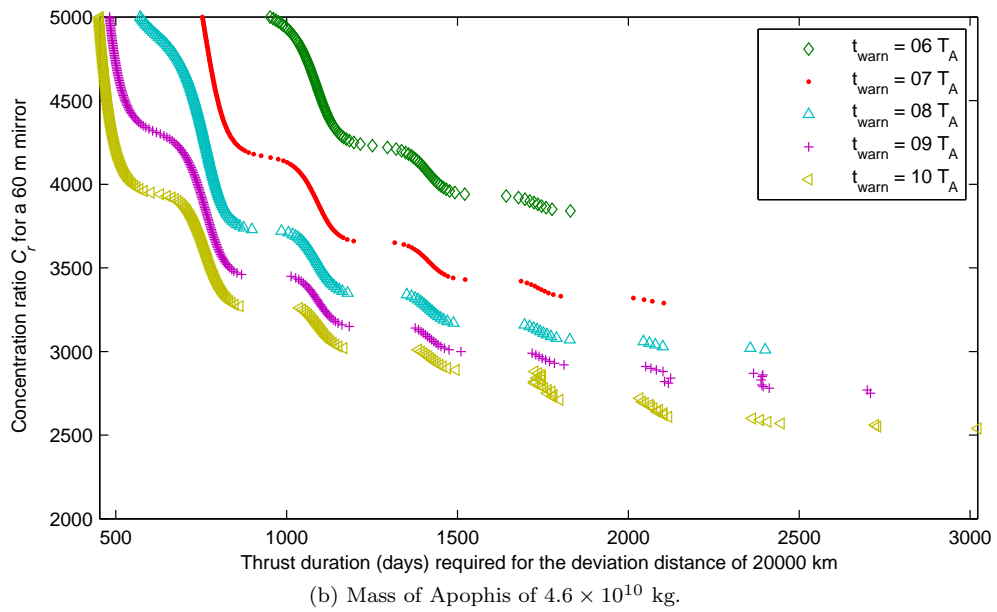
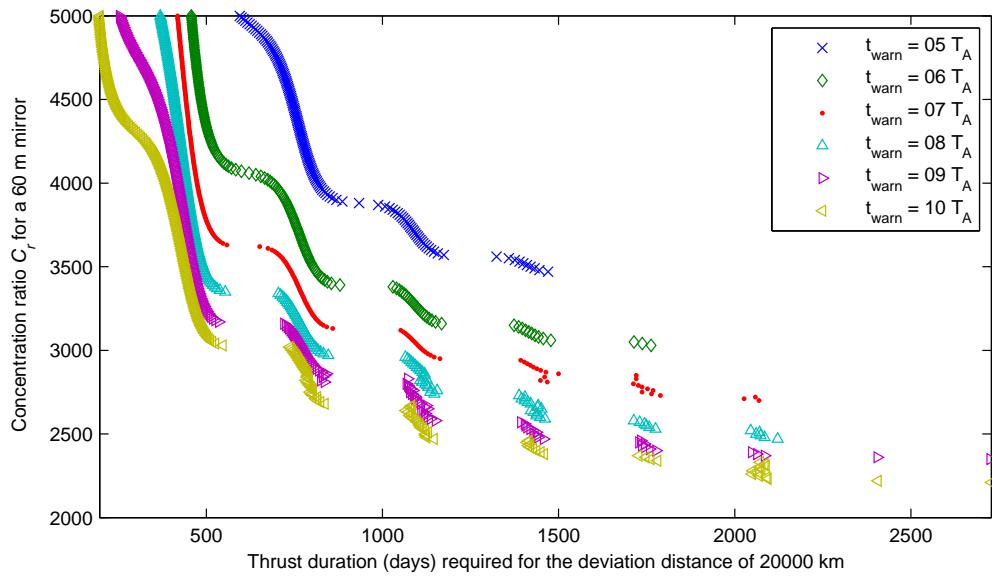


Figure 103: Concentration ratio vs required thrust time for a single 60 m diameter mirror using the laser to achieve a deflection of 20000 km at the 2036 MOID.

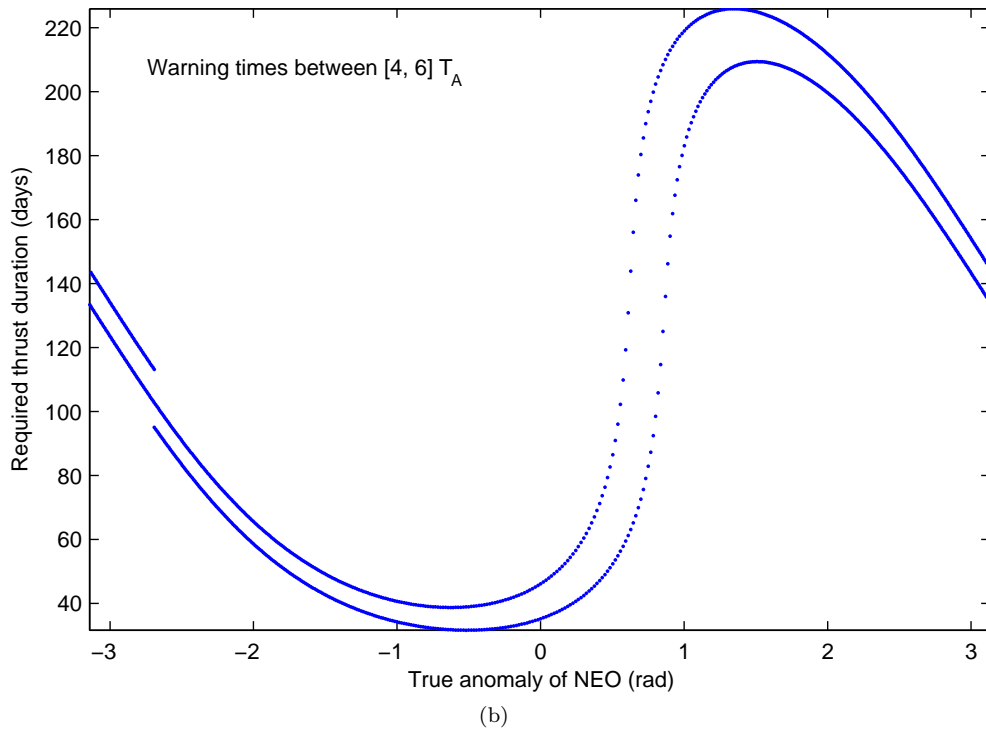
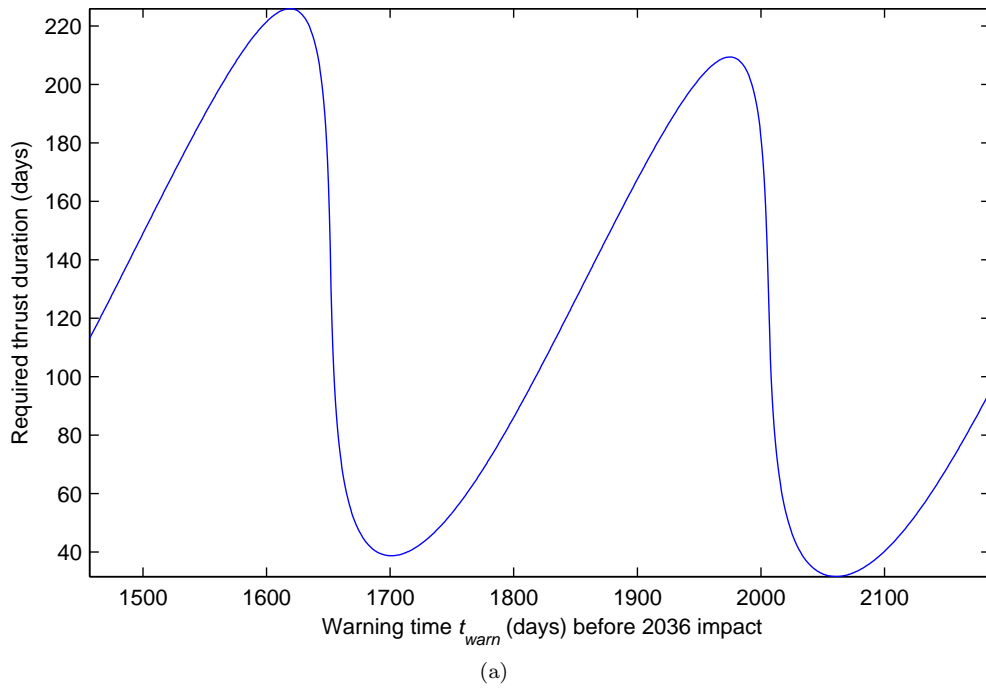


Figure 104: Effect of orbital location at the start of thrust period, on the required duration to achieve a deflection of 10000 km at  $t_{\text{MOID}} = 64796.56736$  MJD using a single 60 m mirror with direct imaging ( $C_r = 1000$ ).

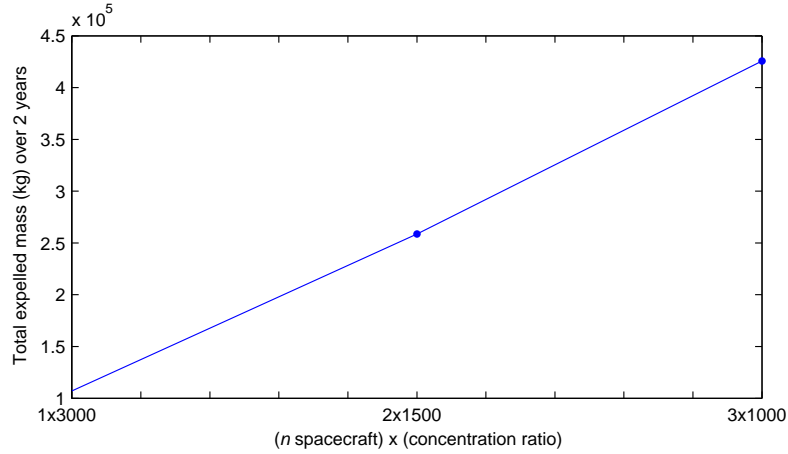
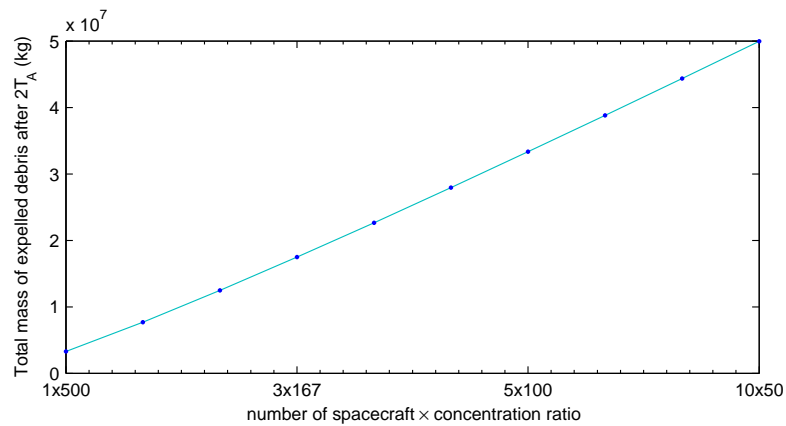
(a) Fixed mirror configuration with laser,  $\eta_{sys} = 25\%$ .(b) Adaptive mirror configuration with direct imaging,  $\eta_{sys} = 90\%$ .

Figure 105: Total asteroid debris mass expelled by sublimation vs a system concentration factor which is composed of the number of spacecraft in the formation multiplied by the individual concentration ratio of each onboard focusing system.

system efficiency of 90% was used. The thrust leg is assumed to start at  $(t_{\text{MOID}} - t_{\text{warn}})$ , and thrust continuously until  $(t_{\text{MOID}} - t_{\text{warn}} + t_{\text{thrust}})$ .

Following the trends in all the simulations, it can clearly be seen that increasing the concentration ratio does not improve the total deviation distance. According to the thrust model in (3.31) and (3.35), the thrust magnitude depends on the input power and surface area illuminated by the beam. As the concentration ratio increases, the area, for a fixed size mirror, decreases and therefore the thrust does not improve. On the other hand, increasing the number of spacecraft and superimposing the beams increases the power density while leaving the size of the spot area unchanged. Therefore, for a larger deflection for the same mirror surface area, the better strategy is to increase the number of spacecraft, each with constant concentration ratio.

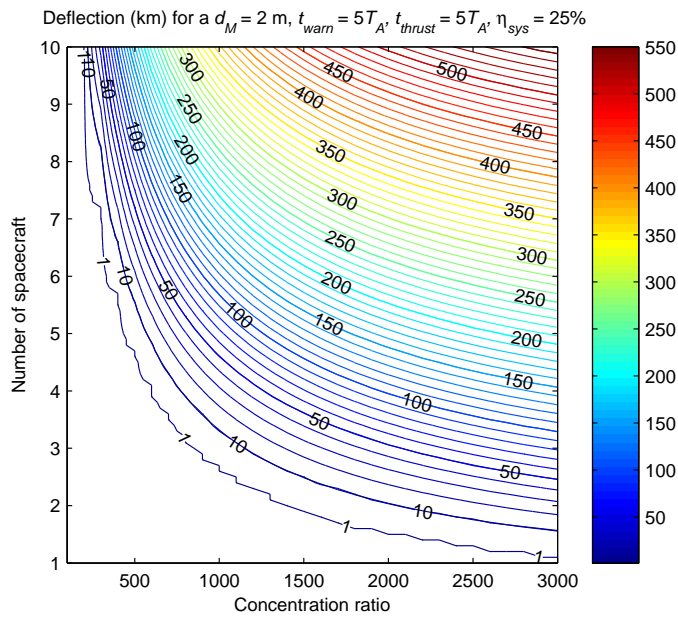


Figure 106: Deflection distance for various concentration ratios and number of spacecraft, assuming a 2 m aperture diameter primary mirror with laser ( $\eta_{sys} = 25\%$ ), a warning time of  $5T_A$  (1617 days), and a thrust period of  $5T_A$  (1617 days).

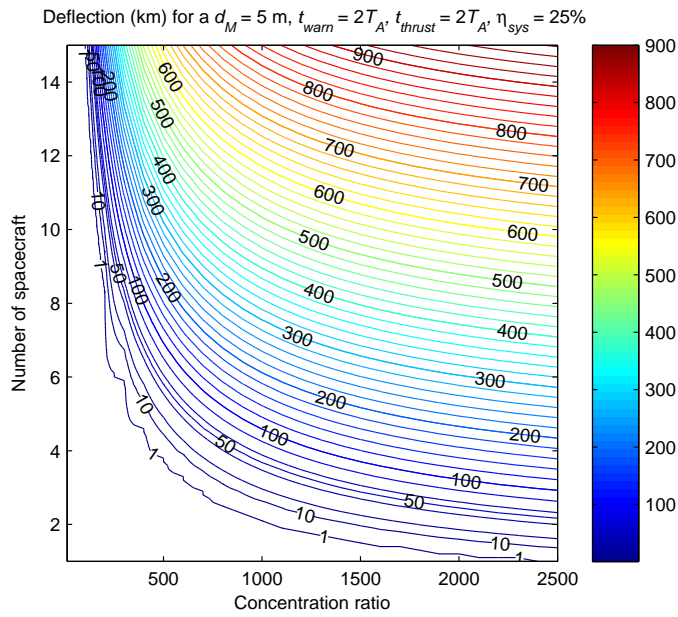


Figure 107: Deflection distance for various concentration ratios and number of spacecraft, assuming a 5 m aperture diameter primary mirror with laser ( $\eta_{sys} = 25\%$ ), a warning time of  $2T_A$  (647 days), and a thrust period of  $2T_A$  (647 days).

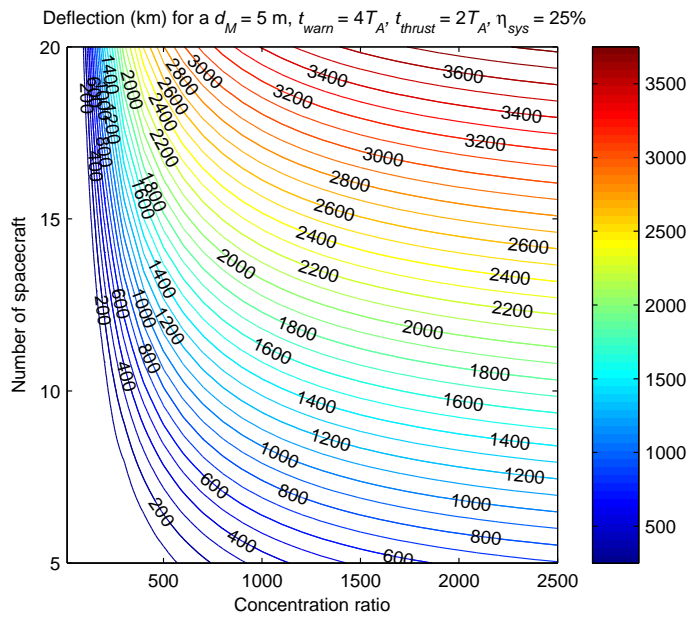


Figure 108: Deflection distance for various concentration ratios and number of spacecraft, assuming a 5 m aperture diameter primary mirror with laser ( $\eta_{sys} = 25\%$ ), a warning time of  $4T_A$  (1294 days), and a thrust period of  $2T_A$  (647 days).

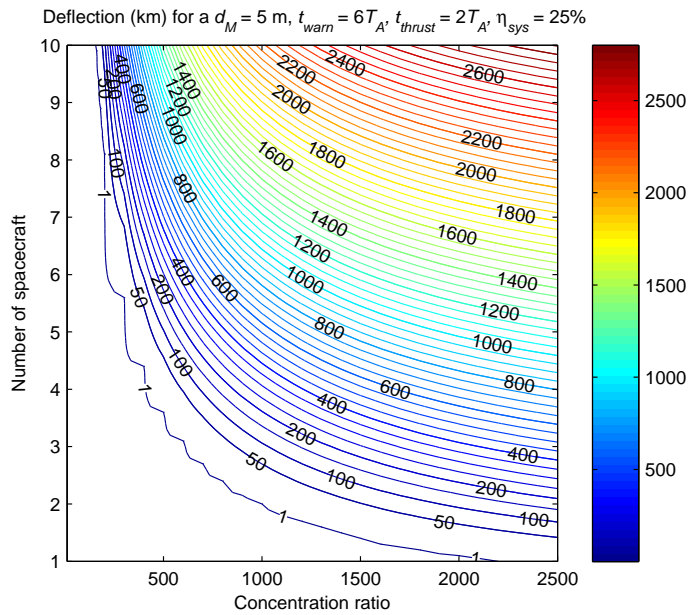


Figure 109: Deflection distance for various concentration ratios and number of spacecraft, assuming a 5 m aperture diameter primary mirror with laser ( $\eta_{sys} = 25\%$ ), a warning time of  $6T_A$  (1941 days), and a thrust period of  $2T_A$  (647 days).

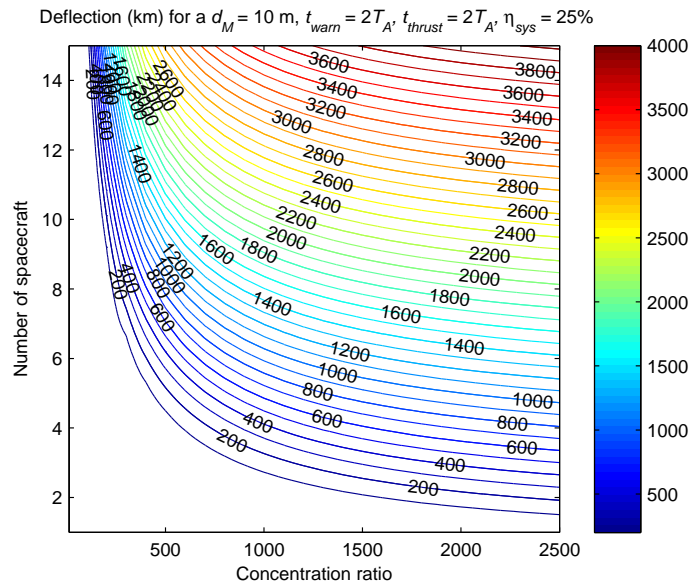


Figure 110: Deflection distance for various concentration ratios and number of spacecraft, assuming a 10 m aperture diameter primary mirror with laser ( $\eta_{sys} = 25\%$ ), a warning time of  $2T_A$  (647 days), and a thrust period of  $2T_A$  (647 days).

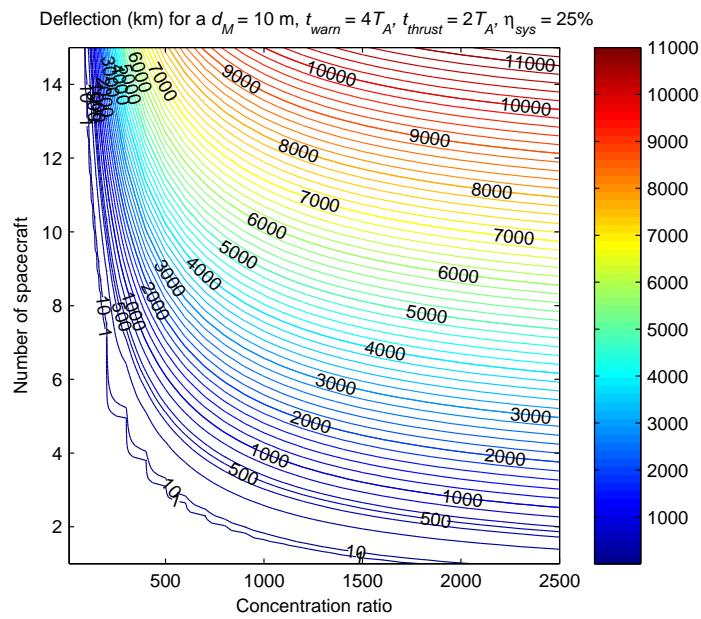


Figure 111: Deflection distance for various concentration ratios and number of spacecraft, assuming a 10 m aperture diameter primary mirror with laser ( $\eta_{sys} = 25\%$ ), a warning time of  $4T_A$  (1294 days), and a thrust period of  $2T_A$  (647 days).

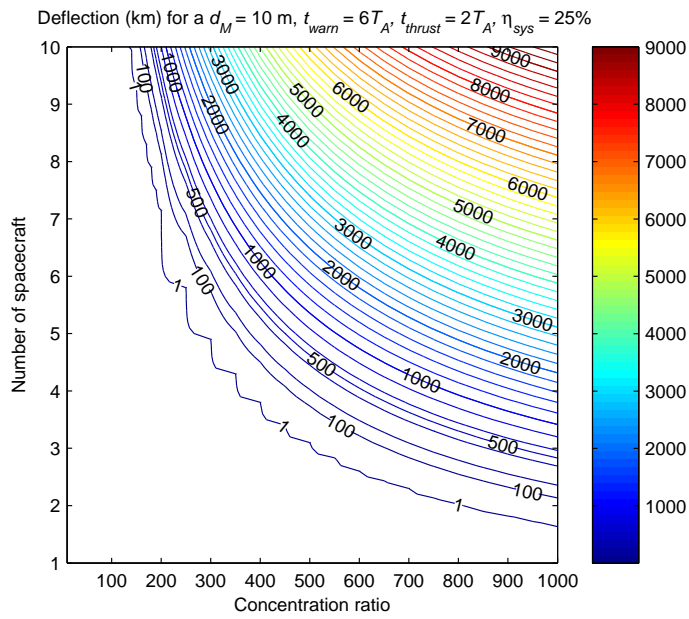


Figure 112: Deflection distance for various concentration ratios and number of spacecraft, assuming a 10 m aperture diameter primary mirror with laser ( $\eta_{sys} = 25\%$ ), a warning time of  $6T_A$  (1941 days), and a thrust period of  $2T_A$  (647 days).

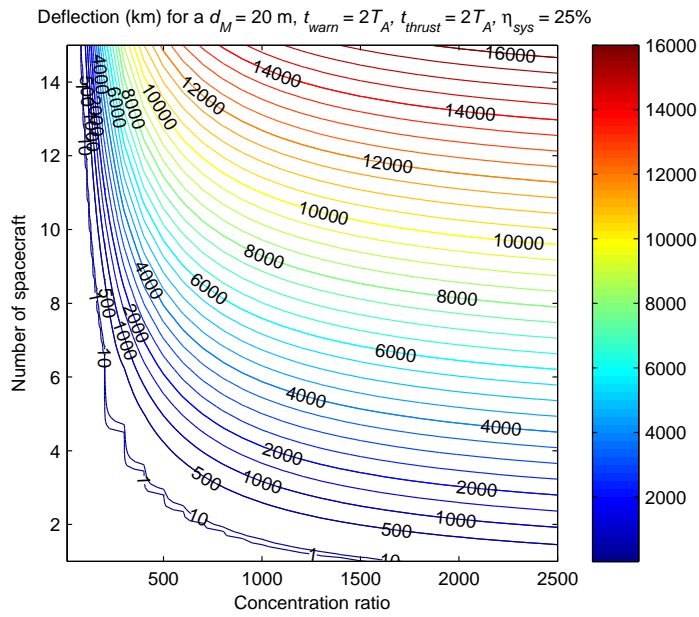


Figure 113: Deflection distance for various concentration ratios and number of spacecraft, assuming a 20 m aperture diameter primary mirror with laser ( $\eta_{sys} = 25\%$ ), a warning time of  $2T_A$  (647 days), and a thrust period of  $2T_A$  (647 days).

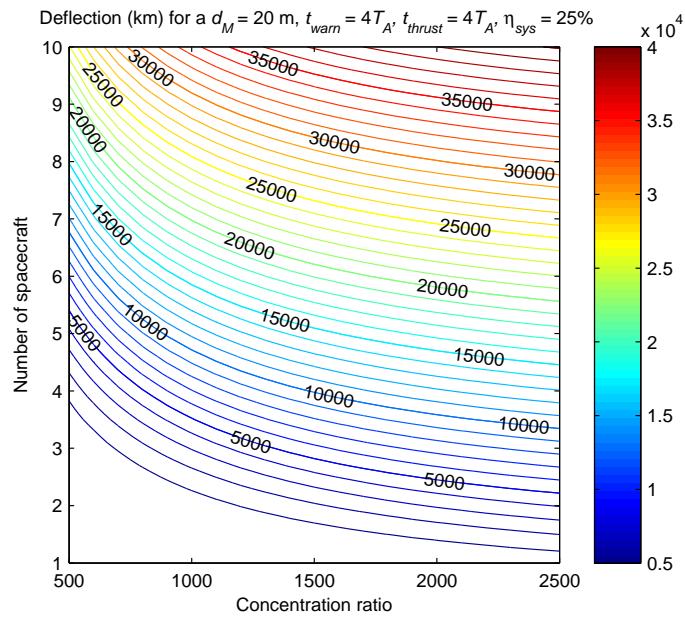


Figure 114: Deflection distance for various concentration ratios and number of spacecraft, assuming a 20 m aperture diameter primary mirror with laser ( $\eta_{sys} = 25\%$ ), a warning time of  $4T_A$  (1294 days), and a thrust period of  $4T_A$  (1294 days).

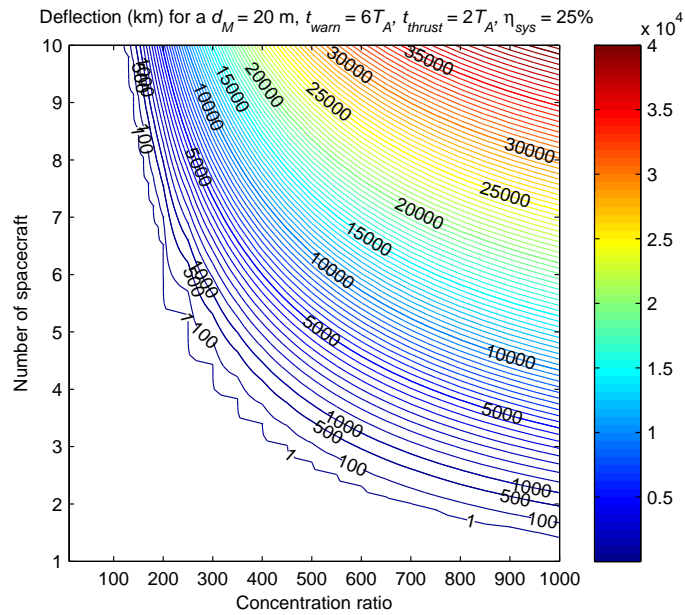


Figure 115: Deflection distance for various concentration ratios and number of spacecraft, assuming a 20 m aperture diameter primary mirror with laser ( $\eta_{sys} = 25\%$ ), a warning time of  $6T_A$  (1941 days), and a thrust period of  $2T_A$  (647 days).

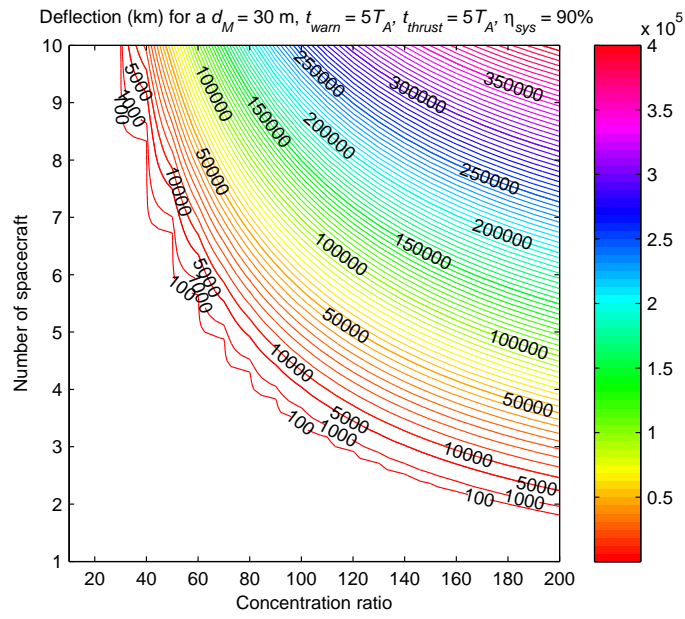


Figure 116: Deflection distance for various concentration ratios and number of spacecraft, assuming a 30 m diameter adaptive mirror with direct imaging ( $\eta_{sys} = 90\%$ ), a warning time of  $5T_A$  (1617 days), and a thrust period of  $5T_A$  (1617 days).

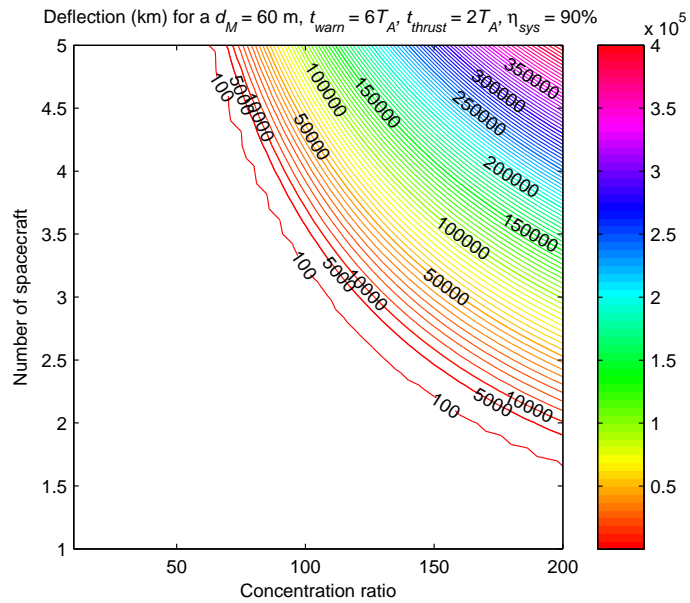


Figure 117: Deflection distance for various concentration ratios and number of spacecraft, assuming a 60 m diameter adaptive mirror with direct imaging ( $\eta_{sys} = 90\%$ ), a warning time of  $6T_A$  (1941 days), and a thrust period of  $2T_A$  (647 days).

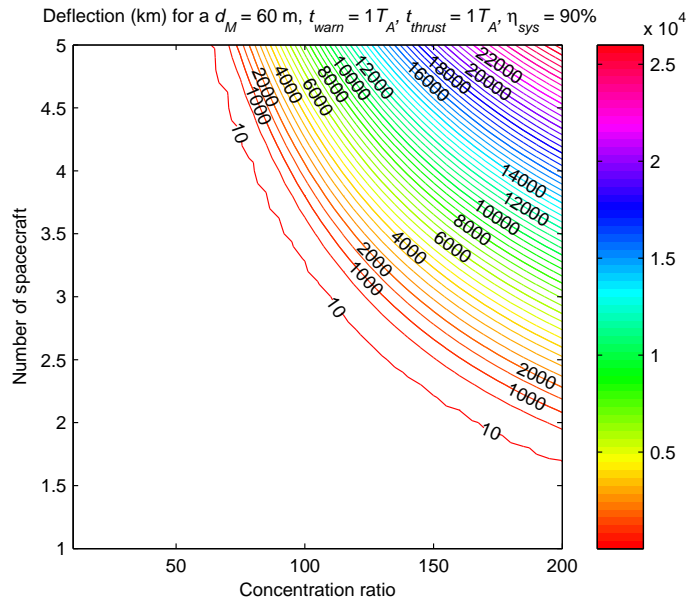


Figure 118: Deflection distance for various concentration ratios and number of spacecraft, assuming a 60 m diameter adaptive mirror with direct imaging ( $\eta_{sys} = 90\%$ ), a warning time of  $1T_A$  (323 days), and a thrust period of  $1T_A$  (323 days).

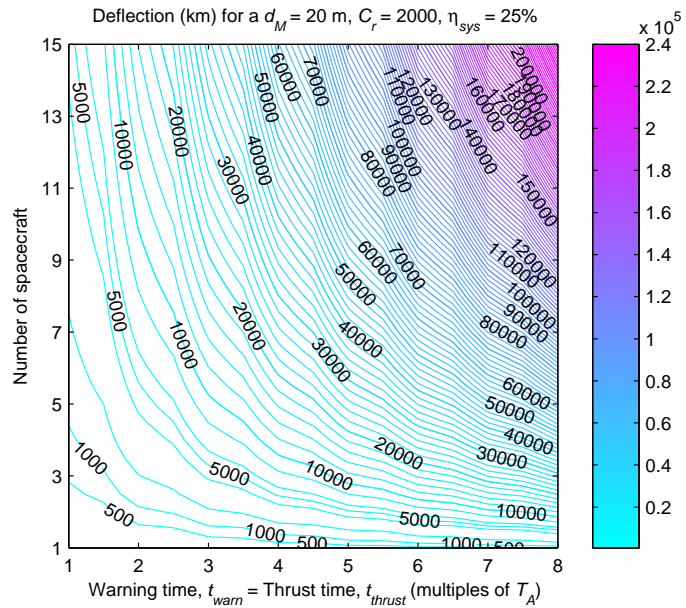


Figure 119: Deflection distance for various warning and thrust times and number of spacecraft, assuming a 20 m diameter adaptive mirror with a laser ( $\eta_{sys} = 25\%$ ) and a concentration ratio of 2000.

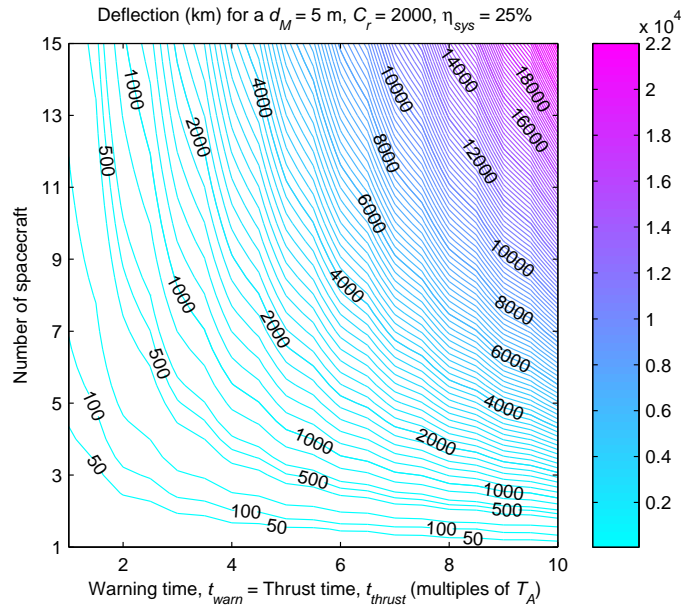


Figure 120: Deflection distance for various warning and thrust times and number of spacecraft, assuming a 5 m diameter adaptive mirror with a laser ( $\eta_{sys} = 25\%$ ) and a concentration ratio of 2000.

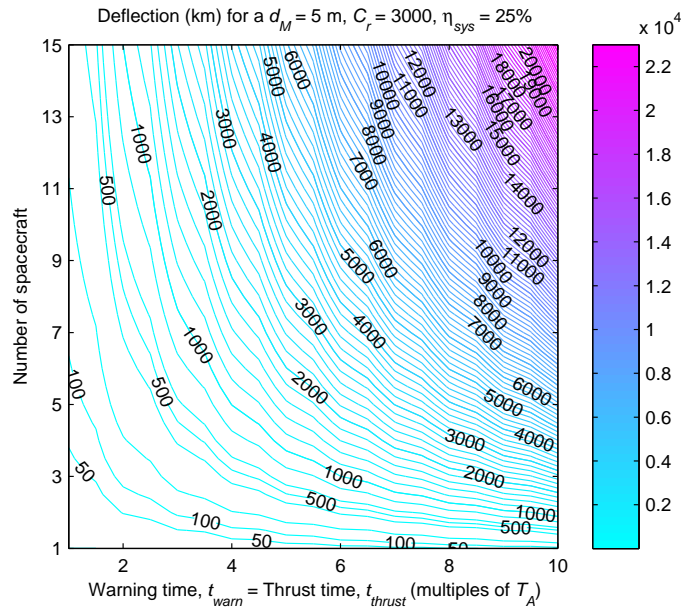


Figure 121: Deflection distance for various warning and thrust times and number of spacecraft, assuming a 5 m diameter adaptive mirror with a laser ( $\eta_{sys} = 25\%$ ) and a concentration ratio of 3000.

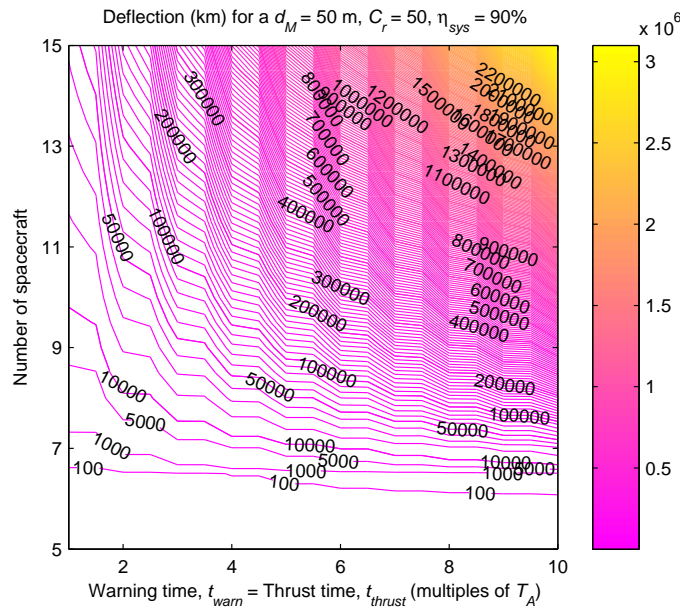


Figure 122: Deflection distance for various warning and thrust times and number of spacecraft, assuming a 50 m diameter adaptive mirror with direct imaging ( $\eta_{sys} = 90\%$ ) and a concentration ratio of 50.

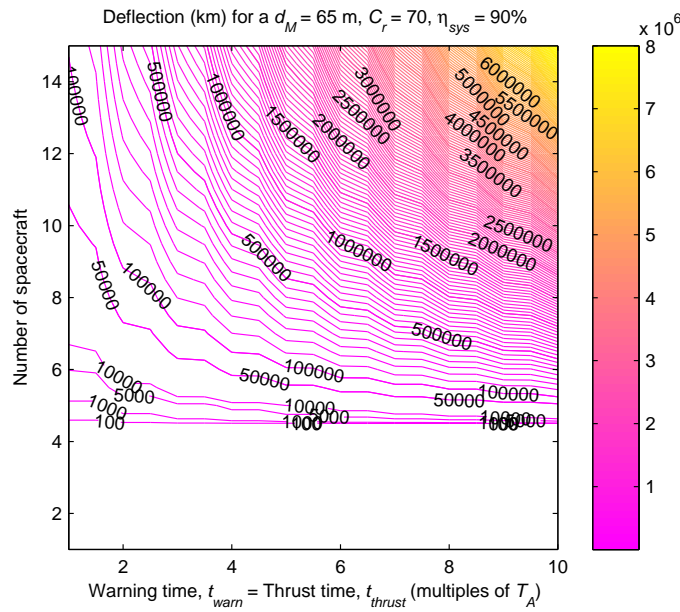


Figure 123: Deflection distance for various warning and thrust times and number of spacecraft, assuming a 65 m diameter adaptive mirror with direct imaging ( $\eta_{sys} = 90\%$ ) and a concentration ratio of 70.

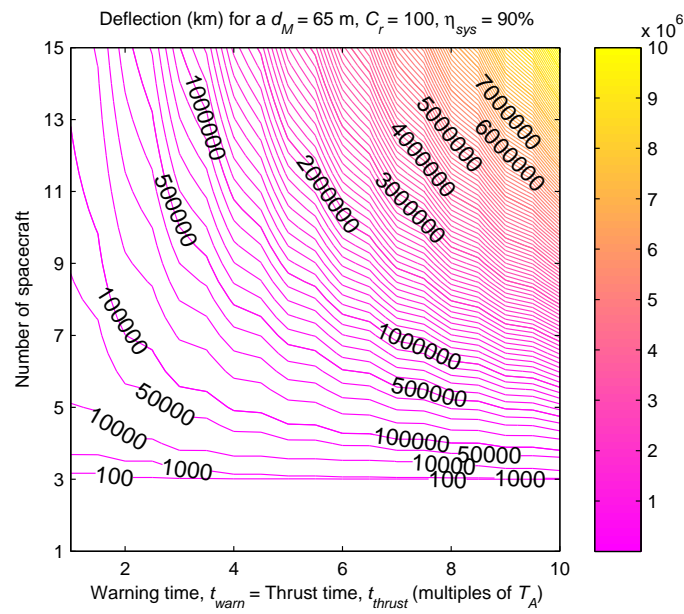


Figure 124: Deflection distance for various warning and thrust times and number of spacecraft, assuming a 65 m diameter adaptive mirror with direct imaging ( $\eta_{sys} = 90\%$ ) and a concentration ratio of 100.

## 5.1.1 Trade-off optimisation

The deflection figures suggest an important point about the system: the system is very flexible and scalable. It is therefore expected that an optimal trade off point exists between warning time, number of spacecraft, size of the spacecraft, deflection and total operation time.

Using the same optimiser EPIC (see Appendix B) as for the funnel orbit dynamics, a multi-objective optimisation was run which minimised the total formation mass while maximising the deviation distance. The optimisation was run using the fixed mirror case.

$$\min_{\xi_{dev}} J = (-(m_{sc}n_{sc}), \Delta r_{dev}(\nu = \nu_{MOID})) \quad (5.1)$$

where the solution state vector is  $\xi_{dev} = [d_{M_1}, n_{sc}, t_{warn}, C_r]$ . The specific parameters are given in Tables 21 – 23, and based on the work developed earlier for system design in Chapter 2.

Table 21: Mirror design parameters for optimisation.

Aperture area of secondary mirror	$A_{M_2} = \pi \text{ m}^2$
Surface area of directional mirror	$A_{M_3} = \pi \text{ m}^2$
Surface area of solar arrays	$A_{sa} = \pi \text{ m}^2$
Laser efficiency	$\eta_L = 0.8$
Reflection efficiency of primary mirror	$\sigma_{M_1} = 0.9$
Absorptivity of the solar arrays	$\alpha_{sa} = 0.8$
Emissivity of the solar arrays	$\epsilon_{sa} = 0.8$
Efficiency of the solar arrays	$\eta_{sa} = 0.4$
Emissivity of the radiator	$\epsilon_R = 0.9$

Table 22: Component mass parameters for optimisation.

Mirror specific mass	$p_M = 0.1 \text{ kg/m}^2$
Laser specific mass	$p_L = 0.005 \text{ kg/W}$
Solar array specific mass	$p_{sa} = 1 \text{ kg/m}^2$
Cable mass as percentage of power system mass	$m_{cable} = 0.2m_{power}$
Mass of the radiator	$m_R = 1.4 \text{ kg}$
Mass of the bus	$m_{bus} = 500 \text{ kg}$
Mass of propellant as percentage of dry mass	$m_{fuel} = 0.3m_{dry}$
Mass of tanks as percentage of mass of propellant	$m_{tanks} = 0.1m_{fuel}$

Table 23: Temperature parameters for optimisation.

Temperature of the solar arrays	$T_{sa} = 373$ K
Temperature of the laser	$T_L = 313$ K
Temperature of secondary mirror surface	$T_{M_2} = 373$ K

The radiators are sized according to the following equations,

$$A_{R1} = \frac{P_r \alpha_{sa} - P_r \eta_{sa} - 2T_{sa}^4 \epsilon_{sa} \sigma A_{sa}}{\epsilon_R \sigma (T_{sa} - \Delta_T)^4} \quad (5.2a)$$

$$A_{R2} = \frac{P_r (1 - \eta_L)}{\epsilon_R \sigma (T_L - \Delta_T)^4} \quad (5.2b)$$

$$A_{R3} = \frac{0.01P_r - 2T_{M_2}^4 \epsilon_{sa} \sigma A_{M_2}}{\epsilon_R \sigma (T_{M_2} - \Delta_T)^4} \quad (5.2c)$$

where  $\sigma$  is the Stefan-Boltzman constant and  $\Delta_T = 10$  K is taken, nominally, as the temperature gradient between the components and the radiator. The total area of the radiators is then,

$$A_R = A_{R1} + A_{R2} + \max(A_{R3}, 0) \quad (5.3)$$

For the mass estimates, a 20% margin was added to the radiator mass, 50% to the mass of the laser assembly, 25% to the mirrors, 15% to the solar arrays, and an overall 20% margin was added to the dry mass. The input power is given by  $P_{in} = \eta_{sa} \sigma_{M_1} A_{M_1} P_r$ .

$$m_R = 1.20(A_R m_R) \quad (5.4a)$$

$$m_L = 1.50(b_L \eta_L P_{in}) \quad (5.4b)$$

$$m_M = 1.25(b_M (A_{M_1} + A_{M_2} + 2A_{M_3})) \quad (5.4c)$$

$$m_{sa} = 1.15(b_{sa} A_{sa}) \quad (5.4d)$$

$$m_{harness} = m_{cable}(m_{sa} + m_L) \quad (5.4e)$$

$$m_{dry} = 1.2(m_{harness} + m_{sa} + m_M + m_L + m_R + m_{bus}) \quad (5.4f)$$

$$\therefore m_{sc} = m_{dry} + m_{fuel} + m_{tanks} \quad (5.4g)$$

Figures 125 – 129 show the various Pareto fronts as a function of the four parameters used in the optimisation, i.e. in  $\xi_{dev}$ . For each run, the number of function evaluations was set to 5000, with a 10 individuals, and a convergence tolerance of  $10^{-4}$ .

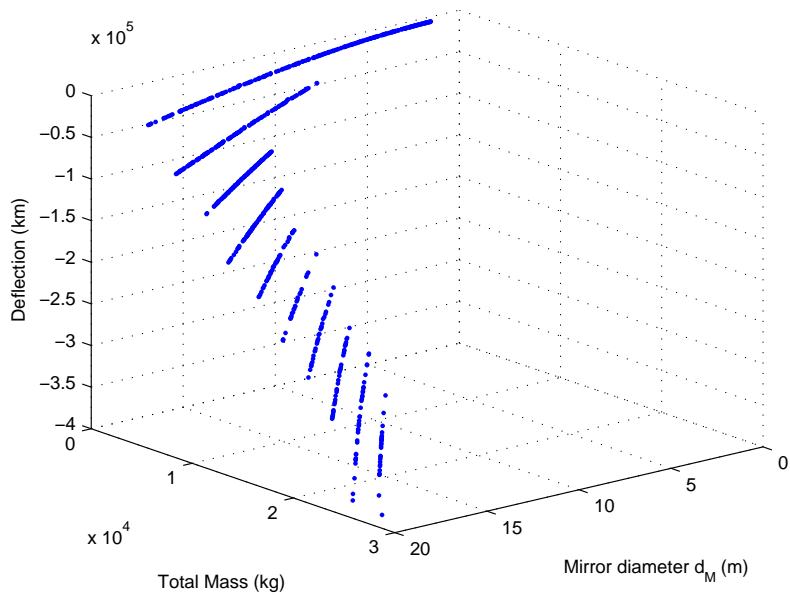


Figure 125: Pareto front for primary mirror aperture diameter, spacecraft mass and deflection distance at the MOID.

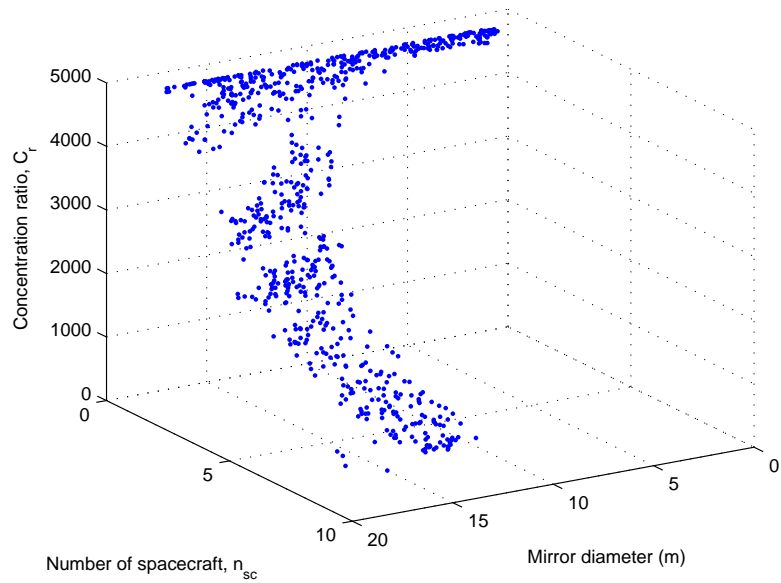


Figure 126: Pareto front for primary mirror aperture diameter, number of spacecraft in the formation, and concentration ratio.

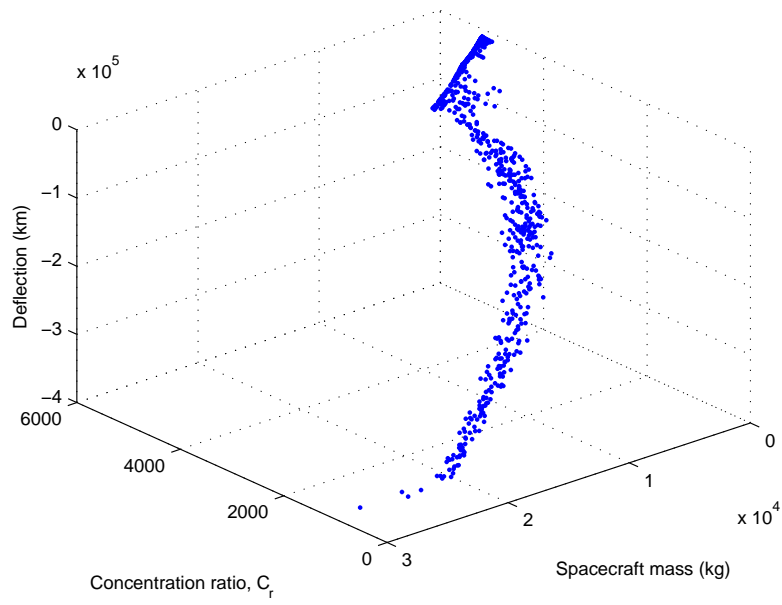


Figure 127: Pareto front for concentration ratio, spacecraft mass and deflection distance at the MOID.

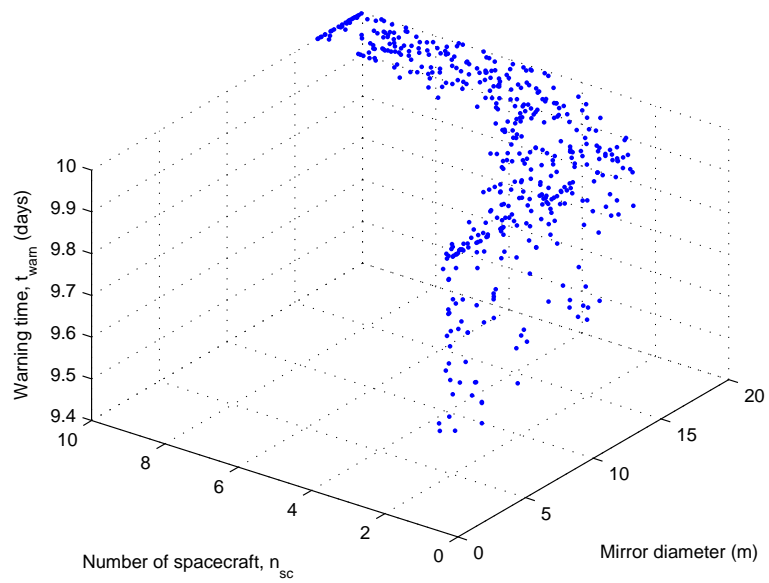


Figure 128: Pareto front for number of spacecraft in the formation, primary mirror aperture diameter and warning time.

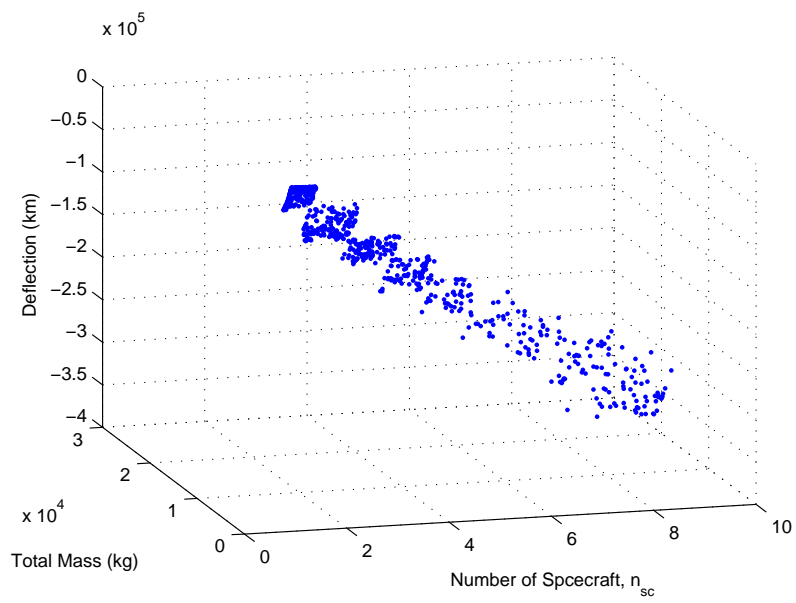


Figure 129: Pareto front for number of spacecraft in the formation, spacecraft mass and deflection distance at the MOID.

## 5.2 DEBRIS CONTAMINATION

The contamination of the mirror surfaces due to the debris plume was modelled based on the work by Kahle et al. (2006). The study, commissioned in part by DLR, is based on a number of assumptions regarding the expansion of the plume and sublimation process. The first assumption holds that the sublimation process is comparable to the generation of tails in comets. The asteroid is assumed to contain a reservoir of material underneath the surface, with the gas expanding both outwards as expected, and inwards through a throat into vacuum within the asteroid itself. This assumption holds true, for example, for a loose rubble-pile asteroid model.

The second assumption is that the plume expansion is similar to the expansion of gas of a rocket engine outside the nozzle. The density of the gas can be computed analytically,

$$\rho(r, \Theta) = \rho^* j_c \frac{d_{spot}^2}{(2r_{spot/sc} + d_{spot})^2} \left( \cos \left( \frac{\pi\Theta}{2\Theta_{max}} \right) \right)^{\frac{2}{\kappa-1}} \quad (5.5)$$

where  $r_{spot/sc}$  is the distance between the spot on the surface of the asteroid and the spacecraft,  $d_{spot}$  is the illuminated spot diameter,  $\Theta$  is the elevation angle of the spacecraft with respect to the  $y$  axis of the asteroid Hill reference frame  $\mathcal{A}$  ( $\Theta = 0^\circ$  means the spacecraft is along the  $y$  axis, while  $\Theta = 90^\circ$  means it is along the  $x$ ). The jet constant  $j_c$  was set to 0.345, the maximum expansion angle  $\varphi_{max} = 130.45^\circ$ , and adiabatic index  $\kappa = 1.4$ , based on the values for diatomic particles [Legge and Boettcher, 1982].

The value  $\rho^*$  is the density at the sublimation point and in the model is computed as the total mass flow  $\dot{m}_{exp}$  divided by the product of the spot area  $A_{spot}$  and gas exhaust velocity  $v_{gas}$ ,

$$\rho^* = \frac{\dot{m}_{exp}}{(A_{spot} v_{gas})} \quad (5.6)$$

Substituting  $\rho^*$  into (5.5),

$$\rho(r, \Theta) = \frac{4\dot{m}_{exp} j_c}{\pi v_{gas}} \frac{1}{(2r_{spot/sc} + d_{spot})^2} \left( \cos \left( \frac{\pi\Theta}{2\Theta_{max}} \right) \right)^{\frac{2}{\kappa-1}} \quad (5.7)$$

This model predicts that the density at a given distance  $\delta r$  is mildly dependent on the size and geometry of the spot. In particular the maximum expansion angle is not a function of the spot geometry. In the case of an extended body which is an order of magnitude bigger than the spot, the expansion cone is probably different from the one reported in the work of Kahle et al.

The third assumption made is that all the particles impacting the surface of the mirror condense and stick to the mirror. The average flow of particles per unit area is given by the product of the density  $\rho(r, \varphi)$  and expelled particle velocity  $\bar{v}_{exp}$ , computed using (3.36), where the velocity of the particles is assumed to be independent of the spacecraft elevation angle  $\Theta$ .

Kahle assumes that the mirror is perpendicular to the flow and that the density of the condensed material is  $\rho_{layer} = 1 \text{ g/cm}^3$  therefore, for the conservation of the mass, the height  $h_{cond}$  of the condensed material on the mirror surface is,

$$h_{cond} = \frac{\rho(r, \Theta) v_{gas}(\rho)}{\rho_{layer}} t_h \quad (5.8)$$

with the time  $t_h$  to reach a given thickness,

$$t_h = \frac{h_{cond}\rho_{layer}}{\rho(r, \Theta) v_{gas}(\rho)} \quad (5.9)$$

The contamination time, therefore, is inversely proportional to the mass flow, while the thrust is directly proportional to the mass flow. In our model the exhaust velocity is constant and function of the sublimation temperature, therefore the thrust depends only on the mass flow. A higher thrust results in a higher mass flow and thus in a faster contamination.

In our case, the primary mirror never directly faces the asteroid nor the plume. For more than half of the orbit, the face of the primary mirror is completely shielded by the spacecraft, and depending on the size, the back of the mirror. The steering mirror, on the other hand, though it is in the plume is not perpendicular to the flow. Following the approach used to compute the contamination of surfaces due to outgassing, a ‘view factor’  $\varphi_{vf}$  was added to (5.9), equal to the angle between the laser beam and the directional steering mirror (if the laser beam is parallel to the  $y$  axis,  $\varphi_{vf}$  is  $45^\circ$ ),

$$\frac{dh_{cond}}{dt} = \frac{\rho_{exp}(2\bar{v}_{exp})}{\rho_{layer}} \cos \varphi_{vf} \quad (5.10)$$

Note that the primary mirror is protected not only from the flow of gas but also from the debris. As the gas expands its velocity increases till it reaches the free molecular flow state, at that point, following the assumption of Kahle, the velocity can be considered constant.

For the asteroid model, the sublimation temperature is 1800 K giving an initial debris velocity  $\bar{v}_{exp} = 552.028$  m/s. This velocity will double after a distance of 1.3 m from the asteroid. At that point, the Knudsen number is about 1, meaning the gas is considered to be in a free molecular state. Note that, although in (5.9) the velocity is considered to be directed toward the mirror, in reality the velocity field will present more scattered directions of motion. Therefore, the debris velocity in (3.36) (on pg. 57) is multiplied by a factor of 2 to account for this expansion of the gas in a vacuum. The layer density  $\rho_{layer}$  is set to  $1 \text{ g/cm}^3$ . The power density on the asteroid surface is decreased based on the contamination of the mirrors. A degradation factor  $\gamma_p$  is applied to the power reaching the asteroid surface, based on the Lambert-Beer-Bouguer law [Kahle et al., 2006],

$$\gamma_p = \exp^{-2v_c h_{cond}} \quad (5.11)$$

where  $v_c = 10^4/\text{cm}$  is the absorption coefficient for forsterite. Equations (3.31) and (5.10) are numerically integrated, along with the Gauss equations in (3.23), for the duration of the deflection mission. Due to the design of the orbit, which is designed to help avoid the plume, the effect of the contamination is small. For e.g., a 20 m mirror with a thrust duration of 7 years generates a maximum of  $0.1 \mu\text{m}$  of contaminant, equivalent to a degradation factor  $\gamma$  of 98% (see Fig. 130).

An important consideration is that the gas flowing toward the steering mirror is continuously illuminated by the laser beam, therefore either the wavelength of the laser is such that there is no interaction or the gas is not cooling down but is further heated up. The additional heat will further expand and likely ionize the gas. If the gas is ionized a simple electrostatic field would maintain the mirrors clean. If the gas is not ionized, since it is not cooling down a condensation is less probable. Assuming

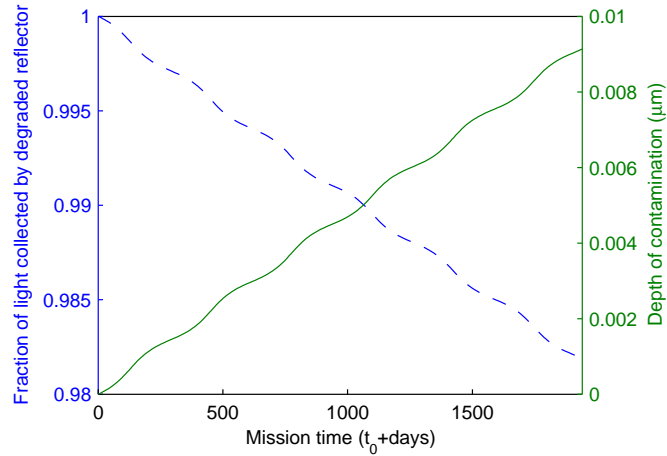


Figure 130: Height (or depth) of contaminant on mirror surface, and power degradation factor for a 7 year sample mission, operating with a 20 m aperture diameter fixed mirror.

that the gas is actually condensing on the surface of the mirror, the condensed layer will be constantly illuminated by the laser, therefore either it is not absorbing the light of the laser or it is heated up and will evaporate again. Thus, it is possible that the laser system is also keeping the mirrors clean.

Figures 131–137 represent the deflection that can be achieved accounting for contamination. The asteroid is deviated continuously until either the mirror cannot be operated due to the contamination or until impact. For the laser option, with small diameter primary mirrors and high concentration ratios (so small spot size), the impact of the contamination is very small. For the direct imaging, which by comparison has a large primary mirror and low concentration ratio, the effect is much more noticeable, as in Figs. 136 and 137.

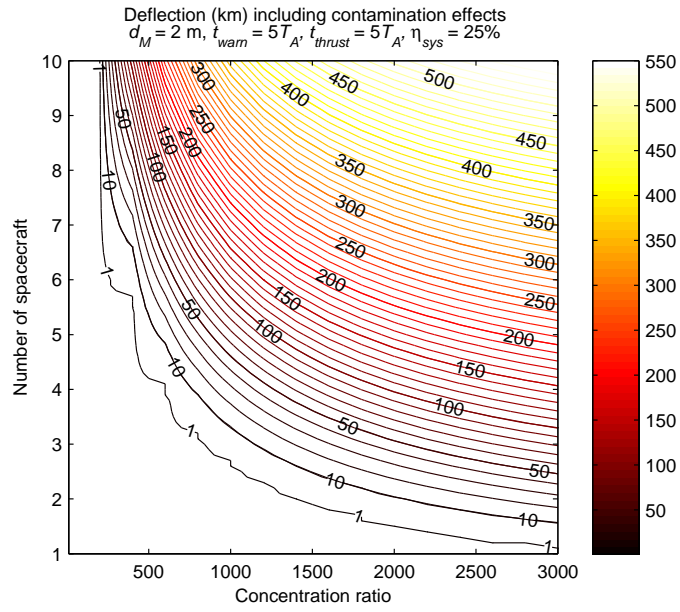


Figure 131: Deflection as a function of concentration ratio and number of spacecraft, including mirror contamination, for a 2 m primary mirror, a warning and thrust time of  $5T_A$  and a system efficiency of 25%. See Fig. 106 for comparison.

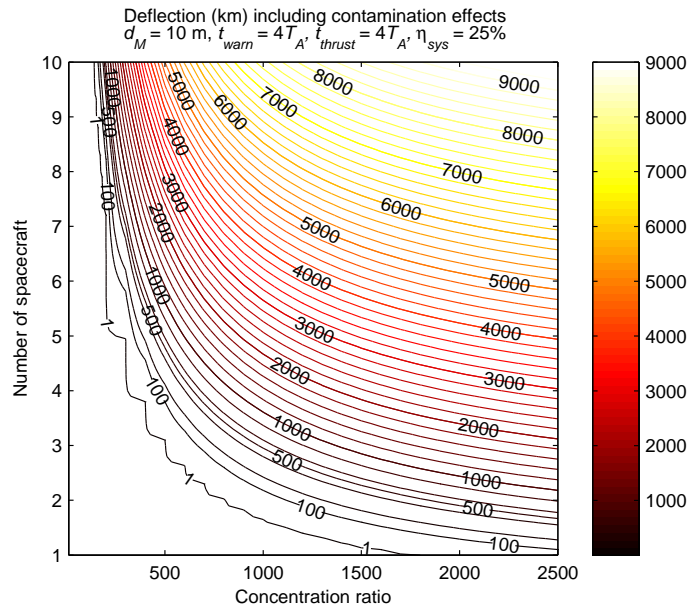


Figure 132: Deflection as a function of concentration ratio and number of spacecraft, including mirror contamination, for a 10 m primary mirror, a warning and thrust time of  $4T_A$  and a system efficiency of 25%. See Fig. 111 for comparison.

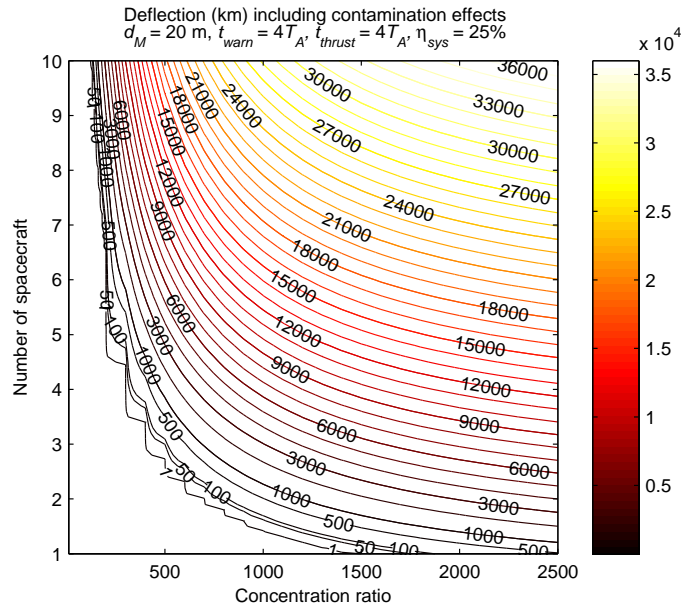


Figure 133: Deflection as a function of concentration ratio and number of spacecraft, including mirror contamination, for a 20 m primary mirror, a warning and thrust time of  $4T_A$  and a system efficiency of 25%. See Fig. 114 for comparison.

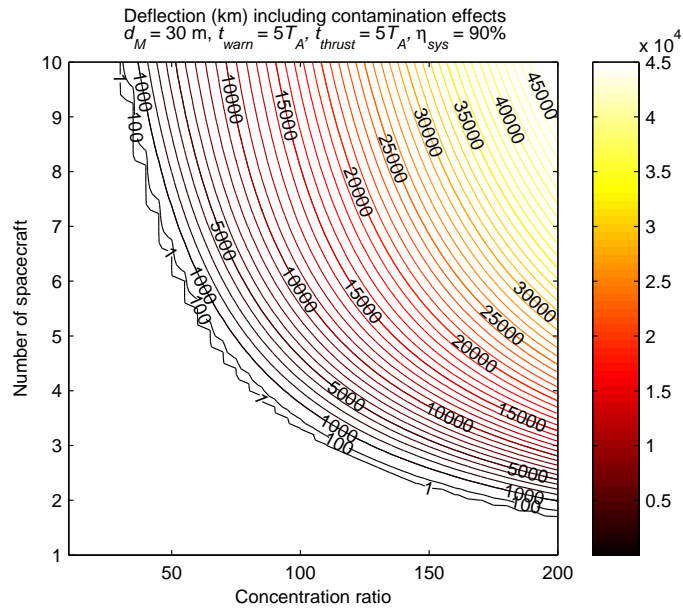


Figure 134: Deflection as a function of concentration ratio and number of spacecraft, including mirror contamination, for a 30 m primary mirror, a warning and thrust time of  $5T_A$  and a system efficiency of 90%. See Fig. 116 for comparison.

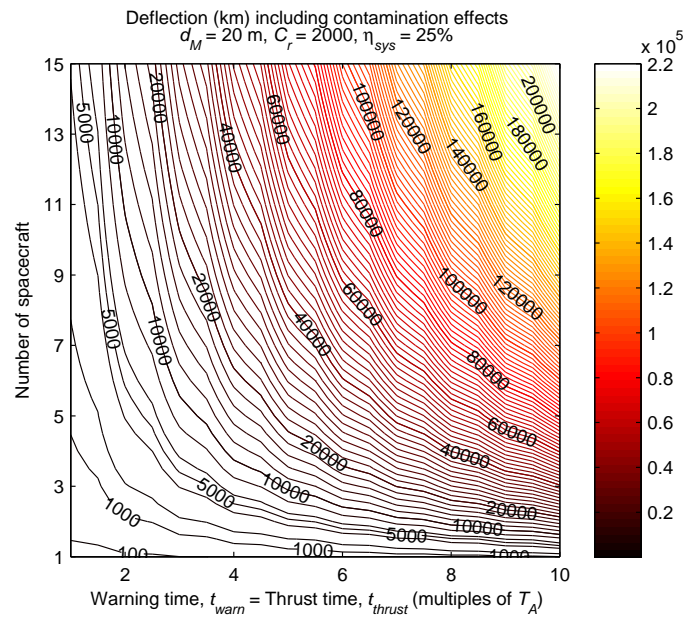


Figure 135: Deflection as a function of the warning time and number of spacecraft, including mirror contamination, for a 20 m primary mirror, concentration ratio of 2000 and a system efficiency of 25%. See Fig. 119 for comparison.

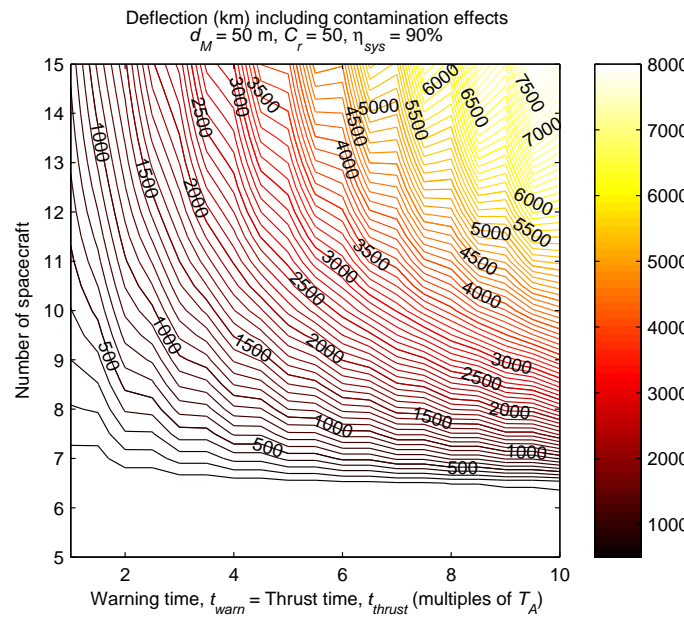


Figure 136: Deflection as a function of the warning time and number of spacecraft, including mirror contamination, for a 50 m primary mirror, concentration ratio of 50 and a system efficiency of 90%. See Fig. 122 for comparison.

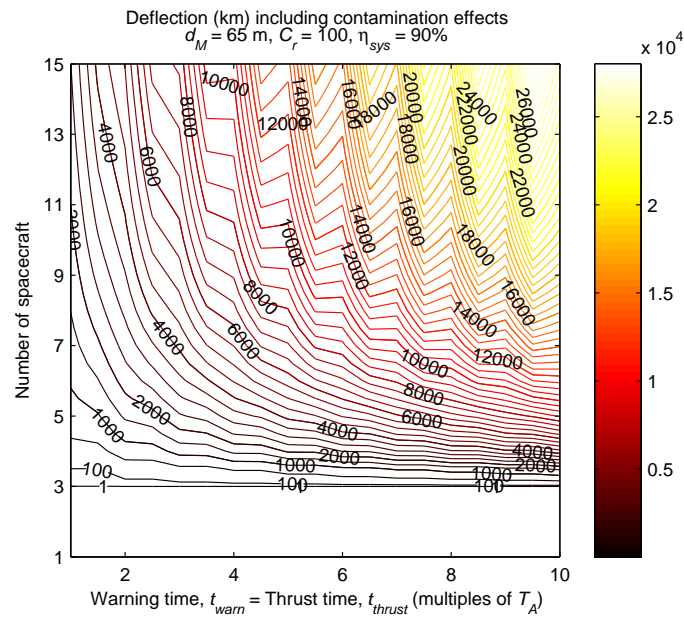


Figure 137: Deflection as a function of the warning time and number of spacecraft, including mirror contamination, for a 65 m primary mirror, concentration ratio of 100 and a system efficiency of 90%. See Fig. 124 for comparison.

## 5.3 ENHANCED YARKOVSKY EFFECT

The direct imaging concept offers an additional, interesting possibility. Even if the power density is not high enough to sublimate the surface material, the heat on the surface will induce a very low thrust by means of the Yarkovsky effect. This effect was first measured in 1991 on the asteroid 6489 Golevka which drifted 15 km over twelve years, equivalent to an induced acceleration of  $10^{-10}$  m/s<sup>2</sup> [Chesley et al., 2003].

The force due to the light projected onto the asteroid is,

$$F_{light} = 2(1 - \alpha_A)\sigma_M C_r A_{spot} P_0 \left(\frac{r_{AU}}{r_{\odot/sc}}\right)^2 + \alpha_A \sigma_M C_r A_{spot} P_0 \left(\frac{r_{AU}}{r_{\odot/sc}}\right)^2 \quad (5.12)$$

given the mirror reflectivity  $\sigma_M$ , absorptivity  $\alpha_A$  and the emissivity  $\epsilon_A$ . The first component is the reflected light and the second component is the absorbed light.

For an asteroid surface temperature  $T_A$ , the emission of photons will add a force component  $F_{ir}$  [Brož, 2006],

$$F_{ir} = \frac{2}{\pi} \frac{\epsilon_A \sigma T_A^4}{c} A_{spot} \quad (5.13)$$

The temperature of the spot surface can be computed with the simple one-dimensional model given by Sanchez Cuartielles et al. (2009).

$$\chi_A \frac{\partial^2 T}{\partial x^2} = \frac{\partial T}{\partial t} \quad (5.14)$$

where

$$\chi_A = \frac{K_A}{\rho_A c_A}$$

is the thermal diffusivity of the material,  $K_A = 2$  W/m/K is the conductivity,  $\rho_A = 2$  kg/m<sup>3</sup> is the density of the material and  $c_A = 750$  J/kg/K is the heat capacity. The boundary conditions are given by,

$$-K_A \frac{\partial T_A}{\partial x_{spot}} + \epsilon_A \sigma T_A^4 = \alpha_A \sigma_M C_r A_{spot} S_0 \left(\frac{r_{AU}}{r_{\odot/sc}}\right)^2 \quad (5.15a)$$

$$T(0, x) = T_0 \quad (5.15b)$$

$$T(t, L) = T_0 \quad (5.15c)$$

The initial surface temperature  $T_0$  is taken to be 278 K, which is assumed here to be constant from the surface down to a depth of 50 m inside the asteroid. A scattering factor  $\Lambda$  of  $2/\pi$  is multiplied by the total force to account for emissions in all directions on a dome. Figure 138 shows the sum of the two force components  $F_{ir}$  in (5.12) and  $F_{light}$  in (5.13) as a function of the surface temperature for two different spot sizes.

Figure 139 shows the deflection that can be achieved with the simple combination of forces given in (5.12) and (5.13), for two different mirror diameters.

The achieved deflection is much lower compared with sublimation, for e.g., for 5 years of operation using 10, 65 m diameter mirrors, the deflection distance with the Yarkovsky effect is  $\sim 1200$  km, while sublimation would produce a deflection of 10000 km. That said, the deviation is still quite useful for moving asteroids into a nearby orbit where smaller deviations are needed.

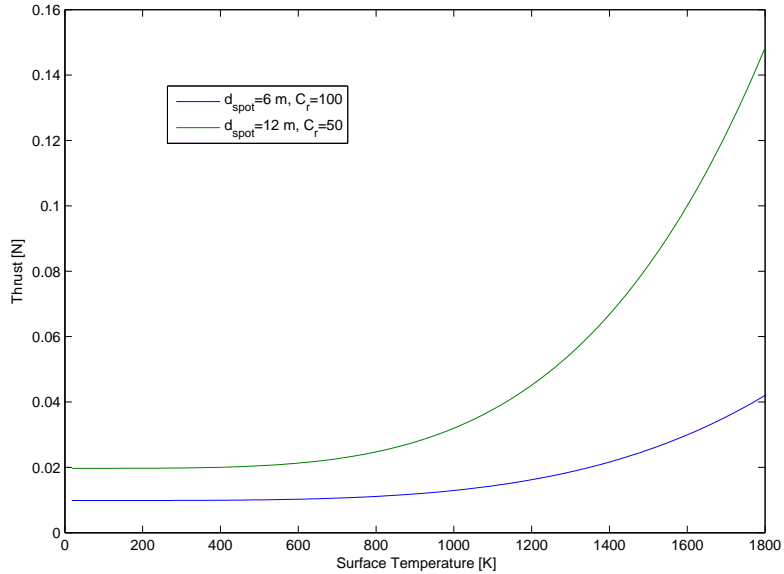


Figure 138: Total thrust due to combined Yarkovsky and solar pressure effects.

#### 5.4 DISCUSSION

For the contamination problem the solar pumped laser option offers a range of possible solutions which can be explored. The primary can be further protected by shielding the exterior part of the spacecraft and by adding baffles along the rim of the mirror. The steering mirror can be protected using a counter flow of inert gas, though this solution would require extra mass, and a shutter that is timed with the flow of debris and gas.

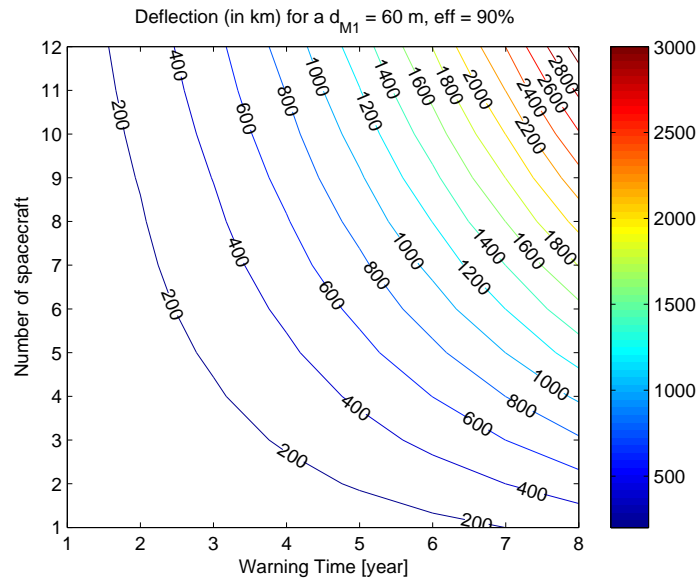
However, if the laser interacts with the plume, or even if the surface of the mirror is kept at high temperature, the system could be potentially self-cleaning. In fact the average time of residence of a contaminant on a surface can be estimated as [Tribble, 2003],

$$\bar{t}_{res} = \tau_0 \exp \frac{E_a}{T_M \bar{R}} \quad (5.16)$$

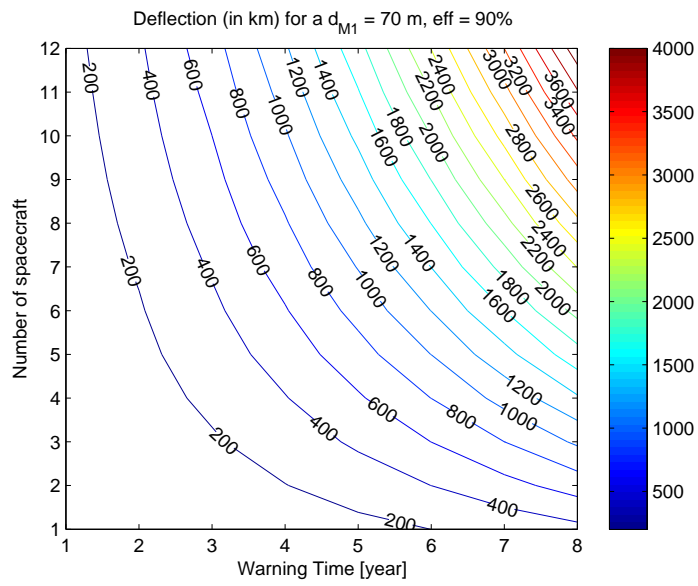
where  $\tau_0$  is oscillation period of molecule, and  $\bar{R} = 8.314472$  J/K·mol is the gas constant. If the temperature  $T_M$  of the mirror or layer of material is kept high, most of the contaminants with a low activation energy  $E_a$  could sublime again after a few seconds of residence.

The absorption of the laser beam by the plume also means a reduction in the power density on the surface. A reduction of the power density would correspond to an interruption of the sublimation process. As the sublimation stops, the plume would dissipate quite fast and the laser would be able to sublime again. Therefore, the overall system would work through a sequence of impulses. These impulses can be timed with the duty cycle of the laser to maximise performance.

As stated above the current computation of the deflection is not optimal, although proper scheduling of the thrusting operations would greatly increase the deflection [Colombo et al., 2009]. In particular, thrusting around the perihelion for deflection



(a) Solar collector with a 60 m aperture diameter and a concentration ratio of 34.



(b) Solar collector with a 70 m aperture diameter and a concentration ratio of 34.

Figure 139: Deflection achievable with the enhanced Yarkovsky effect.

strategies that are pushing in the direction of the velocity is optimal while for other values of the true anomaly the deflection action is not very effective. Although pushing only at the perihelion would increase the warning time, it would also mitigate the contamination problem extending the lifetime.

The direct imaging system may represent a problem if the optics cannot be protected. It is expected that the flow of gas will be excited by the flux of light and therefore will not condense, as predicted by the model of Kahle et al. On the other hand, if the flux is not dense enough to sublimate the debris, this could pose a severe problem. Therefore, the study of the optical system and of the contamination of the optics in the case of the direct imaging remains an open issue.

## CONCLUSION

The beginning of wisdom is found in doubting; by doubting we come to the question, and by seeking we may come upon the truth.

Pierre Abelard

This study addressed some of the problems related to the implementation of the solar sublimation concept for asteroid deflection.

## ORBITAL DYNAMICS AND CONTROL IN PROXIMITY OF AN IRREGULAR BODY

It proved that the mirrors can be maintained at close distance with minimum control. Furthermore, the use of a formation can provide improved orbit determination capabilities both to keep track of the motion of the spacecraft of the spacecraft with respect to the asteroid and of the asteroid with respect to the Sun.

DEPLOYMENT OF A LARGE REFLECTOR IN SPACE Although the direct imaging concept still requires a reflector of considerable aperture, a significant deflection can be achieved with reflectors that are one to two orders of magnitude smaller than the ones proposed in literature for this deflection method. In particular, for the solar pumped laser concept the reflector can be as small as 5 m in diameter. From the preliminary system design, the size and mass of the spacecraft is within present launch capabilities. Furthermore the TRL of the individual elements of technologies involved in indirect solar pumping is higher than 4, and is expected to increase regardless the specific application to asteroid deflection.

CONTAMINATION OF THE OPTICS A basic calculation of the effect on the contaminant on the surface of the mirror was implemented, following a model developed by Kahle et al. The results show that the effect would be minimal as the mirror is placed, by design, outside the main area of the plume however, again, this is an initial calculation only. Further study is required in order to refine and test the model and assumptions used.

Two configurations for the mirrors were analysed and for each one a different strategy for orbit maintenance was considered.

The multi-mirror fixed configuration led to the definition of a particular set of formation orbits composing two symmetric funnels with the principal axis aligned with the  $y$ -axis of the asteroid Hill reference frame. These funnel orbits allow the spacecraft to have very good visibility of the target spot on the surface of the asteroid and, at the same time, allow room for the plume of gas to flow with minimal impingement. The funnel orbits are located outside a limiting sphere where the gravity field of the asteroid can be considered homogenous. This limit sphere imposes requirements on the pointing accuracy and focusing capabilities of the mirror assembly. The orbital

maintenance strategy is based on the computation of the control components that minimise the difference between the current and target value of the relative Keplerian elements. The control compensated for two sources of perturbations: solar radiation pressure due to the large surface area of the mirror assembly and third body effects due to proximity of Apophis, and for the constantly deviating orbit of the NEO. The decrease in mass of Apophis due to the solar sublimation was also accounted for.

A second option considered an adaptive single mirror configuration. For this option, the mirror can be placed at artificial equilibrium points highly inclined over the  $y$ -axis of the Hill frame. From this position the spacecraft sees the target spot from a high angle, however AEPs can be found that allow the spacecraft to maintain a reasonable size of the spot area. A control strategy was proposed that allows the spacecraft to oscillate in a confined region in the proximity of the asteroid with a very low control thrust. Even adding the effect of the gravity field of an elongated body, the magnitude of the required control thrust remains limited. The low level of thrust would suggest the use of FEEP engines, which would lead to a minimal propellant consumption over a long operational period.

An interesting strategy for the navigation was developed and simulated, with the results being quite successful.

The results shows that the solar sublimation concept is an effective solution to the drawbacks of the original idea of a solar sublimation system. However many key points remain open. For example, though it was found that a simple optical lens system cannot collimate the light at the required distance from the asteroid, the arguments in this study are not conclusive and further, more detailed investigations are required. Furthermore, the system design analysis is only partial and does not include any trade-offs between number of spacecraft, achieved deviation, warning time and overall system mass. The design of the spacecraft, therefore, also has room for improvement.

## 6.1 FUTURE WORK

This study answered the primary goal of determining whether solar sublimation is a feasible option for the deflection of the asteroid, but was preliminary in nature and only addressed the major concerns and potential ‘show-stoppers’ for this method. The aim was not to produce an optimal design, but to provide a set of feasible options.

Within the realm of a general study, the next steps would entail:

- A further analysis of the optical system including detailed investigations and designs of solar cells, laser efficiencies and implementation issues such as the heat dissipation (done in this study through radiators) and crystal selection. Also, while the lens option was examined here, an advanced optical designer may be able to produce a collimation lens designed for one specific mission. This would probably require a different set of orbits that were designed in order to minimise the variation in the reflection angle and solar disk size.
- For the control, a number of methods were investigated with the results of the most promising shown here. However, this still needs further work to refine the effect of the tuning weights. Long term simulations are also necessary to see the full reaction after a number of years. The code was written in Matlab, however the simulation time could be reduced, for example, by porting the code over to the programming language c.

- The navigation presented here illustrates that the concept works. The next step is to implement a filtering algorithm to both reduce the errors in the position determination, and to predict the velocity of the NEO. Factors such as eclipse/shadow, partial images and other visual factors will also need to be compensated for in the image recognition algorithm. Due to the high development level of this technology in computing, this should not be a problem to develop.
- A more accurate contamination model should be developed which can either verify the assumptions made here, and/or develop more accurate models based on experimental testing.

## ANALYTICAL DERIVATIONS OF PROXIMAL MOTION EQUATIONS

---

The following appendix outlines the various analytical forms of equations describing the relative position and velocity of one object with respect to another.

### A.1 NON-LINEAR RELATIVE EQUATIONS OF MOTION

Starting with the well known coordinate transform matrix from the inertial heliocentric Cartesian reference frame  $\mathcal{O}$  to the relative rotating perifocal coordinate system  $\mathcal{P}$  where  $\hat{x}^{\mathcal{P}}$  points towards the periapsis of the orbit, and  $\hat{z}^{\mathcal{P}}$  is normal to the orbital plane (see Fig. 140),

$$\mathbf{x}^{\mathcal{O}} = [\mathbf{R}_3(-\Omega) \cdot \mathbf{R}_1(-i) \cdot \mathbf{R}_3(-\omega) \cdot \mathbf{R}_3(-\nu)] \mathbf{x}^{\mathcal{P}} \quad (\text{A.1})$$

where  $\mathbf{R}_i$  are the Euler elementary rotation matrices along the  $i^{\text{th}}$  axis (see Battin (1999) for background on Euler angles). The vector  $\mathbf{x}^{\mathcal{P}} = [\mathbf{r}, \mathbf{v}]$  is,

$$\mathbf{r}^{\mathcal{P}} = \begin{bmatrix} r \cos \nu \\ r \sin \nu \\ 0 \end{bmatrix} = \begin{bmatrix} \frac{a(1-e^2) \cos \nu}{1+e \cos \nu} \\ \frac{a(1-e^2) \sin \nu}{1+e \cos \nu} \\ 0 \end{bmatrix} \quad (\text{A.2})$$

$$\dot{\mathbf{r}}^{\mathcal{P}} = \mathbf{v}^{\mathcal{P}} = \begin{bmatrix} \dot{r} \cos \nu - r \dot{\nu} \sin \nu \\ \dot{r} \sin \nu + r \dot{\nu} \cos \nu \\ 0 \end{bmatrix} = \begin{bmatrix} -\sqrt{\frac{\mu}{a(1-e^2)}} \sin \nu \\ \sqrt{\frac{\mu}{a(1-e^2)}} (e + \cos \nu) \\ 0 \end{bmatrix} \quad (\text{A.3})$$

There is no out-of-plane motion by definition of the coordinate system since  $\hat{x}$ - $\hat{y}$  define the plane of the spacecraft orbit.

Note that these results are valid only for elliptical orbits (i.e.  $0 < e < 1$ ). For circular orbits ( $e = 0$ ),  $\omega = \Omega \Rightarrow 0$  and  $\nu \Rightarrow M$  (mean anomaly) or  $\nu \Rightarrow \theta$  (true latitude) depending on the inclination; see Vallado (2004) for a complete explanation of all the cases (e.g., circular, parabolic).

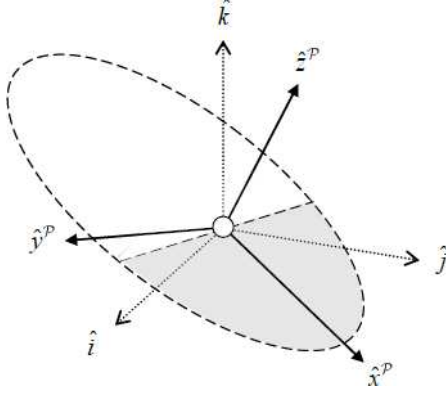


Figure 140: Inertial Cartesian system of the central body  $\mathcal{O}\{\hat{i}, \hat{j}, \hat{k}\}$  and perifocal coordinate system  $\mathcal{P}\{\hat{x}, \hat{y}, \hat{z}\}$ , where  $x$  points towards the periapsis of the orbit,  $x$ - $y$  lie in the orbital plane and  $z$  is normal to  $x$ - $y$ .

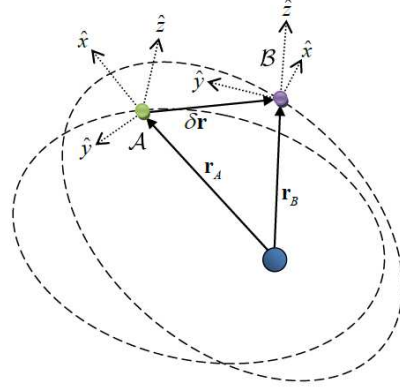


Figure 141: Hill Cartesian reference frames for objects  $A$  and  $B$ , including vectors. NOTE: the diagram is not to scale.

The equations for the position and velocity of an object in inertial space as a function of the Keplerian orbital elements can be found by expanding (A.1) with (A.2) and (A.3),

$$r_x(\mathbf{k}) = r (\cos \Omega \cos(\nu + \omega) - \cos i \sin \Omega \sin(\nu + \omega)) \quad (\text{A.4a})$$

$$r_y(\mathbf{k}) = r (\cos(\nu + \omega) \sin \Omega + \cos i \cos \Omega \sin(\nu + \omega)) \quad (\text{A.4b})$$

$$r_z(\mathbf{k}) = r \sin i \sin(\nu + \omega) \quad (\text{A.4c})$$

$$\begin{aligned} v_x(\mathbf{k}) = & \frac{1}{r} \left( \cos \Omega \left( er \sqrt{\frac{\mu}{p}} \cos(\nu + \omega) \sin \nu - \sqrt{p\mu} \sin(\nu + \omega) \right) \right. \\ & \left. - \cos i \sin \Omega \left( \sqrt{p\mu} \cos(\nu + \omega) + er \sqrt{\frac{\mu}{p}} \sin \nu \sin(\nu + \omega) \right) \right) \end{aligned} \quad (\text{A.4d})$$

$$\begin{aligned} v_y(\mathbf{k}) = & \left( -\frac{\sqrt{p\mu}}{r} + e \sqrt{\frac{\mu}{p}} \cos \nu \right) \sin \nu (\cos \omega \sin \Omega + \cos i \cos \Omega \sin \omega) \\ & + \left( \frac{\sqrt{p\mu} \cos \nu}{r} + e \sqrt{\frac{\mu}{p}} \sin^2 \nu \right) (\cos i \cos \Omega \cos \omega - \sin \Omega \sin \omega) \end{aligned} \quad (\text{A.4e})$$

$$v_z(\mathbf{k}) = \sin i \left( \frac{\sqrt{p\mu} \cos(\nu + \omega)}{r} + e \sqrt{\frac{\mu}{p}} \sin \nu \sin(\nu + \omega) \right) \quad (\text{A.4f})$$

where,

$$h = \|\mathbf{r} \wedge \mathbf{v}\| = \sqrt{p\mu}$$

$$r = \frac{p}{1 + e \cos \nu}$$

$$p = a(1 - e^2)$$

The equations of the definition of the Hill frame given in (3.4) can be expressed in terms of the orbital elements of object  $A$ , where  $\mathbf{G}$  is simply the matrix form of the equations in (3.4).

$$G_{31} = \frac{\mathbf{h}_x}{h} = \frac{1}{h} (r_y(\mathbf{k}_A)v_z(\mathbf{k}_A) - r_z(\mathbf{k}_A)v_y(\mathbf{k}_A)) = \sin i_A \sin \Omega_A \quad (\text{A.5})$$

$$G_{32} = \frac{\mathbf{h}_y}{h} = \frac{1}{h} (r_z(\mathbf{k}_A)v_x(\mathbf{k}_A) - r_x(\mathbf{k}_A)v_z(\mathbf{k}_A)) = -\cos \Omega_A \sin i_A \quad (\text{A.6})$$

$$G_{33} = \frac{\mathbf{h}_z}{h} = \frac{1}{h} (r_x(\mathbf{k}_A)v_y(\mathbf{k}_A) - r_y(\mathbf{k}_A)v_x(\mathbf{k}_A)) = \cos i_A \quad (\text{A.7})$$

$$G_{11} = \frac{r_x(\mathbf{k}_A)}{r_A} = \cos \Omega_A \cos(\nu_A + \omega_A) - \cos i_A \sin \Omega_A \sin(\nu_A + \omega_A) \quad (\text{A.8})$$

$$G_{12} = \frac{r_y(\mathbf{k}_A)}{r_A} = \cos(\nu_A + \omega_A) \sin \Omega_A + \cos i_A \cos \Omega_A \sin(\nu_A + \omega_A) \quad (\text{A.9})$$

$$G_{13} = \frac{r_z(\mathbf{k}_A)}{r_A} = \sin i_A \sin(\nu_A + \omega_A) \quad (\text{A.10})$$

Expanding the cross product  $\hat{\mathbf{h}} \wedge \hat{\mathbf{r}}$  gives the remaining axis,

$$G_{21} = G_{32}G_{13} - G_{33}G_{12} = -\cos i_A \cos(\nu_A + \omega_A) \sin \Omega_A - \cos \Omega_A \sin(\nu_A + \omega_A) \quad (\text{A.11})$$

$$G_{22} = G_{33}G_{11} - G_{31}G_{13} = \cos i_A \cos \Omega_A \cos(\nu_A + \omega_A) - \sin \Omega_A \sin(\nu_A + \omega_A) \quad (\text{A.12})$$

$$G_{23} = G_{31}G_{12} - G_{32}G_{11} = \cos(\nu_A + \omega_A) \sin i_A \quad (\text{A.13})$$

Combining the equations (A.8)–(A.5) for the transformation matrix  $\mathbf{G}$  with the definitions in (A.4), gives the equations for the vector  $\mathbf{r}_B$  in the Hill frame of  $A$  and expressed as a function of the orbital elements,

$$\begin{aligned} r_{B_x} = x &= G_{11}r_x(\mathbf{k}_B) + G_{12}r_y(\mathbf{k}_B) + G_{13}r_z(\mathbf{k}_B) \quad (\text{A.14}) \\ &= r_B \left( \cos(\nu_B + \omega_B) \left( \cos(\Omega_A - \Omega_B) \cos(\nu_A + \omega_A) - \cos i_A \sin(\Omega_A - \Omega_B) \sin(\nu_A + \omega_A) \right) \right. \\ &\quad + \left( \cos i_B \cos(\nu_A + \omega_A) \sin(\Omega_A - \Omega_B) \right. \\ &\quad \left. \left. + \left( \cos i_A \cos i_B \cos(\Omega_A - \Omega_B) + \sin i_A \sin i_B \right) \sin(\nu_A + \omega_A) \right) \sin(\nu_B + \omega_B) \right) \end{aligned}$$

$$\begin{aligned} r_{B_y} = y &= G_{21}r_x(\mathbf{k}_B) + G_{22}r_y(\mathbf{k}_B) + G_{23}r_z(\mathbf{k}_B) \quad (\text{A.15}) \\ &= r_B \left( -\cos(\nu_B + \omega_B) \left( \cos i_A \cos(\nu_A + \omega_A) \sin(\Omega_A - \Omega_B) + \cos(\Omega_A - \Omega_B) \sin(\nu_A + \omega_A) \right) \right. \\ &\quad + \left( \cos(\nu_A + \omega_A) \left( \cos i_A \cos i_B \cos(\Omega_A - \Omega_B) + \sin i_A \sin i_B \right) \right. \\ &\quad \left. \left. - \cos i_B \sin(\Omega_A - \Omega_B) \sin(\nu_A + \omega_A) \right) \sin(\nu_B + \omega_B) \right) \end{aligned}$$

$$\begin{aligned} r_{B_z} = z &= G_{31}r_x(\mathbf{k}_B) + G_{32}r_y(\mathbf{k}_B) + G_{33}r_z(\mathbf{k}_B) \quad (\text{A.16}) \\ &= r_B \left( \cos(\nu_B + \omega_B) \sin i_A \sin(\Omega_A - \Omega_B) \right. \\ &\quad \left. + \left( -\cos i_B \cos(\Omega_A - \Omega_B) \sin i_A + \cos i_A \sin i_B \right) \sin(\nu_B + \omega_B) \right) \end{aligned}$$

Note that if the two objects  $A$  and  $B$  are very close together compared to the distance from the central body, then a common assumption used is  $\mathbf{r}_B^A \equiv \mathbf{r}_B^B$ , therefore  $\mathbf{r}_B^A \approx [r_B, 0, 0]$  where  $\mathcal{A}$  and  $\mathcal{B}$  are the Hill frames centred on objects  $A$  and  $B$  respectively. Here this assumption is not used, and the exact equations for  $\mathbf{r}_B$  are derived.

The unit or directional vector  $\delta\hat{\mathbf{r}}$  from object  $A$  to object  $B$  in the Hill coordinate system centred on object  $A$  is then,

$$\delta\hat{\mathbf{r}}^A(\mathbf{k}_A, \mathbf{k}_B) = \frac{\mathbf{r}_B - \mathbf{r}_A}{r_B - r_A} = \begin{bmatrix} \frac{x - r_A}{\sqrt{(x - r_A)^2 + y^2 + z^2}} \\ \frac{y}{\sqrt{(x - r_A)^2 + y^2 + z^2}} \\ \frac{z}{\sqrt{(x - r_A)^2 + y^2 + z^2}} \end{bmatrix} \quad (\text{A.17})$$

4 where  $[x, y, z]$  are given above (A.14)–(A.16) in terms of orbital element sets for  $A$  and  $B$ . Note that vectors  $\mathbf{r}_A, \mathbf{r}_B$  are measured from the central body of the  $\mathcal{O}$  frame (e.g. the Sun) to objects  $A$  and  $B$  respectively, expressed in the Hill reference frame  $\mathcal{A}$ . Therefore  $\mathbf{r}_A^A = [r_A, 0, 0]$ , which is why there are no  $r_A$  terms in the  $\hat{y}$  and  $\hat{z}$  definitions.

A.2 LINEAR RELATIVE EQUATIONS OF MOTION

Schaub et al. [Schaub et al., 2000; Schaub and Alfriend, 2002; Schaub and Junkins, 2003; Schaub, 2004] developed a set of linear equations that provide a direct mapping between the Cartesian Hill frame  $\mathbf{X} = [x, y, z, \dot{x}, \dot{y}, \dot{z}]^T$  and the set of orbital element differences  $\delta\mathbf{k} = [\delta a, \delta e, \delta i, \delta\Omega, \delta\omega, \delta M]^T$ .

$$\mathbf{X} = \mathbf{F}(\mathbf{k}) \cdot \delta\mathbf{k} \quad \longleftrightarrow \quad \delta\mathbf{k} = \mathbf{F}^{-1}(\mathbf{k}) \cdot \mathbf{X} \quad (\text{A.18})$$

Given the set of Keplerian elements of the chief orbit:  $\mathbf{k} = [a, e, i, \Omega, \omega, \nu]$ , the following basic identities,

$$\theta = \nu + \omega \quad (\text{A.19})$$

$$p = a(1 - e^2) \quad (\text{A.20})$$

$$r = \frac{p}{1 + e \cos \nu} \quad (\text{A.21})$$

$$h = \sqrt{\mu p} \quad (\text{A.22})$$

$$\eta = \sqrt{1 - e^2} \quad (\text{A.23})$$

and the time derivatives,

$$\dot{\nu} = \frac{h}{r^2} \quad (\text{A.24})$$

$$\dot{r} = ae(1 - e^2) \frac{\dot{\nu} \sin \nu}{(1 + e \cos \nu)^2} \quad (\text{A.25})$$

then the matrix  $\mathbf{F}$  is defined as follows,

$$F_{11} = \frac{r}{a} \tag{A.26a}$$

$$F_{12} = -a \cos \nu \tag{A.26b}$$

$$F_{13} = 0 \tag{A.26c}$$

$$F_{14} = 0 \tag{A.26d}$$

$$F_{15} = 0 \tag{A.26e}$$

$$F_{16} = \frac{ae \sin \nu}{\eta} \tag{A.26f}$$

$$F_{21} = 0 \tag{A.27a}$$

$$F_{22} = \frac{r \sin \nu}{\eta^2} (2 + e \cos \nu) \tag{A.27b}$$

$$F_{23} = 0 \tag{A.27c}$$

$$F_{24} = r \cos i \tag{A.27d}$$

$$F_{25} = r \tag{A.27e}$$

$$F_{26} = \frac{r}{\eta^3} (1 + e \cos \nu)^2 \tag{A.27f}$$

$$F_{31} = 0 \tag{A.28a}$$

$$F_{32} = 0 \tag{A.28b}$$

$$F_{33} = r \sin \theta \tag{A.28c}$$

$$F_{34} = -r \cos \theta \sin i \tag{A.28d}$$

$$F_{35} = 0 \tag{A.28e}$$

$$F_{36} = 0 \tag{A.28f}$$

$$F_{41} = \frac{\dot{r}}{a} \tag{A.29a}$$

$$F_{42} = a\dot{\nu} \sin \nu \tag{A.29b}$$

$$F_{43} = 0 \tag{A.29c}$$

$$F_{44} = 0 \tag{A.29d}$$

$$F_{45} = 0 \tag{A.29e}$$

$$F_{46} = \frac{ae\dot{\nu} \cos \nu}{\eta} \tag{A.29f}$$

$$F_{51} = 0 \tag{A.30a}$$

$$F_{52} = \frac{1}{\eta^2} (\dot{r} \sin \nu (2 + e \cos \nu) + r\dot{\nu} \cos \nu (2 + e \cos \nu) - r\dot{\nu} e \sin^2 \nu) \tag{A.30b}$$

$$F_{53} = 0 \tag{A.30c}$$

$$F_{54} = \dot{r} \cos i \tag{A.30d}$$

$$F_{55} = \dot{r} \tag{A.30e}$$

$$F_{56} = \frac{r}{\eta^3} (\dot{r} (1 + e \cos \nu)^2 - 2re\dot{\nu} (1 + e \cos \nu) \sin \nu) \tag{A.30f}$$

$$F_{61} = 0 \quad (\text{A.31a})$$

$$F_{62} = 0 \quad (\text{A.31b})$$

$$F_{63} = \dot{r} \sin \theta + r \dot{\nu} \cos \theta \quad (\text{A.31c})$$

$$F_{64} = -\cos \theta \sin i + r \dot{\nu} \sin \theta \sin i \quad (\text{A.31d})$$

$$F_{65} = 0 \quad (\text{A.31e})$$

$$F_{66} = 0 \quad (\text{A.31f})$$

where  $F_{ij}$  is the component in the  $i^{\text{th}}$  row,  $j^{\text{th}}$  column of the  $6 \times 6$  matrix  $\mathbf{F}$

$$\begin{bmatrix} x \\ y \\ z \\ \dot{x} \\ \dot{y} \\ \dot{z} \end{bmatrix} = \begin{bmatrix} F_{11} & F_{12} & F_{13} & \cdots & \cdots & F_{16} \\ F_{21} & \ddots & & & & F_{26} \\ \vdots & & \ddots & & & \vdots \\ & & & \ddots & & \vdots \\ \vdots & & & & \ddots & F_{56} \\ F_{16} & \cdots & \cdots & F_{64} & F_{65} & F_{66} \end{bmatrix} \begin{bmatrix} \delta a \\ \delta e \\ \delta i \\ \delta \Omega \\ \delta \omega \\ \delta M \end{bmatrix} \quad (\text{A.32})$$

To avoid singularities in the  $e$  and  $\omega$  terms, Schaub expressed his equations in terms of an alternate set of orbital elements  $\mathbf{k}^* = [a, \theta, i, q_1, q_2, \Omega]$ , where

$$\theta = \omega + \nu \quad (\text{A.33})$$

$$q_1 = e \cos \omega \quad (\text{A.34})$$

$$q_2 = e \sin \omega \quad (\text{A.35})$$

in this case the radius vector can be defined as

$$r = \frac{a(1 - q_1^2 - q_2^2)}{1 + q_1 \cos \theta + q_2 \sin \theta} \quad (\text{A.36})$$

The set of equations in the local Hill frame in (3.12) or in the matrix  $\mathbf{F}$ , can also be expressed in terms of this new orbital element set,

$$x = \delta r = \frac{r}{a} \delta a + \frac{v_r}{v_t} r \delta \theta - \frac{r}{p} (2aq_1 + r \cos \theta) \delta q_1 - \frac{r}{p} (2aq_2 + r \sin \theta) \delta q_2 \quad (\text{A.37a})$$

$$y = r (\delta \theta + \cos i \delta \Omega) \quad (\text{A.37b})$$

$$z = (r \sin \theta) \delta i - (r \cos \theta \sin i) \delta \Omega \quad (\text{A.37c})$$

$$\dot{x} = -\frac{v_r}{2a} \delta a + \left( \frac{1}{r} - \frac{1}{p} \right) h \delta \theta + \frac{v_r a q_1 + h \sin \theta}{p} \delta q_1 + \frac{v_r a q_2 - h \cos \theta}{p} \delta q_2 \quad (\text{A.38a})$$

$$\begin{aligned} \dot{y} = & -\frac{3v_t}{2a} \delta a - v_r \delta \theta + \frac{3v_t a q_1 + 2h \cos \theta}{p} \delta q_1 \\ & + \frac{3v_t a q_2 + 2h \sin \theta}{p} \delta q_2 + v_r \cos i \delta \Omega \end{aligned} \quad (\text{A.38b})$$

$$\dot{z} = (v_t \cos \theta + v_r \sin \theta) \delta i + (v_t \sin \theta - v_r \cos \theta) \sin i \delta \Omega \quad (\text{A.38c})$$

where  $v_r$ ,  $v_t$  are the radial and transverse components of the chief velocity vector.

$$v_r = \dot{r} = \frac{h}{p} (q_1 \sin \theta - q_2 \cos \theta)$$

$$v_t = r\dot{\theta} = \frac{h}{p} (1 + q_1 \cos \theta + q_2 \sin \theta)$$

The inverse transformation from Hill Cartesian coordinates  $\mathbf{X}$  to orbital element differences  $\delta \mathbf{k}$  can also be derived analytically – this is generally preferred as the matrix  $\mathbf{F}$  is often close to singular making numerical methods impractical or impossible.

$$\begin{aligned} \delta a = & \frac{a}{pr} (4p + 5ae^2 + ae(6 \cos \nu + e \cos(2\nu))) x + \frac{2a^2 e \sin \nu}{h} \dot{x} \\ & - \frac{ae(2p + 3ae^2 + ae(4 \cos \nu + e \cos(2\nu))) \sin \nu}{p^2} y \\ & + \frac{ar}{h(1-e^2)} (2p + 3ae^2 + e(4 \cos \nu + e \cos(2\nu))) \dot{y} \end{aligned} \quad (\text{A.39})$$

$$\delta \theta = \frac{y}{r} + \frac{e \cos \omega + \cos \theta}{p} z - \frac{h \sin \theta}{\mu(1 + e \cos \nu)} \dot{z} \quad (\text{A.40})$$

$$\delta i = \frac{e \sin \omega + \sin \theta}{p} z + \frac{h \cos \theta}{\mu(1 + e \cos \nu)} \dot{z} \quad (\text{A.41})$$

$$\begin{aligned} \delta q_1 = & \frac{5e \cos \omega + 6 \cos \theta + e \cos(2\nu + \omega)}{2r} x + \sqrt{\frac{p}{\mu}} \sin \theta \dot{x} \\ & - \frac{e}{4p} (4 \sin(2\nu + \omega) + e(\sin(\nu - \omega) + 4 \sin \theta + \sin(3\nu + \omega))) y \\ & + \sqrt{\frac{p}{\mu}} \left( 2 \cos \theta + \frac{e \sin \nu \sin \theta}{1 + e \cos \nu} \right) \dot{y} - \frac{e(e \cos \omega + \cos \theta) \sin \omega}{p \tan i} z \\ & + \frac{he \sin \omega \sin \theta}{\mu \tan i (1 + e \cos \nu)} \dot{z} \end{aligned} \quad (\text{A.42})$$

$$\begin{aligned} \delta q_2 = & \frac{5e \sin \omega + 6 \sin \theta + e \sin(2\nu + \omega)}{2r} x - \sqrt{\frac{p}{\mu}} \cos \theta \dot{x} \\ & + e \frac{4 \cos(2\nu + \omega) + e(-\cos(\nu - \omega) + 4 \cos \theta + \cos(3\nu + \omega))}{4p} y \\ & - \sqrt{\frac{p}{\mu}} \left( \frac{e \cos \theta \sin \nu}{1 + e \cos \nu} + 2 \sin \theta \right) \dot{y} + \frac{e \cos \omega (e \cos \omega + \cos \theta)}{p \tan i} z \\ & - h \frac{e \cos \omega \sin \theta}{\mu \tan i (1 + e \cos \nu)} \dot{z} \end{aligned} \quad (\text{A.43})$$

$$\delta \Omega = -\frac{e \cos \theta + \cos \theta}{p \cos i} z + \frac{h \sin \theta}{\cos i \mu (1 + e \cos \nu)} \dot{z} \quad (\text{A.44})$$

Using the following relations,

$$\delta e = \delta q_2 \sin \omega + \delta q_1 \cos \omega \quad (\text{A.45})$$

$$\delta \omega = \frac{\delta q_2 \cos \omega - \delta q_1 \sin \omega}{e} \quad (\text{A.46})$$

$$\delta M = \left( \delta \theta - \delta \omega - \frac{\sin \nu (2 + e \cos \nu)}{\eta^2} \delta e \right) \frac{\eta^3}{(1 + e \cos \nu)^2} \quad (\text{A.47})$$

(A.39)–(A.44) can be converted back to the conventional set of Keplerian elements  $\delta\mathbf{k} = [\delta a, \delta e, \delta i, \delta\omega, \delta\Omega, \delta M]$ . The inverse matrix  $\mathbf{F}^{-1}$  is defined as follows,

$$F_{11}^{-1} = \frac{r}{a} \tag{A.48a}$$

$$F_{12}^{-1} = -a \cos \nu \tag{A.48b}$$

$$F_{13}^{-1} = 0 \tag{A.48c}$$

$$F_{14}^{-1} = 0 \tag{A.48d}$$

$$F_{15}^{-1} = 0 \tag{A.48e}$$

$$F_{16}^{-1} = \frac{ae \sin \nu}{\eta} \tag{A.48f}$$

$$F_{21}^{-1} = 0 \tag{A.49a}$$

$$F_{22}^{-1} = \frac{r \sin \nu}{\eta^2} (2 + e \cos \nu) \tag{A.49b}$$

$$F_{23}^{-1} = 0 \tag{A.49c}$$

$$F_{24}^{-1} = r \cos i \tag{A.49d}$$

$$F_{25}^{-1} = r \tag{A.49e}$$

$$F_{26}^{-1} = \frac{r}{\eta^3} (1 + e \cos \nu)^2 \tag{A.49f}$$

$$F_{31}^{-1} = 0 \tag{A.50a}$$

$$F_{32}^{-1} = 0 \tag{A.50b}$$

$$F_{33}^{-1} = r \sin \theta \tag{A.50c}$$

$$F_{34}^{-1} = -r \cos \theta \sin i \tag{A.50d}$$

$$F_{35}^{-1} = 0 \tag{A.50e}$$

$$F_{36}^{-1} = 0 \tag{A.50f}$$

$$F_{41}^{-1} = \frac{\dot{r}}{a} \tag{A.51a}$$

$$F_{42}^{-1} = a \dot{\nu} \sin \nu \tag{A.51b}$$

$$F_{43}^{-1} = 0 \tag{A.51c}$$

$$F_{44}^{-1} = 0 \tag{A.51d}$$

$$F_{45}^{-1} = 0 \tag{A.51e}$$

$$F_{46}^{-1} = \frac{ae \dot{\nu} \cos \nu}{\eta} \tag{A.51f}$$

$$F_{51}^{-1} = 0 \quad (\text{A.52a})$$

$$F_{52}^{-1} = \frac{1}{\eta^2} (\dot{r} \sin \nu (2 + e \cos \nu) + r \dot{\nu} \cos \nu (2 + e \cos \nu) - r \dot{\nu} e \sin^2 \nu) \quad (\text{A.52b})$$

$$F_{53}^{-1} = 0 \quad (\text{A.52c})$$

$$F_{54}^{-1} = \dot{r} \cos i \quad (\text{A.52d})$$

$$F_{55}^{-1} = \dot{r} \quad (\text{A.52e})$$

$$F_{56}^{-1} = \frac{r}{\eta^3} (\dot{r} (1 + e \cos \nu)^2 - 2r e \dot{\nu} (1 + e \cos \nu) \sin \nu) \quad (\text{A.52f})$$

$$F_{61}^{-1} = 0 \quad (\text{A.53a})$$

$$F_{62}^{-1} = 0 \quad (\text{A.53b})$$

$$F_{63}^{-1} = \dot{r} \sin \theta + r \dot{\nu} \cos \theta \quad (\text{A.53c})$$

$$F_{64}^{-1} = -\cos \theta \sin i + r \dot{\nu} \sin \theta \sin i \quad (\text{A.53d})$$

$$F_{65}^{-1} = 0 \quad (\text{A.53e})$$

$$F_{66}^{-1} = 0 \quad (\text{A.53f})$$

A state-transition matrix  $\Phi_{\mathbf{X}}$  was developed by Gim and Alfriend (2003) in order to directly determine the position and velocity state vector of the formation spacecraft at any given point in time, given the initial state.

$$\mathbf{X}(t) \approx \Phi_{\mathbf{X}}(t, t_0) \mathbf{X}(t_0) \quad (\text{A.54})$$

The definition of the matrix is based in part on the above two matrices  $\mathbf{F}$  and  $\mathbf{F}^{-1}$ .

$$\Phi_{\mathbf{X}}(t, t_0) = \left[ \frac{\partial \mathbf{X}(t)}{\partial \mathbf{X}(t_0)} \right] = \mathbf{F}(t) \left[ \frac{\partial \delta \mathbf{k}(t)}{\partial \delta \mathbf{k}(t_0)} \right] \mathbf{F}^{-1}(t_0) \quad (\text{A.55})$$

The only remaining unknown is the matrix  $\Phi_{\delta \mathbf{k}}$ , based on a  $6 \times 6$  standard identity matrix. The only time variant parameter is  $\delta \nu$  in the set  $\delta \mathbf{k}$ , or  $\delta \theta$  in the set  $\delta \mathbf{k}^*$ , which can be expressed in the form,

$$\delta \nu = \Phi_{21} \delta a + \varkappa \delta e + \Phi_{22} \delta \nu_0 \quad (\text{A.56})$$

$$\delta \theta = \delta \nu + \delta \omega = \Phi_{21} \delta a + \Phi_{22} \delta \nu_0 + \Phi_{24} \delta q_1 + \Phi_{25} \delta q_2 \quad (\text{A.57})$$

For the entire derivation, see Schaub and Junkins (2003). The matrix is therefore given by,

$$\Phi_{\delta \mathbf{k}^*} = \left[ \frac{\partial \delta \mathbf{k}^*(t)}{\partial \delta \mathbf{k}^*(t_0)} \right] = \begin{bmatrix} 1 & 0 & 0 & 0 & 0 & 0 \\ \Phi_{21} & \Phi_{22} & 0 & \Phi_{24} & \Phi_{25} & 0 \\ 0 & 0 & 1 & 0 & 0 & 0 \\ 0 & 0 & 0 & 1 & 0 & 0 \\ 0 & 0 & 0 & 0 & 1 & 0 \\ 0 & 0 & 0 & 0 & 0 & 1 \end{bmatrix} \quad (\text{A.58})$$

where

$$\Phi_{21} = (M - M_0) \frac{-3a\eta}{2r^2} \quad (\text{A.59})$$

$$\Phi_{22} = \left(\frac{r}{r_0}\right)^2 \quad (\text{A.60})$$

$$\Phi_{24} = \frac{\varkappa q_1}{e} - \frac{q_2}{e^2} \left(1 - \left(\frac{r}{r_0}\right)^2\right) \quad (\text{A.61})$$

$$\Phi_{25} = \frac{\varkappa q_2}{e} - \frac{q_1}{e^2} \left(1 - \left(\frac{r}{r_0}\right)^2\right) \quad (\text{A.62})$$

and

$$\begin{aligned} \varkappa = \frac{1}{e\eta^2} & \left( (q_1 \sin \theta - q_2 \cos \theta) (2 + q_1 \cos \theta + q_2 \sin \theta) \right. \\ & \left. - (q_1 \sin \theta_0 - q_2 \cos \theta_0) (2 + q_1 \cos \theta_0 + q_2 \sin \theta_0) \left(\frac{r}{r_0}\right)^2 \right) \end{aligned} \quad (\text{A.63})$$

The variables  $q_1$  and  $q_2$  are defined above in (A.34) and (A.35) and are from the set  $\delta\mathbf{k}^*$ , used here to avoid singularities due to  $e$  or  $\omega$ .

## OPTIMISATION ROUTINES

The following is an excerpt from [Maddock and Vasile, 2008a] outlining the optimisation procedure used in the research. The work is based on proprietary software package EPIC (Evolutionary Programming and Interval Computation) developed by Vasile for use in local and global trajectory optimisation for space mission analysis. For further reading, see [Vasile, 2005a,b, 2008; Vasile and Locatelli, 2009].

## B.1 OPTIMISATION PROCEDURE

Normally in literature, single objective optimisation and multiobjective optimisation are treated as two distinct problems with different algorithms developed to address either one or the other. Many approaches for both single and multiobjective optimisation are biologically inspired. Some derive their inspiration from evolutionary processes, e.g., [Coello Coello et al., 2007; Price et al., 2005; Deb et al., 2000, 2002], while others from social behaviours in animals, e.g., [Kennedy and Eberhart, 1995; Elbeltagi et al., 2005; Reyes-Sierra and Coello Coello, 2007].

Vasile [Maddock and Vasile, 2008a; Vasile, 2008; Vasile and Locatelli, 2009] developed a unified formulation that can be applied to the solution of both single and multiobjective problems in which the aim is to find a set of optimal solutions rather than a single one. A hybrid behavioural-search approach tries to collect into an archive  $A_g$  as many feasible solutions, either locally or Pareto optimal, as possible. The behavioural search is hybridised with a domain decomposition technique in order to extend the exploration of the search space. The stochastic part of the algorithm is based on a meta-heuristic that selects and implements an appropriate set of actions (i.e. heuristics derived from various bio-inspired approaches) for a small group of agents aimed at finding the optimal set. The deterministic part partitions the search domain, depending on the outcome of the stochastic part, and directs the search toward areas of the solution space that are either unexplored or particularly promising.

## B.2 GENERAL PROBLEM FORMULATION

The general problem both for single and multiobjective optimisation is to find a set  $X$ , contained in a given domain  $D$ , of solutions  $\mathbf{u}$  such that the property  $P(\mathbf{u})$  is true for all  $\mathbf{u} \in X \subseteq D$ ,

$$X = \{\mathbf{u} \in D \mid P(\mathbf{u})\} \quad (\text{B.1})$$

where the domain  $D$  is a hyper-rectangle defined by the upper and lower bounds of the components of the vector  $\mathbf{u}$ ,

$$D = \{u_i \mid u_i \in [b_i^l \quad b_i^u] \subseteq \Re, i = 1, \dots, n\} \quad (\text{B.2})$$

All the solutions satisfying property  $P$  are defined to be optimal with respect to  $P$ , or ‘ $P$ -optimal’, and  $X$  can be said to be a  $P$ -optimal set. Now, the property  $P$  might not identify a unique set, for example if  $P$  is the Pareto optimality then  $X$  can collect all

the points belonging to a local Pareto front. Therefore we can define a global optimal set  $X_{opt}$  such that all the elements of  $X_{opt}$  dominate the elements of any other  $X$ ,

$$X_{opt} = \{\mathbf{u}^* \in D \mid P(\mathbf{u}^*) \wedge \forall \mathbf{u} \in X \Rightarrow \mathbf{u}^* \prec \mathbf{u}\} \quad (\text{B.3})$$

where  $\mathbf{u}^* \prec \mathbf{u}$  represents the dominance of the  $\mathbf{u}^*$  solution over the  $\mathbf{u}$  solution.

If we are looking for local minima, the property  $P$  is to be a local minimiser or a solution  $\mathbf{u}^*$  can be said to dominate solution  $\mathbf{u}$  if the associated value of the objective function  $f(\mathbf{u}^*) < f(\mathbf{u})$ . In this case  $X_{opt}$  would contain the global optimum or a set of global optima all with the same value of  $f$ . In the following we will look for the union of  $X$  and  $X_{opt}$ .

In the case of multiple objective problems, given a set of solution vectors we can associate to each one of them a scalar dominance index  $I_d$  such that,

$$I_d(\mathbf{u}_j) = \left[ \{i \mid i \wedge j \in N_p \wedge \mathbf{u}_i \prec \mathbf{u}_j\} \right] \quad (\text{B.4})$$

where  $[\square]$  is the cardinality of a set\*, and  $N_p$  is the set of the indices of all the given solution vectors. Here and in the following, a solution vector  $\mathbf{u}_i$  is said to be dominating a solution vector  $\mathbf{u}_j$  if the values of all the components of the objective vector  $\mathbf{f}(\mathbf{u}_i)$  are lower than or equal to the values of all the components of the objective vector  $\mathbf{f}(\mathbf{u}_j)$  and at least one component is strictly lower. In this case, for the  $j^{\text{th}}$  solution,  $P(\mathbf{u}_j)$  simply defines the property of being not-dominated by any other solution in the set  $N_p$ , thus:

$$X = \{\mathbf{u}_j \in D \mid I_d(\mathbf{u}_j) = 0\} \quad (\text{B.5})$$

For constrained problems, the property  $P$  is to be optimal, either locally or Pareto, and feasible at the same time.

### B.3 BEHAVIOURAL-BASED SEARCH

A population of virtual agents is deployed in the search space. Each agent is associated to a solution vector  $\mathbf{u}$  and endowed with a set of basic actions forming a behaviour. The entire population evolves through a number of steps toward the feasible set  $X$ . At each evolutionary step, the agents collect clues about the environment and implement actions according to an action selection mechanism. Some of these actions are devoted to acquire new information, others to displace the agents toward the local minima, while other actions are instead used to exchange information among the agents.

The basic idea is that most of the bio-inspired global optimisation approaches implement some form of basic behaviour derived from nature: from mating of Evolutionary Algorithms (EA) to the flying of bird flocks in Particle Swarm Optimisation (PSO) to the social behaviour of ants in Ant Colony Optimisation (ACO). Some of those behaviours can be classified as *social*, such as crossover in genetic algorithms, because they are devised to exchange pieces of information among the individuals. Other behaviours can be classified as *individualistic* because they aim at improving the individual status of each individual.

We implement a set of actions, each one producing an outcome  $\mathbf{u}_{ke}$ , derived from PSO, EA and DE (Differential Evolution) and a very simple, basic action selection

---

\*“In formal set theory, the cardinality is a type of number defined in such a way that any method of counting sets using it gives the same result (this is not true for the ordinal numbers). Cardinal numbers are obtained by collecting all ordinal numbers which are obtainable by counting a given set. The cardinality of a set is also frequently referred to as the power of a set.” [Weisstein, 2009].

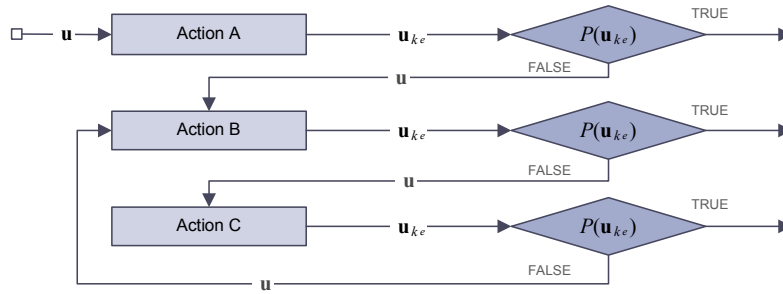


Figure 142: Action selection mechanism for individualistic behaviour.

mechanism. In particular, for individualistic behaviours (see Fig. 142), each agent can perform three types of actions: **A**, **B** and **C**. This general scheme accommodates two types of heuristics: Action **A** generates always the same outcome every time is performed once a solution vector  $\mathbf{u}$  is given (e.g. inertia in PSO), while Actions **B** and **C** generate different values for the same  $\mathbf{u}$  every time they are performed (e.g. mutation in EA). These last two actions are repeated until an improvement is registered or a maximum number of attempts is reached. The index  $k_e$  is increased by one every time an action is performed, and every action makes use of the agent status, the status of other agents and of the outcome of the preceding actions.

After an initialisation is performed by sampling the solution space by Latin Hypercube, each solution vector is associated to an agent. Each agent is then evaluated and social behaviours (such as crossover) are implemented. After exchanging information with the other agents, each one can implement a set of individualistic actions (such as mutation, for example). The archive collects all the solutions for which  $P$  is true at every evolutionary step. Furthermore, at termination the entire population is added to the archive. Note that the property  $P$  required for feasible and for unfeasible agents is different: feasible agents are required to be either locally or Pareto optimal and to remain feasible, while unfeasible agents are required to simply become feasible. As a consequence, the entire population of agents is divided into two subpopulations: one aiming at being optimal, the other aiming at being feasible. The overall algorithm, called Multiagent Collaborative Search (MACS), is represented in Fig. 143 and briefly outlined below.

**STEP 0. INITIALISATION** Generate an initial population of agents  $\Pi_0$  within  $D$  through a Latin Hypercube (i.e., a non-collapsing design where points/agents are evenly spread when projected along a single parameter axis) [van Dam et al., 2007]. A hyperrectangle  $S^{\mathbf{u}_j^0}$  is associated to the  $j^{\text{th}}$  agent  $\mathbf{u}_j^0 \in \Pi_0$ . The initial size  $\rho(\mathbf{u}_j^0)$  of each region  $S^{\mathbf{u}_j^0}$  is fixed to 1 (i.e., the initial local region of each agent corresponds to the whole set  $D$ ). The effort  $s(\mathbf{u}_j^0)$  dedicated to agent  $\mathbf{u}_j^0 \in \Pi_0$  is fixed to the same value  $s_{\text{max}}$  (equal to  $n$  in the computations) for all agents in  $\Pi_0$ . Set  $k = 0$ .

**STEP 1. COLLABORATION** Agents collaborate with each other (social behaviour). The collaborations give rise to a set of new solutions denoted by  $Q_{k+1}$ .

**STEP 2. SELECTION** A subset of members of the set  $\Pi_k \cup Q_{k+1}$  will be selected to give rise to the new updated population  $\Pi_{k+1}$ .

- STEP 3. REPULSION The population is updated through a repulsion mechanism: when the reciprocal distance of a number of agents goes below a given threshold, the worst one according to  $P$  is re-generated randomly within  $D$ .
- STEP 4. FILTERING The population is ranked according to the assigned  $P$ . A *filter* partitions the population  $\Pi_{k+1}$  into two subsets:  $\Pi_{k+1}^{in}$ , the population fraction within the filter made of the best agents according to the property  $P$ , and  $\Pi_{k+1}^{out}$ , the population fraction outside the filter.
- STEP 5. INDIVIDUALISTIC ACTIONS A set of actions, specified by a *behaviour*, are applied to each agent  $\mathbf{u}_j^{k+1} \in \Pi_{k+1}$ . These allow local exploration within,  $S^{\mathbf{u}_j^{k+1}}$  of the region around the agent. They are repeatedly applied until either an improvement is observed or the number  $s(\mathbf{u}_j^{k+1})$  of actions is reached. If an agent  $\mathbf{u}_j^{k+1}$  generates an improvement, population  $\Pi_{k+1}$  is updated by replacing  $\mathbf{u}_j^{k+1}$  with its improvement. The agents in  $\Pi_{k+1}^{in}$  versus  $\Pi_{k+1}^{out}$  perform different sequences of actions. In particular, the ones in  $\Pi_{k+1}^{out}$  only perform a random sampling of  $D$  through mutation.
- STEP 6. HYPERRECTANGLE UPDATE The size parameter  $\rho$  and the effort parameter  $s$  associated to each agent within the filter are updated.
- STEP 7. ARCHIVE UPDATE Apply filtering and update archive  $A_l$ .
- STEP 8. STOPPING RULE A stopping rule is checked. If it is not satisfied, then set  $k = k + 1$  and go back to Step 1. If it is satisfied, then update the archive  $A_l$  by adding the current population, i.e., set  $A_l = A_l \cup \Pi_{k+1}$ . The search is terminated after a given number of function evaluations.

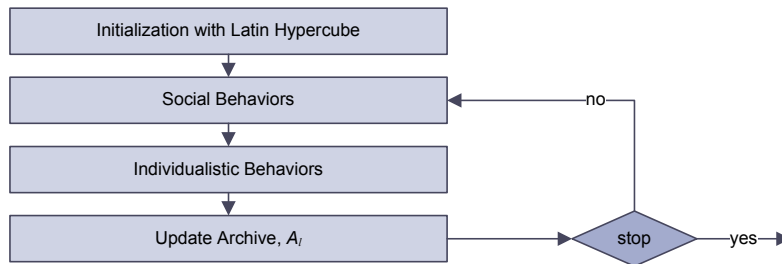


Figure 143: Overall algorithm for the Multiagent Collaborative Search (MACS)

B.4 DOMAIN DECOMPOSITION

In the case of single objective optimisation, the number of local minima is expected to be finite (for physical reasons). In the case of multiobjective optimisation different portions of the Pareto front in the criteria space can correspond to different portions of the solution space. Therefore, the search space can be decomposed into a finite number of subsets, each containing a portion of the optimal set  $X$  such that  $X \cap D \neq \emptyset$ . The initial domain  $D$  is progressively decomposed into smaller domains  $D_l \subseteq D$  according

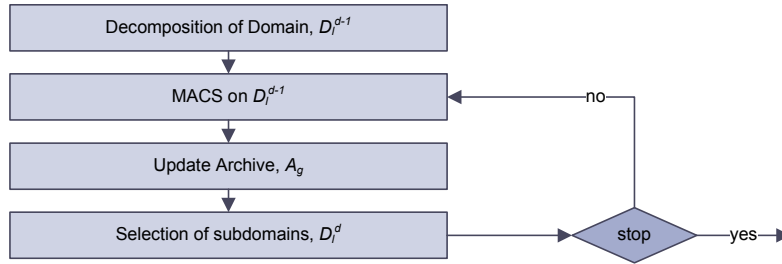


Figure 144: Hybrid domain decomposition and stochastic search.

to a decomposition strategy. The decomposition strategy is based on the output of the stochastic search step and produces a number  $M$  of subdomains  $D_l$  such that,

$$\bigcup_{l=1}^M D_l = D \tag{B.6}$$

Decomposition (B.6) is then iteratively applied to the subdomains  $D_l$  that need further exploration, so that

$$\bigcup_{l=1}^M D_l^{(d)} = D_i^{(d-1)} \tag{B.7}$$

where  $d$  is the decomposition depth.

In this implementation we use a simple regular cutting of each coordinate into two halves. Since the interest is to widely explore the search space and to collect as many elements of  $X$  as possible, after each stochastic search the largest subdomain  $D_l$  with the least number of collected samples belonging to  $X$  is selected for further decomposition provided that the number of times  $n_b$  its parent subdomains have already been decomposed without improvement is below a given threshold.

We use the following merit function to balance the search of completely unexplored subdomains against those containing elements of  $X$ ,

$$\Psi_{D_l} = (1 - \nu)\varpi_{D_l} + \nu\phi_{D_l} \tag{B.8}$$

where  $\varpi_{D_l}$  is the density of already discovered solutions in  $D_l$ ,  $\phi_{D_l}$  is the best fitness in  $D_l$  and  $\nu$  is a weighting factor used to favour either convergence or exploration.

The partitioning cycle is stopped when a given number of subdomains have been generated, or when the size of the archive has been exceeded. Note that in order to collect as many solutions belonging to  $X$  as possible while maintaining a low computational cost, we used a local archive  $A_l$  of limited size for each run of the MACS algorithm. We then store all the globally, non-dominated solutions for all the subdomains in a global archive,  $A_g$ .

The overall algorithm combining the MACS and the domain decomposition technique is called Evolutionary Programming and Interval Computation or EPIC [Vasile, 2005a,b, 2008; Vasile and Locatelli, 2009].

B.5 SINGLE VERSUS MULTIPLE OBJECTIVE OPTIMISATION

Although the problem formulation through the definition of  $P$  is general and applicable to both single objective (SOO) and multiple objective optimisation (MOO)

problems, either constrained or not, the actual property is substantially different depending on the type of problem.

For box constrained single objective problems, the property  $P$  is to be a local minimiser in  $D$ . If  $S^{\mathbf{u}}$  is the local portion of the search space containing the agent  $\mathbf{u}$ , then the property can be formally expressed as follows:

$$f(\mathbf{u}) > f(\mathbf{u}_{k_e}) + \epsilon \Rightarrow P(\mathbf{u}_{k_e}) = \text{true} \quad (\text{B.9})$$

where  $\epsilon$  is a minimum required local improvement. For multiobjective problems, the property  $P$  is defined by the value of the scalar dominance index  $I_d$ , thus:

$$I_d(\mathbf{u}) > I_{d,\epsilon}(\mathbf{u}_{k_e}) \Rightarrow P(\mathbf{u}_{k_e}) = \text{true} \quad (\text{B.10})$$

where  $\epsilon$  is now the minimum expected improvement in the computation of the dominance. Note that this easily accommodates the concept of  $\epsilon$  dominance.

When multiple outcomes with the same dominance index are generated by either social or individualistic actions, the one that corresponds to the longest vector difference in the criteria space with respect to  $\mathbf{u}$  is considered. Note that in many situations the action selection scheme in Fig. 143 generates a number of solutions that are dominated by the agent  $\mathbf{u}$ . Many of them can have the same dominance value; therefore in order to rank them, we use the modified dominance index:

$$I_d(\mathbf{u}_i) = \left[ \{j \mid f(\mathbf{u}_{k_e}) = f(\mathbf{u})\} \right] \kappa + \left[ \{j \mid f(\mathbf{u}_{k_e}) > f(\mathbf{u})\} \right] \quad (\text{B.11})$$

where  $\kappa$  is equal to one if there is at least one component of  $f(\mathbf{u})$  which is better than the corresponding component of  $f(\mathbf{u}_{k_e})$ , and is equal to zero otherwise.

Now, if for the  $k_e^{\text{th}}$  outcome, the dominance index in (B.11) is not zero but is lower than the number of components of the objective vector, then the agent  $\mathbf{u}$  is only partially dominating the  $k_e^{\text{th}}$  outcome. Among all the partially dominated outcomes with the same dominance index, we chose the one that satisfies the condition:

$$\min_{k_e} \langle (f(\mathbf{u}) - f(\mathbf{u}_{k_e})), \hat{\mathbf{e}} \rangle \quad (\text{B.12})$$

where

$$\hat{\mathbf{e}} = \frac{[1, 1, 1, \dots, 1]^T}{\sqrt{N_f}} \quad (\text{B.13})$$

is the unit vector of dimension  $N_f$ , and  $N_f$  is the number of objective functions.

Since the partially dominated outcomes of one agent could dominate other agents or the outcomes of other agents at the end of every evolution cycle all the outcomes are added to the archive. Then, the dominance index in (B.4) is computed for all the elements in  $A_l$  and only the non-dominated ones are preserved.

## B.6 CONSTRAINT HANDLING TECHNIQUE

The algorithm described above solves box-constrained problems. Since in most of the cases the imposed constraints are nonlinear, an extension of the algorithm was developed in order to account for nonlinear inequality constraints explicitly.

At each generation, the population of agents is divided into two subpopulations with a different  $P$  is assigned to each one, namely the property in (B.9) or (B.10) is assigned

to the subpopulation of feasible agents while the following property is assigned to the subpopulation of unfeasible agents:

$$F(\mathbf{u}) > F(\mathbf{u}_{k_e}) + \epsilon \Rightarrow P(\mathbf{u}_{k_e}) = \text{true} \quad (\text{B.14})$$

where

$$\min_{\mathbf{u} \in D} F = \sum_{j=1}^m \max([0, C_j]) \quad (\text{B.15})$$

The two subpopulations are evolved in parallel and agents are allowed to migrate from one population to the other, i.e., if a feasible agent becomes unfeasible it is inserted in the subpopulation of unfeasible agents and assigned to the solution of the constraints. On the other hand, if an unfeasible agent becomes feasible it is inserted into the population of feasible agents and a different property  $P$  is assigned to it. As a result, the final optimal solution is either feasible or minimises the infeasibility. This procedure does not maintain feasibility for any one of the agents. Feasibility can be preserved once a feasible set has been found by defining the following augmented function  $F^*$  for the feasible agents:

$$\min_{\mathbf{u} \in D} F^* = \begin{cases} f & \text{if every } C_j \leq 0 \\ f + \max(C) & \text{if any } C_j > 0 \end{cases} \quad (\text{B.16})$$

The described strategy of co-evolving two populations with two different goals allows a flexible search for feasible optimal solutions; in fact through (B.16) feasibility can be maintained on all or only part of the feasible solutions.

If all the feasible solutions are forced to remain feasible during the whole search process, the global exploration of the solution space may be penalised. The subpopulation of feasible agents could remain stuck in a niche along the boundary of the feasible region. Therefore, in order to search more extensively along the boundary of the feasible region, a subset of the feasible solutions is allowed to temporarily violate the constraint and become unfeasible. Feasibility is always preserved only for the best agent.

Note that if in (B.16),  $f$  is substituted with the dominance index  $I_d$  then the described constraint handling technique can be extended to the multiobjective case.

## B.7 PRELIMINARY OPTIMISATION TEST CASES

The proposed optimisation approach was extensively tested on several space related problems with a single objective. Here the interest is to apply EPIC at first to a single objective case and then to a multiobjective problem. Therefore a preliminary test was performed, applying EPIC to two well known problems in literature. For further details about these test functions, please refer to [Deb et al., 2000, 2002].

The first test case, *DEB*, is a constrained multiobjective optimisation problem with a convex Pareto front. The constraint  $C$  fragments the admissible Pareto front into a disconnected set. Running EPIC with a single level of branching and a limited population of 10 agents with 5 explorers, iterated for 12000 function evaluations, led to the result reported in Fig. 145 where the constraint is represented with a continuous line while the solutions found by EPIC are represented by points. The test was repeated 20 times with nearly identical results.

The second test case, *ZDT4*, is commonly recognised as one of the most challenging problems since it has  $21^9$  different local Pareto fronts of which only one corresponds to

Table 24: Parameters for the two preliminary test cases for EPIC.

ID	Parameters	Objective Function and Constraint
<i>DEB</i>	$y \in [0 \ 1]$	$f_1 = y_1$
	$i = 1, \dots, n$	$f_2 = g \left( 1 - \sqrt{\frac{f_1}{g}} \right) + 1$ given $g = 1 + \frac{9}{(n-1)} \sum_{i=2}^n y_i$
	$a = 0.2$ $b = 10$	$C = (f_2 - e) \cos \theta - f_1 \sin \theta$
	$c = 1$ $d = 6$	$-a \left  \sin \left( b\pi \left( (f_2 - e) \sin \theta - f_1 \cos \theta \right)^c \right) \right ^d$
	$e = 1$ $n = 10$	
<i>ZDT4</i>	$y \in [0 \ 1]$	$f_1 = y_1$
	$y_i \in [-5 \ 5]$	$f_2 = g \left( 1 - \sqrt{\frac{f_1}{g}} \right)$
	$i = 2, \dots, n$	given $g = 1 + 10(n-1) + \sum_{i=2}^n (y_i^2 - 10 \cos(4\pi y_i))$
	$n = 10$	

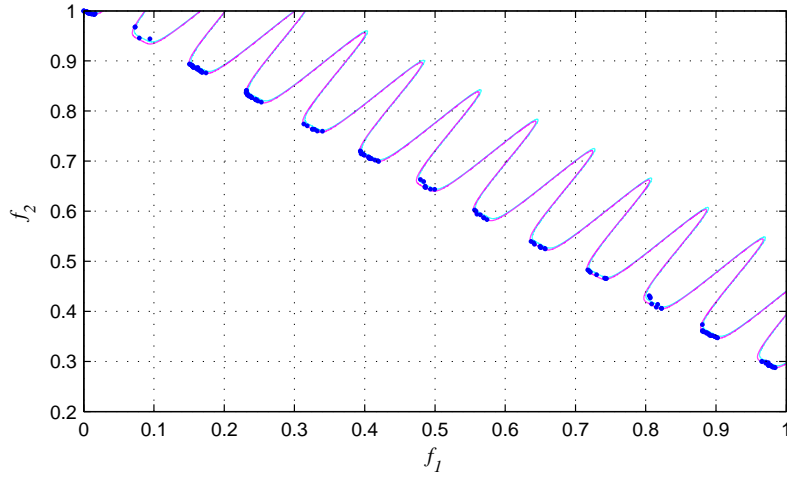


Figure 145: Admissible Pareto front for the test case *DEB*. The constraint is represented by a continuous line, the points represent the solutions found by EPIC.

the global Pareto-optimal front. In this case the exploration capabilities of each single agents are enough to locate the correct front with very limited effort. In fact, even with just five agents it was possible to reconstruct the correct Pareto front 20 times over 20 different runs (see Fig. 146a). The total number of function evaluations was fixed to 20000 for each of the runs, although already after 10000 function evaluations EPIC was always able to locate the global front (see Fig. 146b).

Despite the small number of agents, the sampled points of the Pareto front are quite well distributed with just few, limited interruptions. The use of a limited number of agents instead of a large population is related to the complexity of the algorithm. In fact, the computational cost of the procedure for the management of the local archive  $A_l$  is of the order  $n_A(n_p + n_A)$ , where  $n_A$  is the archive size and  $n_p$  is the population size, while the cost of the implementation of the individualistic-social behaviours is of the order  $n_p(n + n_p)$ . Therefore, even if the overall algorithm is polynomial in the population dimension, the computational cost would increase quadratically with the number of agents.

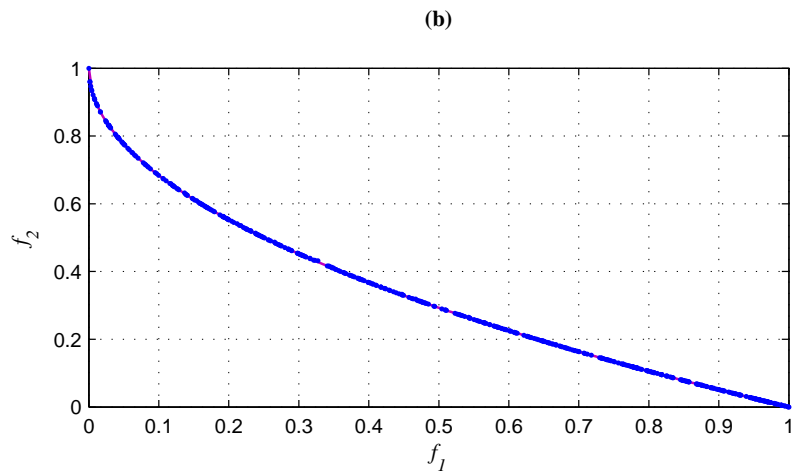
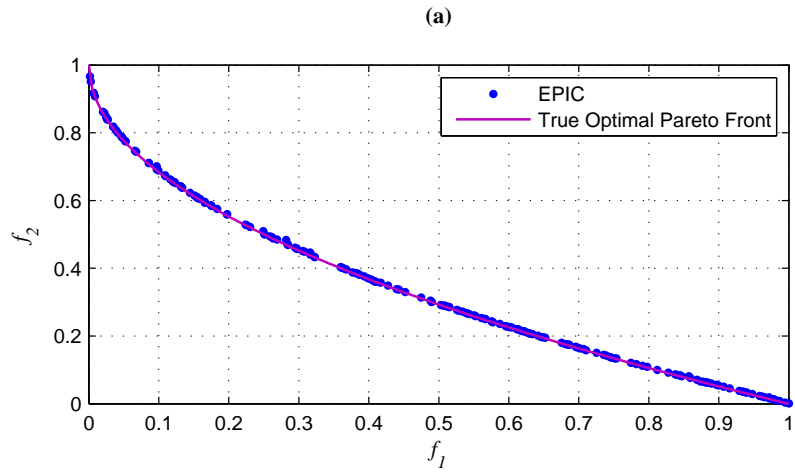


Figure 146: Admissible Pareto fronts for the test case *ZDT4*. The global Pareto-optimal front is represented by a continuous line, and the points represent the solutions found by EPIC.

As an additional proof of the effectiveness of MACS, we compare the average Euclidean distance of 500 uniformly spaced points on the true optimal Pareto front from an equal number of points belonging to the solution found by EPIC with the analogous performance metric found in [Deb et al., 2000] for NSGA-II, SPEA and PAES (see Table 25).

Table 25: Comparison of the average Euclidian distances between 500 uniformly space points on the optimal Pareto front for various optimisation algorithms.

Approach	Average Euclidian Distance	Standard Deviation
EPIC	$1.542 \times 10^{-3}$	$5.19 \times 10^{-4}$
NSGA-II	0.513053	0.118460
SPEA	7.340299	6.572516
PAES	0.854816	0.527238

## EQUATIONS FOR THE PROXIMITY-QUOTIENT CONTROL LAW

The following appendix lists the full derivations of the equations for the Proximity-Quotient control law, or Q-law, developed by Petropoulos starting in 2003 [Petropoulos, 2003, 2005]. A discussion and example transfer are also included at the end.

### c.1 DERIVATION OF EQUATIONS

#### *Gauss' Variational Equations*

The Gauss planetary equations in 3.28 are repeated here, for a disturbing or control acceleration  $\mathbf{u}$  in the radial  $r$ , tangential  $t$  and normal  $h$  directions [Battin, 1999].

$$\frac{da}{dt} = \frac{2a^2}{p\sqrt{\mu}} \left( e \sin \nu u_r + \frac{p}{r} u_t \right) \quad (\text{C.1a})$$

$$\frac{de}{dt} = \frac{1}{p\sqrt{\mu}} \left[ p \sin \nu u_r + \left( (p+r) \cos \nu + re \right) u_t \right] \quad (\text{C.1b})$$

$$\frac{di}{dt} = \frac{r \cos \theta}{p\sqrt{\mu}} u_h \quad (\text{C.1c})$$

$$\frac{d\Omega}{dt} = \frac{r \sin \theta}{p\sqrt{\mu} \sin \nu} u_h \quad (\text{C.1d})$$

$$\frac{d\omega}{dt} = \frac{1}{e\sqrt{p\mu}} \left[ -p \cos \nu u_r + (p+r) \sin \nu u_t \right] - \frac{r \sin \theta \cos i}{\sqrt{p\mu} \sin i} u_h \quad (\text{C.1e})$$

$$\frac{d\nu}{dt} = \frac{p\sqrt{\mu}}{r^2} + \frac{1}{ep\sqrt{\mu}} \left[ p \cos \nu u_r - (p+r) \sin \nu u_t \right] \quad (\text{C.1f})$$

where the thrust acceleration components can also be defined in terms of magnitude and in-plane angle  $\alpha$  and out of plane angle  $\beta$  (see Fig. 147),

$$u_r = \|\mathbf{u}\| \cos \beta \sin \alpha \quad (\text{C.2a})$$

$$u_t = \|\mathbf{u}\| \cos \beta \cos \alpha \quad (\text{C.2b})$$

$$u_h = \|\mathbf{u}\| \sin \beta \quad (\text{C.2c})$$

Note that  $u \equiv \|\mathbf{u}\|$ . The latter term is used here to avoid confusion with the variable  $\mu$ , used for the gravitational constant of the central body.

#### *Optimised Control Equations*

Based on the Gauss equations above, an analytic expression can be found for each of the orbital elements the gives the maximum rate of change possible of that element, over the orbit. In mathematical terms, this can be expressed as,

$$\dot{\mathbf{k}}_{xx} = \max_{\alpha, \beta, \nu} (\dot{\mathbf{k}}) \quad (\text{C.3})$$

which is determined by the optimal location along the orbit  $\nu$ , and the direction of thrust at that point  $\alpha, \beta$  that maximise the rate of change of the orbital element  $\dot{\mathbf{k}}$ . A

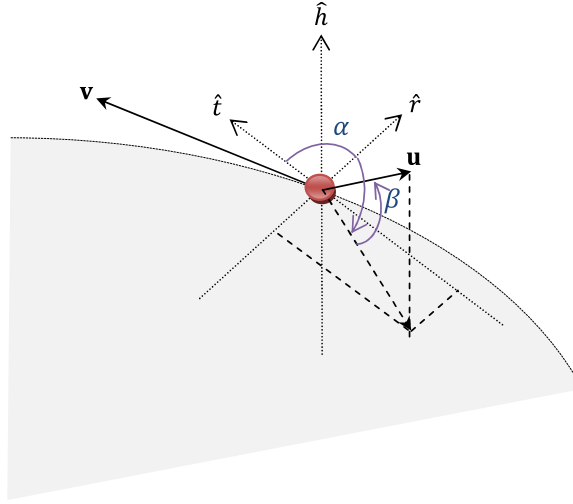


Figure 147: In-plane angle  $\alpha$  of thrust acceleration vector  $\mathbf{u}$  which lies in the orbital plane and measured positive clockwise from the tangential axis; and the out-of-plane angle  $\beta$ , measured from the orbital plane and positive in the direction of the angular momentum vector.

more complete rationale behind these derivations can be found in Petropoulos (2003); Gefert and Hack (1999).

$$\dot{a}_{xx}(a, e) = 2\|\mathbf{u}\|\sqrt{\frac{a^3(1+e)}{\mu(1-e)}} \quad (\text{C.4a})$$

$$\dot{e}_{xx}(a, e) = 2\|\mathbf{u}\|\sqrt{\frac{p}{\mu}} \quad (\text{C.4b})$$

$$\dot{i}_{xx}(a, e, \omega) = \sqrt{\frac{p}{\mu}} \frac{\|\mathbf{u}\|}{\sqrt{1 - (e \sin \omega)^2 - e|\cos \omega|}} \quad (\text{C.4c})$$

$$\dot{\Omega}_{xx}(a, e, i, \omega) = \sqrt{\frac{p}{\mu}} \frac{\|\mathbf{u}\| \csc i}{\sqrt{1 - (e \cos \omega)^2 - e|\sin \omega|}} \quad (\text{C.4d})$$

$$\begin{aligned} \dot{\omega}_{xx}(a, e) &= \frac{1}{1+b} \left( \frac{\|\mathbf{u}\|}{e\sqrt{\mu p}} \sqrt{(p \cos \nu_{xx})^2 + ((p + r_{xx}) \sin \nu_{xx})^2} \right) \\ &+ \frac{b}{1+b} \left( \sqrt{\frac{p}{\mu}} \frac{\|\mathbf{u}\| |\cos i| \csc i}{\sqrt{1 - (e \cos \omega)^2 - e|\sin \omega|}} \right) \end{aligned} \quad (\text{C.4e})$$

where,

$$\begin{aligned} \cos \nu_{xx} &= -\frac{1}{e} - \frac{\left(\frac{2}{3}\right)^{\frac{1}{3}} e^2}{\left(9e^3 - 9e^5 + \sqrt{3}\sqrt{27e^6 - 54e^8 + 27e^{10} + 4e^{12}}\right)^{\frac{1}{3}}} \\ &+ \frac{\left(9e^3 - 9e^5 + \sqrt{3}\sqrt{27e^6 - 54e^8 + 27e^{10} + 4e^{12}}\right)^{\frac{1}{3}}}{18^{\frac{1}{3}} e^2} \end{aligned} \quad (\text{C.5})$$

$$r_{xx} = \frac{a(1 - e^2)}{1 + e \cos \nu_{xx}} \quad (\text{C.6})$$

The Q-law is designed for orbit-to-orbit transfers, not point-to-point. When specifying the initial and targets states, the orbital location (in this case the true anomaly  $\nu$ ) is determined by the control law, not specified by the user a priori.

Note that the equation for  $\dot{\omega}_{xx}$  in (C.4e) is split into two components: in-plane and out-of-plane with an additional tuning parameter  $b$  to alter the weighting of the two parts. If  $b = 0$ , then  $\dot{\omega}_{xx}$  only accounts for the in-plane component of  $\omega$ , else if  $b = 1$ , both the in-plane and out-of-plane components are accounted for equally. Generally, the in-plane component is weighted more heavily due to the cost difference (in  $\Delta v$ ) between ‘lateral’ manoeuvres within the orbital plane versus a change in the inclination of the orbital plane.

#### Control Law

The Q-law is given by the following equation,

$$Q = S_r \left[ S_a W_a \left( \frac{\Delta a}{\dot{a}_{xx}} \right)^2 + W_e \left( \frac{\Delta e}{\dot{e}_{xx}} \right)^2 + W_i \left( \frac{\Delta i}{\dot{i}_{xx}} \right)^2 + W_\Omega \left( \frac{\Delta \Omega}{\dot{\Omega}_{xx}} \right)^2 + W_\omega \left( \frac{\Delta \omega}{\dot{\omega}_{xx}} \right)^2 \right] \quad (\text{C.7})$$

Integrating (C.4) into (C.7),

$$\begin{aligned} Q = & \left( 1 + W_p \exp^k \left( 1 - \frac{r_p}{(r_p)_{min}} \right) \right) \left[ \frac{W_a \Delta a^2 \left( 1 + \left( \frac{\Delta a}{a_{rm}} \right)^n \right)^{\frac{1}{q}} (1 - e) \mu}{4a^3 \|\mathbf{u}\|^2 (1 + e)} \right. \\ & + \frac{W_e \Delta e^2 \mu}{4p \|\mathbf{u}\|^2} + \frac{W_i \Delta i^2 \mu \kappa_1^2}{a \|\mathbf{u}\|^2 (1 - e^2)} + \frac{W_\Omega \Delta \Omega^2 \kappa_2^2 \sin^2 i}{p \|\mathbf{u}\|^2} \\ & \left. + \frac{W_\omega \Delta \omega^2 (1 + b)^2 p e^2 \mu}{\|\mathbf{u}\|^2 [p^2 x^2 + (p + r)^2 (1 - x^2)]} + \frac{W_\omega \Delta \omega^2 (1 + b)^2 \mu \kappa_2^2 \sin^2 i}{ab^2 \|\mathbf{u}\|^2 (1 - e^2) \cos i^2} \right] \end{aligned} \quad (\text{C.8})$$

where  $\Delta k$  is the difference between the target ( $k_T$ ) and initial/current states ( $k, k_i$ ), and  $W_k \geq 0$  are optional weights that alter the focus of the control, i.e. if a certain orbital element has priority over another, for example if it is compulsory to change the semi-major axis and eccentricity, and optional to change the inclination, with the RAAN and argument of periapsis left as free variables, an appropriate set of weights might be:  $W_a = 1$ ,  $W_e = 1$ ,  $W_i = 0.5$ ,  $W_\Omega = W_\omega = 0$ .

The value of  $Q$  should always be greater than or equal to zero, therefore in order to determine the optimal direction of thrust, the derivative  $dQ/dt$  should be negative in order to drive  $Q$  towards zero. It is of interest to note that the equation for  $Q$  is independent of the thrust angles  $\alpha, \beta$ , while the equation for  $dQ/dt$  is not.

$$\min_{\alpha, \beta} \frac{dQ}{dt}, \quad \text{where} \quad \frac{dQ}{dt} = \sum_k \frac{\partial Q}{\partial k} \frac{dk}{dt} \quad \text{for} \quad k = \{a, e, i, \Omega, \omega\} \quad (\text{C.9})$$

In [Petropoulos, 2005], Petropoulos added a series of penalty functions  $S$ . In particular, a function  $S_r$  was added to include a minimum radius of periapsis term, for e.g. if one was orbiting around a planet. As the output of the Q-law is based on a minimisation function,  $S_r$  increases exponentially as one approaches the minimum value  $(r_p)_{min}$  given for the radius of periapsis.

$$S_r = 1 + W_p \exp^k \left( 1 - \frac{r_p}{(r_p)_{min}} \right) \quad (C.10)$$

where  $W_p$  is a weighting parameter.

An byproduct of the original Q-law was that for orbital changes involving the semi-major axis,  $Q$  would tend towards zero as  $\Delta a$  either converged towards zero (as desired) or infinity. To compensate for this, a penalty function  $S_a$  was added to ensure  $a_i \rightarrow a_T$ .

$$S_a = \left( 1 + \left( \frac{\Delta a}{a_T m} \right)^n \right)^{\frac{1}{q}} \quad (C.11)$$

A number of tuning parameters,  $k$ ,  $m$ ,  $q$  and  $n$  are included that can be set by the user.

A set of effectivities, or efficiencies, were also added by Petropoulos (2004, 2005). In his words:

While the thrust angles  $\alpha$  and  $\beta$ , ensure the optimal rate of reduction of  $Q$  at the current true anomaly, they do not provide any information about how effective the thrust is, as compared with other locations on the osculating orbit. Thus, it is natural to define the effectivity of the thrust at the current true anomaly. A mission designer may then chose to prevent the spacecraft from thrusting if the effectivity is below some cut-off value. Broadly speaking, the greater the cut-off, the greater the expected propellant savings and the longer the expected flight time.

Two effectivities can be applied: the first is an ‘absolute effectivity’  $\eta_{abs}$ , which is a ratio between the minimum value of  $\dot{Q}$  at the current location along the orbit transfer (i.e. at a specific true anomaly  $\nu$ ), and the minimum value of  $\dot{Q}$  along the entire ‘orbit’ where the orbit is propagated for one period starting at that true anomaly. Along the transfer, the orbital elements at each point in time are constantly changing. In this case, the ‘orbit’ is defined as the set of orbital elements at that particular instance of time. This is equivalent to the gravitational orbit the spacecraft would take if the thrust was turned off. The relative efficiency  $\eta_{rel}$  is similar in that it compares the different possible values of  $\dot{Q}$  however as a percent ratio compared with the maximum possible and minimum possible  $\dot{Q}$  along one full propagated orbit. The merit of effectivities can be seen if one considers the difference between thrusting at perigee or apogee of a highly elliptic orbit, in order to increase the semi-major axis.

$$\eta_{abs} = \frac{\dot{Q}_n}{\dot{Q}_{nn}} \quad (C.12a)$$

$$\eta_{rel} = \frac{\dot{Q}_n - \dot{Q}_{nx}}{\dot{Q}_{nn} - \dot{Q}_{nx}} \quad (C.12b)$$

given

$$\dot{Q}_n = \min_{\alpha, \beta} \dot{Q} \quad (\text{C.13})$$

$$\dot{Q}_{nn} = \min_{\nu} \dot{Q}_n \quad (\text{C.14})$$

$$\dot{Q}_{nx} = \max_{\nu} \dot{Q}_n \quad (\text{C.15})$$

where  $\dot{Q}_{nn}$  gives the location along the orbit corresponding largest possible negative  $Q$  (judiciously quantifying the ‘best’ or more efficient location to apply the thrust), and  $\dot{Q}_{nx}$  gives the largest positive  $Q$  corresponding to the worst, i.e. least efficient location to apply thrust in order to manoeuvre to the target orbit. The first variable  $\dot{Q}_n$  is simply the output of the minimisation of the  $Q$ -law from (C.9), which finds an optimised direction of thrust to achieve the desired orbit transfer.

#### *Partial Differential Equations of $Q$*

Each component of the minimisation function in (C.9) has a corresponding analytical equation:  $dk/dt$  are given by the Gauss planetary equations in (C.1), and the partial derivatives  $\partial Q/\partial k$  were manually derived, and are given below.

$$\begin{aligned} \frac{\partial Q}{\partial a} = & \frac{4S_p}{a} \left[ W_a \Delta a^2 \cdot \frac{p(1-e)}{a^2(1+e)} \left( \frac{n \left( \frac{\Delta a}{a_T m} \right)^{n-1}}{a_T m q S_a} + \frac{2S_a}{\Delta a} - \frac{3S_a}{a} \right) \right. \\ & - W_e \Delta e^2 - W_i \Delta i^2 \cdot \mu \kappa_1^2 - W_\Omega \Delta \Omega^2 \cdot 4 \sin^2 i \kappa_2^2 + W_\omega \Delta \omega^2 \cdot \frac{(2(1+b)p\kappa_2 e)^2}{\gamma(\gamma\kappa_2 + bpe|\cos i| \csc i)^3} \\ & \left. \cdot \left[ \kappa_2 (\gamma^2 + 2r(p + r_{xx})(x^2 - 1) + 2a(p + r_{xx} - r_{xx}x^2)(e^2 - 1) + abe(e^2 - 1)\gamma|\cos i| \csc i) \right] \right] \\ & - S'_p(1-e) \left[ W_a \Delta a^2 \cdot \frac{-pS_a(e-1)}{a^3(1+e)} + W_e \Delta e^2 + W_i \Delta i^2 \cdot 4\kappa_1^2 + W_\Omega \Delta \Omega^2 \cdot 4 \sin^2 i \kappa_2^2 \right. \\ & \left. + W_\omega \Delta \omega^2 \cdot \frac{4(1+b)^2 p^2 \kappa_2^2 e^2}{(\gamma\kappa_2 + bpe|\cos i| \csc i)^2} \right] \end{aligned} \quad (\text{C.16})$$

$$\begin{aligned}
\frac{\partial Q}{\partial e} = & \frac{S_p}{4} \left[ W_a \Delta a^2 \cdot \frac{-p S_a (e-1)}{a^3 (1+e)} + W_e \Delta e^2 + W_i \Delta i^2 \cdot 4\kappa_1^2 \right. \\
& \left. + W_\Omega \Delta \Omega^2 \cdot 4\kappa_2^2 \sin^2 i + W_\omega \Delta \omega^2 \cdot \frac{(2(1+b)ep\kappa_2)^2}{(\gamma\kappa_2 + bpe|\cos i| \csc i)^2} \right] \\
& + S'_p a \left[ W_a \Delta a^2 \cdot \frac{-S_a p}{a^3 (1+e)} \left( \frac{e-1}{e+1} - 1 \right) + W_e \Delta e^2 \cdot 2 \left( \frac{1}{\Delta e} - \frac{e}{e^2-1} \right) \right. \\
& - W_i \Delta i^2 \cdot \left( \frac{8\kappa_1^2 e}{e^2-1} + 8\kappa_1 p \left( -|\cos \omega| - \frac{e \sin^2 \omega}{\sqrt{1-e^2 \sin^2 \omega}} \right) \right) \\
& - W_\omega \Delta \omega^2 \cdot \frac{8(1+b)^2 p^3 \kappa_2^2 e^3}{(\gamma\kappa_2 + bpe|\cos i| \csc i)^3} \left[ a\gamma\kappa_2 \left( a - \frac{p}{e^2} \right) \right. \\
& + \frac{\kappa_2 p}{\gamma e} (p^2 xy - (p+r)^2 xy - 2apx^2 e \\
& \left. + \frac{(p+r)(x^2-1)[2ae(1+xe)(2+xe) + p(x+ye)]}{(1+xe)^2} + pb(ae-p)|\cos i| \csc i \right] \\
& \left. - W_\Omega \Delta \Omega^2 \cdot 8p\kappa_2 \sin^2 i \left( \frac{\kappa_2}{e^2-1} - |\sin \omega| - \frac{e \cos^2 \omega}{\sqrt{1-e^2 \cos^2 \omega}} \right) \right]
\end{aligned} \tag{C.17}$$

$$\begin{aligned}
\frac{\partial Q}{\partial i} = & 2S_p \kappa_2^2 \left[ W_i \Delta i^2 + W_\Omega \Delta \Omega^2 \cdot \cos i \sin i \right. \\
& \left. + W_\omega \Delta \omega^2 \cdot \frac{b(1+b^2)p^3 e^3 \mu (\operatorname{sgn}(\cos i) \csc^2 i - \partial|\cos i|)}{(\gamma\kappa_2 + bpe|\cos i| \csc i)^3} \right]
\end{aligned} \tag{C.18}$$

$$\frac{\partial Q}{\partial \Omega} = S_p [W_\Omega \Delta \Omega^2 \cdot 2\kappa_2^2 \sin^2 i] \tag{C.19}$$

$$\begin{aligned}
\frac{\partial Q}{\partial \omega} = & 2S_p e \left[ W_i \Delta i^2 \cdot \kappa_1 \sin \omega \left( -\frac{e \cos \omega}{\sqrt{1-e^2 \sin^2 \omega}} + \partial|\cos \omega| \right) \right. \\
& + W_\Omega \Delta \Omega^2 \cdot \kappa_2 \cos \omega \sin^2 i \left( \frac{e \sin \omega}{\sqrt{1-e^2 \cos^2 \omega}} - \partial|\sin \omega| \right) \\
& \left. + W_\omega \Delta \omega^2 \cdot \frac{(1+b)^2 p^2 \kappa_2 e}{(\gamma\kappa_2 + bpe|\cos i| \csc i)^2} \left( \kappa_2 + \frac{bpe^2 \mu |\cos i| \cos \omega \csc i \left( \frac{e \sin \omega}{\sqrt{1-e^2 \cos^2 \omega}} - \partial|\sin \omega| \right)}{\gamma\kappa_2 + bpe|\cos i| \csc i} \right) \right]
\end{aligned} \tag{C.20}$$

where,

$$\gamma = \sqrt{p^2 x^2 + (1-x^2)(p+r_{xx})^2} \tag{C.21}$$

$$\kappa_1 = -e|\cos \omega| + \sqrt{1-e^2 \sin^2 \omega} \tag{C.22}$$

$$\kappa_2 = -e|\sin \omega| + \sqrt{1-e^2 \cos^2 \omega} \tag{C.23}$$

$$S_p = \frac{\mu}{p\|\mathbf{u}\|^2} S_r = \frac{\mu}{p\|\mathbf{u}\|^2} \left( 1 + W_p \exp^k \left( 1 - \frac{r_p}{(r_p)_{min}} \right) \right) \quad (\text{C.24})$$

$$S'_p = \frac{\exp^k \left( 1 - \frac{r_p}{(r_p)_{min}} \right) kW_p \mu}{4p(r_p)_{min} \|\mathbf{u}\|^2} \quad (\text{C.25})$$

$$x = \cos \nu_{xx} = -\frac{1}{e} - \frac{\left(\frac{2}{3}\right)^{\frac{1}{3}} e^2}{(9e^3 - 9e^5 + \sqrt{3}\sqrt{27e^6 - 54e^8 + 27e^{10} + 4e^{12}})^{\frac{1}{3}}} \quad (\text{C.26})$$

$$+ \frac{(9e^3 - 9e^5 + \sqrt{3}\sqrt{27e^6 - 54e^8 + 27e^{10} + 4e^{12}})^{\frac{1}{3}}}{18^{\frac{1}{3}} e^2}$$

$$y = \frac{1}{e^2} + \frac{\left(\frac{2}{3}\right)^{\frac{1}{3}} e^2 \left( 27e^2 - 45e^4 + \frac{\sqrt{3}(162e^5 - 432e^7 + 270e^9 + 48e^{11})}{2\sqrt{27e^6 - 54e^8 + 27e^{10} + 4e^{12}}} \right)}{3(9e^3 - 9e^5 + \sqrt{3}\sqrt{27e^6 - 54e^8 + 27e^{10} + 4e^{12}})^{\frac{4}{3}}}$$

$$+ \frac{27e^2 - 45e^4 + \frac{\sqrt{3}(162e^5 - 432e^7 + 270e^9 + 48e^{11})}{2\sqrt{27e^6 - 54e^8 + 27e^{10} + 4e^{12}}}}{18^{\frac{1}{3}} e^2 3(9e^3 - 9e^5 + \sqrt{3}\sqrt{27e^6 - 54e^8 + 27e^{10} + 4e^{12}})^{\frac{2}{3}}}$$

$$+ \frac{2\left(\frac{2}{3}\right)^{\frac{1}{3}} e^2}{(9e^3 - 9e^5 + \sqrt{3}\sqrt{27e^6 - 54e^8 + 27e^{10} + 4e^{12}})^{\frac{1}{3}}}$$

$$+ \frac{\left(\frac{2}{3}\right)^{\frac{2}{3}} (9e^3 - 9e^5 + \sqrt{3}\sqrt{27e^6 - 54e^8 + 27e^{10} + 4e^{12}})^{\frac{1}{3}}}{e^3} \quad (\text{C.27})$$

For the partial derivatives of the trigonometric functions  $\partial|\sin x|$  and  $\partial|\cos x|$ , given a function  $g(x) = |f(x)|$ , the derivative with respect to  $x$  is  $g'(x) = f'(x)f(x)/|f(x)|$ .

$$\frac{\partial|\cos x|}{\partial x} = \begin{cases} \frac{-\sin x \cos x}{|\cos x|} & \text{if } x \neq \frac{n\pi}{2} \\ 0 & \text{if } x = \frac{n\pi}{2} \end{cases} \quad (\text{C.28})$$

$$\frac{\partial|\sin x|}{\partial x} = \begin{cases} \frac{\cos x \sin x}{|\sin x|} & \text{if } x \neq n\pi \\ 0 & \text{if } x = n\pi \end{cases} \quad (\text{C.29})$$

where  $n$  is any integer value.

## c.2 DISCUSSION

One of the issues found when using the Q-law was the sensitivity of  $dQ/dt$  to the magnitude of the orbital elements  $k$ , and their variation  $\Delta k$ . Figures 148–152 show the values of  $\dot{Q}$  for a sample transfer manoeuvre between two Earth-centric orbits.

The initial state vector  $\mathbf{k}_0 = [a, e, i, \Omega, \omega, \nu]$  and target state vector  $\mathbf{k}_T$  (with no specified target  $\nu$ ) are set to,

$$\mathbf{k}_0 = [R_{\oplus} + 7000 \text{ km}, 0.5, 1.3 \text{ rad}, 0.01 \text{ rad}, 0.01 \text{ rad}, 1.44 \text{ rad}]$$

$$\mathbf{k}_T = [R_{\oplus} + 10000 \text{ km}, 0.8, 0.1 \text{ rad}, 0.8\pi \text{ rad}, 1.2\pi \text{ rad}]$$

Table 26: Minimum and maximum values of  $dQ/dt$  corresponding to Figures 148–152.

Target orbital element in $\mathbf{k}$	min $\dot{Q}$	max $\dot{Q}$	Corresponding figure no.
$a$	-42.2456655327675	42.245665532767	148
$e$	-99.6125362956156	99.6125362956156	149
$i$	-6555922.77168483	6555922.77168483	150
$\Omega$	-135922.74398538	135922.74398538	151
$\omega$	-77646153487.0223	77646153487.0224	152

with  $(r_p)_{min} = R_{\oplus} = 6378.16$  km, the magnitude of the thrust  $\|\mathbf{u}\| = 9.3e-03$  km/s, integer weights of  $W_k = 0 \mid 1$ , gravitational constant  $\mu_{\oplus} = 398600.446192176$  km<sup>3</sup>/s<sup>2</sup>, and tuning parameters:  $W_p = 1$ ,  $k = 1$ ,  $m = 3$ ,  $n = 4$ ,  $q = 2$ , and  $b = 0.01$ .

Each of the five figures corresponds to a change in one of the elements of the state vector (given a weight  $W = 1$ ), with the remaining elements set as free variables (set by  $W = 0$ ). The thrust angles,  $\alpha$  and  $\beta$ , are varied between  $[0, 2\pi]$  to show the different values of the function  $dQ/dt$ . The result is a series of regular peaks and valleys, in quadrants. A local, constrained, nonlinear multivariable optimisation function in Matlab, `fmincon`, was used to numerically determine the minimum and maximum points on each graph, which correspond to the direction of applied thrust which should maximise, or minimise, the rate of change of the orbital element(s) in question, at that specific point along the orbit. The function `fmincon` employs a sequential quadratic programming (SQP) method, and was used in conjunction with a multi-start approach, using 10 runs of randomly seeded initial conditions with bounds of  $0 \leq [\alpha_0, \beta_0] \leq 2\pi$ . Table 26 shows the values of the maxima and minima corresponding to the figures. As expected, the absolute values of the minima and maxima are the same.

As can be seen from the table and figures, the values for  $dQ/dt$  range from  $10^2$  to  $10^{11}$  depending on the orbital element. Here, each orbital element was run in isolation, however in the majority of cases, a transfer between two orbits involves a desired change in a number of the orbital elements, not just one. Since the cost function  $\dot{Q}$  is a sum of the components of  $dQ/dt$ , the large difference in magnitude makes it difficult to achieve an ‘optimal’ or near-optimal transfer.

An example transfer is shown below. The first is an orbital transfer between two Earth-centric orbits, as above. The required change is for the semi-major axis and eccentricity, with the other three elements left as free variables.

$$\mathbf{k}_0 = [7452.7, 0.2, 0.17453, 0.2, 0.2, 0.2]$$

$$\mathbf{k}_T = [9000, 0.4, \text{free}, \text{free}, \text{free}]$$

$$W = [1, 1, 0, 0, 0]$$

The thrust was set to a maximum of 60 N with a spacecraft mass of 2000 kg, giving a total acceleration of 0.03 m/s<sup>2</sup>. The applied thrust can only be turned on (60 N) or off (0 N), no partial control of the thrust was allowed. The units are km and rad. The minima for  $dQ/dt$  was found using `fmincon` with a time step of 100 s, and a multi-

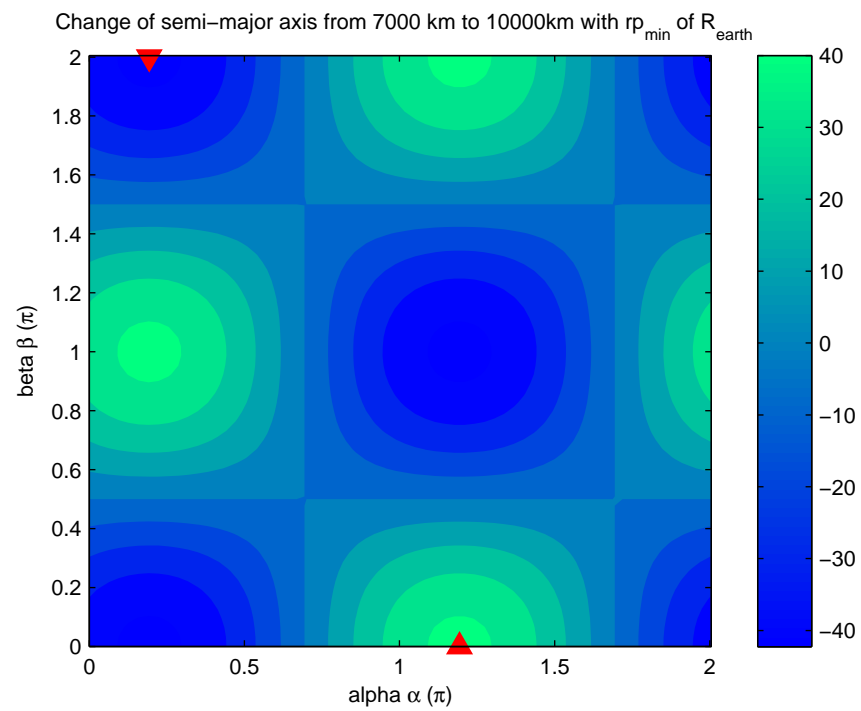


Figure 148: Values of  $dQ/dt$  for the range of thrust angles  $\alpha, \beta$ , and weights  $W = [1, 0, 0, 0, 0]$ . The maximum  $\blacktriangle$  and minimum  $\blacktriangledown$  points for  $dQ/dT$  found by the local optimiser are indicated.

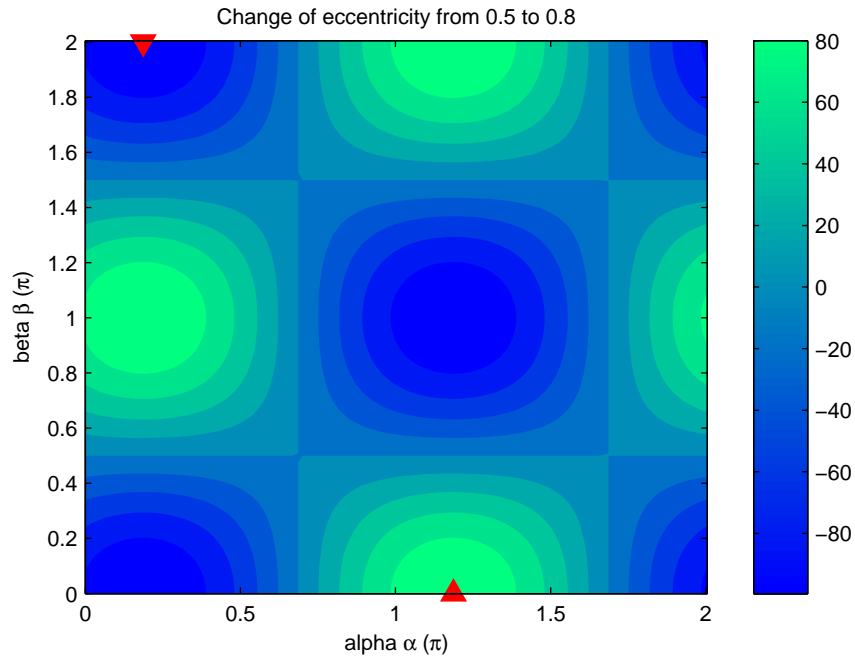


Figure 149: Values of  $dQ/dt$  for the range of thrust angles  $\alpha, \beta$ , and weights  $W = [0, 1, 0, 0, 0]$ . The maximum  $\blacktriangle$  and minimum  $\blacktriangledown$  points for  $dQ/dT$  found by the local optimiser are indicated.

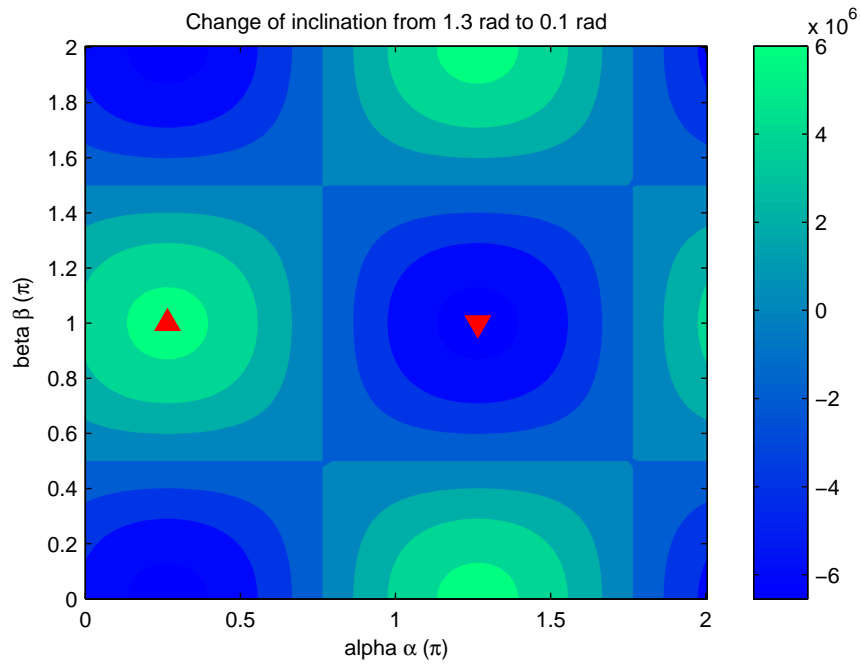


Figure 150: Values of  $dQ/dt$  for the range of thrust angles  $\alpha, \beta$ , and weights  $W = [0, 0, 1, 0, 0]$ . The maximum  $\blacktriangle$  and minimum  $\blacktriangledown$  points for  $dQ/dT$  found by the local optimiser are indicated.

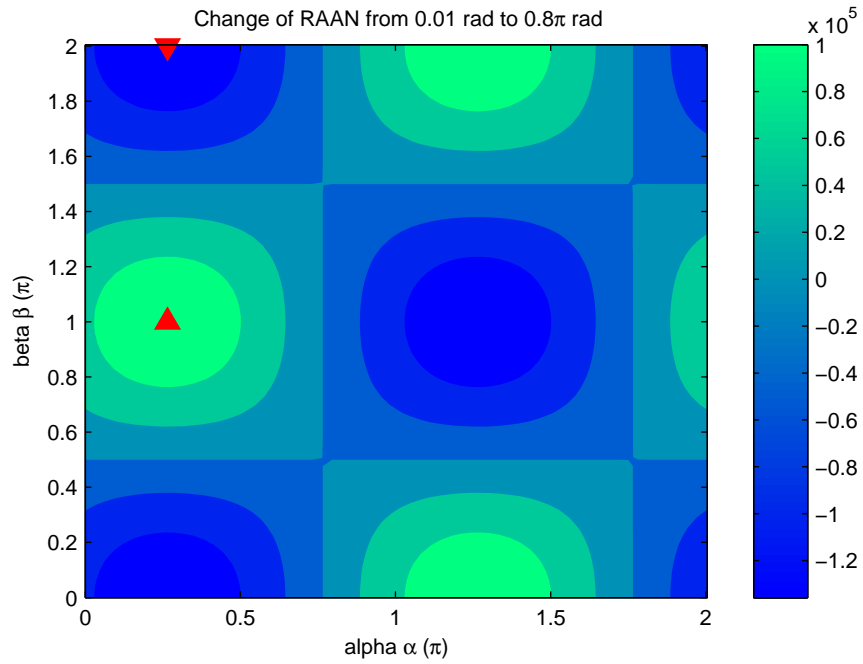


Figure 151: Values of  $dQ/dt$  for the range of thrust angles  $\alpha, \beta$ , and weights  $W = [0, 0, 0, 1, 0]$ . The maximum  $\blacktriangle$  and minimum  $\blacktriangledown$  points for  $dQ/dT$  found by the local optimiser are indicated.

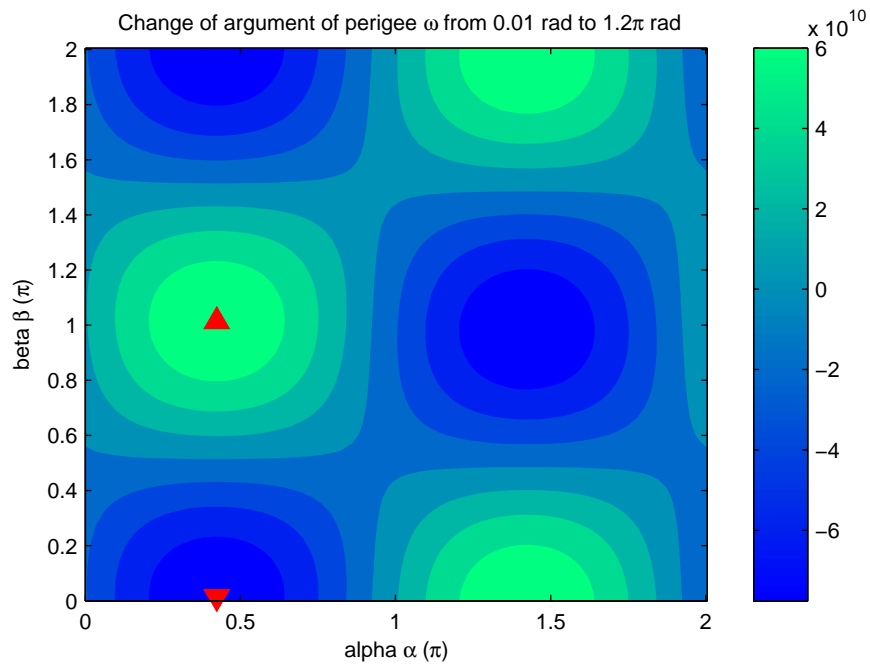


Figure 152: Values of  $dQ/dt$  for the range of thrust angles  $\alpha, \beta$ , and weights  $W = [0, 0, 0, 0, 1]$ . The maximum  $\blacktriangle$  and minimum  $\blacktriangledown$  points for  $dQ/dT$  found by the local optimiser are indicated.

start run with 10 random initial conditions. The orbit was propagated by numerically integrating the Gauss equations with `ode45` in Matlab (over the same 100 s time step).

Figure 153 shows the variation in the orbital elements over the transfer duration, in this case around 3.5 days. The other parameters are not adversely affected by the applied thrust, with the inclination varying by only  $10^{-9}$  rad, the RAAN by  $10^{-8}$  rad and the argument of perigee between  $10^{-8}$  rad. Figure 154 shows the multi-revolution transfer, with the original and final target orbits identified, and the directions of thrust represented as arrows along the orbit. While the transfer is 3D, only the 2D projection is shown since there was no intended change in the out-of-plane direction. Lastly, Fig. 155 shows the resulting thrust angles as calculated by the Q-law. The points calculated at each time step are shown as dots, with the lines added for clarity to see how the thrust angles changed over time. Note that in the simulation, the thrust angles are kept constant for the duration of the time step, i.e. over the 100 s in this case.

The effectivities were used to allow for coasting phases depending on how effective applying a thrust would be, and to help reduce the ‘chatter’ when the spacecraft approached the target orbit. Since the thrust is restricted to an ‘on-off’ scheme, the resulting transfer will alternately over and under-shoot the target value if the thrust is too large for the time step. An obvious solution would be to reduce either the time step and/or thrust level applied depending on the proximity to the target orbit.

Algorithm 1 shows an implementation of this concept. Cut-off values for the effectivity,  $\eta_{abs_L}, \eta_{rel_L}$  are introduced, as well as a tolerance value  $\tau$  which effects the proximity of the current state to the target element state. In this example,  $\tau(t_0) = 0.1$  and  $\eta_{abs_L}(t_0) = \eta_{rel_L}(t_0) = 0.5$ . Essentially, as the spacecraft gets closer to the target orbit, the thrust is applied for smaller and smaller periods, only at the most efficient times.

---

**Algorithm 1** Thrust effectivity.

---

```

if  $|\Delta k_i| < \tau k_T$  then
     $\eta_{abs_L} \Rightarrow \sqrt{\eta_{abs_L}}$ 
     $\tau \Rightarrow \tau^{1.2}$ 
end if

if  $(\eta_{abs} \leq \eta_{abs_L})$  or  $(\eta_{rel} \leq \eta_{rel_L})$  then
    Thrust is turned off,  $u_i = 0$ 
else
    Thrust is turned on,  $u_i = u_{max}$ 
end if

```

---

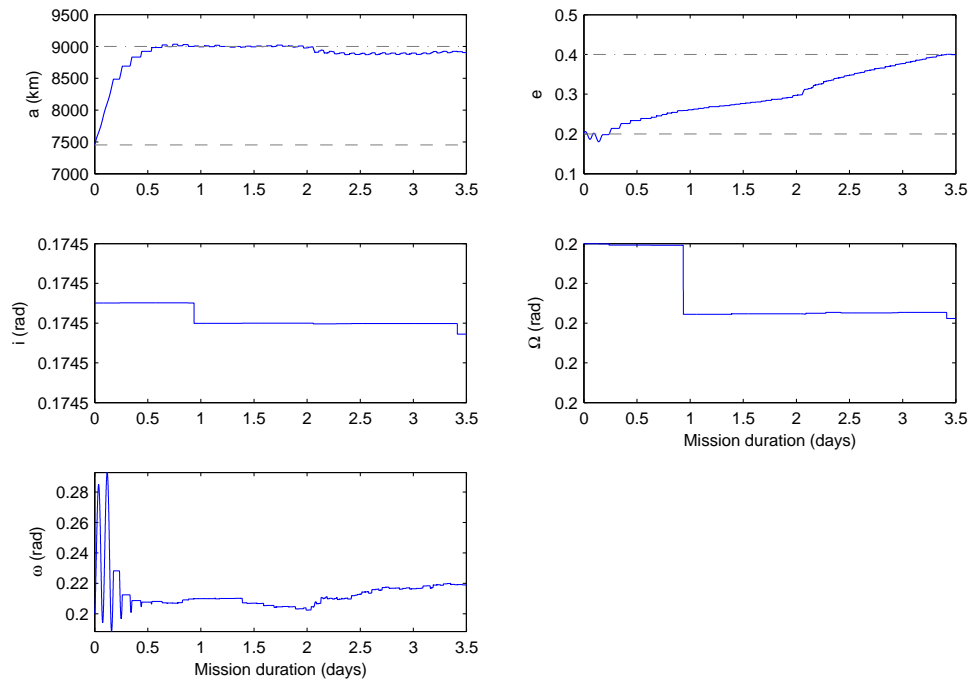


Figure 153: Change in orbital elements during a transfer around the Earth, with  $a$  from 7452.7  $\rightarrow$  9000 km, and  $e$  from 0.2  $\rightarrow$  0.4. The variance between the initial to final orbit for other free parameters are:  $(i_T - i_0) = \Delta i = 3.9082e-8$  rad,  $\Delta \Omega = 1.8859e-7$  rad and  $\Delta \omega = -0.01812$  rad.

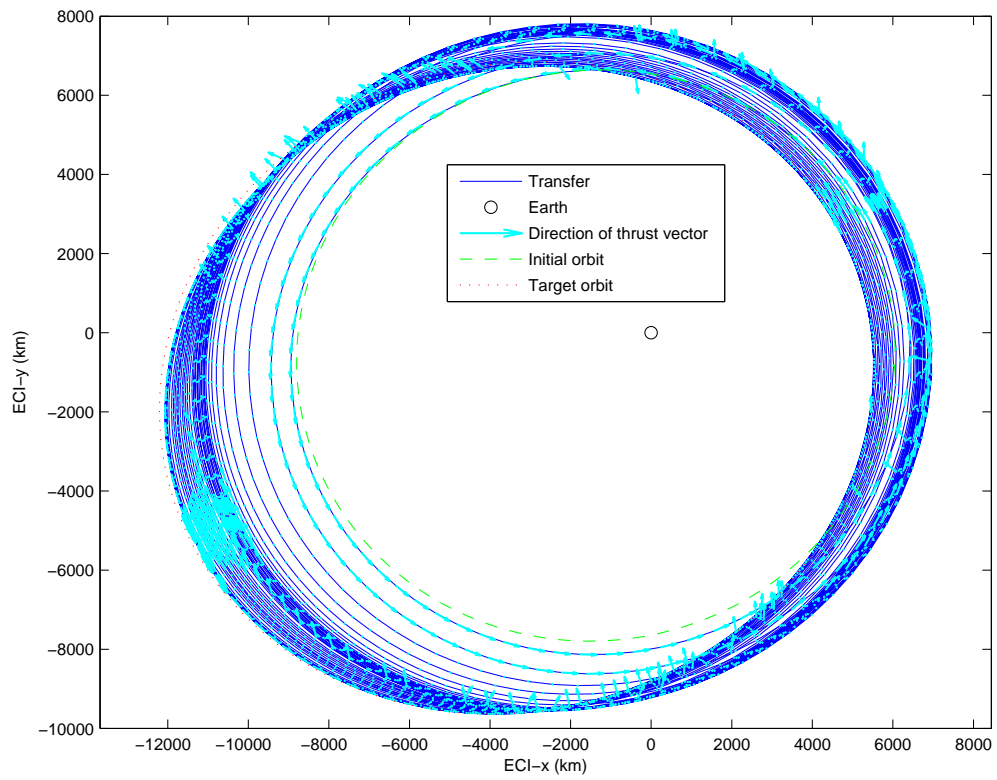
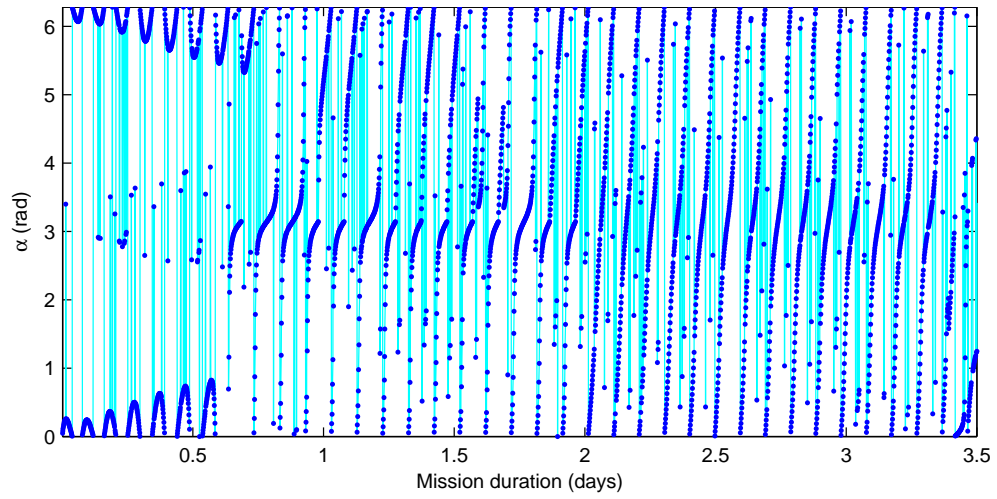
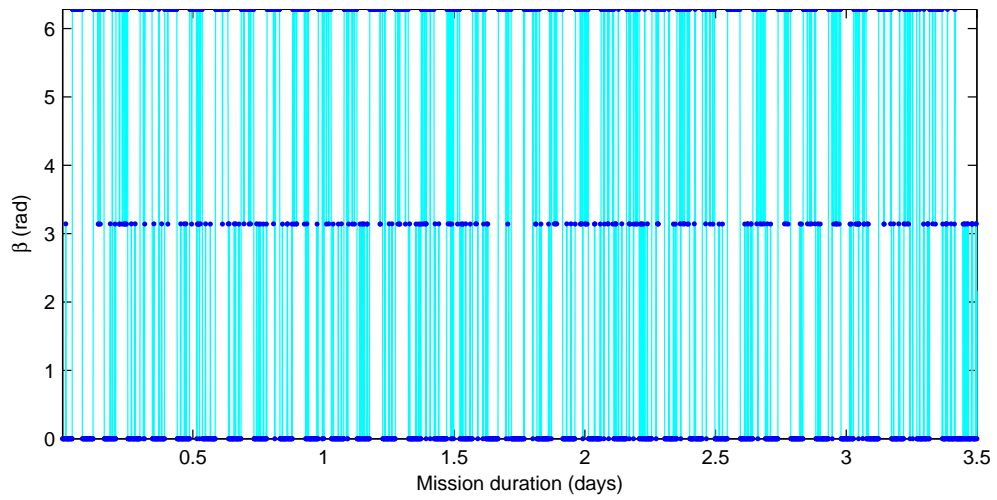


Figure 154: Orbital transfer shown in the Earth-centric inertial (ECI) reference frame. The total transfer time is 3.5 days.



(a) Variation of calculated in-plane angle  $\alpha$ .



(b) Variation of calculated out-of-plane angle  $\beta$

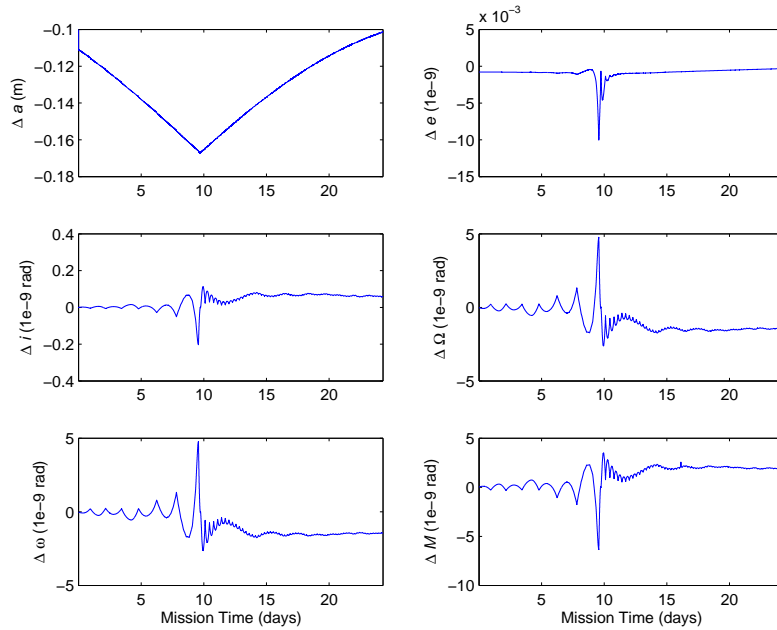
Figure 155: Direction of thrust vector calculated by  $\hat{Q}_n$ . The maximum magnitude of the applied thrust is 60 N, for a 2000 kg spacecraft.

## FUNNEL CONTROL RESULTS

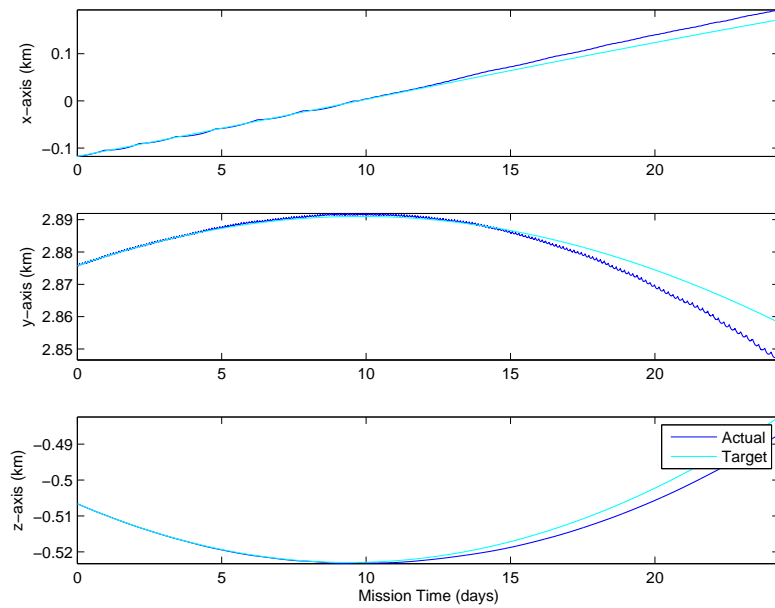
The following contains the results of the control law for the funnel orbits using both the least squares method and the integration method presented in Section 3.6, each for three time steps  $\delta t = [1, 10, 60]$  s and for the four test orbits  $\delta \mathbf{k}_{5/2}, \delta \mathbf{k}_{5/3}, \delta \mathbf{k}_{5/4}, \delta \mathbf{k}_{5/5}$  listed in Table 17. The results for the first orbit,  $\delta \mathbf{k}_{5/1}$  are shown previously in Figs. 70 – 75 for the least squares method, and Figs. 64 – 69 for the integration method.

Table 27: Cross reference between figure numbers and simulation inputs for the results in Appendix D.

Control law type	Time step $\delta t$ (s)	Figure numbers
Least squares	1	156 – 163
	10	164 – 171
	60	172 – 179
Integration	1	180 – 187
	10	188 – 195
	60	196 – 199



(a) Variations in the orbital element differences.



(b) Variations in the Hill frame components.

Figure 156: Least squares control law for spacecraft formation  $\delta \mathbf{k}_{5/2}$  at time step of  $\delta t = 1$  s using the fixed mirror configuration with a system efficiency of 25% and weights,  $W = [1e-6, 1e6, 1, 1, 1, 1]$ .

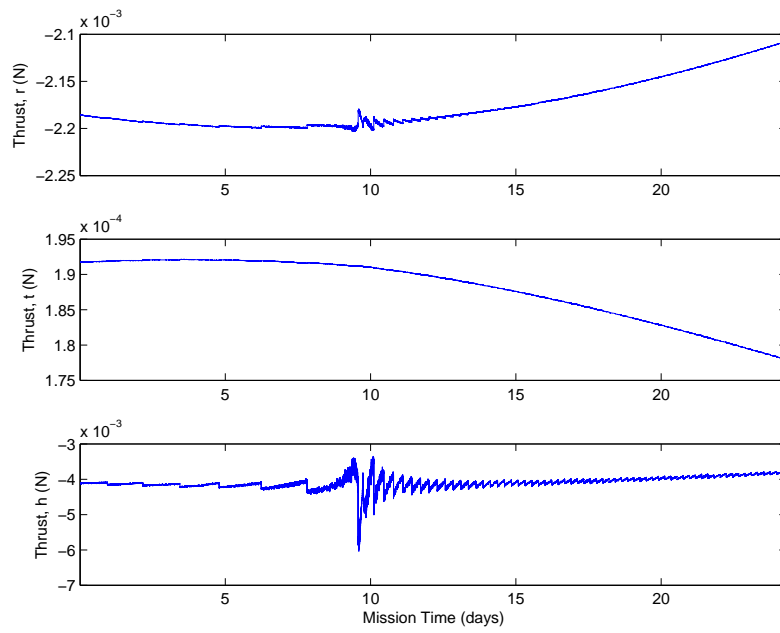
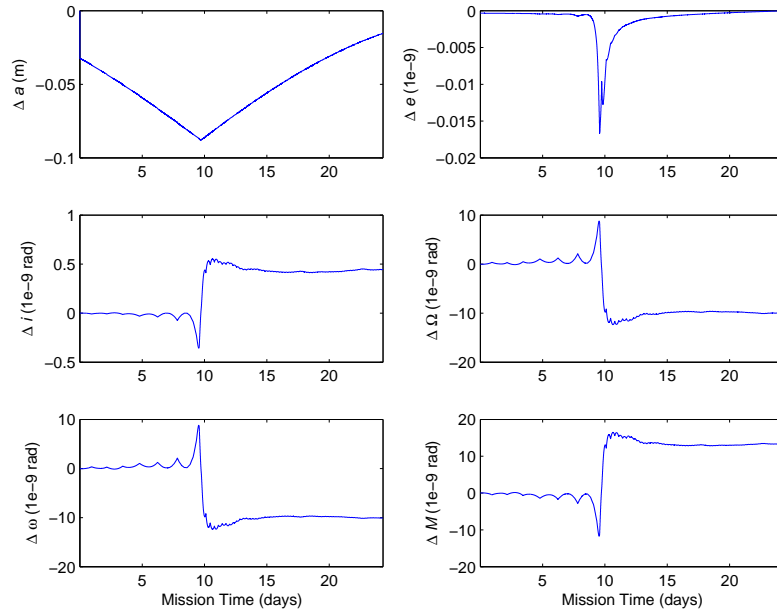
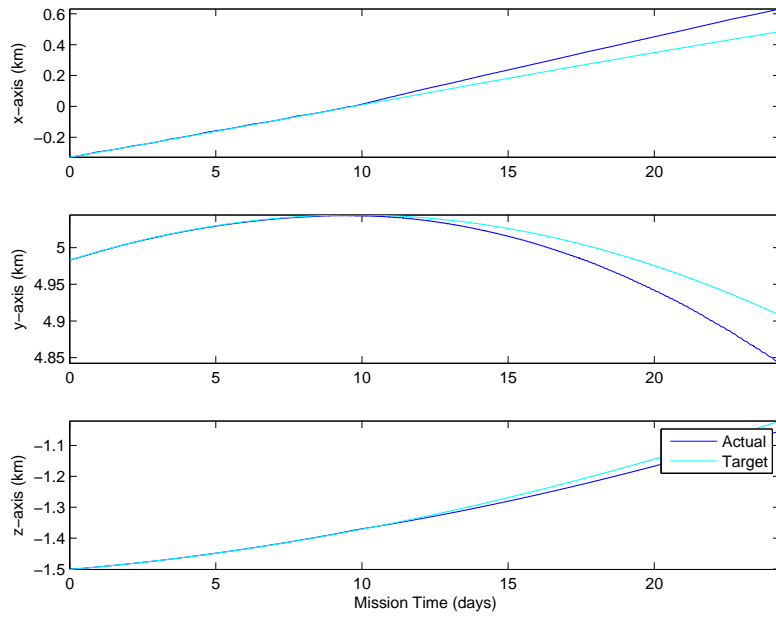


Figure 157: Least squares control law for spacecraft formation  $\delta \mathbf{k}_{5/2}$  at time step of  $\delta t = 1$  s using the fixed mirror configuration with a system efficiency of 25% and weights,  $W = [1e-6, 1e6, 1, 1, 1, 1]$ .



(a) Variations in the orbital element differences.



(b) Variations in the Hill frame components.

Figure 158: Least squares control law for spacecraft formation  $\delta \mathbf{k}_{5/3}$  at time step of  $\delta t = 1$  s using the fixed mirror configuration with a system efficiency of 25% and weights,  $W = [1e-6, 1e6, 1, 1, 1, 1]$ .

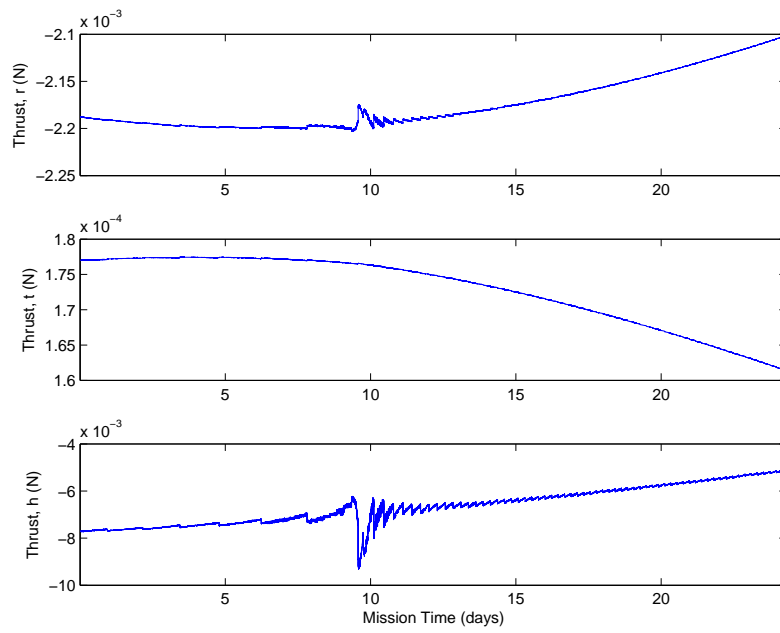
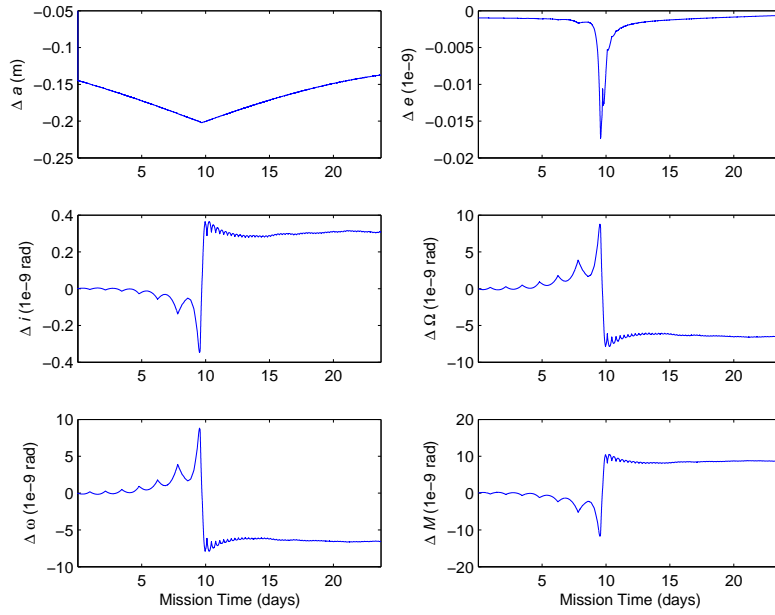
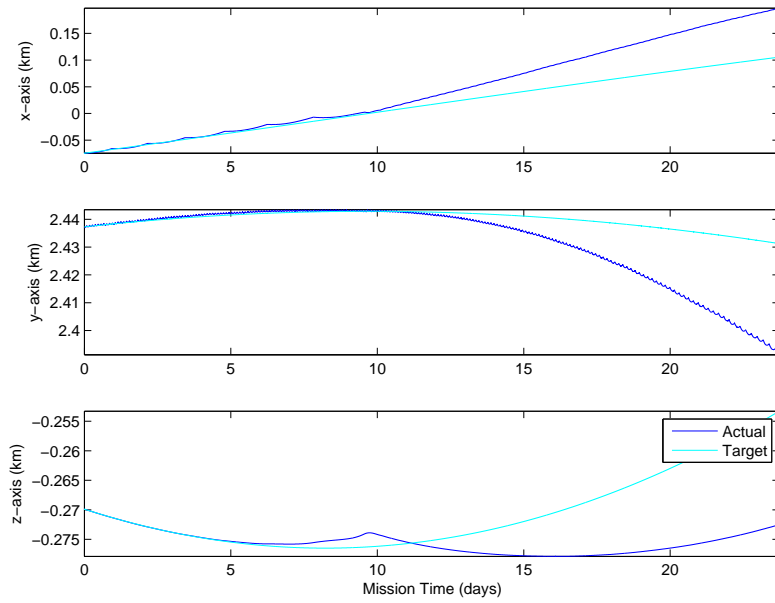


Figure 159: Least squares control law for spacecraft formation  $\delta \mathbf{k}_{5/3}$  at time step of  $\delta t = 1$  s using the fixed mirror configuration with a system efficiency of 25% and weights,  $W = [1e-6, 1e6, 1, 1, 1, 1]$ .



(a) Variations in the orbital element differences.



(b) Variations in the Hill frame components.

Figure 160: Least squares control law for spacecraft formation  $\delta \mathbf{k}_{5/4}$  at time step of  $\delta t = 1$  s using the fixed mirror configuration with a system efficiency of 25% and weights,  $W = [1e-6, 1e6, 1, 1, 1, 1]$ .

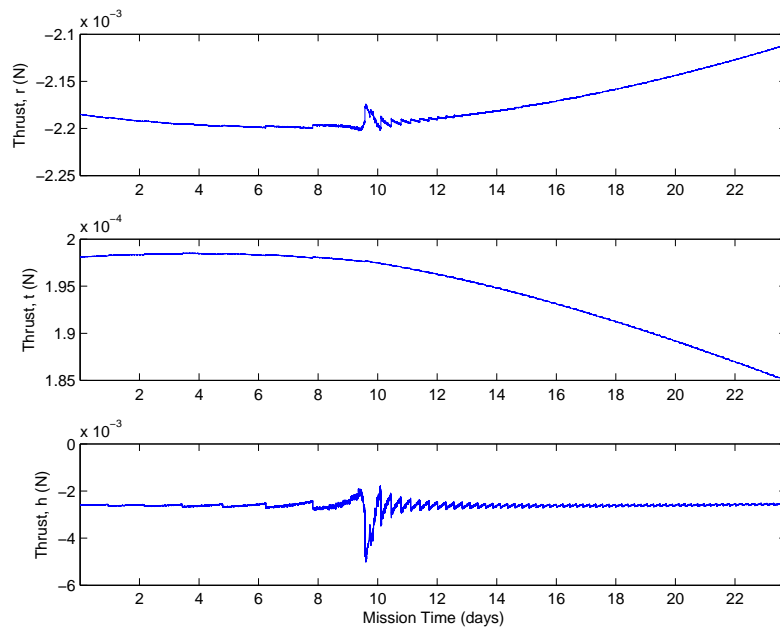
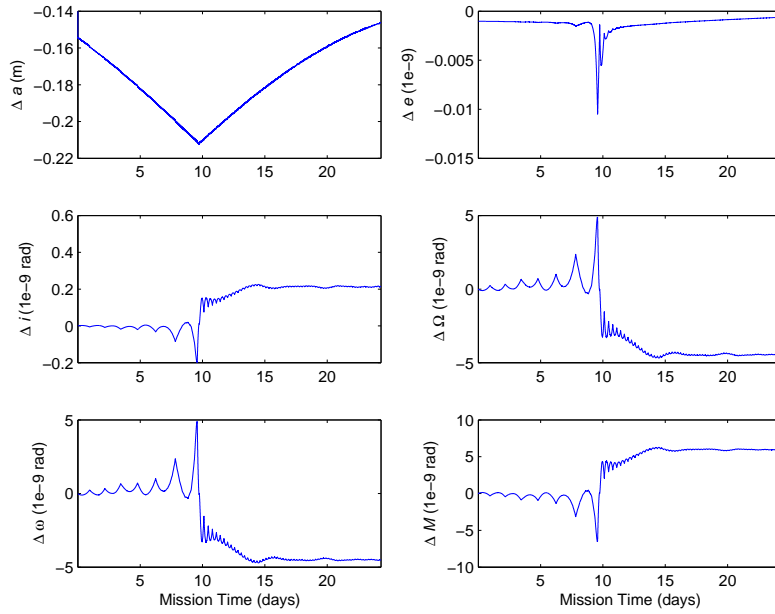
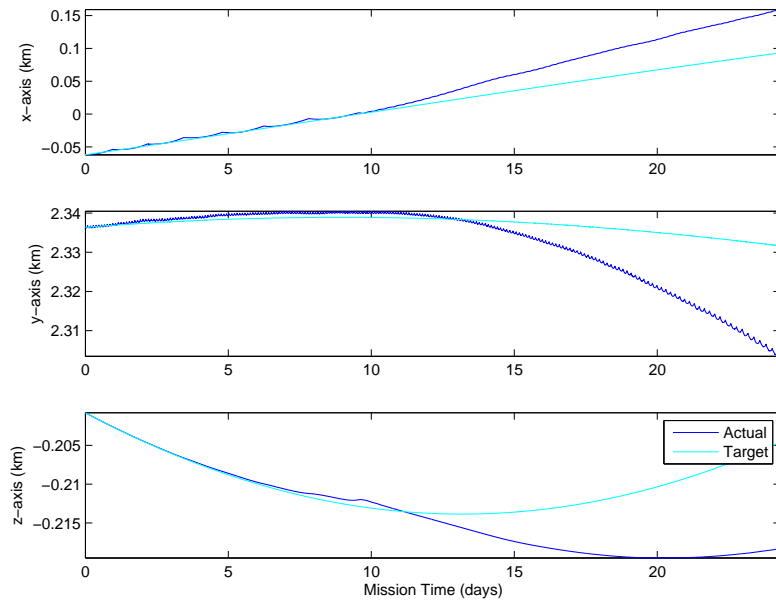


Figure 161: Least squares control law for spacecraft formation  $\delta \mathbf{k}_{5/4}$  at time step of  $\delta t = 1$  s using the fixed mirror configuration with a system efficiency of 25% and weights,  $W = [1e-6, 1e6, 1, 1, 1, 1]$ .



(a) Variations in the orbital element differences.



(b) Variations in the Hill frame components.

Figure 162: Least squares control law for spacecraft formation  $\delta \mathbf{k}_{5/5}$  at time step of  $\delta t = 1$  s using the fixed mirror configuration with a system efficiency of 25% and weights,  $W = [1e-6, 1e6, 1, 1, 1, 1]$ .

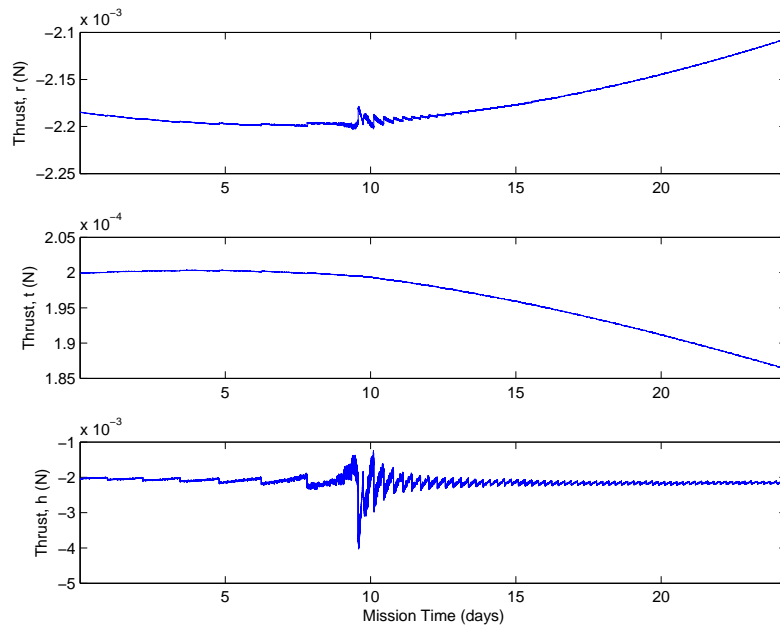
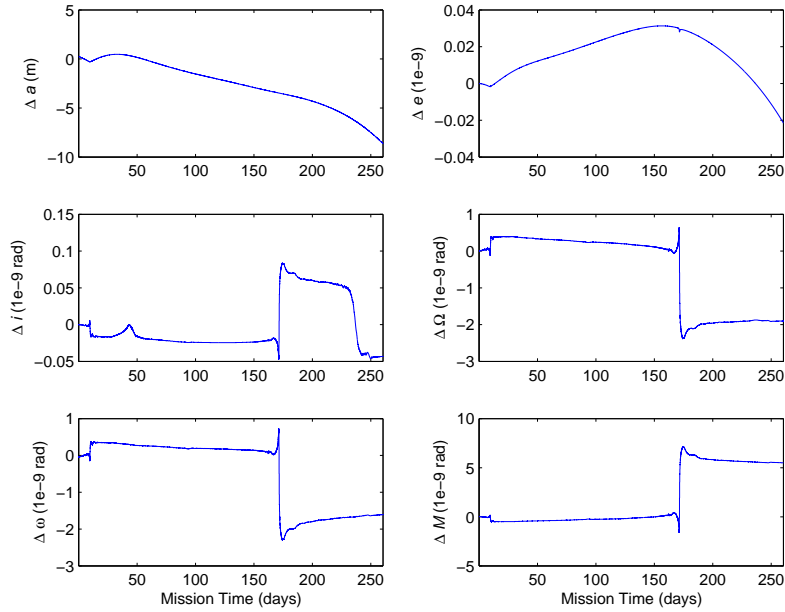
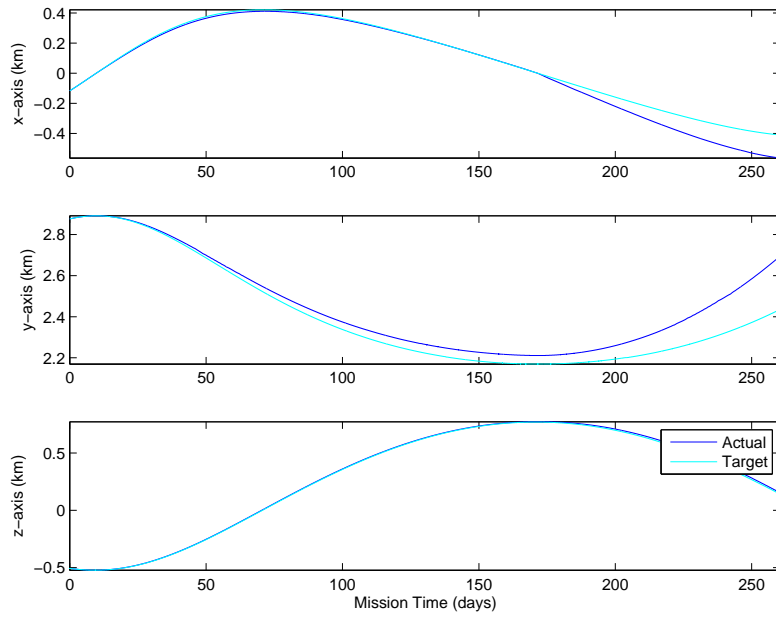


Figure 163: Least squares control law for spacecraft formation  $\delta \mathbf{k}_{5/5}$  at time step of  $\delta t = 1$  s using the fixed mirror configuration with a system efficiency of 25% and weights,  $W = [1e-6, 1e6, 1, 1, 1, 1]$ .



(a) Variations in the orbital element differences.



(b) Variations in the Hill frame components.

Figure 164: Least squares control law for spacecraft formation  $\delta \mathbf{k}_{5/2}$  at time step of  $\delta t = 10$  s using the fixed mirror configuration with a system efficiency of 25% and weights,  $W = [1e-6, 1e6, 1, 1, 1, 1]$ .

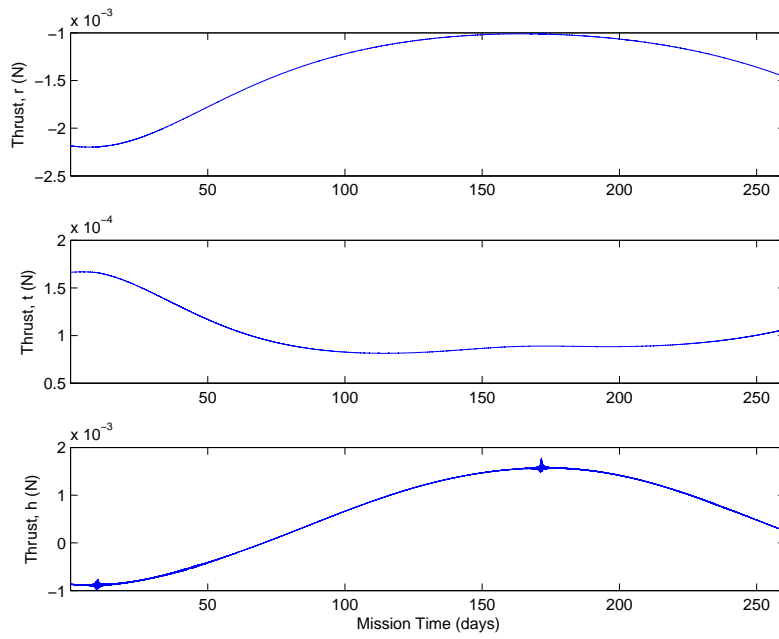
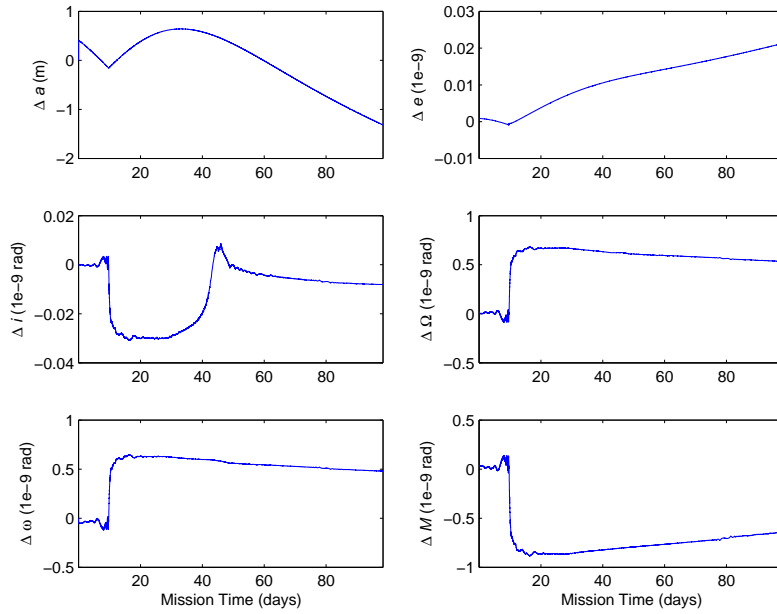
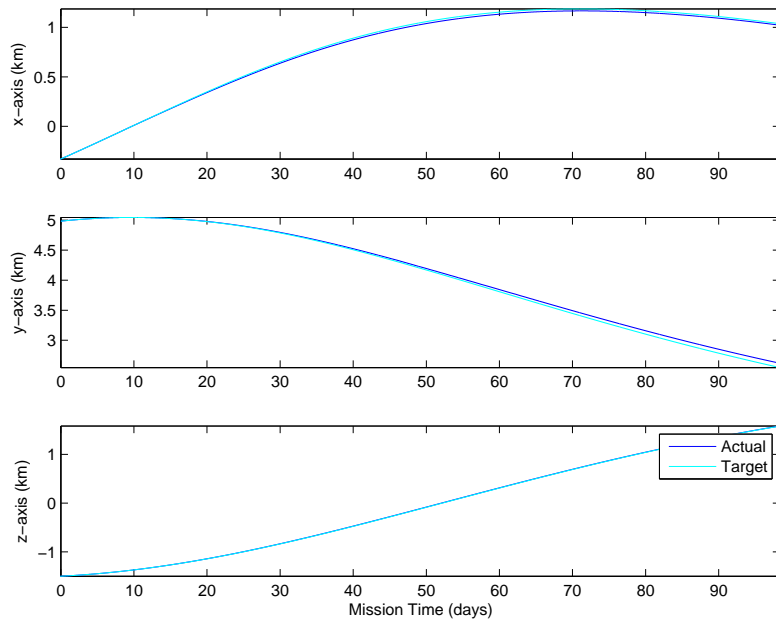


Figure 165: Least squares control law for spacecraft formation  $\delta \mathbf{k}_{5/2}$  at time step of  $\delta t = 10$  s using the fixed mirror configuration with a system efficiency of 25% and weights,  $W = [1e-6, 1e6, 1, 1, 1, 1]$ .



(a) Variations in the orbital element differences.



(b) Variations in the Hill frame components.

Figure 166: Least squares control law for spacecraft formation  $\delta \mathbf{k}_{5/3}$  at time step of  $\delta t = 10$  s using the fixed mirror configuration with a system efficiency of 25% and weights,  $W = [1e-6, 1e6, 1, 1, 1, 1]$ .

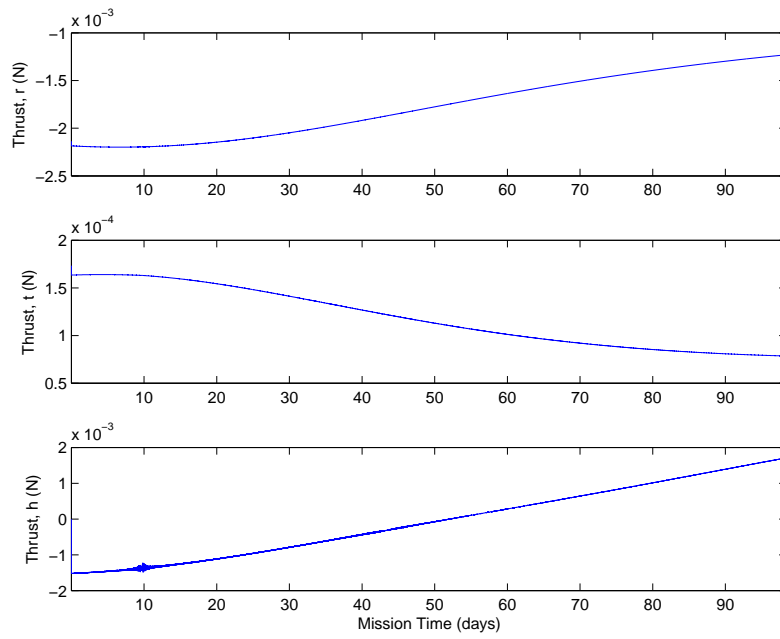
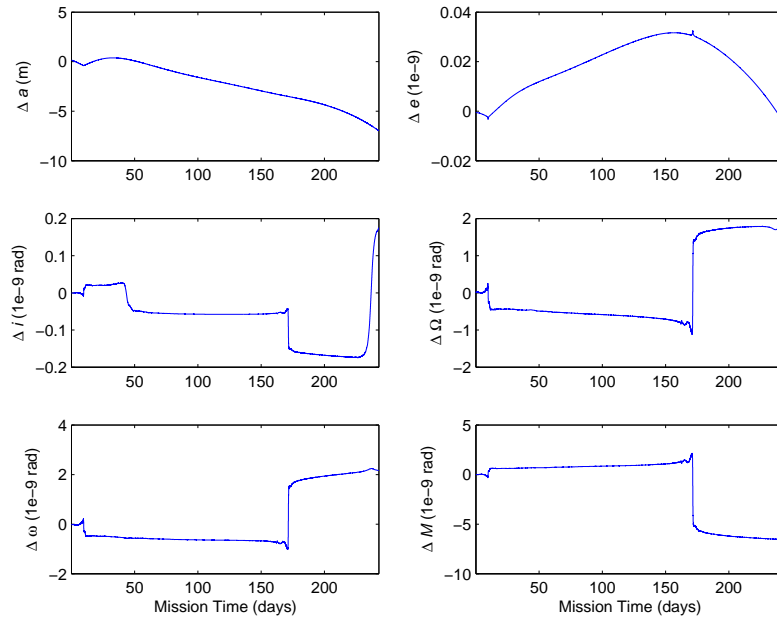
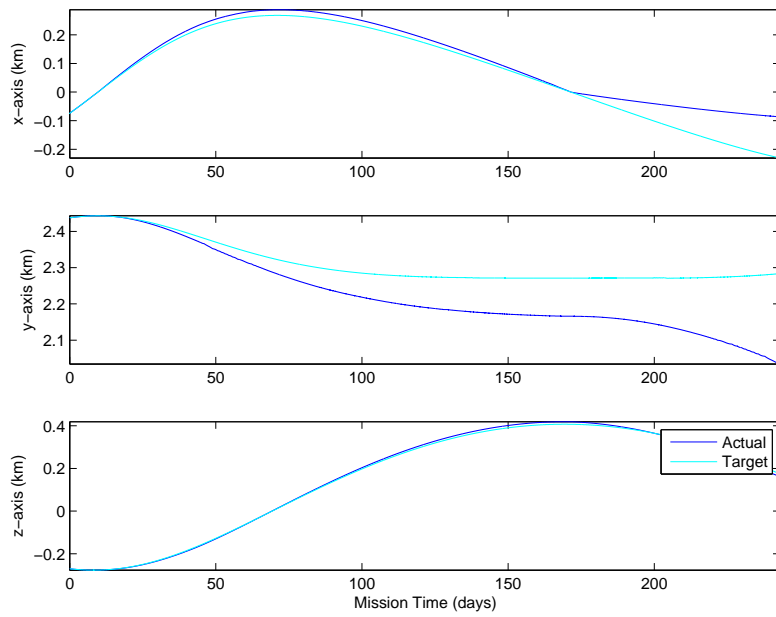


Figure 167: Least squares control law for spacecraft formation  $\delta \mathbf{k}_{5/3}$  at time step of  $\delta t = 10$  s using the fixed mirror configuration with a system efficiency of 25% and weights,  $W = [1e-6, 1e6, 1, 1, 1, 1]$ .



(a) Variations in the orbital element differences.



(b) Variations in the Hill frame components.

Figure 168: Least squares control law for spacecraft formation  $\delta \mathbf{k}_{5/4}$  at time step of  $\delta t = 10$  s using the fixed mirror configuration with a system efficiency of 25% and weights,  $W = [1e-6, 1e6, 1, 1, 1, 1]$ .

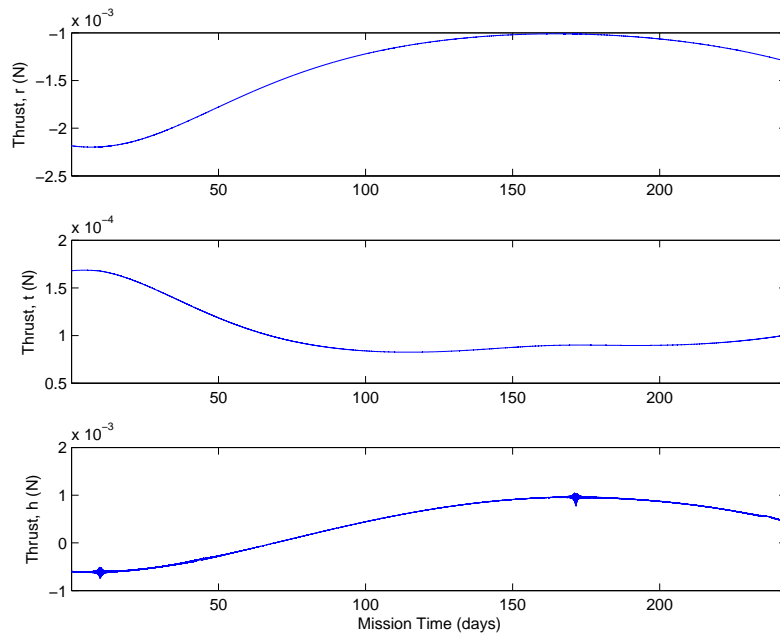
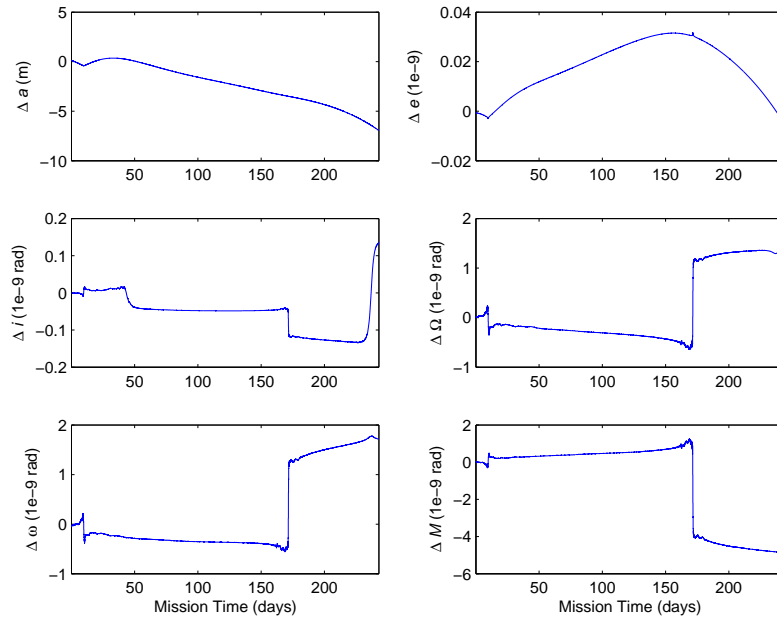
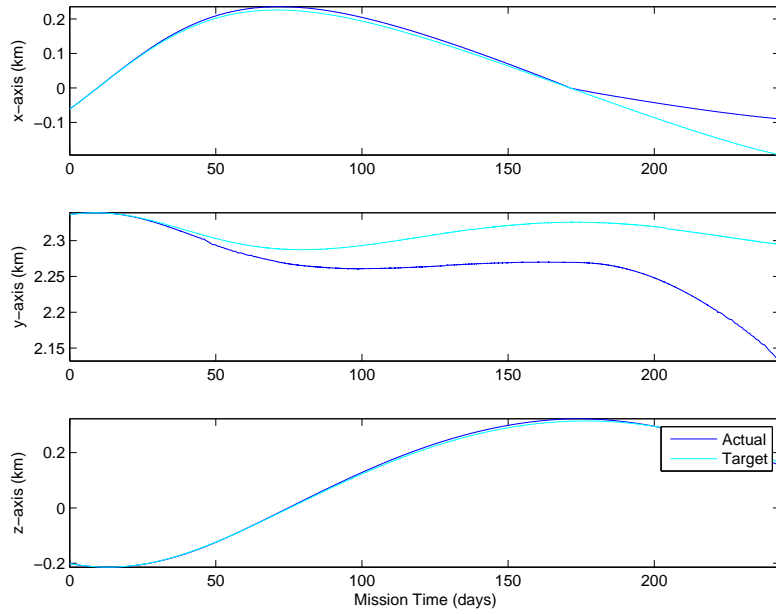


Figure 169: Least squares control law for spacecraft formation  $\delta \mathbf{k}_{5/4}$  at time step of  $\delta t = 10$  s using the fixed mirror configuration with a system efficiency of 25% and weights,  $W = [1e-6, 1e6, 1, 1, 1, 1]$ .



(a) Variations in the orbital element differences.



(b) Variations in the Hill frame components.

Figure 170: Least squares control law for spacecraft formation  $\delta \mathbf{k}_{5/5}$  at time step of  $\delta t = 10$  s using the fixed mirror configuration with a system efficiency of 25% and weights,  $W = [1e-6, 1e6, 1, 1, 1, 1]$ .

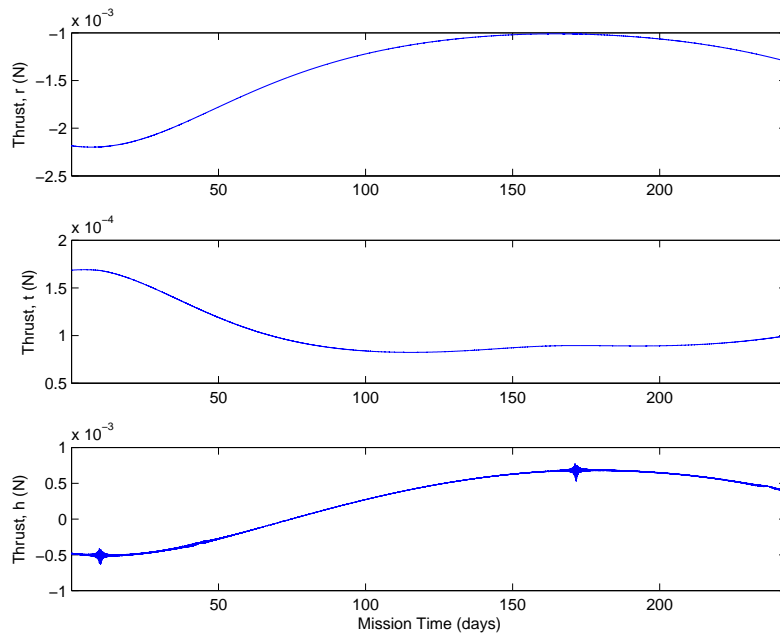
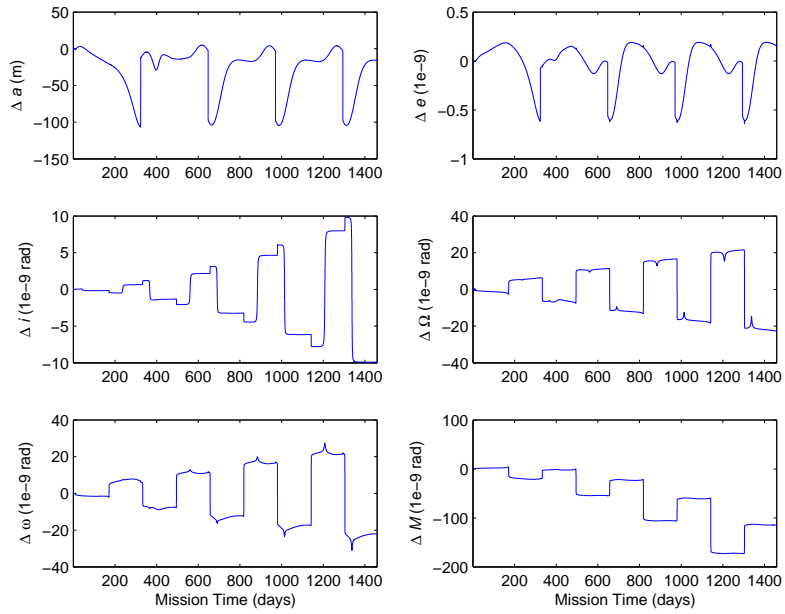
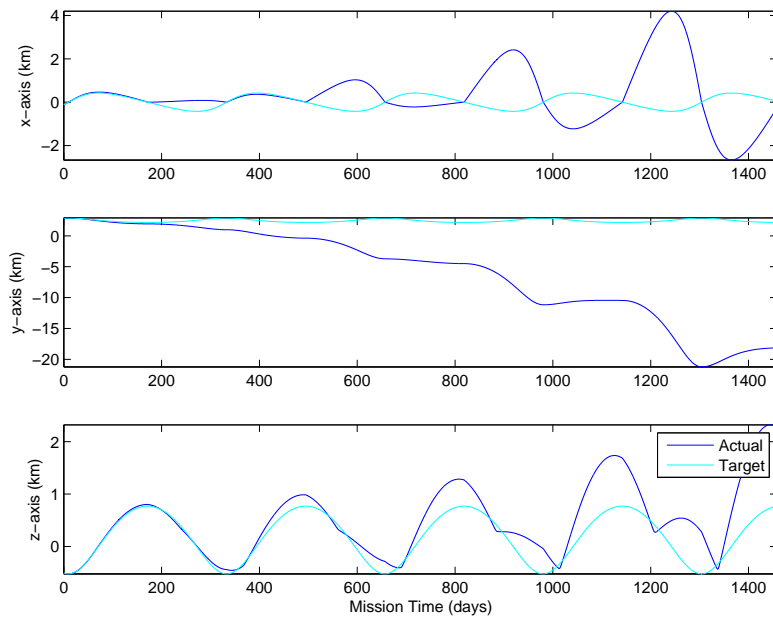


Figure 171: Least squares control law for spacecraft formation  $\delta \mathbf{k}_{5/5}$  at time step of  $\delta t = 10$  s using the fixed mirror configuration with a system efficiency of 25% and weights,  $W = [1e-6, 1e6, 1, 1, 1, 1]$ .



(a) Variations in the orbital element differences.



(b) Variations in the Hill frame components.

Figure 172: Least squares control law for spacecraft formation  $\delta \mathbf{k}_{5/2}$  at time step of  $\delta t = 60$  s using the fixed mirror configuration with a system efficiency of 25% and weights,  $W = [1e-6, 1e6, 1, 1, 1, 1]$ .

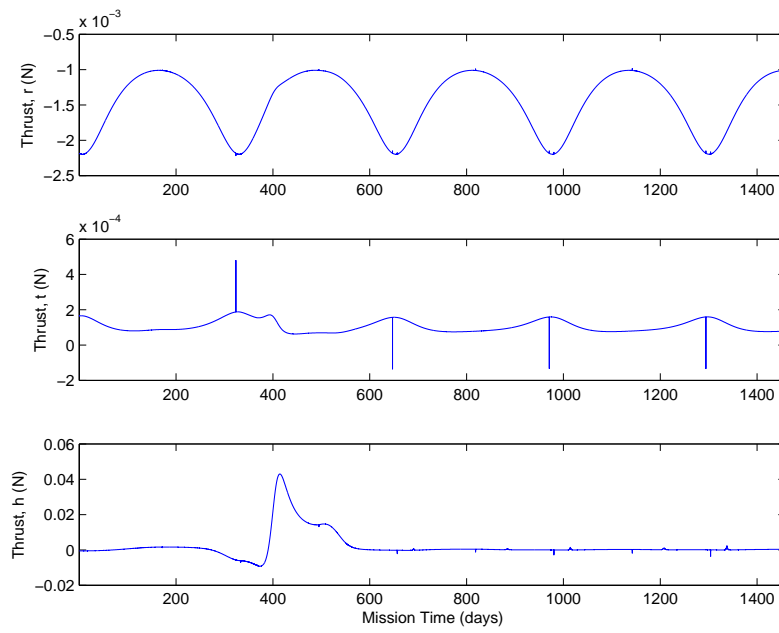
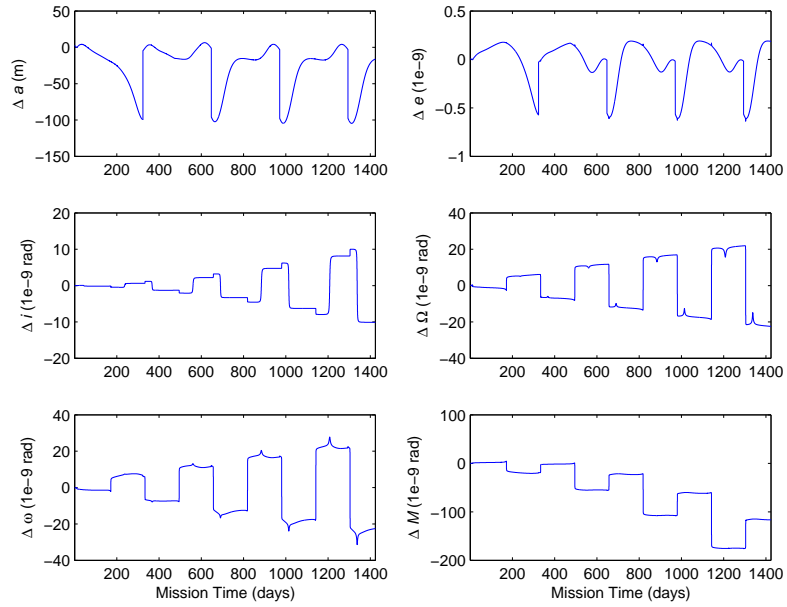
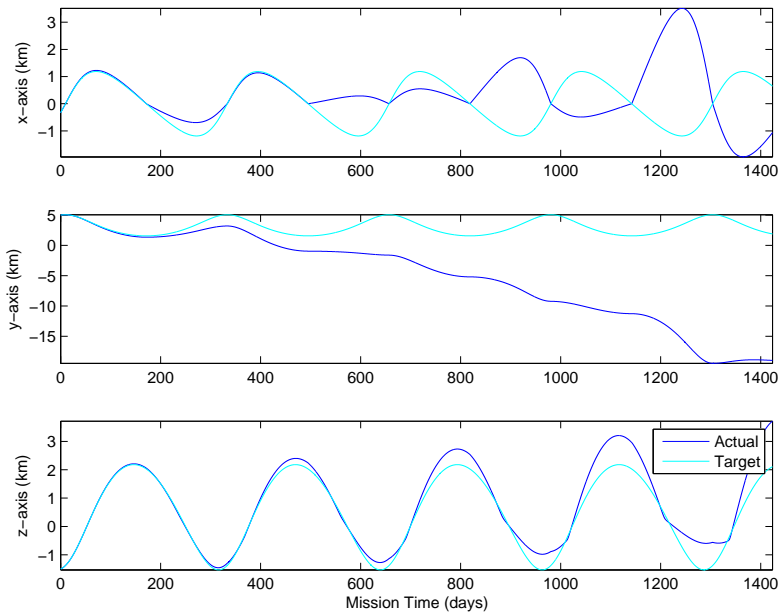


Figure 173: Least squares control law for spacecraft formation  $\delta \mathbf{k}_{5/2}$  at time step of  $\delta t = 60$  s using the fixed mirror configuration with a system efficiency of 25% and weights,  $W = [1e-6, 1e6, 1, 1, 1, 1]$ .



(a) Variations in the orbital element differences.



(b) Variations in the Hill frame components.

Figure 174: Least squares control law for spacecraft formation  $\delta \mathbf{k}_{5/3}$  at time step of  $\delta t = 60$  s using the fixed mirror configuration with a system efficiency of 25% and weights,  $W = [1e-6, 1e6, 1, 1, 1, 1]$ .

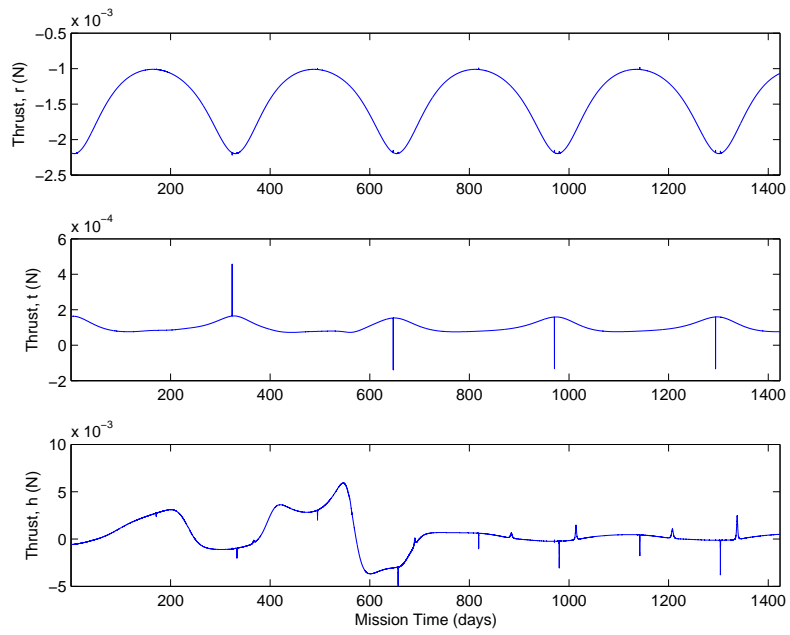
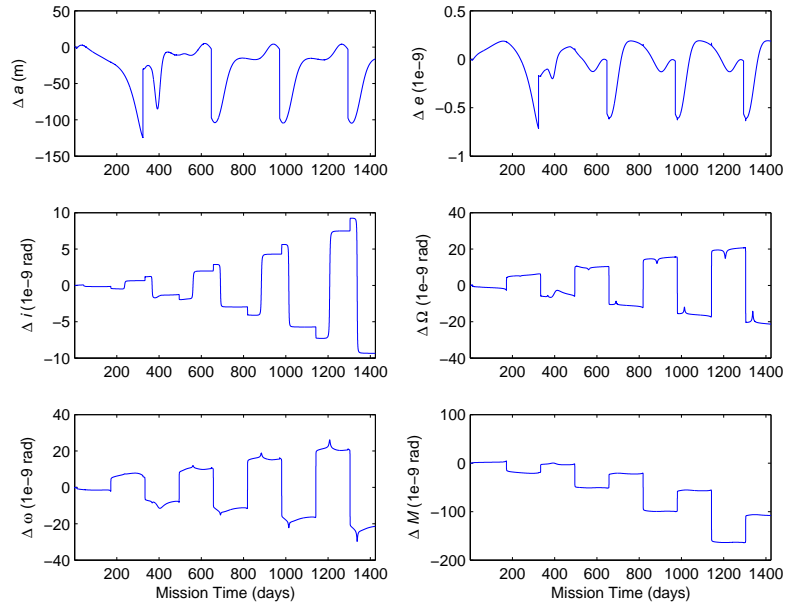
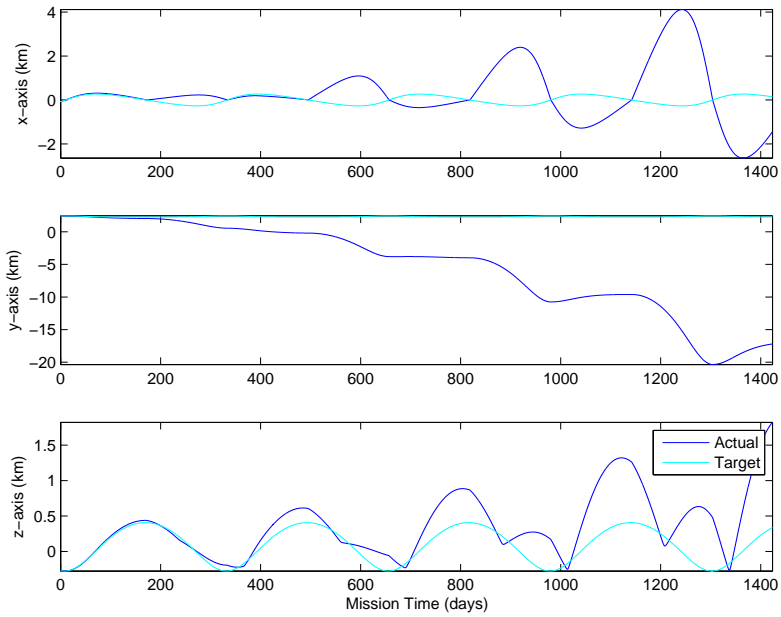


Figure 175: Least squares control law for spacecraft formation  $\delta \mathbf{k}_{5/3}$  at time step of  $\delta t = 60$  s using the fixed mirror configuration with a system efficiency of 25% and weights,  $W = [1e-6, 1e6, 1, 1, 1, 1]$ .



(a) Variations in the orbital element differences.



(b) Variations in the Hill frame components.

Figure 176: Least squares control law for spacecraft formation  $\delta \mathbf{k}_{5/4}$  at time step of  $\delta t = 60$  s using the fixed mirror configuration with a system efficiency of 25% and weights,  $W = [1e-6, 1e6, 1, 1, 1, 1]$ .

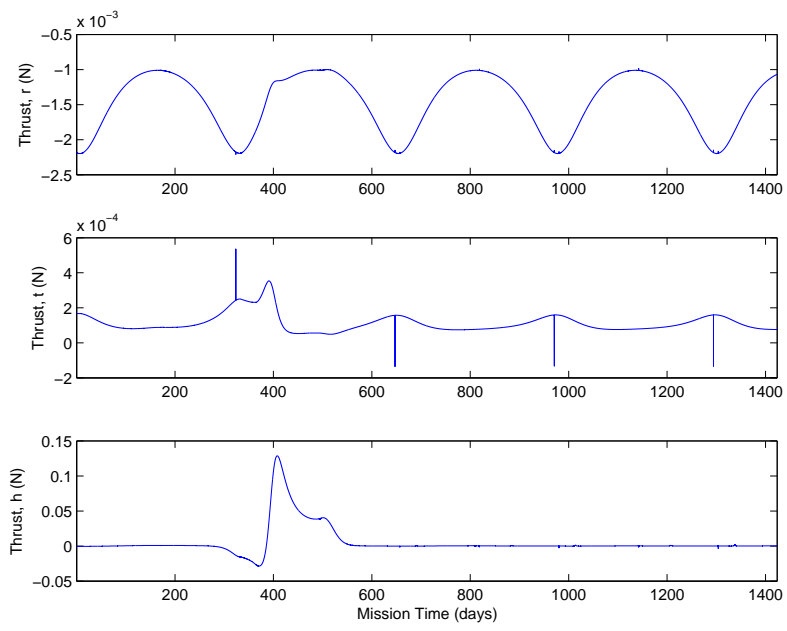
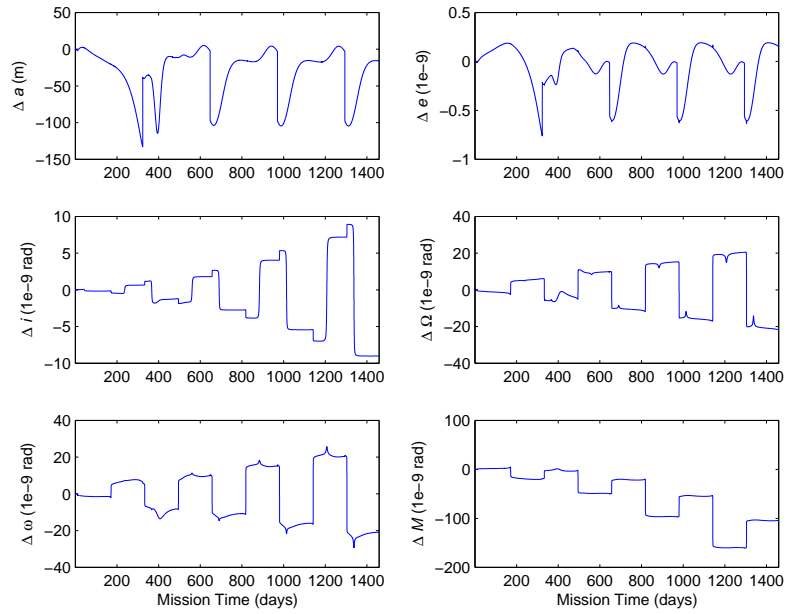
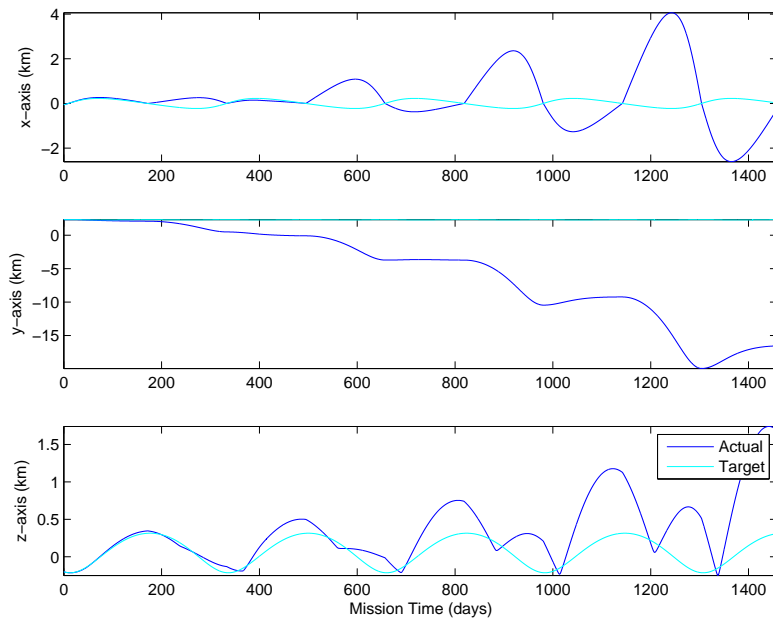


Figure 177: Least squares control law for spacecraft formation  $\delta \mathbf{k}_{5/4}$  at time step of  $\delta t = 60$  s using the fixed mirror configuration with a system efficiency of 25% and weights,  $W = [1e-6, 1e6, 1, 1, 1, 1]$ .



(a) Variations in the orbital element differences.



(b) Variations in the Hill frame components.

Figure 178: Least squares control law for spacecraft formation  $\delta \mathbf{k}_{5/5}$  at time step of  $\delta t = 60$  s using the fixed mirror configuration with a system efficiency of 25% and weights,  $W = [1e-6, 1e6, 1, 1, 1, 1]$ .

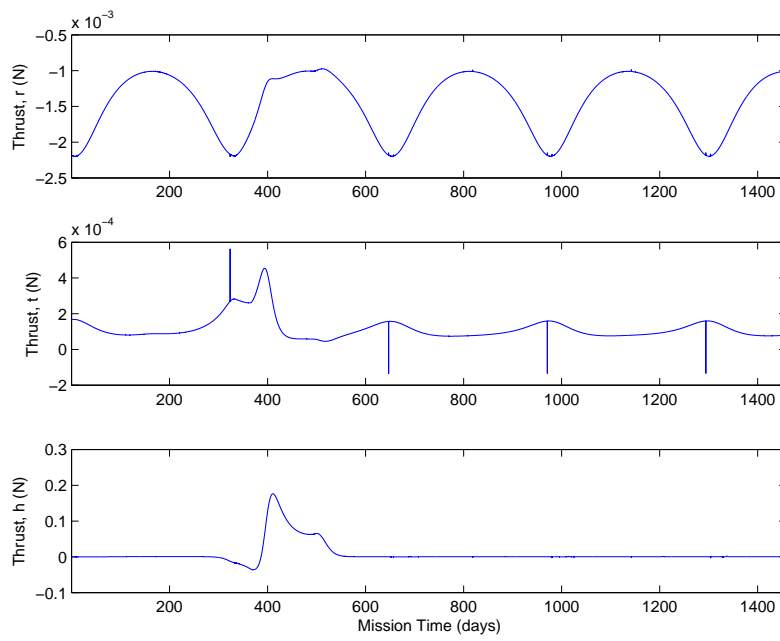
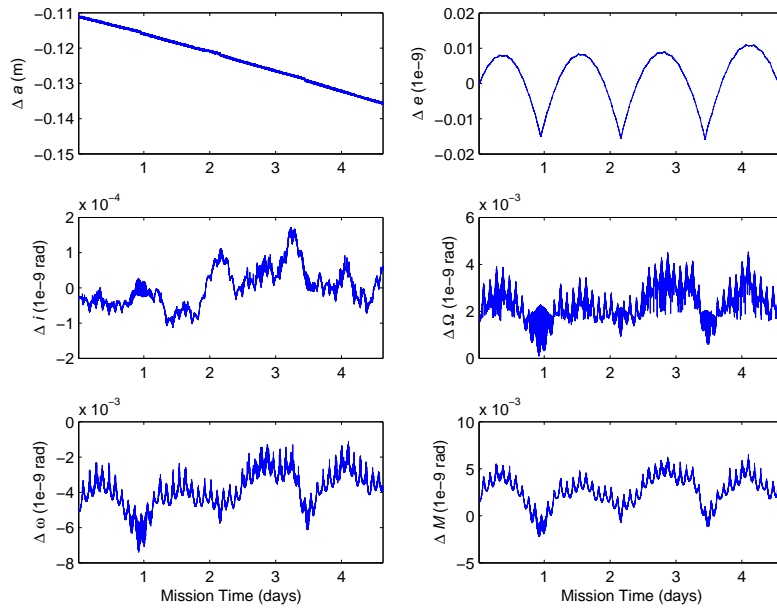
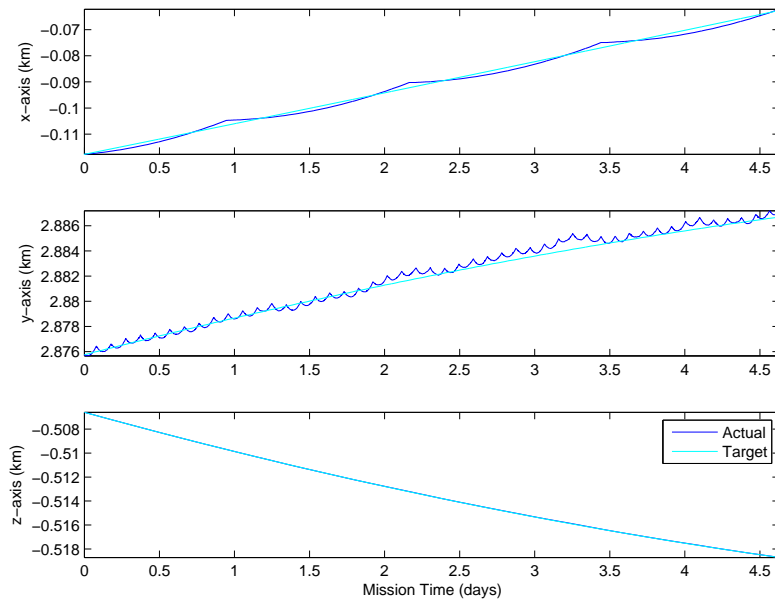


Figure 179: Least squares control law for spacecraft formation  $\delta \mathbf{k}_{5/5}$  at time step of  $\delta t = 60$  s using the fixed mirror configuration with a system efficiency of 25% and weights,  $W = [1e-6, 1e6, 1, 1, 1, 1]$ .



(a) Variations in the orbital element differences.



(b) Variations in the Hill frame components.

Figure 180: Integration control law for spacecraft formation  $\delta \mathbf{k}_{5/2}$  at time step of  $\delta t = 1$  s using the fixed mirror configuration with a system efficiency of 25%.

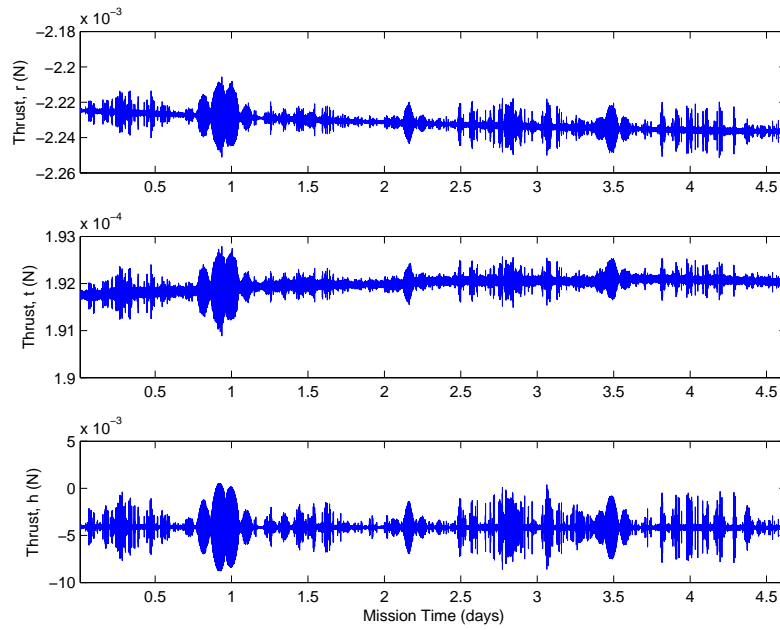
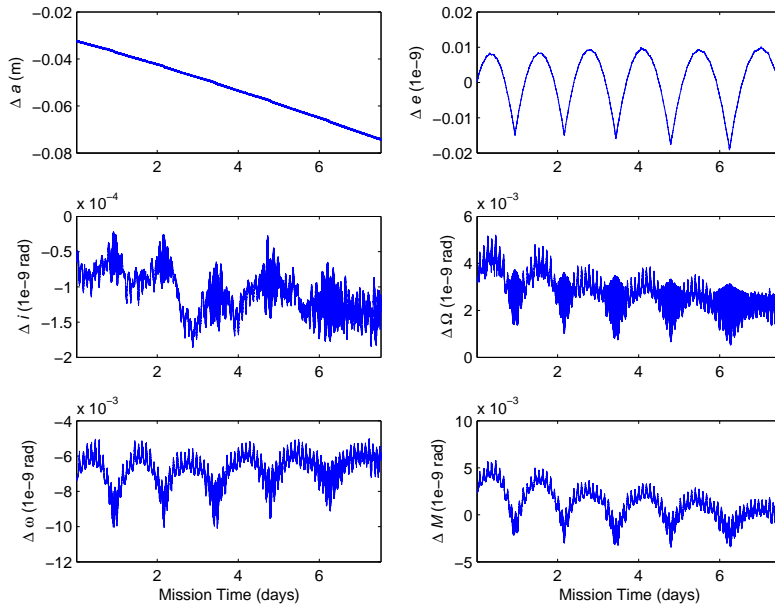
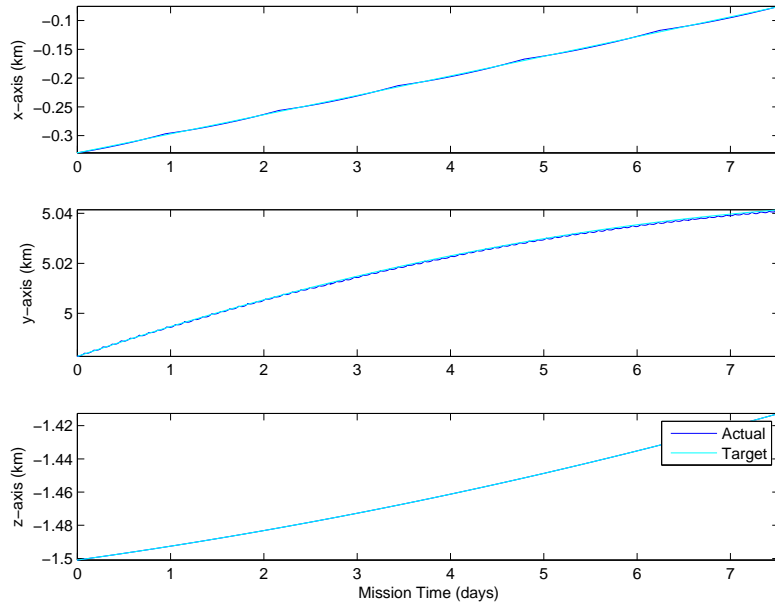


Figure 181: Integration control law for spacecraft formation  $\delta\mathbf{k}_{5/2}$  at time step of  $\delta t = 1$  s using the fixed mirror configuration with a system efficiency of 25%.



(a) Variations in the orbital element differences.



(b) Variations in the Hill frame components.

Figure 182: Integration control law for spacecraft formation  $\delta \mathbf{k}_{5/3}$  at time step of  $\delta t = 1$  s using the fixed mirror configuration with a system efficiency of 25%.

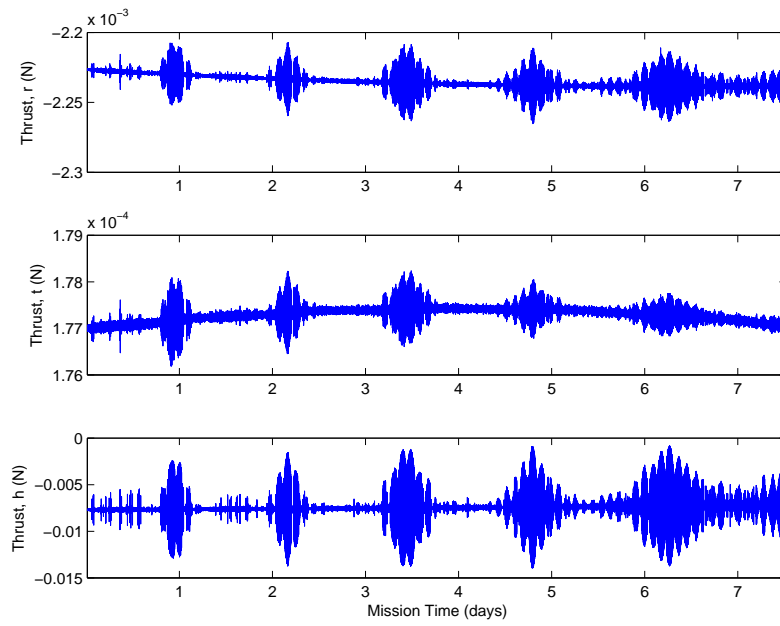
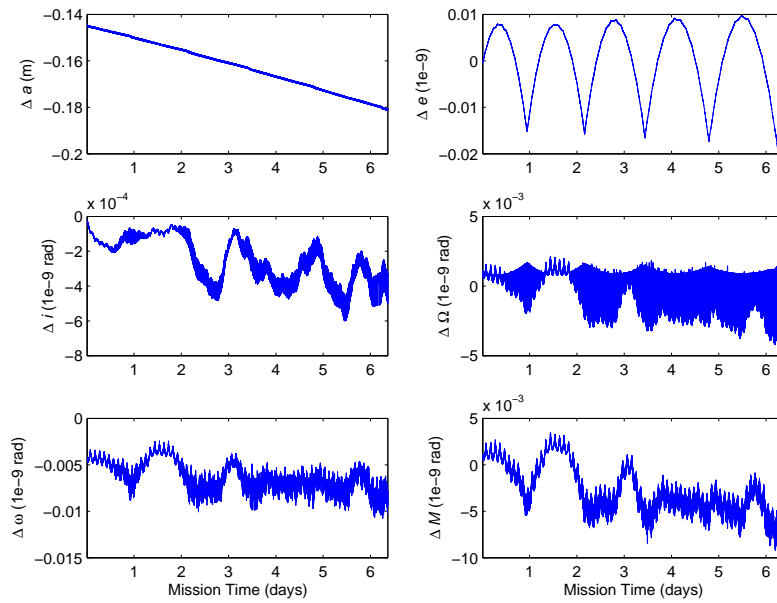
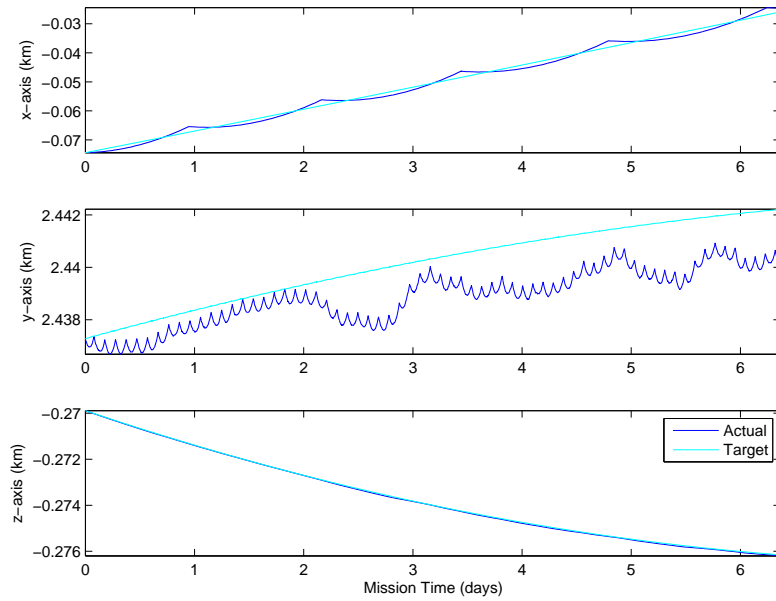


Figure 183: Integration control law for spacecraft formation  $\delta\mathbf{k}_{5/3}$  at time step of  $\delta t = 1$  s using the fixed mirror configuration with a system efficiency of 25%.



(a) Variations in the orbital element differences.



(b) Variations in the Hill frame components.

Figure 184: Integration control law for spacecraft formation  $\delta\mathbf{k}_{5/4}$  at time step of  $\delta t = 1$  s using the fixed mirror configuration with a system efficiency of 25%.

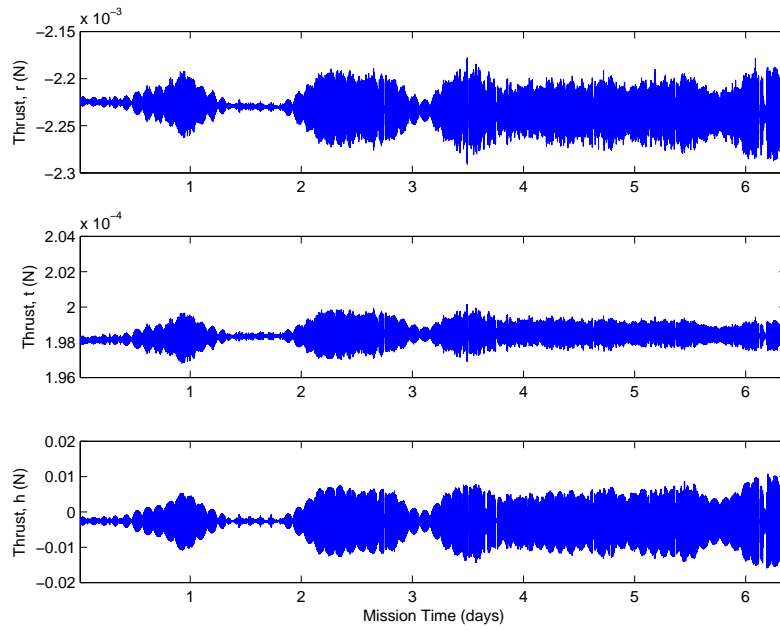
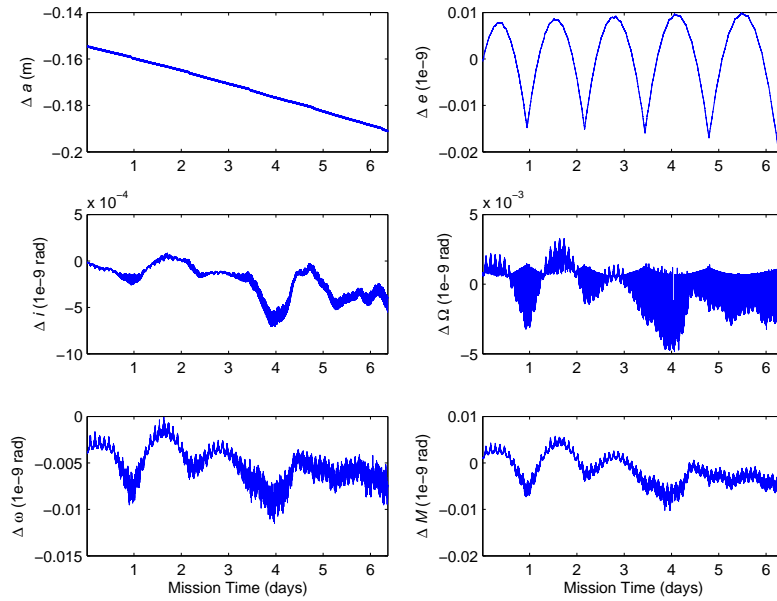
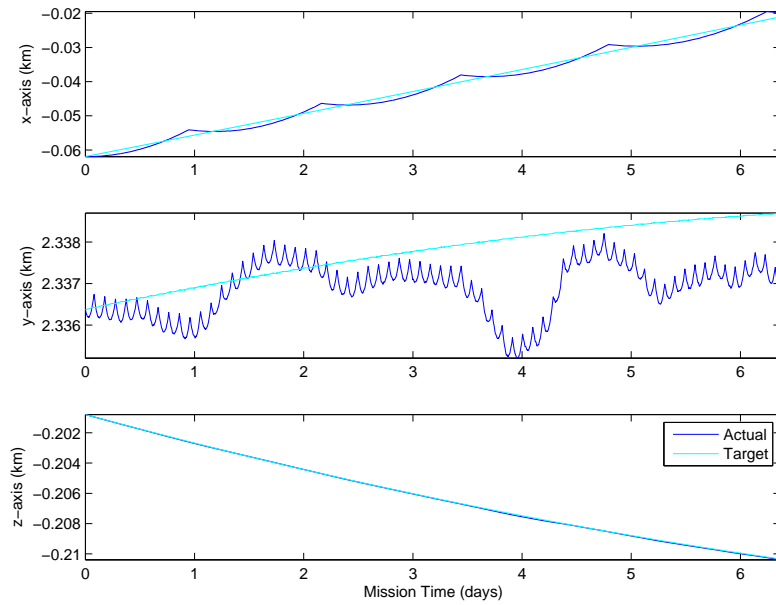


Figure 185: Integration control law for spacecraft formation  $\delta\mathbf{k}_{5/4}$  at time step of  $\delta t = 1$  s using the fixed mirror configuration with a system efficiency of 25%.



(a) Variations in the orbital element differences.



(b) Variations in the Hill frame components.

Figure 186: Integration control law for spacecraft formation  $\delta \mathbf{k}_{5/5}$  at time step of  $\delta t = 1$  s using the fixed mirror configuration with a system efficiency of 25%.

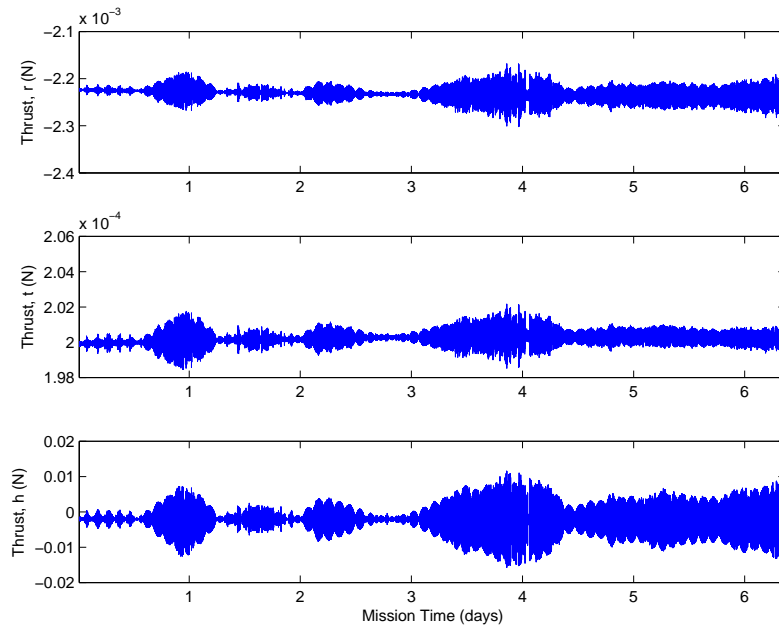
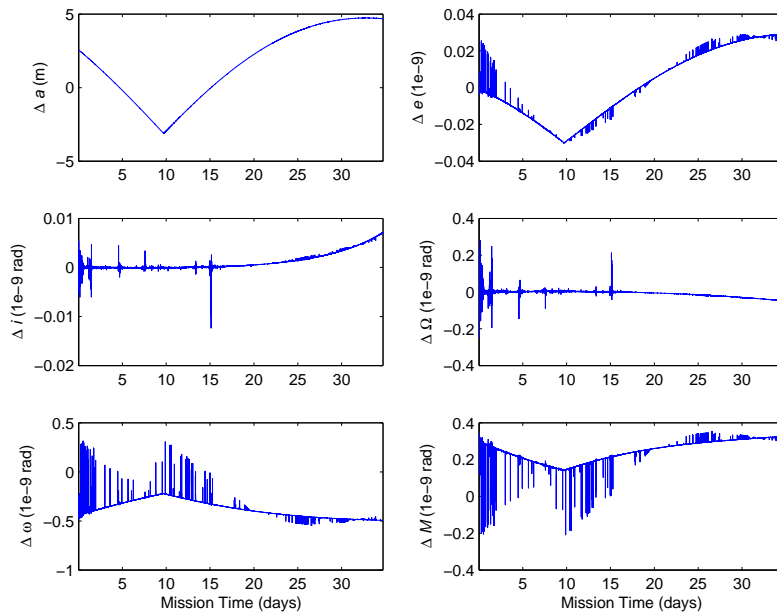
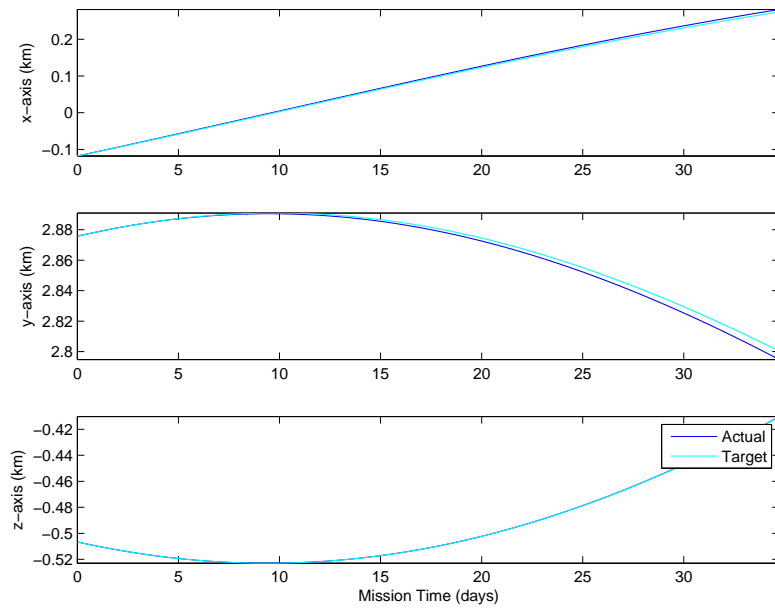


Figure 187: Integration control law for spacecraft formation  $\delta\mathbf{k}_{5/5}$  at time step of  $\delta t = 1$  s using the fixed mirror configuration with a system efficiency of 25%.



(a) Variations in the orbital element differences.



(b) Variations in the Hill frame components.

Figure 188: Integration control law for spacecraft formation  $\delta \mathbf{k}_{5/2}$  at time step of  $\delta t = 10$  s using the fixed mirror configuration with a system efficiency of 25%.

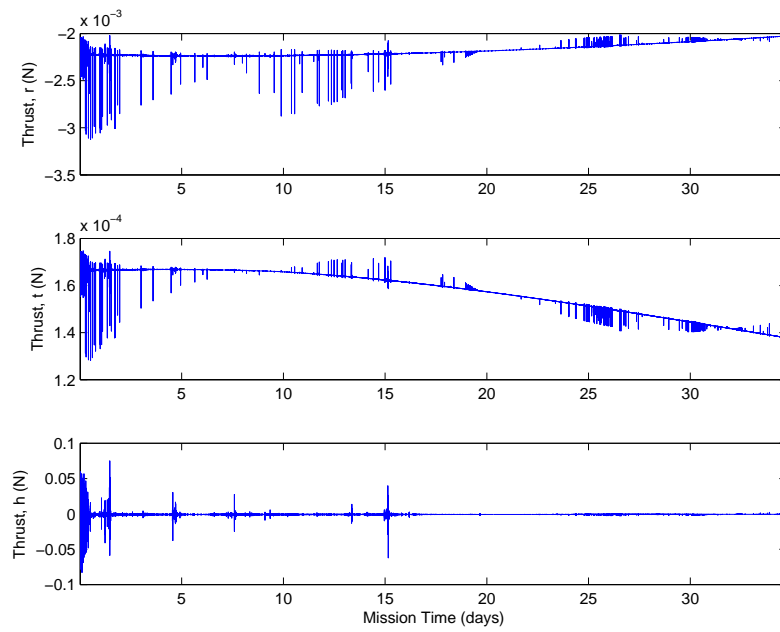
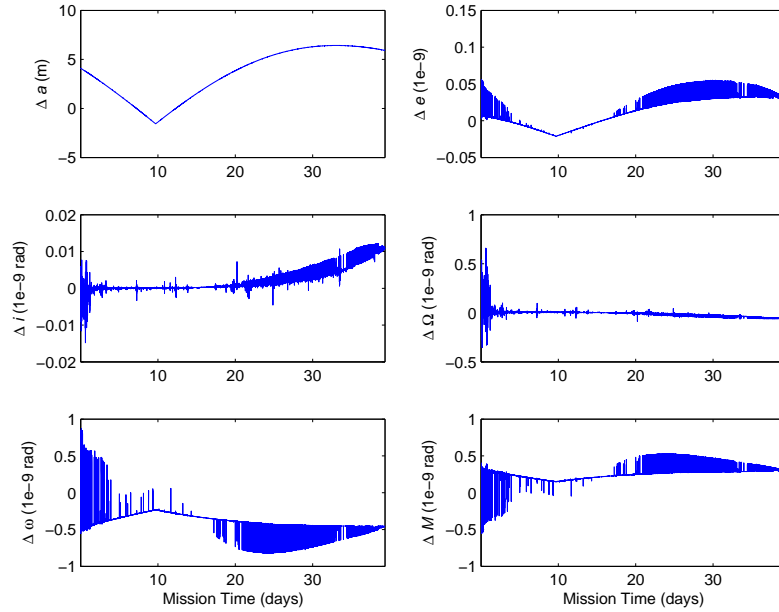
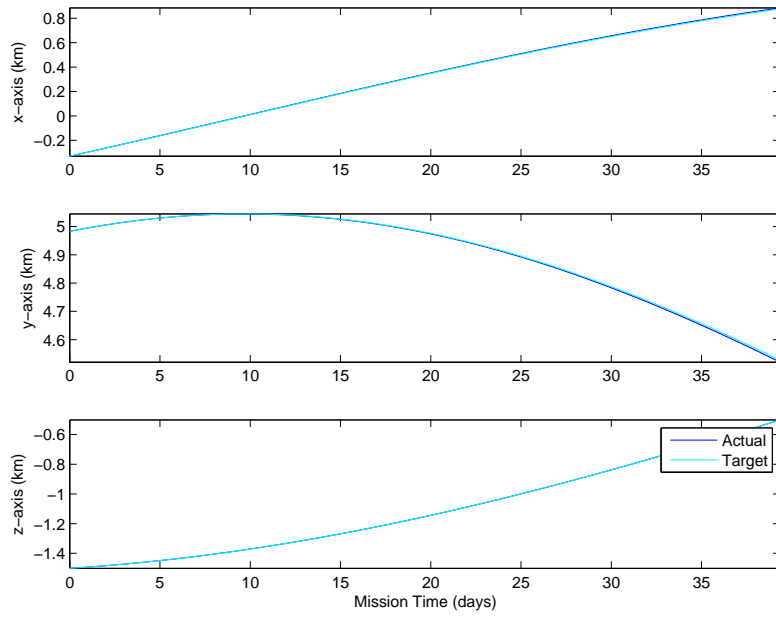


Figure 189: Integration control law for spacecraft formation  $\delta \mathbf{k}_{5/2}$  at time step of  $\delta t = 10$  s using the fixed mirror configuration with a system efficiency of 25%.



(a) Variations in the orbital element differences.



(b) Variations in the Hill frame components.

Figure 190: Integration control law for spacecraft formation  $\delta \mathbf{k}_{5/3}$  at time step of  $\delta t = 10$  s using the fixed mirror configuration with a system efficiency of 25%.

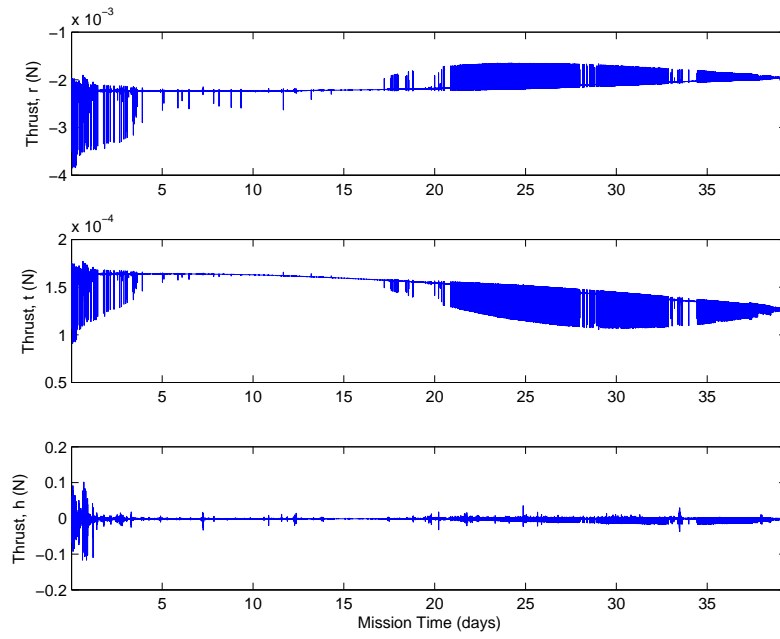
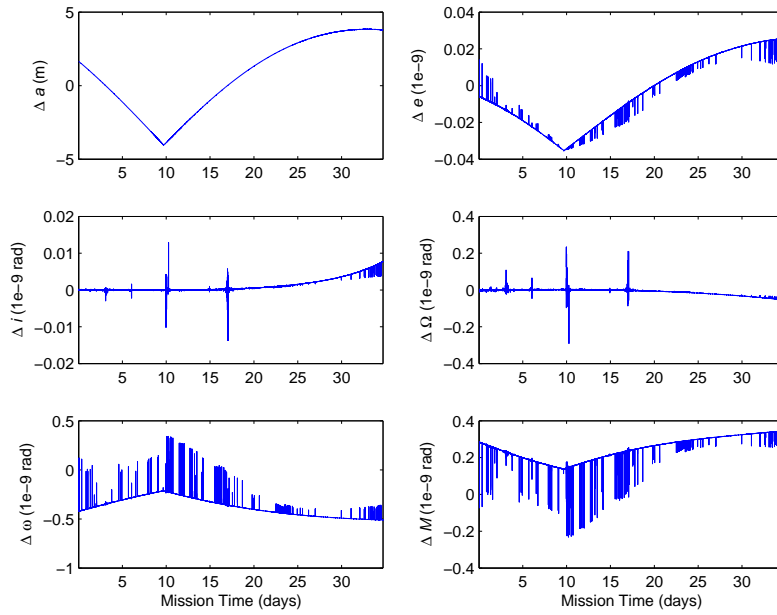
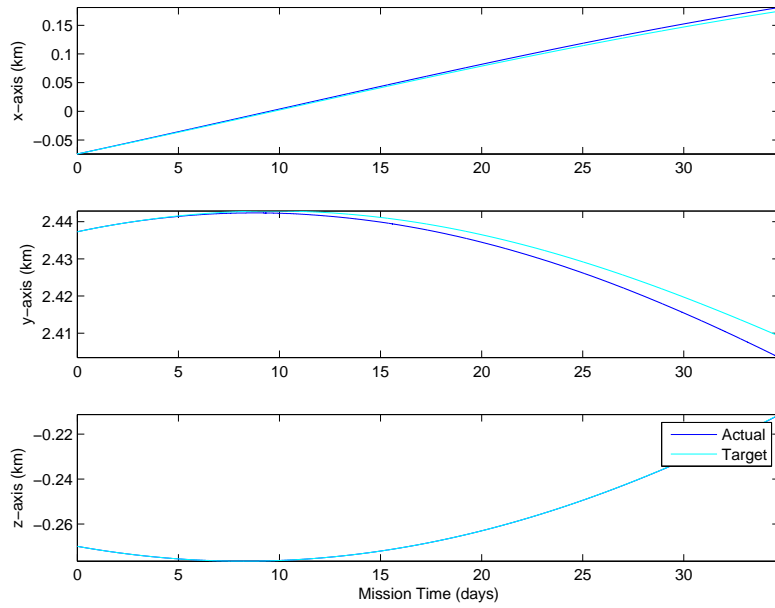


Figure 191: Integration control law for spacecraft formation  $\delta \mathbf{k}_{5/3}$  at time step of  $\delta t = 10$  s using the fixed mirror configuration with a system efficiency of 25%.



(a) Variations in the orbital element differences.



(b) Variations in the Hill frame components.

Figure 192: Integration control law for spacecraft formation  $\delta \mathbf{k}_{5/4}$  at time step of  $\delta t = 10$  s using the fixed mirror configuration with a system efficiency of 25%.

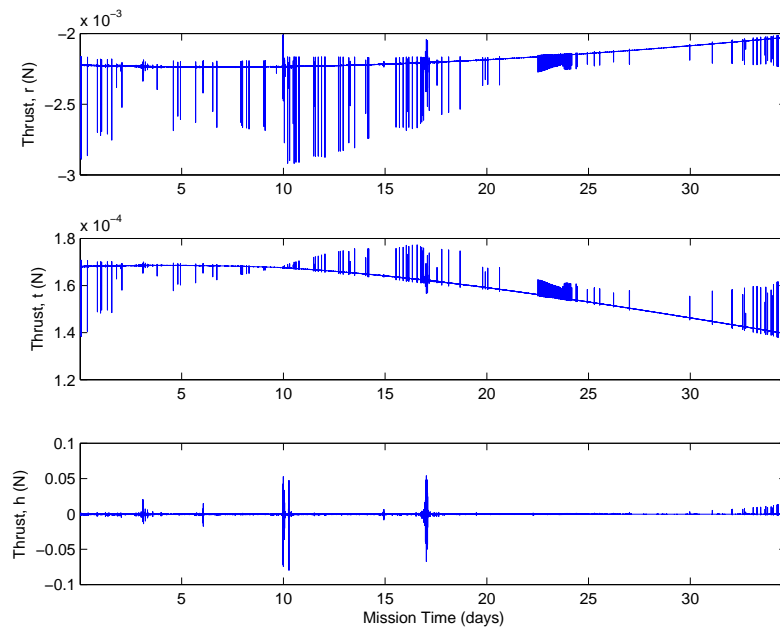
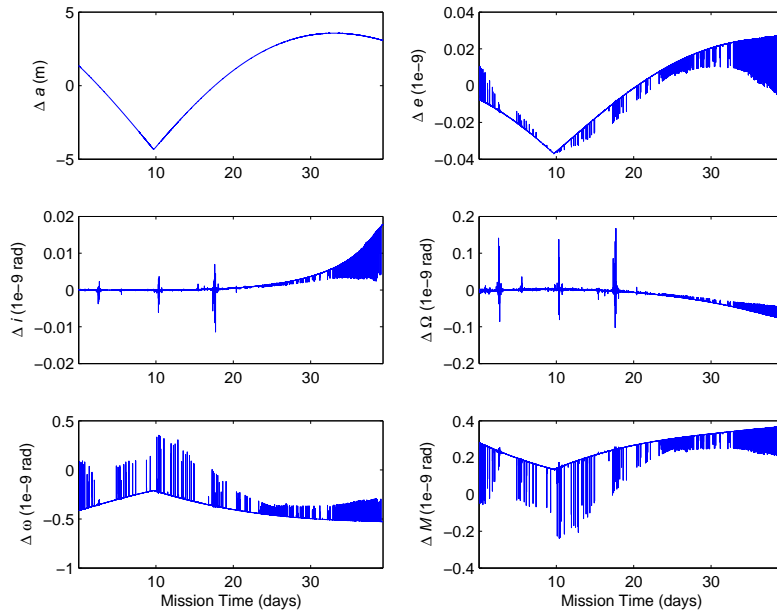
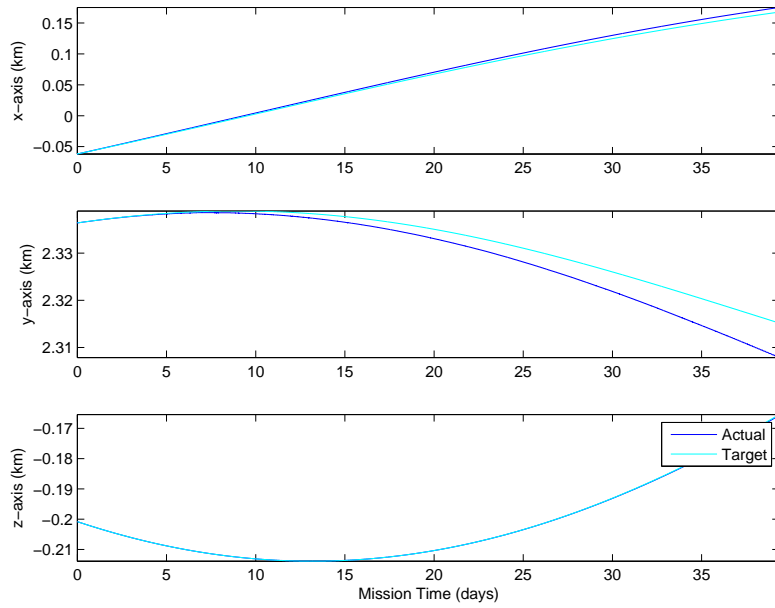


Figure 193: Integration control law for spacecraft formation  $\delta \mathbf{k}_{5/4}$  at time step of  $\delta t = 10$  s using the fixed mirror configuration with a system efficiency of 25%.



(a) Variations in the orbital element differences.



(b) Variations in the Hill frame components.

Figure 194: Integration control law for spacecraft formation  $\delta \mathbf{k}_{5/5}$  at time step of  $\delta t = 10$  s using the fixed mirror configuration with a system efficiency of 25%.

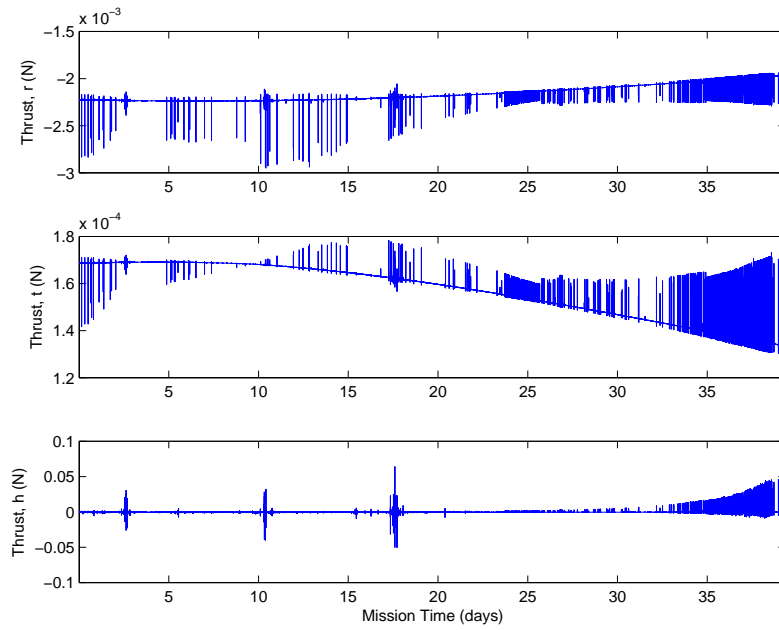
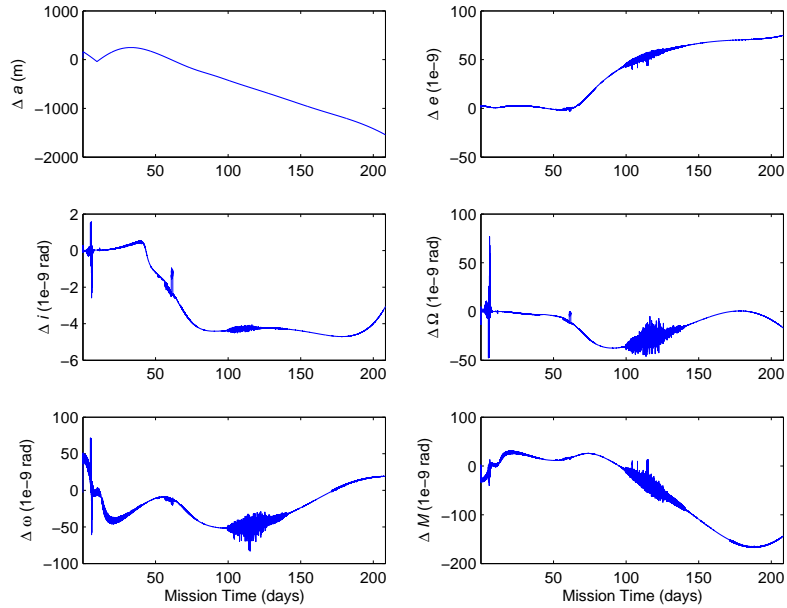
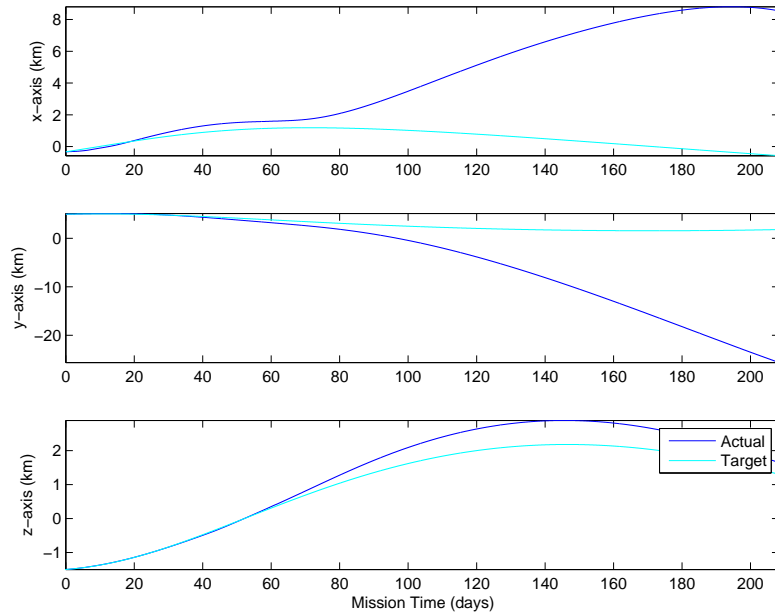


Figure 195: Integration control law for spacecraft formation  $\delta \mathbf{k}_{5/5}$  at time step of  $\delta t = 10$  s using the fixed mirror configuration with a system efficiency of 25%.



(a) Variations in the orbital element differences.



(b) Variations in the Hill frame components.

Figure 196: Integration control law for spacecraft formation  $\delta \mathbf{k}_{5/3}$  at time step of  $\delta t = 60$  s using the fixed mirror configuration with a system efficiency of 25%.

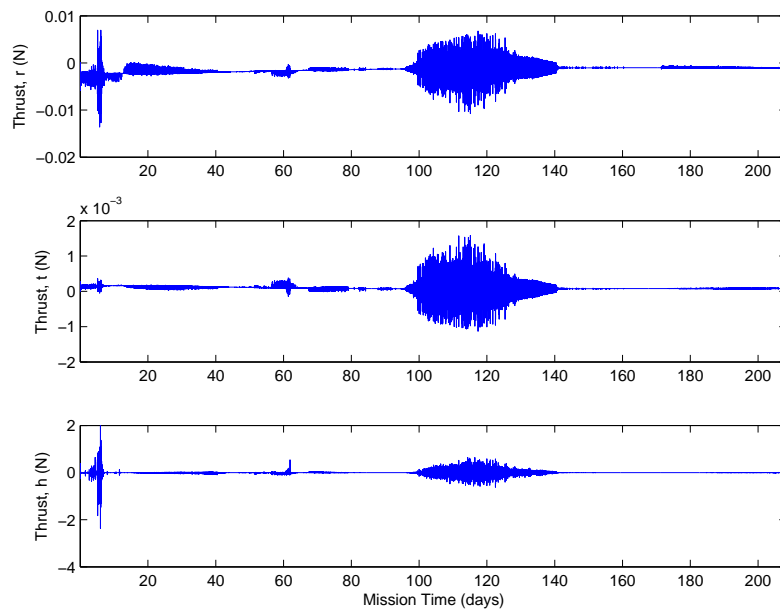
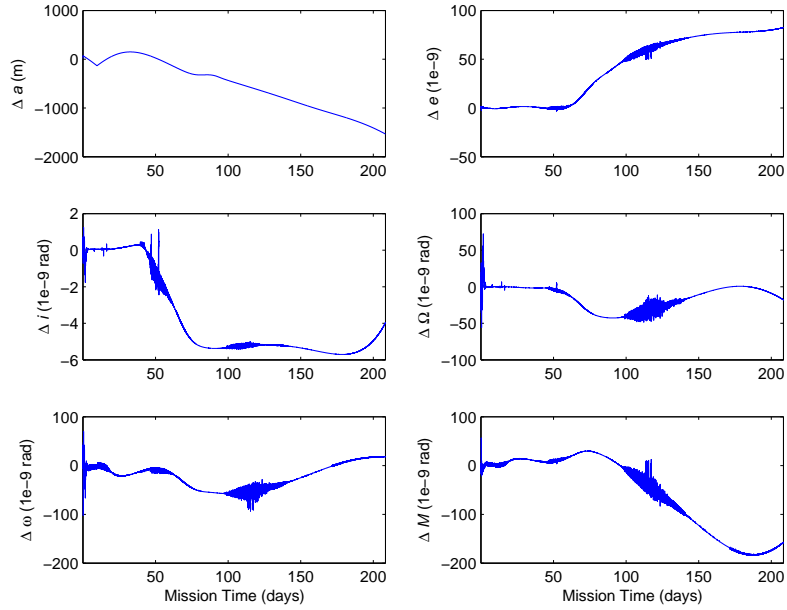
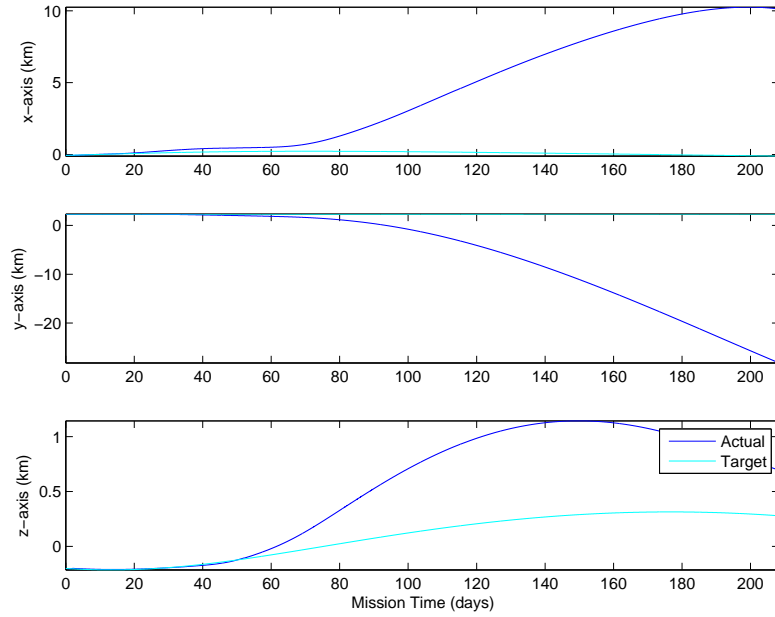


Figure 197: Integration control law for spacecraft formation  $\delta \mathbf{k}_{5/3}$  at time step of  $\delta t = 60$  s using the fixed mirror configuration with a system efficiency of 25%.



(a) Variations in the orbital element differences.



(b) Variations in the Hill frame components.

Figure 198: Integration control law for spacecraft formation  $\delta \mathbf{k}_{5/5}$  at time step of  $\delta t = 60$  s using the fixed mirror configuration with a system efficiency of 25%.

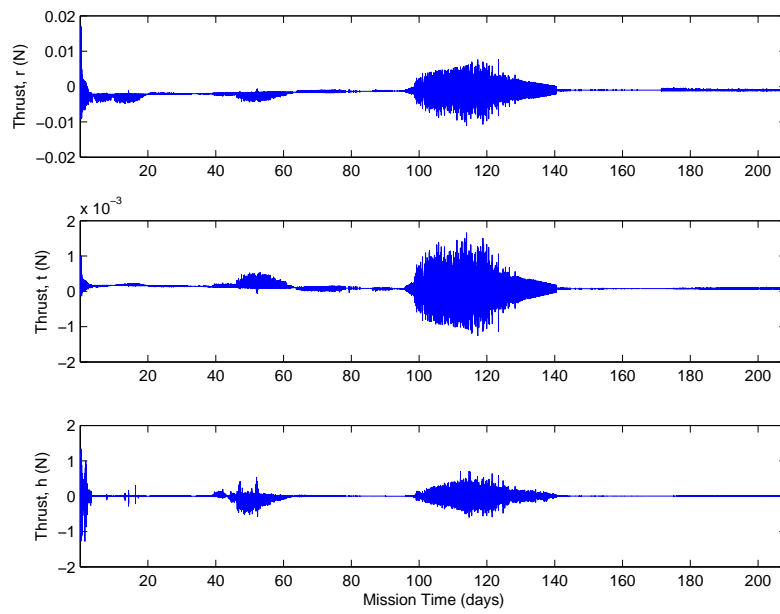


Figure 199: Integration control law for spacecraft formation  $\delta \mathbf{k}_{5/5}$  at time step of  $\delta t = 60$  s using the fixed mirror configuration with a system efficiency of 25%.

## BIBLIOGRAPHY

---

- Adams, J., Robertson, A., Zimmerman, K., and How, J. 1996. Technologies for spacecraft formation flying. In: Proceedings of the Institute of Navigation (ION) GPS-96. (Cited on page 41.)
- Adams, R. A. 2000. Calculus of several variables. Addison Wesley Longman Ltd., 4th edition. (Cited on page 17.)
- Adbel-Hadi, Y. A.-F. 2005. Development of optical concentrator systems for directly solar pumped laser systems. PhD thesis, Technischen Universität Berlin. (Cited on page 31.)
- Alfriend, K. T. and Yan, H. 2005. Evaluation and comparison of relative motion theories. *Journal of Guidance, Control and Dynamics*, 28(2):254–261. (Cited on page 44.)
- Arkin, R. C. 1998. Behavioural-based robotics. MIT Press, Cambridge, MA. (Cited on page 45.)
- Arslanturk, C. 2006. Optimum design of space radiators with temperature-dependent thermal conductivity. *Applied Thermal Engineering*, 26:1149–1157. (Cited on page 36.)
- ASTM 2006. Astme490–2000a(2006)2006: Standard solar constant and zero air mass solar spectral irradiance tables. Technical report, American Society for Testing and Materials International, West Conshohocken PA, USA. (Cited on page 20.)
- Badawy, A. and McInnes, C. R. 2009. Small spacecraft formation using potential functions. *Acta Astronautica*, 65(11–12):1783–1788. (Cited on page 45.)
- Balch, T. and Arkin, R. C. 1998. Behavior-based formation control for multirobot teams. *IEEE Transactions on Robotics and Automation*, 14(6):926–939. (Cited on page 45.)
- Battin, R. H. 1999. An Introduction to the Mathematics and Methods of Astrodynamics. AIAA Education Series, revised edition. (Cited on pages 53, 59, 174, and 194.)
- Beard, R., Lawton, J., and Hadaegh, F. 2001. A coordination architecture for spacecraft formation control. *IEEE Transactions on Control System Technology*, 9(6):777–790. (Cited on page 44.)
- Beech, M. and Steel, D. I. 1995. On the definition of the term meteoroid. *Quarterly Journal of the Royal Astronomical Society*, 36(3):281–284. (Cited on page 3.)
- Beichman, C. A., Wolf, N. J., and Lindensmith, C. A. 1999. The Terrestrial Planet Finder (TPF) : a NASA Origins Program to search for habitable planets. Number JPL 99-3. NASA Jet Propulsion Laboratory and California Institute of Technology. (Cited on page 42.)

- Bekey, I. 2002. Very large yet extremely lightweight space imaging systems. In: MacEwen, H. A. (Editor), *Highly Innovative Space Telescope Concepts*. SPIE, 4849(1):17–27. (Cited on pages 34 and 42.)
- Bennett, H. E. 2005. United States patent 6914232: Device to control laser spot size. (Cited on page 127.)
- Blake, C. and Misra, A. 2008. Dynamics and control of satellite formations using a quasi-rigid body formulation. In: *Advances in the Astronautical Sciences*, Galveston, Texas. 130:691–710. (Cited on page 45.)
- Bringhurst, R. 2002. *The Elements of Typographic Style*. Version 2.5. Hartley & Marks, Publishers, Point Roberts, WA, USA. (Cited on page xxiv.)
- Brož, M. 2006. *Yarkovsky Effect and the Dynamics of the Solar System*. PhD thesis, Faculty of Mathematics and Physics, Astronomical Institute, Charles University, Prague, Czech Republic. (Cited on page 167.)
- Burns, R., McLaughlin, C. A., Leitner, J., and Martin, M. 2000. TechSat 21: formation design, control, and simulation. In: *IEEE Aerospace Conference Proceedings*, Big Sky, Montana. 7:19–25. (Cited on page 44.)
- Bus, S. J. and Binzel, R. P. 2002. Phase II of the small main-belt asteroid spectroscopy survey. *Icarus*, 158:106–177. (Cited on page 3.)
- Bus, S. J., Vilas, F., and Barucci, M. A. 2002. Visible-wavelength spectroscopy of asteroids. *Asteroids III*, pages 169–182. (Cited on page 3.)
- Carpenter, B. and Lyons, J. 2002. Lightweight flexible solar array experiment summary. Technical report, Preliminary Technology and Science Validation Report, NASA Goddard Space Flight Center. (Cited on page 36.)
- Carter, T. E. and Humi, M. 1987. Fuel-optimal rendezvous near a point in general Keplerian orbit. *Journal of Guidance, Control and Dynamics*, 10(6):567–573. (Cited on page 47.)
- Carusi, A., Valsecchi, G. B., D’abramo, G., and Bottini, A. 2002. Deflecting NEOs in route of collision with the Earth. *Icarus*, 159(2):417–422. (Cited on page 8.)
- Chapman, C., Morrison, D., and Zellner, B. 1975. Surface properties of asteroids: A synthesis of polarimetry, radiometry and spectrophotometry. *Icarus*, 25:104–130. (Cited on page 3.)
- Chesley, S. R. 2005. Potential impact detection for near-Earth asteroids: The case of 99942 Apophis (2004 MN<sub>4</sub>). In: *Asteroids, Comets, Meteors Proceedings*. IAU Symposium, 229:215–228. (Cited on page 50.)
- Chesley, S. R., Ostro, S. J., Vokrouhlický, D., Capek, D., Giorgini, J. D., Nolan, M. C., Margot, J.-L., Hine, A. A., Benner, L. A. M., and Chamberlin, A. B. 2003. Direct detection of the Yarkovsky effect via radar ranging to asteroid 6489 Golevka. *Science*, 302:1739–1742. (Cited on page 167.)
- Chmielewski, A. B., Noca, M., and Ulvestad, J. 2000. ARISE antenna. *IEEE Aerospace Conference Proceedings*, 7:439–445. (Cited on page 34.)

- Chung, L. R. 2006. Orbit determination methods for deep space drag-free controlled laser interferometry missions. MSc thesis, University of Maryland, Maryland, USA. (Cited on page 126.)
- Clohessy, W. H. and Wiltshire, R. S. 1960. Terminal guidance system for satellite rendezvous. *Journal of Astronautical Sciences*, 29(9):653–678. (Cited on page 47.)
- Coello Coello, C. A., Lamont, G., and Van Veldhuizen, D. 2007. *Evolutionary Algorithms for Solving Multi-Objective Problems*. Springer, New York, 2nd edition. (Cited on page 184.)
- Colombo, C. 2009. Optimal trajectory design for interception and deflection of Near Earth Objects. Phd, University of Glasgow. (Cited on page 8.)
- Colombo, C., Sanchez Cuartielles, J. P., Vasile, M., and Radice, G. 2006. A comparative assessment of different deviation strategies for dangerous NEO. In: *International Astronautical Congress*, Valencia, Spain. (Cited on page 1.)
- Colombo, C., Vasile, M., and Radice, G. 2009. Semi-analytical solution for the optimal low-thrust deflection of Near-Earth Objects. *Journal of Guidance, Control and Dynamics*, 32(3):796–809. (Cited on pages 8, 34, 51, 52, 56, 68, 81, 82, and 168.)
- Conway, B. 2001. Near-optimal deflection of Earth-approaching asteroids. *Journal of Guidance, Control and Dynamics*, 24(5):1035–1037. (Cited on page 8.)
- Das, A. and Cobb, R. 1998. TechSat21space missions using collaborating constellations of satellites. In: *Small Satellite Conference*, Reston, Virginia. AIAA, (SSC98-VI-1). (Cited on page 44.)
- Deb, K., Pratap, A., and Meyarivan, T. 2000. Fast elitist multi-objective genetic algorithm: NGA-II. Technical Report 200001, KanGAL. (Cited on pages 184, 190, and 193.)
- Deb, K., Pratap, A., and Meyarivan, T. 2002. Constrained test problems for multi-objective evolutionary optimization. Technical Report 200002, KanGAL. (Cited on pages 184 and 190.)
- Delbò, M., Cellino, A., and Tedesco, E. 2007. Albedo and size determination of potentially hazardous asteroids: (99942) Apophis. *Icarus*, 188:266–269. (Cited on pages 51 and 124.)
- Elbeltagi, E., Hegazy, T., and Grierson, D. 2005. Comparison among five evolutionary-based optimization algorithms. *Advanced Engineering Informatics*, 19:43–53. (Cited on page 184.)
- Freeland, R. E., Bilyeu, G. D., Veal, G. R., Steiner, M. D., and Carson, D. E. 1997. Large inflatable deployable antenna flight experiment results. *Acta Astronautica*, 41(4–10):267–277. (Cited on page 34.)
- Fridlund, C. V. M. 2004. The Darwin mission. *Advances in Space Research*, 34:613–617. (Cited on page 42.)
- Fröhlich, C. 2003. Solar irradiance variations. In: *ISCS-2003 Symposium*, Tatranská Lomnica, Slovakia. 535:183–193. (Cited on page 21.)

- Gefert, L. and Hack, K. 1999. Low-thrust control law development for transfer from low earth orbits to high energy elliptical parking orbits. In: AIAA/AAS Astrodynamics Specialists' Conference. (AAS 99-410):1695–1712. (Cited on page 195.)
- Gill, E., D'Amico, S., and Montenbruck, O. 2007. Autonomous formation flying for the PRISMA mission. *Journal of Spacecraft and Rockets*, 44(3):671–681. (Cited on page 44.)
- Gim, D.-W. and Alfriend, K. 2003. State transition matrix of relative motion for the perturbed noncircular reference orbit. *Journal of Guidance, Control and Dynamics*, 26(6):956–971. (Cited on pages 50 and 182.)
- Hall, C. D. and Ross, I. M. 1997. Dynamics and control problems in the deflection of Near-Earth Objects. *Advances in the Astronautical Sciences*, 67(640):1–18. (Cited on page 8.)
- Hedgepeth, J. M. and Miller, R. K. 1987. Structural concepts for large solar concentrators. Contractor report 4075, NAS1-17536, NASA Langley Research Center. (Cited on page 25.)
- Hedgepeth, J. M. and Miller, R. K. 1988. Structural concepts for large solar concentrators. *Acta Astronautica*, 17(1):79–89. (Cited on page 25.)
- Hu, W. and Scheeres, D. J. 2002. Spacecraft motion about slowly rotating asteroids. *Journal of Guidance, Control and Dynamics*, 25(4):765–775. (Cited on pages 78 and 79.)
- Inalhan, G., Tillerson, M., and How, J. P. 2002. Relative dynamics and control of spacecraft formations in eccentric orbits. *Journal of Guidance, Control and Dynamics*, 25(1):48–60. (Cited on page 47.)
- Ivashkin, V. V. 2004. Possibility of using laser action on a celestial body approaching the earth. *Doklady Physics (Doklady Akademii Nauk)*, 49(8):476–479. (Original text in Russian). (Cited on page 8.)
- Izzo, D. 2005. On the deflection of potentially hazardous objects. In: AIAA/AAS Space Flight Mechanics Conference, Copper Mountain, Colorado. (Cited on page 8.)
- Kahle, R., Kührt, E., Hahn, G., and Knollenberg, J. 2006. Physical limits of solar collectors in deflecting Earth-threatening asteroids. *Aerospace Science and Technology*, 10:253–263. (Cited on pages 1, 12, 160, and 161.)
- Kapila, V., Sparks, A., Buffington, J., and Yan, Q. 1999. Spacecraft formation flying: Dynamics and control. In: American Control Conference. pages 4137–4141. (Cited on page 44.)
- Karlgaard, C. D. and Lutze, F. H. 2003. Second order relative motion equations. *Advances in the Astronautical Sciences*, 109(3):2429–2448. (Cited on page 47.)
- Kasdin, N. J., Gurfil, P., and Kolemen, E. 2005. Canonical modelling of relative spacecraft motion via epicyclic orbital elements. *Celestial Mechanics and Dynamical Astronomy*, 92(4):337–370. (Cited on page 47.)
- Kennedy, J. and Eberhart, R. 1995. Particle swarm optimization. In: IEEE International Conference on Neural Networks. pages 1942–1948. (Cited on page 184.)

- Kristiansen, R. and Nicklasson, P. J. 2009. Spacecraft formation flying: A review and new results on state feedback control. *Acta Astronautica*, 65:1537–1552. (Cited on page 44.)
- Kubota, T., Hashimoto, T., Sawai, S., Kawaguchi, J., Ninomiya, K., Uo, M., and Baba, K. 2003. An autonomous navigation and guidance system for MUSES-C asteroid landing. *Acta Astronautica*, 52:125–131. (Cited on page 120.)
- Landis, G. A. 1994. Prospects for solar pumped semiconductor lasers. In: *SPIE Laser Power Beaming*, Los Angeles CA. 2121(SPIE 2121-09):58–65. (Cited on page 32.)
- Lando, M., Kagan, J., Linyekin, B., and Dobrusin, V. 2003. A solar-pumped Nd:YAG laser in the high collection efficiency regime. *Optics Communications*, 222:371–381. (Cited on page 31.)
- Lawden, D. F. 1963. *Optimal Trajectories for Space Navigation*. Butterworths, London, UK. (Cited on page 47.)
- Lawson, P. R. 2001. The terrestrial planet finder. In: *IEEE Aerospace Conference Proceedings*, Big Sky, Montana. IEEE, 4:2005–2011. (Cited on page 42.)
- Lawton, J. 2000. A behaviour based approach to multiple spacecraft formation flying. Phd thesis, Electrical and Computing Engineering, Brigham Young University. (Cited on page 45.)
- Legge, H. and Boettcher, R. 1982. Modelling control thrust plume flow and impingement. In: *International Symposium on Rarefied Gas Dynamics*. pages 983–992. (Cited on page 160.)
- Lu, E. T. and Love, S. G. 2005. Gravitational tractor for towing asteroids. *Nature*, 438:177–178. (Cited on page 8.)
- Lunan, D. 1992. Need we protect Earth from space objects and if so, how? *Space Policy*, 8(1):90–91. (Cited on pages 1 and 11.)
- Luque, A., Martí, A., Cuadra, L., Algora, C., Wahnou, P., Salal, G., Benítez, P., Bett, A. W., Gombert, A., Andreev, V. M., Jassaud, C., Van Roosmalen, J., Alonso, J., Räuber, A., Strobel, G., Stolz, W., Bitnar, B., Stanley, C., Conesa, J., Van Sark, W., Barnham, K., Danz, R., Meyer, T., Luque-Heredia, I., Kenny, R., and Christofides, C. 2004. FULLSPECTRUM: A new PV wave making more efficient use of the solar spectrum. In: *European Photovoltaic Solar Energy Conference*, Paris, France. (Cited on page 33.)
- Maddock, C., Sanchez Cuartielles, J. P., Vasile, M., and Radice, G. 2007. Comparison of single and multi-spacecraft configurations for NEA deflection by solar sublimation. In: Belbruno, E. (Editor), *New Trends in Astrodynamics and Applications III*. American Institute of Physics, 886:303–316. (Cited on page 8.)
- Maddock, C. and Vasile, M. 2008a. Design of optimal spacecraft-asteroid formations through a hybrid global optimization approach. *Journal of Intelligent Computing and Cybernetics*, 1(2):239–268. (Cited on pages 52, 58, and 184.)
- Maddock, C. and Vasile, M. 2008b. Extension of the proximity-quotient control law for low-thrust propulsion. In: *International Astronautical Congress, Astrodynamics Symposium: Guidance and Control*, Glasgow, UK. (Cited on page 93.)

- Mauro, M. 2005. Trajectory Optimization for Spacecraft Flying in Formation. Testi di Dottorato di Ricerca in Ingegneria Aerospaziale (PhD Thesis), Politecnico di Milano. (Cited on pages 41 and 44.)
- McInnes, C. 2003. Deflection of Near-Earth Asteroids by kinetics energy impacts from retrograde orbits. *Planetary and Space Science*, 52:587–590. (Cited on page 8.)
- McInnes, C. R. 1995. Autonomous ring formation for a planar constellation of satellites. *Journal of Guidance, Control and Dynamics*, 18(5):1215–1217. (Cited on page 45.)
- McQuade, F., Ward, R., and McInnes, C. R. 2002. The autonomous configuration of satellite formations using generic potential functions. In: *International Symposium, Formation Flying, Missions and Technologies*, Toulouse, France. (Cited on page 45.)
- Melosh, H. J. and Nemchinov, I. V. 1993. Solar asteroid diversion. *Nature*, 366:21–22. (Cited on pages 1 and 11.)
- Melosh, H. J., Nemchinov, I. V., and Zetzer, Y. I. 1994. Non-nuclear strategies for deflecting comets and asteroids. In: Gehrels, T. (Editor), *Hazard due to comets and asteroids*, pages 1111–1132. University of Arizona Press. (Cited on pages 8 and 12.)
- Mitchell, J. W. and Richardson, D. L. 2003. A third order analytical solution for the relative motion with a circular reference orbit. *Journal of the Astronautical Sciences*, 51(1):1–12. (Cited on page 47.)
- Mohr, P. J., Taylor, B. N., and Newell, D. B. 2006. CODATA recommended values of the fundamental physical constants. (Cited on page xxiv.)
- Morrison, D. 2006. Asteroid and comet impacts: the ultimate environmental catastrophe. *Philosophical Transactions of the Royal Society*, 364:2041–2054. (Cited on page 7.)
- NASA Near Earth Object program 2009a. 99942 Apophis (2004 MN4) impact risk. Online database, <http://neo.jpl.nasa.gov/risk/a99942.html>. (Cited on pages 50 and 51.)
- NASA Near Earth Object program 2009b. Potentially hazardous asteroids. Online resource, <http://neo.jpl.nasa.gov/neo/pha.html>. (Cited on pages 3, 5, and 6.)
- Near-Earth Object Science Definition Team 2003. Study to determine the feasibility of extending the search for Near-Earth Objects to smaller limiting diameters. Technical report, National Aeronautics and Space Administration (NASA). (Cited on page 7.)
- nLIGHT 2006. nLIGHT demonstrates 73% wall-plug efficiency. Press Release, <http://www.nlight.net/news/releases>. (Cited on page 32.)
- Olds, J., Charania, A. C., Graham, M., and Wallace, J. 2004. The league of extraordinary machines: A rapid and scalable approach to planetary defense against asteroid impactors. Final report, NASA Institute for Advanced Concepts (NIAC) Phase I. (Cited on page 8.)
- Park, S.-Y. and Mazanek, D. D. 2005. Deflection of Earth-crossing asteroids/comets using rendezvous spacecraft and laser ablation. *Journal of Astronautical Sciences*, 53(1):21–37. (Cited on page 8.)

- Persson, S., Jacobsson, B., and Gill, E. 2005. PRISMA – demonstration mission for advanced rendezvous and formation flying technologies and sensors. In: International Astronautical Congress. (IAC-05-B5.6.B.07). (Cited on page 44.)
- Petropoulos, A. 2003. Simple control laws for low-thrust orbit transfers. In: AIAA/AAS Astrodynamics Specialists' Conference, Montana, U.S.A. AIAA. (Cited on pages 2, 93, 194, and 195.)
- Petropoulos, A. 2004. Low-thrust orbit transfers using candidate Lyapunov functions with a mechanism for coasting. In: AIAA/AAS Astrodynamics Specialists' Conference, Providence, Rhode Island. AIAA, (AIAA 2004-5089). (Cited on page 197.)
- Petropoulos, A. 2005. Refinements to the Q-law for low-thrust orbit transfers. In: AIAA/AAS Astrodynamics Specialists' Conference, California, U.S.A. AIAA. (Cited on pages 194 and 197.)
- Pizarro-Chong, A. and Misra, A. 2008. Dynamics of multi-tethered satellite formations containing a parent body. *Acta Astronautica*, 63:1188–1201. (Cited on page 45.)
- Price, K. V., Storn, R. M., and Lampinen, J. A. 2005. *Differential Evolution: A Practical Approach to Global Optimization*. Springer. (Cited on page 184.)
- Remo, J. L. 1994. Classifying and modeling NEO material properties and interactions. In: Gehrels, T., Matthews, M. S., and Schumann, A. (Editors), *Hazards due to comets and asteroids*, Space Science Series, pages 551–596. University of Arizona Press, Tucson, AZ. (Cited on page 57.)
- Reyes-Sierra, M. and Coello Coello, C. A. 2007. A study of techniques to improve the efficiency of a multi-objective particle swarm optimizer. In: *Evolutionary Computation in Dynamic and Uncertain Environments*. pages 269–296. (Cited on page 184.)
- Roberts, J. 2005. *Satellite Formation Flying for an Interferometry Mission*. PhD Thesis, College of Aeronautics, Cranfield University, United Kingdom. (Cited on page 44.)
- Rossi, A., Marzari, F., and Farinella, P. 1999. Orbital evolution around irregular bodies. *Earth, Planets, Space*, 51:1173–1180. (Cited on page 79.)
- Sai Vaddi, V. V. S. 2003. *Modelling and Control of Satellite Formations*. PhD Thesis, Texas A&M University, USA. (Cited on pages 44 and 46.)
- Sanchez Cuartielles, J. P. 2009. *Asteroid Hazard Mitigation: Deflection Models and Mission Analysis*. PhD thesis, University of Glasgow. (Cited on pages 8 and 10.)
- Sanchez Cuartielles, J. P., Colombo, C., Vasile, M., and Radice, G. 2007. A multi-criteria assessment of deflection methods for dangerous NEOs. In: Belbruno, E. (Editor), *New Trends in Astrodynamics and Applications III*. American Institute of Physics, 886:317–333. (Cited on pages 1, 14, and 87.)
- Sanchez Cuartielles, J. P., Colombo, C., Vasile, M., and Radice, G. 2009. Multi-criteria comparison among several mitigation strategies for dangerous Near Earth Objects. *Journal of Guidance, Control and Dynamics*, 32(1):121–142. (Cited on pages 9, 10, 11, 24, 34, 39, 56, 58, and 167.)

- Sanchez Cuartielles, J. P., Vasile, M., and Radice, G. 2008. On the consequences of a fragmentation due to a NEO mitigation strategy. In: International Astronautical Congress, Glasgow, UK. (IAC-08-C1.3.10). (Cited on page 11.)
- Scharf, D., Hadaegh, F., and Ploen, S. 2003. A survey of spacecraft formation flying guidance and control (Part I): Guidance. In: American Control Conference, Denver, Colorado. IEEE, pages 1733–1739. (Cited on page 44.)
- Scharf, D., Hadaegh, F., and Ploen, S. 2004. A survey of spacecraft formation flying guidance and control (Part II): Control. In: American Control Conference, Pasadena, California. IEEE, 4:2976–2985. (Cited on pages 44 and 45.)
- Schaub, H. 2004. Relative orbit geometry through classical orbit element differences. *Journal of Guidance, Control and Dynamics*, 27(5):839–848. (Cited on pages 48 and 177.)
- Schaub, H. and Alfriend, K. 2002. Hybrid cartesian and orbit element feedback law for formation flying spacecraft. *Journal of Guidance, Control and Dynamics*, 25(2):1–8. (Cited on pages 48 and 177.)
- Schaub, H. and Junkins, J. L. 2003. Analytical mechanics of space systems. AIAA Education Series. AIAA, Virginia, U.S.A., first edition. (Cited on pages 2, 48, 177, and 182.)
- Schaub, H., Vadali, S., Junkins, J. L., and Alfriend, K. 2000. Spacecraft formation flying control using mean orbit elements. *Journal of the Astronautical Sciences*, 48(1):69–87. (Cited on page 177.)
- Scheeres, D. J., Hsiao, F.-Y., and Vinh, N. X. 2003. Stabilizing motion relative to an unstable orbit: Applications to spacecraft formation flight. *Journal of Guidance, Control and Dynamics*, 26(1):62–73. (Cited on page 47.)
- Scheeres, D. J. and Schweickart, R. L. 2004. The mechanics of moving asteroids. In: Planetary Defense Conference: Protecting Earth from Asteroids, Orange County, California. AIAA. (Cited on page 8.)
- Schultz, A. C. and Parker, L. E. 2002. Multi-Robot Systems: From Swarms to Intelligent Automata. Number ISBN: 1-4020-0679-9. Kluwer Academic Publisher, The Netherlands. (Cited on page 44.)
- Schweickart, R. L. 2005. A call to (considered) action: International space development conference. Occasional Paper 0501, B612 Foundation. (Cited on page 51.)
- Schweighart, S. and Sedwick, R. 2002. High-fidelity linearized J2 model for satellite formation flight. *Journal of Guidance, Control and Dynamics*, 25(6):1073–1080. (Cited on page 47.)
- Sengupta, P. 2006. Dynamics and Control of Satellite Relative Motion in a Central Gravitational Field. PhD Thesis, Texas A&M University. (Cited on pages 44 and 47.)
- Shaltens, R. and Mason, L. 1999. 800 hours of operational experience from a 2 kWe solar dynamic system. Technical Report NASA/TM–208840, NASA John H. Glenn Research Center, Cleveland, Ohio. (Cited on page 31.)

- Shaltens, R. and Wong, W. 2007. Advanced stirling technology development at NASA glenn research center. Technical Report 44135-3191, NASA John H. Glenn Research Center, Cleveland, Ohio. (Cited on page 31.)
- Smith, L., Barrera, M. J., Campbell, E. T., Fedman, K. A., Peterson, G. E., and Smith, G. N. 2004. Deflecting a Near Earth Object with today's space technology. In: Planetary Defense Conference: Protecting Earth from Asteroids. (Cited on page 8.)
- Song, Y.-J., Park, J.-Y., and Choi, K.-H. 2007. Optimal deflection of Earth-crossing object using a power limited spacecraft. In: AIAA/AAS Space Flight Mechanics Conference, Sedona, AZ. American Astronautical Society. (Cited on pages 81 and 82.)
- Spitale, J. N. 2002. Asteroid hazard mitigation using the Yarkovsky effect. *Science*, 296:77. (Cited on page 8.)
- Tan, K.-H. and Lewis, M. A. 1997. Virtual structures for high-precision cooperative mobile robot control. *Autonomous Robots*, 4:387–403. (Cited on page 44.)
- Tedeschi, W. J., Remo, J. L., Schulze, J. F., and Young, R. P. 1995. Experimental hypervelocity impact effects on simulated planetesimal materials. *International Journal of Impact Engineering*, 17:837–848. (Cited on page 8.)
- Tholen, D. J. 1989. Asteroid taxonomic classifications. *Asteroids II*, pages 1139–1150. (Cited on page 3.)
- Tribble, A. C. 2003. *The Space Environment*. Princeton University Press, revised edition. (Cited on page 168.)
- Tschauner, J. and Hempel, P. 1965. Rendezvous zu einem in elliptischer bahn umlaufenden ziel (Rendezvous with a target in elliptic orbit). *Acta Astronautica*, 11(2):104–109. (Original language in German). (Cited on page 47.)
- Vadali, S. R., Vaddiz, S. S., and Alfriend, K. T. 2002. An intelligent control concept for formation flying satellites. *International Journal of Robust Nonlinear Control*, 12:97–115. (Cited on page 46.)
- Vallado, D. A. 2004. *Fundamentals of Astrodynamics and Applications*. The Space Technology Library. Microcosm Press and Kluwer Academic Publishers, 2nd edition. (Cited on pages 34, 47, 48, 87, and 174.)
- van Dam, E. R., Husslage, B., den Hertog, D., and H., M. 2007. Maximin latin hypercube designs in two dimensions. *Operations Research*, 55:158–169. (Cited on page 186.)
- Vasile, M. 2005a. A hybrid multi-agent collaborative search applied to the solution of space mission design problems. In: *Global Optimization Workshop*. (Cited on pages 184 and 188.)
- Vasile, M. 2005b. Robust mission design through evidence theory and multiagent collaborative search. *Annals of the New York Academy of Science*, 1065:152–173. (Cited on pages 184 and 188.)

- Vasile, M. 2008. Multi-Objective Memetic Algorithms, volume 171 of Studies in Computational Intelligence, chapter Hybrid Behavioral-Based Multiobjective Space Trajectory Optimization, pages 231–253. Springer. (Cited on pages 58, 184, and 188.)
- Vasile, M. and Colombo, C. 2008. Optimal impact strategies for asteroid deflection. *Journal of Guidance, Control and Dynamics*, 31(4):858–872. (Cited on page 8.)
- Vasile, M. and Locatelli, M. 2009. A hybrid multiagent approach for global trajectory optimization. *Journal of Global Optimization*, 44(4):461–479. (Cited on pages 184 and 188.)
- Vasile, M., Maddock, C., Radice, G., and McInnes, C. 2009a. Call for ideas: NEO Encounter 2029, NEO deflection through a multi-mirror system. Technical Report Ariadna ID: 08/4301, Contract Number: 21665/08/NL/CB, ESA/ESTEC Advanced Concepts Team. (Cited on page 34.)
- Vasile, M., Maddock, C., and Summerer, L. 2009b. Conceptual design of a multi-mirror system for asteroid deflection. In: *International Symposium on Space Technology and Science*, Tsukuba, Japan. (Cited on page 81.)
- Walker, J. 1984. Satellite constellations. *Journal of the British Interplanetary Society*, 37:559–572. (Cited on page 42.)
- Wang, J., Davis, A., Clayton, R., and Hashimoto, A. 1999. Evaporation of single crystal forsterite: Evaporation kinetics, magnesium isotope fractionation, and implications of mass-dependent isotopic fractionation of a diffusion-controlled reservoir. *Geochimica et Cosmochimica Acta*, 63(6):953–966. (Cited on page 57.)
- Wang, P. and Yang, D. 2003. The study of relative dynamics for spacecraft formation flying in eccentric orbits. *Aircraft Engineering and Aerospace Technology*, 75(3):256–261. (Cited on page 47.)
- Wang, P. K. C. and Hadaegh, F. Y. 1996. Coordination and control of multiple micro-spacecraft moving in formation. *Journal of Astronautical Science*, 44(3):315–335. (Cited on page 44.)
- Wei, J. 2002. Analysis of configuration and design and research of control for satellite groups based on two-station-system. PhD thesis, Xidian University, Xi'an, China. (Cited on page 48.)
- Weisstein, E. W. 2009. Cardinal number. *MathWorld – A Wolfram Web Resource*, <http://mathworld.wolfram.com/CardinalNumber.html>. (Cited on page 185.)
- Weksler, M. and Shwartz, J. 1988. Solar-pumped solid-state lasers. *Journal of Quantum Electronics*, 24(6):1222–1228. (Cited on pages 31 and 32.)
- Wie, B. 1998. *Space Vehicle Dynamics and Control*. Education Series. AIAA. (Cited on page 120.)
- Wua, Y.-T., Renb, J.-X., Guob, Z.-Y., and Liangb, X.-G. 2003. Optimal analysis of a space solar dynamic power system. *Solar Energy*, 74:205–215. (Cited on page 31.)
- Xiangyu, H., Hutao, C., and Pingyuan, C. 2004. An autonomous optical navigation and guidance for soft landing on asteroids. *Acta Astronautica*, 54:763–771. (Cited on page 120.)

- Yoo, S.-M., Song, Y.-J., Park, S.-Y., and Choi, K.-H. 2009. Spacecraft formation flying for earth-crossing object deflections using a power limited laser ablating. *Advances in Space Research*, 43:1873–1889. (Cited on page 8.)
- Young, C. G. 1966. A sun-pumped CW one-watt laser. *Applied Optics*, 5:993–997. (Cited on page 29.)